Doctoral Dissertation
博士論文

Building the model of redshift-space galaxy power spectrum based on machine learning and its application to SDSS data for cosmology inference
（機械学習を用いた赤方偏移空間銀河パワースペクトルのモデル構築とSDSSデータの宇宙論推定への応用）

A Dissertation Submitted for the Degree of Doctor of Philosophy

December 2020
令和２年１２月博士（理学）申請

Department of Physics, Graduate School of Science,
The University of Tokyo
東京大学大学院理学系研究科
物理学専攻

Yosuke Kobayashi
小林　洋祐

Acknowledgments

I appreciate the great and patient encouragement from Prof. Masahiro Takada, my thesis advisor, and Prof. Takahiro Nishimichi at Yukawa Institute for Theoretical Physics (YITP), Kyoto University. These two people are my main collaborators and adivisors throughout my Ph.D. program. From them I have learned many things on cosmology and verious numerical skills. I also would like to thank my collaborators, Ryuichi Takahashi, Hironao Miyatake, Ken Osato, and other members in the Dark Quest collaboration for their useful and helpful discussions. I sincerely thank both former and present members of Kavli Institute for the Physics and Mathematics of the Universe, especially Kazuyuki Akitsu, Ryoma Murata, Hiroko Niikura, Tomomi Sunayama, Youngsoo Park, Sunao Sugiyama, and Toshiki Kurita, for various warm hospitality and daily conversations.

My graduate research is supported by the Advanced Leading Graduate Course for Photon Science at the University of Tokyo. The numerical computation used in this thesis were in part carried out on the Cray XC50 supercomputer at Center for Computational Astrophysics, CfCA, of National Astronomical Observatory of Japan. The observational data used in this thesis were provided by the Sloan Digital Sky Survey collaborations.

Kashiwa, January 2021

Yosuke Kobayashi

Abstract

The redshift-space power spectrum, characterizing the three-dimensional distribution of galaxies collected by wide-area spectroscopic surveys, is one of the most powerful probes of cosmological parameters. To obtain unbiased and stringent cosmological constraints, we need a sufficiently accurate theoretical template to meet the statistical precision expected by modern large-scale surveys. At the same time, we have to make a proper treatment on the uncertainty of the galaxy bias, i.e., the relationship between the spatial pattern of the observed galaxies and the underlying density field dominated by dark matter. A standard analysis method used in the literature is to use the analytic theoretical prediction based on the perturbation theory (PT) of the large-scale structure formation, with a set of nuisance parameters that model galaxy bias. However, the PT-based models cease to be accurate on smaller scales where the PT breaks down due to strong nonlinearities, and cannot extract cosmological information contained in such scales. To tackle this problem, in this dissertation, I present the achievements in three important steps: the construction of a theoretical template, the theoretical assessment of the cosmological parameter constraints, and the cosmological parameter inference from the real survey data.

For the theoretical template, we use an ensemble of high-resolution N-body simulations for 101 flat-geometry wCDM cosmology to construct an emulation software enabling fast, accurate computations of the redshift-space power spectrum of dark matter halos that is valid up to $k_{\mathrm{max}} \simeq 0.6\,h\,\mathrm{Mpc}^{-1}$, based on a feed-forward neural network. Galaxies, at least massive, early-type galaxies, tend to reside in dark matter halos with masses larger than $10^{12}\,h^{-1}\,M_{\odot}$, which our emulator can handle. The emulated redshift-space halo power spectrum includes various nonlinear effects relevant for the clustering of the observed galaxies, that are difficult to accurately model with an analytic method such as the PT. Aided by simple recipes to connect the simulated halos to the observed galaxies, our emulator has the flexibility to express the complex galaxy formation physics and its variety among galaxy samples based on different selection criteria. The emulator-based method enables us to compute the redshift-space galaxy power spectrum for a set of input parameters at less than one CPU second. This corresponds to a factor of 10^6 reduction in computational time compared to brute-force method (run N-body simulations, identify halos, populate galaxies, and then measure the power spectrum from a mock galaxy catalog).

For the assessment of cosmological constraints, we investigate how the nuisance parameters contained in our approach affect the cosmological parameter constraints from the redshift-space galaxy power spectrum which simulates a real galaxy survey. We show that there is the cosmological information content available in the power spectrum on scales smaller than those where the PT is valid, even after the marginalization over various nuisance parameters.

For cosmology inference, we first perform validation tests of the emulator-based method by comparing the emulator-based predictions with the hypothetical power spectrum measured from mock catalogs of SDSS galaxies. We found that our method can recover the underlying cosmological parameters to within the statistical credible intervals. We also confirmed that we can obtain more stringent constraints on cosmological parameters using the power spectrum information beyond $k = 0.1\,h\,\mathrm{Mpc}^{-1}$ up to 0.2 or 0.3 $h\,\mathrm{Mpc}^{-1}$, where the PT-based models tend to break down. We then apply our method to the SDSS-III galaxy power spectrum assuming the flat ΛCDM cosmology. We obtain the constraints on cosmological parameters such as Ω_m, σ_8, and H_0, which are comparable with the recent analysis based on the PT-based method. We succeed to obtain cosmological parameter constraints from the full N-body simulation-based method for the first time, and the method developed here should be useful for upcoming surveys such as Subaru Prime Focus Spectrograph, Dark Energy Survey Instrument, *Euclid* and Roman Space Telescope.

Contents

Chapter 1

Introduction

1.1 Dark Universe

Cosmology, which is the challenge to understand the large-scale and fundamental nature of the Universe, has become a precision science. Over past a few decades, the observational constraints on the cosmological model has become very stringent based on the progress of the observational technology and enlargement of the cosmological surveys. In particular, the cosmic microwave background (CMB) and the large-scale structure of the Universe is the main cosmological probes, are investigated in various satellite or ground-based surveys.

The discovery by Edwin Hubble in 1929 revealed that the universe is expanding, and the distance r to our nearby galaxy is related to its recession velocity v as

$$v = cz = H_0 r, \tag{1.1}$$

where c is the speed of light, z is the redshift, and H_0 is the constant which we call as the Hubble constant today. To explain the expanding Universe, cosmologists introduced the cosmological constant to the Einstein equation, which Albert Einstein once introduced to realize the static Universe. In the late 1990s, a research group led by Saul Perlmutter and another one led by Adam Riess and Brian P. Schmidt discovered that the cosmological constant is significantly non-zero and the expansion of the Universe is accelerated, through the observation of Type Ia supernovae. Although more than two decades has passed since its observational discovery, the physical process of accelerated expansion remains to be elucidated. Some cosmologists attribute it to an unknown energy component of the Universe, and call it the dark energy. Other people are struggling to explain the accelerated expansion by modifying the General Relativity.

On the other hand, the matter component which suppress the expansion by the gravity, also has a mystery. In the 1930s, Fritz Zwicky noticed that the apparent velocities of galaxies in the Coma Cluster have a large variance. This velocity dispersion was much larger than that calculated from the number of galaxies and its average mass, and it suggested the existence of some “dark” mass which cannot be detected by light. Later, the galactic rotation curves, which are the profiles of rotation velocity of stars and gas within a galaxy as a function of distance from the galactic center, were found to be flat at at very large distances. This flat rotation curve convinced the existence of dark matter.

Today, the cosmological model which has these two dark components is strongly supported by the results of various cosmological probes, such as the cosmic microwave background (CMB) and the large-scale structure of the Universe. The cosmological model with the cold dark matter and the dark energy in the form of cosmological constant, i.e., the so-called ΛCDM model, has been the concordance model during the past two decades. One of the most important goal in modern cosmology is to determine the parameters which characterize ΛCDM model, or to falsify the ΛCDM model. To this end, we focus on the galaxy clustering on the large-scale structure.

1.2 Cosmology with galaxy clustering

One of the powerful observation of cosmology is the three-dimensional spatial distribution of galaxies spread over the large-scale structure, i.e., the galaxy clustering (see Fig. 1.1). Since the 1980s, the galaxy redshift surveys (spectroscopic surveys) have been conducted to observe the three-dimensional galaxy maps, by measuring the angular postions and spectroscpic redshifts of galaxies. The fist galaxy redshift surveys is the CfA Redshift Survey [1], completed in 1981, observing about 2400 galaxies and it reported the characteristic structures such as filaments and voids. In 1998, the Sloan Digital Sky Survey (SDSS) [1], targeting over 1,000,000 galaxies, was started. The SDSS spectroscopic survey for the first time detected the Baryon Acoustic Oscillation which makes the characteristcic bump in the measured correlation function of galaxies, and also succeeded to constrain the cosmological parameters from the galaxy clustering. Now, to further elucidate the fundamental cosmology and to make more stringent tests of the standard ΛCDM model, there are a number of ongoing and upcoming wide-area galaxy redshift surveys, e.g., the SDSS-III Baryon Oscillation Spectroscopic Survey [BOSS] [2], the SDSS-IV extended Baryon Oscillation Spectroscopic Survey [3], the Subaru Prime Focus Spectrograph [4], the Dark Energy Spectroscopic Instrument [5], the ESA *Euclid* satellite mission [6], and the NASA Roman Space Telescope [7].

The galaxy distributions observed by spectroscopic surveys are modulated by the Doppler effect due to the line-of-sight peculiar velocities of galaxies, and exhibits characteristic anisotropies, called the redshift-space distortions (RSD) [8, 9, 10]. The RSD effect is useful to improve cosmological constraints by breaking degeneracies between the cosmological parameters and uncertainties in galaxy bias relative to the underlying matter distribution.

In order to exploit the full information from galaxy redshift surveys, we need a sufficiently accurate theoretical template that enables a high-fidelity comparison with the measured clustering statistics of galaxies to obtain robust constraints on

---

[1] `https://www.sdss.org`

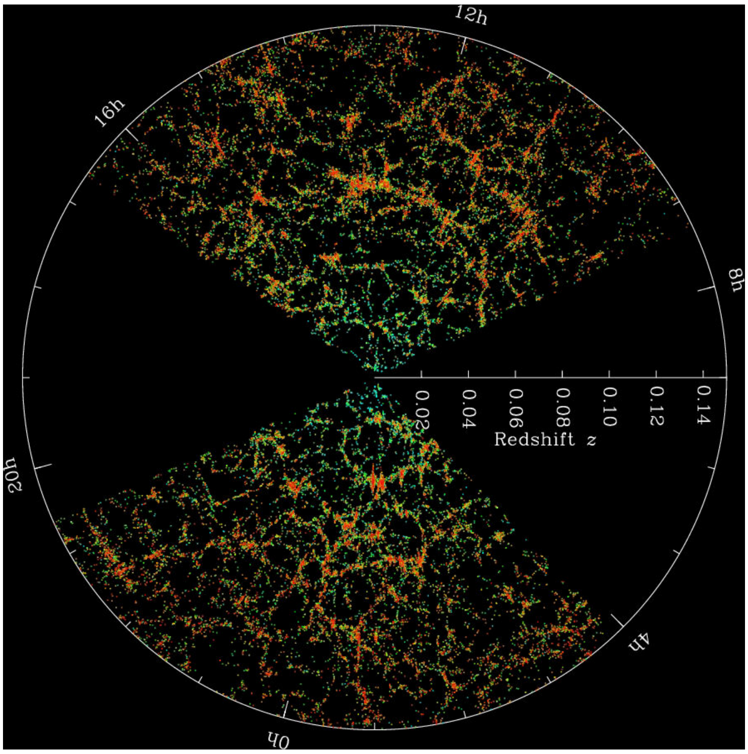

Figure 1.1: A thin slice of three-dimensional galaxy map observed in the SDSS-III Baryon Oscillatio Spectroscopic Survey [2]. Taken from `http://www.sdss3.org/science/`.

cosmological parameters. The standard approach has been analytic prescriptions based on the perturbation theory of large-scale structure [11, 12]. This approach describes the distribution of galaxies in terms of a series expansion of both the matter density and velocity fields with a set of free coefficients/terms including bias parameters [13, 14]. A further refined model enforcing the mass and momentum conservations, the so-called Effective Field Theory of Large-Scale Structure, has also been developed [15]. These models have been applied to actual data sets to obtain cosmological constraints [16, 17, 18, 19, 20, 21]. While these perturbation theory-based templates give useful predictions at linear and quasi-nonlinear scales up to $k \sim 0.2\,h\,\mathrm{Mpc}^{-1}$, the application of these models to on even smaller scales is still disturbed by even higher-order contributions of both the density and velocity fields as well as nonperturbative effects arising from the small-scale dynamics, i.e., formation of galaxies (or dark matter halos) [22, 23, 24, 25, 26, 27, 28]. Consequently, the cosmological analysis on the galaxy power spectrum has been typically limited to the wave number $k \lesssim 0.15\ h\,\mathrm{Mpc}^{-1}$ [18, 17]. In other words, the clustering information on the higher-k scales does not seem useful for cosmology in this method, because the information is used to basically constrain higher-order bias parameters and other nuisance parameters that need to be introduced for the theoretical consistency of models.

1.3 Aim of this thesis

In this thesis, we take an alternative approach to the galaxy clustering cosmology. We develop a simulation-based theoretical template, called *emulator*, with the aim to obtain accurate model predictions for redshift-space galaxy power spectrum.

Our basic philosophy is similar to that of Dark Quest [29]; it is based on the fact that the redshift-space power spectrum of halos can be accurately modeled by using N-body simulations. Then, a model of the halo-galaxy connection, which a user adopts, can be combined with the emulator outputs to compute the redshift-space power spectrum of galaxies for a galaxy sample of interest. Given uncertainties in physics of galaxy formation and evolution, a large number of nuisance parameters to model the halo-galaxy connection need to be introduced and then be marginalized over to obtain unbiased constraints on cosmological parameters (also see [30, 31] for the study based on a similar motivation). Using an ensemble of the cosmological N-body simulations for 101 cosmological models in the six-dimensional parameter space of the flat wCDM cosmology around the best-fit model to the *Planck* CMB data [32], we construct an emulator for the redshift-space halo power spectrum by utilizing a feed-forward neural network. The emulator of halo power spectrum, developed in this way, includes various complicated effects on nonlinear scales. We carefully assess the performance and validation of the emulator outputs by comparing with the redshift-space power spectra directly measured from the N-body simulations in validation sets that are not used in the training.

The second aim of this thesis is to assess cosmological information content in the redshift-space power spectrum of galaxies. For this purpose, we use a suite of halo catalogs, constructed from high-resolution N-body simulations, to build mocks of galaxies that resemble the SDSS-III BOSS galaxies, using the halo occupation distribution (HOD) method [33, 34, 35, 36]. To create realistic mock catalogs, we include a number of nuisance parameters that model the relation between the distributions of galaxies and their host dark matter halos — so-called the halo-galaxy connection. We then measure the redshift-space galaxy power spectrum as our hypothetical observables of the galaxy clustering. We evaluate the sensitivity of redshift-space galaxy power spectrum to each of model parameters using different mock catalogs of galaxies that are generated from changes in each of model parameters (cosmological parameters and the halo-galaxy connection parameters). In doing this we also include apparent anisotropic clustering patterns in the redshift-space galaxy distribution that are caused if an assumed cosmological model, which needs to be employed to convert the observed angular separations and redshifts to the comoving coordinates in the clustering analysis, is different from the underlying true cosmology – the so-called Alcock-Paczyński (AP) effect [37, 38]. Thus we use the redshift-space power spectra of galaxies, measured from these mocks, to numerically evaluate the Fisher information matrix for the SDSS-like galaxies, and then assess the cosmological information content up to the quasi-nonlinear regime ($k_{\rm max} = 0.3\ h\,{\rm Mpc}^{-1}$in our exercise), after marginalization over the halo-galaxy connection parameters. Our study is somewhat based on the similar motivation to the previous works [39, 30], but our work is different in the sense that we purely rely on the N-body simulations to assess cosmological information contents inherent in the redshift-space power spectrum of host halos up to the nonlinear regime, while the previous works used the perturbation theory-based model.

As the third achievement of this thesis, we perform the cosmological analysis on the actual galaxy redshift survey data. Having an emulator-based versatile template on hand, we apply it to galaxy catalogs in the SDSS-III BOSS Final Data Release. We measure the redshift-space galaxy power spectrum by ourselves, and infer the cosmological parameters which characterize the concordance flat ΛCDM model. We also test our emulator-based analysis pipeline by using mock galaxy catalogs with different prescriptions of the halo-galaxy connection.

Outline of this thesis

This thesis is structured as follows: in Chapter 2, we briefly review the basics of the large-scale structure in the standard ΛCDM cosmology. In Chapter 3, we describe the formulation on the galaxy clustering observed by galaxy redshift surveys, and add the discription of the halo model formalism we are employing throughout this thesis. Chapter 4 is dedicated to describe the technical aspects of the power spectrum measurement, and explain how we take into account the window function effect in real surveys. In Chapter 5, we describe our development of the simulation-based emulator. which is based on Ref. [40]. Chapter 6 present our assessment of the cosmological parameters from the redshift-space galaxy power spectrum following the halo model formalism, based on Ref. [31]. Chapter 7 describes our results of the cosmology inference on the SDSS-III galaxy data, and finally in Chapter 8 we put concluding remarks.

Chapter 2

Large-Scale Structure of the Universe

In this chapter, we review the linear cosmological perturbation theory, which is well established and well describes the large-scale behavior of the fluctuations of matter and radiation.

Although the Universe on large scales is assumed to be homogeneous and isotropic at zeroth order, we actually observe that it has a complicated structure of matter or galaxy distributions. It is because the Universe is not completely homogeneous, and this inhomogeous nature is formulated as a perturbative theory.

2.1 Background Universe

The modern cosmology describes the behaviour of the Universe based on two fundamental principles:

- Cosmological Principle — The Universe is homogeneous and isotropic on large spatial scales, roughly over $\mathcal{O}(100)\,\mathrm{Mpc}$.
- General Relativity — The dynamics of the Universe is determined by the Einstein equation.

From the first assumption, the spacetime metric of the Universe is the Friedmann-Robertson-Walker (FRW) metric:

$$\mathrm{d}s^2 = -\mathrm{d}t^2 + a(t)^2\left[\frac{\mathrm{d}r^2}{1-Kr^2} + r^2(\mathrm{d}\theta^2 + \sin^2\theta\mathrm{d}\phi^2)\right], \tag{2.1}$$

where τ is the conformal time, $a(t)$ is the scale factor, which specifies the physical size of the Universe, and $a = 1$ at present. K is the constant spatial curvature, and $K > 0, K = 0$, and $K < 0$ correspond to the closed-, flat-, and open-geometry Universe. The observation of the Cosmic Microwave Background (CMB) suggests the our Universe has a flat-geometry, and hence we will often use $K = 0$ in the rest of this thesis.

2.1.1 Einstein equation

The gravitational evolution of the Universe is governed by the Einstein equation. The Einstein equation describes the relation between the geometry of the Universe and the energy components:

$$G_{\mu\nu} = 8\pi G T_{\mu\nu}, \tag{2.2}$$

where $G_{\mu\nu}$ is the Einstein tensor and $T_{\mu\nu}$ is the energy-momentum tensor. $G_{\mu\nu}$ is defined using the rich tensor $R_{\mu\nu}$ and rich scalar R as

$$G_{\mu\nu} = R_{\mu\nu} - \frac{1}{2}Rg_{\mu\nu} + \Lambda g_{\mu\nu}, \tag{2.3}$$

where $g_{\mu\nu}$ is the spacetime metric, which is the FRW metric in this case. Λ is called the cosmological constant that can cause the accelerated expansion of the Universe. The energy momentum tensor takes the form of

$$T_{\mu\nu} = (\rho + p)u_\mu u_\nu + pg_{\mu\nu}, \tag{2.4}$$

where ρ and p are the energy density and pressure of the Universe, and u_μ is the 4-velocity of the observer. In the homogeneous and isotropic Universe, it is

$$T_{\mu\nu} = \mathrm{diag}(\rho, p, p, p). \tag{2.5}$$

With Eqs. (2.1), (2.5), the (00)- and (ii)-components of the Einstein equation [Eq. (2.2)] reduce to

$$\left(\frac{\dot{a}}{a}\right)^2 = \frac{8\pi G}{3}\rho + \frac{\Lambda}{3} - \frac{K}{a^2} \tag{2.6}$$

$$\frac{\ddot{a}}{a} = -\frac{4\pi G}{3}(\rho + 3p) + \frac{\Lambda}{3}, \tag{2.7}$$

where the first one is called the Friedmann equation, which descibes the time evolution of the scale factor, i.e., the expansion history of the Universe, with the energy components.

In addition, the energy-momentum conservation, $\nabla_\mu T^\mu_\nu$, implies

$$\dot{\rho} = -3\frac{\dot{a}}{a}(\rho + p). \tag{2.8}$$

Only two among Eqs. (2.6), (2.7), and (2.8) are independent. We further impose the equation of state which relates the energy density and pressure as $P = w\rho$. w is called the equation of state parameter. The Universe consists of three main energy components with different w:

- Matter ($w = 0$) — The non-relativistic particles, e.g., the dark matter and baryon (usual matter).

- Radiation ($w = \frac{1}{3}$) — The relativistic particles, e.g., the photons and neutrinos.
- Dark energy ($w < -\frac{1}{3}$) — The energy component with negative pressure. $w = -1$ for the cosmological constant.

From Eq. (2.8), the energy densities of matter and radiation evolves as $\rho_\mathrm{m} \propto a^{-3}$ and $\rho_\mathrm{r} \propto a^{-4}$, respectively. The evolution of dark energy density depends on the w_de, in general a function of time, and is given by

$$\rho_\mathrm{de} \propto \exp\left\{-3\int \frac{\mathrm{d}a}{a}[1 + w_\mathrm{de}(a)]\right\}. \tag{2.9}$$

In the case that w_de is a constant across time, the dark energy density evolves as $\rho_\mathrm{de} \propto a^{-3(1+w_\mathrm{de})}$. Such a cosmological model is called wCDM model, for which we will construct the theoretical model in Chapter 5.

2.1.2 Redshift and cosmological distance

The distance to a distant galaxy is measured from the elongation of wavelength of light emitted from it. We define the redshift z using the rate of change of wavelength:

$$1 + z \equiv \frac{\lambda}{\lambda_0} = \frac{1}{a(t_0)}, \tag{2.10}$$

where λ is the observed wavelength of light, and λ_0 is one when the light is emitted, and $a(t_0)$ is the scale factor at which the galaxy resides.

While the redshift is the direct observable, e.g., in galaxy redshift surveys, the cosmological distance is calculated assuming some cosmological model from the redshift. In the FRW metric [Eq. (2.1)] with $\mathrm{d}\theta = \mathrm{d}\phi = 0$, the light propagates along the geodesic so that

$$\mathrm{d}^2 s = -\mathrm{d}t^2 + a^2(t)\frac{\mathrm{d}r^2}{1 - Kr^2} = 0 \Leftrightarrow \frac{\mathrm{d}t}{a(t)} = \frac{\mathrm{d}r}{\sqrt{1 - Kr^2}}. \tag{2.11}$$

We define the comoving distance as

$$\chi \equiv \int_0^r \frac{\mathrm{d}r}{\sqrt{1 - Kr^2}} = \int_{t_0}^t \frac{\mathrm{d}t}{a(t)}. \tag{2.12}$$

Here we define the Hubble parameter at cosmic time t,

$$H(t) \equiv \frac{\dot{a}(t)}{a(t)}, \tag{2.13}$$

to represent the expansion rate of the Universe. The comoving distance is also written in terms of H as

$$\chi(z) = \int_a^1 \frac{\mathrm{d}a}{a^2 H(a)} = \int_0^z \frac{\mathrm{d}z}{H(z)}. \tag{2.14}$$

In galaxy surveys, we compute the comoving coodinates of galaxies following the last expresion. Inversely, we can also write the radial distance r in the FRW metric as a function of χ,

$$r(\chi) = S_K(\chi) \equiv \begin{cases} \frac{\sin(\sqrt{K}\chi)}{\sqrt{K}} & (K > 0) \\ \chi & (K = 0) \\ \frac{\sinh(\sqrt{-K}\chi)}{\sqrt{-K}} & (K < 0) \end{cases} \tag{2.15}$$

We can also define the distance using the apparent angular size of an object. Suppose we observe the object with the length perpendicular to the line-of-sight is ℓ, whose apparent angular size is $\Delta\theta$. In the FRW metric,

$$\ell = ar\Delta\theta = \frac{r(z)}{1+z}\Delta\theta. \tag{2.16}$$

The (physical) angular diameter distance, $D_{\rm A}$, is defined as

$$D_{\rm A}(z) = \frac{\ell}{\Delta\theta} = \frac{r(z)}{1+z} = \frac{S_K(\chi)}{1+z}, \tag{2.17}$$

where we used Eq. (2.15).

2.1.3 Friedmann equation and cosmological parameters

The expansion history of the Universe is governed by the Friedmann equation, Eq. (2.6). The Friedmann equation is rewritten as

$$H^2 = \left(\frac{\dot{a}}{a}\right)^2 = \frac{8\pi G}{3}\rho. \tag{2.18}$$

Here the total energy density ρ is the sum over different energy components,

$$\rho = \rho_{\rm r} + \rho_{\rm m} + \rho_{\rm de} + \rho_K, \tag{2.19}$$

where we include the cosmological constant as the dark energy density $\rho_{\rm de}$ and also regard the curvature term as the energy density. We define the Hubble constant H_0 as the present value of Hubble parameter,

$$H_0^2 \equiv H^2(z=0) = \frac{8\pi G}{3}\rho(z=0) \equiv \frac{8\pi G}{3}\rho_{\rm cr}. \tag{2.20}$$

where we define the critical energy density $\rho_{\rm cr}$ as the present value of total energy density. We discuss the energy density of each energy component in terms of its ratio to the critical density:

$$\Omega_{i0} \equiv \frac{\rho_{i0}}{\rho_{\rm cr}} = \frac{8\pi G\rho_{i0}}{3H_0^2}, \tag{2.21}$$

where ρ_{i0} is the energy density of the component i. The density parameters are also defined as a function of time, i.e.,

$$\Omega_i(z) \equiv \frac{\rho_i(z)}{\rho_{\rm cr}(z)}, \tag{2.22}$$

where

$$\rho_{\rm cr}(z) \equiv \frac{3}{8\pi G} H^2(z). \tag{2.23}$$

The $\Omega_i(z)$ is related to Ω_{i0} as

$$\Omega_i(z) = \frac{H_0^2}{H^2(z)} \frac{\rho_i(z)}{\rho_{i0}} \Omega_{i0}. \tag{2.24}$$

The parameters such as H_0 and $\Omega_{\rm i0}$ (in the rest of this thesis we often drop "0") specify the cosmological model, and are called the cosmological parameters. Since the Hubble constant H_0 characterizes the recession velocity, it is usually in unit of km/s/Mpc. In stead of H_0, we often discuss the dimesionless Hubble constant defined as $h \equiv H_0/(100$ km/s/Mpc). Using Eq. (2.6), we can write the Hubble parameter in terms of H_0 and density parameters:

$$H^2(a) = H_0^2 \left\{ \Omega_{\rm m0} a^3 + \Omega_{\rm r0} a^4 - \Omega_{\rm K0} a^3 + \Omega_{\rm de0} \exp\left[-3 \int \frac{{\rm d}a}{a} (1 + w_{\rm de}(a)) \right] \right\}. \tag{2.25}$$

In the past Universe, the radiation is the dominant energy component. After that the radiation energy become lower than that of matter. The epoch of matter-radiation equality is

$$a_{\rm eq} = \frac{\rho_{\rm r0}}{\rho_{\rm m0}} = \frac{\Omega_{\rm r0}}{\Omega_{\rm m0}}. \tag{2.26}$$

The present radiation density $\rho_{\rm r0}$ is determined by the CMB temperature today, which leads to the determination of $\Omega_{\rm r0} h^2$. Thus substantially $a_{\rm eq}$ is determined by $\Omega_{\rm m0} h^2$. Since matter energy density drops as $\propto a^{-3}$, in the late Universe the dark energy become dominant.

2.2 Cosmological perturbation theory in Newtonian approximation

We describe the energy components that constitute the Universe — such as matter and radiation — as cosmological “fluid”. The dynamics and evolution of the cosmological fluid is driven by gravity and interactions between different components of the fluid. Since we are mainly interested in the spatial scales smaller than the horizon scale, which is $\sim 1/aH(a)$ in the comoving scale, we consider the gravity within the Newtonian picture in this section.

In Newtonian picture, the cosmological fluid follows the continuity and Euler equations.

$$\frac{\partial\rho}{\partial t} + \nabla_{\mathbf{r}} \cdot (\rho\mathbf{u}) = 0, \tag{2.27}$$

$$\left[\frac{\partial}{\partial t} + \mathbf{u} \cdot \nabla_{\mathbf{r}}\right] \mathbf{u} = -\frac{1}{\rho}\nabla_{\mathbf{r}} p - \nabla_{\mathbf{r}}\phi, \tag{2.28}$$

where ρ and p are the mass density and the pressure (respectively) of the fluid, $\mathbf{u}$ is the velocity, and ϕ is the gravitational potential. All the quantities listed above are a field which is a function of the physical coordinates $\mathbf{r}$ and the cosmic time t. The gravitational potential is determined by the Poisson equation,

$$\nabla_{\mathbf{r}}^2\phi(\mathbf{r}, t) = 4\pi G\rho_{\mathrm{tot}}(\mathbf{r}, t). \tag{2.29}$$

where ρ_{tot} is the total energy density of the Universe, which can be different from ρ, the density of fluid component we focus on.

So far we use the physical spatial coordinates for the fluid equations. In the expanding Universe, it is convenient to transform the physical spatial coordinates $\mathbf{r}$ to the comoving coordinates $\mathbf{x}$. These are related as $\mathbf{r} = a(t)\mathbf{x}$ using the scale factor $a(t)$, and the velocity field, $\mathbf{u}(t)$, is decomposed as

$$\mathbf{u}(t) = \dot{\mathbf{r}} = \dot{a}\mathbf{x} + a\dot{\mathbf{x}} \equiv \dot{a}\mathbf{x} + \mathbf{v}, \tag{2.30}$$

where we define the peculiar velocity $\mathbf{v} \equiv a\dot{\mathbf{x}}$, which is the velocity component other than the expansion of the background Universe. In this coordinate transformation, the derivatives are transformed as

$$\begin{pmatrix} \left.\frac{\partial}{\partial t}\right|_{\mathbf{r}} \\ \nabla_{\mathbf{r}} \end{pmatrix} = \begin{pmatrix} 1 & \left.\frac{\partial \mathbf{x}}{\partial t}\right|_{\mathbf{r}} \\ 0 & a^{-1} \end{pmatrix} \begin{pmatrix} \left.\frac{\partial}{\partial t}\right|_{\mathbf{x}} \\ \nabla_{\mathbf{x}} \end{pmatrix} = \begin{pmatrix} 1 & -H\mathbf{x} \\ 0 & a^{-1} \end{pmatrix} \begin{pmatrix} \left.\frac{\partial}{\partial t}\right|_{\mathbf{x}} \\ \nabla_{\mathbf{x}} \end{pmatrix}, \tag{2.31}$$

where H is the Hubble paramter. We hereafter omit subscript $\mathbf{x}$ in the derivatives in the comoving frame. Using this, we can rewrite the continuity and Euler equations as

$$\frac{\partial\rho}{\partial t} + 3H\rho + \frac{1}{a}\nabla \cdot (\rho\mathbf{v}) = 0, \tag{2.32}$$

$$\frac{\partial\mathbf{v}}{\partial t} + H\mathbf{v} + \frac{1}{a}(\mathbf{v} \cdot \nabla)\mathbf{v} = -\frac{1}{a\rho}\nabla p - \frac{1}{a}\nabla\Phi. \tag{2.33}$$

where we redefine the gravitational potential in comoving coordinates,

$$\Phi = \phi + \frac{a\ddot{a}}{2}|\mathbf{x}|^2. \tag{2.34}$$

Here we define the density and pressure fluctuations,

$$\delta(\mathbf{x},t) = \frac{\rho(\mathbf{x},t)}{\bar{\rho}(t)} - 1, \tag{2.35}$$

$$\delta p(\mathbf{x},t) = p(\mathbf{x},t) - \bar{p}(t). \tag{2.36}$$

where $\bar{\rho}(t)$ and $\bar{p}(t)$ are the mean density and pressure, which depend on the cosmic time t. The continuity and Euler equations derived above are written in terms of the fluctuations,

$$\frac{\partial\delta}{\partial t} + \frac{1}{a}\nabla\cdot[(1+\delta)\mathbf{v}] = 0, \tag{2.37}$$

$$\frac{\partial\mathbf{v}}{\partial t} + H\mathbf{v} + \frac{1}{a}(\mathbf{v}\cdot\nabla)\mathbf{v} = -\frac{1}{a\bar{\rho}(1+\delta)}\nabla\delta p - \frac{1}{a}\nabla\Phi. \tag{2.38}$$

By combining with the (ii)-component of background Einstein equation [Eq. (2.7)], the Poisson equation for Φ in the comoving coordinates is

$$\nabla^2\Phi = 4\pi G a^2(\bar{\rho}_{\rm tot}\delta_{\rm tot} + 3\delta p_{\rm tot}), \tag{2.39}$$

where $\delta_{\rm tot}$ and $\delta p_{\rm tot}$ are the density and pressure fluctuations of the total cosmological fluid. In the matter-dominated Universe, we can ignore the pressure fluctuations and Eq. (2.39) reduces to

$$\nabla^2\Phi = 4\pi G a^2\bar{\rho}_{\rm m}\delta_{\rm m}. \tag{2.40}$$

2.2.1 Jeans instability

So far we have introduced the nonlinear equations for the dynamics of cosmic fluid. Hereafter we consider the density and pressure fluctuations and $\delta p(\mathbf{x},t)$, and the velocity as small perturbations, i.e., $|\delta(\mathbf{x},t)|, |\delta p(\mathbf{x},t)|, |\mathbf{v}| \ll 1$, and ignore higher-order terms of these fluctuations. With this treatment, the continuity and Euler equations Eqs. (2.37) and (2.38) reduces to

$$\dot{\delta} + \frac{1}{a}\nabla\cdot\mathbf{v} = 0, \tag{2.41}$$

$$\dot{\mathbf{v}} + H\mathbf{v} = -\frac{1}{a\bar{\rho}}\nabla\delta p - \frac{1}{a}\nabla\Phi. \tag{2.42}$$

Combining these two and the Poisson equation [Eq. (2.39)] yields

$$\ddot{\delta} + 2H\dot{\delta} - \frac{\nabla^2(\delta p)}{a^2\bar{\rho}} = 4\pi G a^2(\bar{\rho}_{\rm tot}\delta_{\rm tot} + 3\delta p_{\rm tot}). \tag{2.43}$$

Using the sound speed defined as

$$c_{\mathrm{s}}^2 = \left(\frac{\partial p}{\partial \rho}\right)_S, \tag{2.44}$$

Eq. (2.43) is written as

$$\ddot{\delta} + 2H\dot{\delta} - \left(4\pi G\bar{\rho}\delta + \frac{c_{\mathrm{s}}^2}{a^2}\nabla^2\delta\right) = 4\pi G a^2(\bar{\rho}_{\mathrm{res}}\delta_{\mathrm{res}} + 3\delta p_{\mathrm{res}}). \tag{2.45}$$

where we define $\bar{\rho}_{\mathrm{res}}\delta_{\mathrm{res}} = \bar{\rho}_{\mathrm{tot}}\delta_{\mathrm{tot}} - \bar{\rho}\delta$ and $\delta p_{\mathrm{res}} = \delta p_{\mathrm{tot}} - \delta p$ to split the fluid component we focus on from the total fluid that generates the gravitational potential.

In the following we consider a single-component fluid and ignore the right-hand-side of the above equation. While this equation describe the evolution of density fluctuations, it contains the spatial derivative ∇, hence it is convenient to move on to the Fourier space. By defining the Fourier-space fluctuation fields,

$$\tilde{\delta}(\mathbf{k}, t) = \int \mathrm{d}^3x e^{-i\mathbf{k}\cdot\mathbf{x}}\delta(\mathbf{x}, t), \tag{2.46}$$

where we will often omit the tilde in this thesis. the evolution of the density fluctuation is

$$\ddot{\tilde{\delta}} + 2H\dot{\tilde{\delta}} - \left(4\pi G\bar{\rho} - \frac{c_{\mathrm{s}}^2 k^2}{a^2}\right)\tilde{\delta} = 0. \tag{2.47}$$

From this equation, we see the evolution of $\tilde{\delta}(\mathbf{k})$ depends on the wave number $k = |\mathbf{k}|$, and largely governed by the sign of $4\pi G\bar{\rho} - \frac{c_{\mathrm{s}}^2 k^2}{a^2}$. We define the Jeans wave number

$$k_{\mathrm{J}} = \frac{\sqrt{4\pi G a^2\bar{\rho}}}{c_{\mathrm{s}}}, \tag{2.48}$$

which yields $4\pi G\bar{\rho} - \frac{c_{\mathrm{s}}^2 k^2}{a^2} = 0$. On large scales where $k < k_{\mathrm{J}}$, the fluctuations $\tilde{\delta}(\mathbf{k})$ grow rapidly due to gravity, while on small scales where $k > k_{\mathrm{J}}$, the fluctuations decay as they oscillate due to that the pressure overwhelms the gravity.

2.2.2 Evolution of the density fluctuations

We focus on large scales where $k \ll k_{\mathrm{J}}$, fluid such as matter. Then, Eq. (2.47) leads to

$$\ddot{\delta} + 2H\dot{\delta} - 4\pi G\bar{\rho}\delta = 0. \tag{2.49}$$

This equation In the ΛCDM cosmology, the solution to this equation is

$$\delta \propto H(a),\ H(a)\int_0^a \frac{\mathrm{d}a}{a^3 H(a)^3} \tag{2.50}$$

The Hubble parameter in the late-time Universe is (by ignoring the radiation)

$$H^2(a) = H_0^2 \left[\frac{\Omega_{\mathrm{m}0}}{a^3} + \Omega_{\Lambda 0} + \frac{1 - \Omega_{\mathrm{m}0} - \Omega_{\Lambda 0}}{a^2} \right] \tag{2.51}$$

decreases as the Universe evolves, and hence only the solution

$$D_+(a) = H(a) \int_0^a \frac{\mathrm{d}a}{a^3 H^3(a)} \tag{2.52}$$

is the growing mode. We call this solution the linear growth factor, and it is also written by

$$D_+(z) = \frac{5}{2} \frac{1}{1+z} \Omega_{\mathrm{m}}(z) \int_0^1 \mathrm{d}x \left[\frac{\Omega_{\mathrm{m}}(z)}{x} + \Omega_\Lambda(z) x^2 + 1 - \Omega_{\mathrm{m}}(z) - \Omega_\Lambda(z) \right]^{-3/2}. \tag{2.53}$$

2.2.3 Peculiar velocity field

We describe the linear-theory treatment of (peculiar) velocity field, v, which is essential to understand the redshift-space distortions. Taking the rotation of linearized Euler equation [Eq. (2.42)],

$$\frac{\partial}{\partial t}(\nabla \times \mathbf{v}) + \frac{\dot{a}}{a}(\nabla \times \mathbf{v}) = 0, \tag{2.54}$$

which means the rotation of velocity $\nabla \times \mathbf{v}$ is damped as $\propto a^{-1}$ in linear theory. Thus, we can write the velocity as a field generated by some potential,

$$\mathbf{v} = -\nabla \psi(\mathbf{x}, t) \tag{2.55}$$

Combining it with the linearized continuity equation [Eq. (2.41)],

$$\nabla^2 \psi = aHf\delta, \tag{2.56}$$

where we define the linear growth rate,

$$f \equiv \frac{\mathrm{d} \ln D_+}{\mathrm{d} \ln a}. \tag{2.57}$$

In Fourier space, the velocity potential is related to the density perturbation as

$$\tilde{\psi}(\mathbf{k}, t) = -\frac{aHf}{k^2} \tilde{\delta}(\mathbf{k}, t), \tag{2.58}$$

and the Fourier-space velocity is

$$\tilde{\mathbf{v}}(\mathbf{k}, t) = -i\mathbf{k}\tilde{\psi}(\mathbf{k}, t) = aHf \frac{i\mathbf{k}}{k^2} \tilde{\delta}(\mathbf{k}, t). \tag{2.59}$$

Similarly to the linear growth factor D_+, the linear growth rate is also written using the density parameters,

$$f(z) = -1 - \frac{\Omega_\mathrm{m}(z)}{2} + \Omega_\Lambda(z) + \left\{ \int_0^1 \mathrm{d}x \left[\frac{\Omega_\mathrm{m}(z)}{x} + \Omega_\Lambda(z) x^2 + 1 - \Omega_\mathrm{m}(z) - \Omega_\Lambda(z) \right]^{-3/2} \right\}^{-1}, \tag{2.60}$$

within the ΛCDM cosmology in the late-time Universe. In addition, the linear growth rate is also well approximated by

$$f(z) \simeq [\Omega_\mathrm{m}(z)]^{0.55}. \tag{2.61}$$

In galaxy redshift surveys, the combination of linear growth rate and the variance of linear matter density fluctuations, $f\sigma_8$ is commonly constrained, as we will see later.

2.3 Correlation function and power spectrum

The cosmological information in the large-scale strucure is contained in its statistical properties, since the large-scale structure is thought to have evolved from the quantum fluctuations produced in the early Universe. In addition, the primordial fluctuations produced by the inflation is thought to be near Gaussian, and the statistical properties of a Gaussian random field is perfectly determined only by the two-point statistics. Thus, in the cosmological context, the two-point statistics is of primary importance.

2.3.1 Correlation function

The two-point correlation function of a density field is defined as

$$\xi(\mathbf{x}_1 - \mathbf{x}_2) = \langle \delta(\mathbf{x}_1) \delta(\mathbf{x}_2) \rangle \,, \tag{2.62}$$

where we assume the correlation function is invariant with respect to the spatial translations, i.e., it is a function of the difference between two spatial points, $\mathbf{x}_1$ and $\mathbf{x}_2$.

In the case of the galaxies (or other discrete tracers of matter), the two-point correlation function $\xi(\mathbf{x}_1 - \mathbf{x}_2)$ is equivalent to the “excess probability” that two galaxies is observed at two positions $\mathbf{x}_1$ and $\mathbf{x}_2$, as we see below. Suppose that we consider a galaxy distribution whose number density field is $n(\mathbf{x})$. The probability that a galaxy is in a small volume δV at a position $\mathbf{x}$ is

$$\mathrm{Prob}_1(\mathbf{x}) = \langle n(\mathbf{x}) \rangle \, \delta V = \bar{n} \delta V, \tag{2.63}$$

where we require δV to be sufficiently small so that the number of galaxies in this volume can be either zero or unity. Likewise, the joint probability that two galaxies are in small volumes $\delta V_1, \delta V_2$ at two positions $\mathbf{x}_1, \mathbf{x}_2$ (respectively) is

$$\begin{aligned}\mathrm{Prob}_2(\mathbf{x}_1, \mathbf{x}_2) &= \langle n(\mathbf{x}_1) n(\mathbf{x}_2)\rangle\, \delta V_1 \delta V_2 \\ &= \bar{n}^2 \left\langle [1+\delta(\mathbf{x}_1)][1+\delta(\mathbf{x}_2)]\right\rangle \delta V_1 \delta V_2 \\ &= \bar{n}^2 \left[1+\xi(\mathbf{x}_1 - \mathbf{x}_2)\right] \delta V_1 \delta V_2. \end{aligned} \tag{2.64}$$

In the case that the galaxies are uniformly distributed, i.e., the galaxy distribution is a (three-dimensional) Poisson process, this two-point probability is a simple multiplication of one-point probabilities,

$$\mathrm{Prob}_2(\mathbf{x}_1, \mathbf{x}_2) = \mathrm{Prob}_1(\mathbf{x}_1)\mathrm{Prob}_1(\mathbf{x}_2) = \bar{n}^2 \delta V_1 \delta V_2, \tag{2.65}$$

since the numbers of galaxies at two positions are statistically independent. By comparing Eqs. (2.64) and (2.65), we see that the two-point correlation function is also seen as the excess probability that we observe two galaxies at two different positions.

2.3.2 Power spectrum

In cosmology, from the theoretical point of view, it is useful to discuss the fluctuations in Fourier space. We consider the two-point correlation of the Fourier-space density fluctuations,

$$\begin{aligned}\langle \delta(\mathbf{k})\delta(\mathbf{k}')\rangle &= \int \mathrm{d}^3x \int \mathrm{d}^3x' e^{-\mathbf{k}\cdot\mathbf{x} - \mathbf{k}'\cdot\mathbf{x}'} \langle \delta(\mathbf{x})\delta(\mathbf{x}')\rangle \\ &= \int \mathrm{d}^3x \int \mathrm{d}^3x' e^{-\mathbf{k}\cdot\mathbf{x} - \mathbf{k}'\cdot\mathbf{x}'} \xi(\mathbf{x} - \mathbf{x}'). \end{aligned} \tag{2.66}$$

Using the translational invariance of the correlation function, the above equation reduces to

$$\begin{aligned}\langle \delta(\mathbf{k})\delta(\mathbf{k}')\rangle &= (2\pi)^3 \delta_{\mathrm{D}}(\mathbf{k}+\mathbf{k}') \int \mathrm{d}^3x e^{-i\mathbf{k}\cdot\mathbf{x}} \xi(\mathbf{x}) \\ &\equiv (2\pi)^3 \delta_{\mathrm{D}}(\mathbf{k}+\mathbf{k}') P(\mathbf{k}), \end{aligned} \tag{2.67}$$

where $\delta_{\mathrm{D}}(\mathbf{k})$ is the Dirac's delta function and we define the power spectrum $P(\mathbf{k})$. We see that the two-point correlation function and the power spectrum are the Fourier counterpart of each other,

$$P(\mathbf{k}) = \int \mathrm{d}^3x e^{-i\mathbf{k}\cdot\mathbf{x}} \xi(\mathbf{x}), \;\; \xi(\mathbf{x}) = \int \frac{\mathrm{d}k}{(2\pi)^3} e^{i\mathbf{k}\cdot\mathbf{x}} P(\mathbf{k}). \tag{2.68}$$

Assuming the rotational invariance of the corraltion function, i.e., $\xi(\mathbf{x}) = \xi(x)$ where $x = |\mathbf{x}|$, the power spectrum is also written as a function of $k = |\mathbf{k}|$ and does not depend on the direction of $\mathbf{k}$. Then Eq. (2.68) is

$$P(k) = 4\pi \int_0^\infty x^2 \mathrm{d}x \frac{\sin(kx)}{kx} \xi(x) = 4\pi \int_0^\infty x^2 \mathrm{d}x j_0(kx)\xi(x), \tag{2.69}$$

$$\xi(x) = \int_0^\infty \frac{k^2 \mathrm{d}k}{2\pi^2} \frac{\sin(kx)}{kx} P(k) = \int_0^\infty \frac{k^2 \mathrm{d}k}{2\pi^2} j_0(kx)P(k), \tag{2.70}$$

where $j_0(x)$ is the zeroth-order spherical Bessel function.

2.3.3 Evolution of linear matter power spectrum

The linear matter power spectrum is quite important to discuss a lot of cosmological probes of the large-scale structure. In this subsection, we describe its basic properties.

The power spectrum of initial density fluctuations is usually assumed to be a power law form:

$$P_{\mathrm{init}}(k) \propto k^{n_{\mathrm{s}}}, \tag{2.71}$$

where n_{s} is called the spectral tilt. n_{s} is one of the cosmological parameters. According to the discussions by Harrison [41] and Zeldovich [42], the variance of density fluctuations on the Hubble scale should be the same across time, and then n_{s} is expected to be unity. The spectrum with n_{s} is called the Harrison-Zeldovich spectrum. In addition, n_{s} is well constrained by the CMB anisotropy experiments, which also suggest $n_{\mathrm{s}} \simeq 1$.

Within the Hubble scale, the density fluctuations experience the evolution according to various physical processes, depending on the wave number. However, in linear theory the fluctuation for each $\mathbf{k}$ mode evolves independently from other modes, and hence the evolution is characterized by a simple form:

$$\delta(k, z) = T(k) \frac{D_+(z)}{D_+(z_{\mathrm{init}})} \delta(k, z_{\mathrm{init}}) \tag{2.72}$$

where $D_+(z)$ is the growing-mode linear growth factor described above, and we introduce the transfer function $T(k)$, which charaterizes the k dependence of the evolution. The shape of $T(k)$ is determined by the Einstein-Boltzmann equations of various energy components, and there is no exact simple analytic solution. The exact numerical calculation of transfer function is done using the linear Boltzmann solver such as CAMB[1] [43]. Using this, the linear matter power spectrum is evolved as

$$P(k) = \left[\frac{D_+(z)}{D_+(z_{\mathrm{init}})} \right]^2 T^2(k) P_{\mathrm{init}}(k). \tag{2.73}$$

The transfer function depends mainly on the matter-radiation equality a_{eq}. Since in the radiation-dominated era the evolution of fluctuations on subhorizon scales

---

[1] https://camb.info/

is supressed compared to those on superhorizon scales (which evolve as $\propto a^2$), the transfer function becomes smaller. In the matter-dominated era, the fluctuations on superhorizon and subhorizon scales grows at the same rate. Due to the difference between the matter and radiation-dominated era, the transfer function behaves as

$$T(k) \propto \begin{cases} 1 & (k \ll k_{\rm eq}) \\ k^{-2} & (k \gg {\rm eq}) \end{cases}, \tag{2.74}$$

where $k_{\rm eq} = a_{\rm eq} H(a_{\rm eq})$ is the Hubble scale at the matter-radiation equality. As we mentioned in Sec. 2.1.3, $a_{\rm eq}$ is determined by $\Omega_{\rm m}h^2$, and hence this shape of transfer function also mainly depends on $\Omega_{\rm m}h^2$. Aside from this behaviour, the characteristic features such as Baryon Accoustic Oscillations (BAO) is also contained in the transfer function.

2.3.4 Variance of density fluctuations

One of the cosmological parameters in which we are interested in this thesis is in the form of the variance of density fluctuations. It characterize the strength of the matter clustering. Here we describe its formulation.

Suppose we sample masses enclosed in a sphere with radius R at many points in the Universe. This mass at some point is given by

$$\begin{aligned} M &= \int_{|\mathbf{x}|<R} {\rm d}^3x \rho(\mathbf{x}) = \int_{|\mathbf{x}|<R} {\rm d}^3x \bar{\rho}[1+\delta(\mathbf{x})] \\ &= \frac{4\pi R^3}{3}\bar{\rho} + \int_{|\mathbf{x}|<R} {\rm d}^3x \bar{\rho}\delta(\mathbf{x}) \\ &\equiv \bar{M} + \delta M, \end{aligned} \tag{2.75}$$

where $\bar{\rho}$ is the mean matter density in the Universe, and we defined the mean mass $\bar{M}$ and the fluctuation δM. The mass fluctuation is expressed by

$$\frac{\delta M}{\bar{M}} = \frac{3}{4\pi R^3}\int_{|\mathbf{x}|<R} {\rm d}^3x \delta(\mathbf{x}) = \int {\rm d}^3x W_R(|\mathbf{x}|)\delta(\mathbf{x}), \tag{2.76}$$

where we introduce the window function $W_R(x)$. As the window, the top-hat window function,

$$W_R(x) = \frac{3}{4\pi R^3}\Theta(R-x), \tag{2.77}$$

using the Heaviside step function $\Theta(x)$, is typically used.

With these definitions, we can calculate the mass variance smoothed in the sphere of radius R,

$$\sigma^2(R) \equiv \left\langle \left(\frac{\delta M}{\bar{M}}\right)^2 \right\rangle = \int \frac{k^2 \mathrm{d}k}{2\pi^2} \tilde{W}^2(kR) P(k), \tag{2.78}$$

where

$$\tilde{W}^2(kR) = \int \mathrm{d}^3 x e^{-i\mathbf{k}\cdot\mathbf{x}} W_R(|\mathbf{x}|), \tag{2.79}$$

and in the case of top-hat window,

$$W(kR) = \frac{3}{(kR)^3}[\sin(kR) - kR\cos(kR)]. \tag{2.80}$$

As $\sigma^2(R)$ is in the form of an integral of power spectrum, we can see it as the amplitude of fluctuations. Conventionally, σ_8, the variance of linear fluctuations smoothed in $R = 8\,h^{-1}$ Mpc, is used as a cosmological parameter.

2.4 The nonlinear treatment of fluctuations

In linear theory, the treatment of the evolution of density and velocity fields are highly simple. This is because the evolution of each k mode is independent from other mode, within linear theory. When we consider the nonlinearity of density and velocity fields, the calculation becomes highly complicated.

The system of the continuous, Euler, and Poisson equations [Eqs. (2.37), (2.38), and (2.39)], becomes

$$\frac{\partial \delta}{\partial \tau} + \nabla \cdot [(1+\delta)\mathbf{u}] = 0, \tag{2.81}$$

$$\frac{\partial \mathbf{u}}{\partial \tau} + \left[\frac{3}{2}\frac{\Omega_\mathrm{m}(z)}{f^2(z)} - 1\right]\mathbf{u} + (\mathbf{u}\cdot\nabla)\mathbf{u} + \frac{3}{2}\frac{\Omega_\mathrm{m}(z)}{f^2(z)}\nabla\phi = 0, \tag{2.82}$$

$$\nabla^2 \phi = 0, \tag{2.83}$$

where we define the normalized velocity $\mathbf{u} = \mathbf{v}/(aHf)$ and grativational potential $\phi = 4\pi G a^2 \bar{\rho} \Phi$, and used the time variable $\tau = \ln D_+$. Furthermore, we define the velocity divergence:

$$\theta \equiv -\nabla \cdot \mathbf{u}, \tag{2.84}$$

and in Fourier space it leads to

$$\mathbf{u}(\mathbf{k}) = \frac{i\mathbf{k}}{k^2}\theta(\mathbf{k}). \tag{2.85}$$

Using the above equations, we obtain the evolution equations of nonlinear density and velocity fields:

$$\begin{aligned}
&\frac{\partial\delta(\mathbf{k})}{\partial\tau} - \theta(\mathbf{k}) \\
&= \int \frac{\mathrm{d}^3k_1}{(2\pi)^3}\frac{\mathrm{d}^3k_2}{(2\pi)^3}(2\pi)^3\delta_{\mathrm{D}}(\mathbf{k}_1+\mathbf{k}_2-\mathbf{k})\alpha(\mathbf{k}_1,\mathbf{k}_2)\theta(\mathbf{k}_1)\delta(\mathbf{k}_2), \qquad (2.86)\\
&\frac{\partial\theta(\mathbf{k})}{\partial\tau} - \frac{3}{2}\frac{\Omega_{\mathrm{m}}(z)}{f^2(z)}\delta(\mathbf{k}) + \left[\frac{3}{2}\frac{\Omega_{\mathrm{m}}(z)}{f^2(z)} - 1\right]\theta(\mathbf{k}) \\
&= \int \frac{\mathrm{d}^3k_1}{(2\pi)^3}\frac{\mathrm{d}^3k_2}{(2\pi)^3}(2\pi)^3\delta_{\mathrm{D}}(\mathbf{k}_1+\mathbf{k}_2-\mathbf{k})\beta(\mathbf{k}_1,\mathbf{k}_2)\theta(\mathbf{k}_1)\theta(\mathbf{k}_2), \qquad (2.87)
\end{aligned}$$

where we define two integration kernels,

$$\alpha(\mathbf{k}_1,\mathbf{k}_2) \equiv 1 + \frac{\mathbf{k}_1\cdot\mathbf{k}_2}{k_1^2}, \quad \beta(\mathbf{k}_1,\mathbf{k}_2) \equiv \frac{|\mathbf{k}_1+\mathbf{k}_2|^2(\mathbf{k}_1\cdot\mathbf{k}_2)}{2k_1^2k_2^2}. \qquad (2.88)$$

In Eqs. (2.86) and (2.87), the evolutions of density and velocity fields are contributed by the couplings among different wave vector modes. Due to this complicated mode coupling, the exact analytic solutions to the above evolution equations have never been derived. The standard analytic approach to this issue is the perturbative expansion of the density and velocity divergence,

$$\delta = \delta^{(1)} + \delta^{(2)} + \ldots, \qquad (2.89)$$

$$\theta = \theta^{(1)} + \theta^{(2)} + \ldots, \qquad (2.90)$$

where $\delta^{(n)}$ and $\theta^{(n)}$ are of the nth order of the linear perturbation, δ_{L}. This perturbation theory approach is highly powerful on relatively large scales (small k) where the fluctuation does not exceed $\mathcal{O}(1)$, which is typically $k \lesssim 0.2\,h\,\mathrm{Mpc}^{-1}$ at redshift $z \lesssim 1$. On the other hand, due to the truncation of higher-order terms, it tends to fail to capture the fluctuations on smaller scales where the nonlinearity becomes even severer.

In this thesis, we adopt an alternative appproach based on numerical simulations, targeting mainly on these nonlinear-scale clustering.

Chapter 3

Galaxy Clustering

In this section, we describe the galaxy clustering, which is the main probe of the large-scale structure. The galaxy clustering is the spatial distribution of galaxies on the large-scale structure, and is observed by galaxy redshift surveys. A difficulty in the galaxy clustering is that it is “biased” from the underlying matter clustering. To extract cosmological information from the observed galaxy clustering, we inevitably need to take into account the galaxy bias. In addition, there are two important effects in galaxy redshift surveys: the redshift-space distortions (RSD) and the Alcock-Paczyński (AP) effect. These effects imprint the clustering statistics measured from the three-dimensional galaxy map the distinct anisotropic patterns.

3.1 Galaxy bias

In the cosmological theory, our primary interest on the large-scale structure is in the matter distribution in the Universe, as is described in Chapter 2. However, what we can directly observe with a telescope is the distributions of galaxies, not of matter itself. There is in general some discrepancy between the distribution of matter and that of discrete objects (e.g., galaxies and halos), called “bias”.

The relation between the flactuations of matter density field δ and of the number density field of galaxies (or other discrete matter tracers) $\delta_{\rm g}$ is written with some functional of δ:

$$\delta_{\rm g}(\mathbf{x}) = \mathcal{F}_{\rm g}[\delta], \tag{3.1}$$

where $\mathcal{F}_{\rm g}$ is a functional which can depend on the whole spatial configuration of matter density field, i.e., the bias can be nonlocal. However, on large scales where the linear theory is valid, we can simply model the bias as a constant:

$$\delta_{\rm g} = b_{\rm g}\delta, \tag{3.2}$$

where the constant $b_{\rm g}$ is called linear bias.

In the case of dark matter halos, the linear bias as a function of mass is well calibrated using N-body simulations, and the fitting formulae is well universal over different cosmology and redshift. One of the well-known fitting formulae is presented in Ref. [44].

However, the galaxy distributions are governed by the complex physical process of the galaxy formation and evolution, on which we still do not have sufficient understanding. Moreover, the galaxies targeted in galaxy surveys are selected under some selection criteria, such as the color and magnitude cuts. Therefore, we cannot determine the bias of obvserved galaxies from the first principles, which is the main uncertainty on doing the cosmology using galaxy clustering.

3.2 Redshift-space distortions

A galaxy redshift survey constructs a three-dimensional map of taget galaxies, by measuring their spectroscopic redshifts and angular positions on the celestial sphere. Redshifts observed by the spectroscopy does not have their "true" values which purely come from the homogeneous and isotropic expansion of the Universe, but have a contribution of the Doppler effect of light propagated from the galaxies, arising from their peculiar motions. Due to this Doppler shift, the observed redshift z_{obs} is related to the true one z as

$$z_{\mathrm{obs}} = z + \frac{\mathbf{v}\cdot\hat{\mathbf{n}}}{a}, \tag{3.3}$$

where $\mathbf{v}$ is the peculiar velocity of a galaxy relative to the observer, $\hat{\mathbf{n}}$ is the unit vector along the line-of-sight direction, a is the scale factor where the galaxy resides. This effect is called the redshift-space distortions (RSD) [8, 9, 10].

The redshift-space distortions induces an anisotropy in the galaxy clustering. To measure the clustering statistics, e.g., power spectrum, we convert the galaxies' redshifts into the comoving distances, assuming some fiducial cosmological model. The three-dimensional space of comoving coordinates reconstructed in this way is called "redshift space" to distinguish it from real space. In redshift space, the positions of galaxies appear to be modulated by their peculiar velocities along the line-of-sight direction as

$$\mathbf{s} = \mathbf{x} + \frac{\mathbf{v}\cdot\hat{\mathbf{n}}}{aH(a)}\hat{\mathbf{n}}, \tag{3.4}$$

where $\mathbf{x}$ and $\mathbf{s}$ are the positions in real and redshift space, and $H(a)$ is the Hubble expansion rate at scale factor a.

The real- and redshift-space density fields are connected since the mass or the number of matter tracers is conserved,

$$\left[1+\delta^{\mathrm{S}}(\mathbf{s})\right]\mathrm{d}^3 s = \left[1+\delta(\mathbf{x})\right]\mathrm{d}^3 x, \tag{3.5}$$

where $\delta(\mathbf{x})$ is the density contrast in real space, and we denote the redshift-space quantities by the superscript "S". By simply multiplying $e^{i\mathbf{k}\cdot\mathbf{s}}$ and integrating

Eq. (3.5), we obtain

$$
\begin{aligned}
(2\pi)^3\delta_{\rm D}(\mathbf{k}) + \delta^{\rm S}(\mathbf{k}) &= \int {\rm d}^3x e^{i\mathbf{k}\cdot\mathbf{s}}[1+\delta(\mathbf{x})] \\
&= \int {\rm d}^3x e^{i\mathbf{k}\cdot\mathbf{x}}[1+\delta(\mathbf{x})]e^{i[(\mathbf{k}\cdot\hat{\mathbf{n}})(\mathbf{u}\cdot\hat{\mathbf{n}})]}, \qquad (3.6)
\end{aligned}
$$

where we use Eq. (3.4) and the normalized velocity $\mathbf{u} \equiv \mathbf{v}/(aH)$. The two-point correlation of the Fourier-space density field in redshift space is

$$
\begin{aligned}
&\left\langle \left[(2\pi)^3\delta_{\rm D}(\mathbf{k}) + \delta^{\rm S}(\mathbf{k})\right]\left[(2\pi)^3\delta_{\rm D}(\mathbf{k}') + \delta^{\rm S}(\mathbf{k}')\right]\right\rangle \\
&= (2\pi)^6\left\langle\delta_{\rm D}(\mathbf{k})\delta_{\rm D}(\mathbf{k}')\right\rangle + \left\langle\delta^{\rm S}(\mathbf{k})\delta^{\rm S}(\mathbf{k}')\right\rangle \\
&= \left\langle \int {\rm d}^3x e^{i\mathbf{k}\cdot\mathbf{x}}[1+\delta(\mathbf{x})]e^{i[(\mathbf{k}\cdot\hat{\mathbf{n}})(\mathbf{u}\cdot\hat{\mathbf{n}})]}\int {\rm d}^3x' e^{i\mathbf{k}'\cdot\mathbf{x}'}[1+\delta(\mathbf{x}')]e^{i[(\mathbf{k}'\cdot\hat{\mathbf{n}}')(\mathbf{u}'\cdot\hat{\mathbf{n}}')]}\right\rangle \\
&= \int {\rm d}^3x e^{i\mathbf{k}\cdot\mathbf{x}}\int {\rm d}^3x' e^{i\mathbf{k}'\cdot\mathbf{x}'}\left\langle[1+\delta(\mathbf{x})][1+\delta(\mathbf{x}')]e^{i[(\mathbf{k}\cdot\hat{\mathbf{n}})(\mathbf{u}\cdot\hat{\mathbf{n}})+(\mathbf{k}'\cdot\hat{\mathbf{n}}')(\mathbf{u}'\cdot\hat{\mathbf{n}}')]}\right\rangle \qquad (3.7)
\end{aligned}
$$

where we denote $\mathbf{u}(\mathbf{x}')$ as $\mathbf{u}'$ for simplicity.

3.2.1 Plane-parallel approximation

To proceed with the calculation, it is quite useful to adopt the (global) plane-parallel approximation (also called the distant-observer approximation). This approximation is that we assume all the particles (such as galaxies and halos) share the same line-of-sight direction. With this treatment, the $\langle ...\rangle$ in Eq. (3.7) has the invariance with respect to spatial translations, i.e., it can be seen as a function of $\mathbf{r} = \mathbf{x} - \mathbf{x}'$. Thus, we proceed with Eq. (3.7) as

$$
\begin{aligned}
&\int {\rm d}^3x \int {\rm d}^3x' e^{i(\mathbf{k}+\mathbf{k}')\cdot\mathbf{x}'}e^{i\mathbf{k}\cdot(\mathbf{x}-\mathbf{x}')}\left\langle[1+\delta(\mathbf{x})][1+\delta(\mathbf{x}')]e^{i[k_\parallel u_\parallel(\mathbf{x})+k'_\parallel u_\parallel(\mathbf{x}')]}\right\rangle \\
&= (2\pi)^3\delta_{\rm D}(\mathbf{k}+\mathbf{k}')\int {\rm d}^3r e^{i\mathbf{k}\cdot\mathbf{r}}\left\langle[1+\delta(\mathbf{x})][1+\delta(\mathbf{x}')]e^{ik_\parallel[u_\parallel(\mathbf{x})-u_\parallel(\mathbf{x}')]}\right\rangle, \qquad (3.8)
\end{aligned}
$$

where $\parallel$ denotes the component along the line-of-sight direction. We introduce μ to denote the directional cosine between $\mathbf{k}$ and the line-of-sight,

$$
\mu \equiv \hat{\mathbf{n}}\cdot\hat{\mathbf{k}} = \frac{k_\parallel}{k}. \qquad (3.9)
$$

In the plane-parallel approximation, we define the redshift-space power spectrum as

$$
\left\langle\delta^{\rm S}(\mathbf{k})\delta^{\rm S}(\mathbf{k}')\right\rangle = (2\pi)^3\delta_{\rm D}(\mathbf{k}+\mathbf{k}')P^{\rm S}(\mathbf{k}), \qquad (3.10)
$$

and Eq. (3.8) leads to

$$
(2\pi)^3\delta_{\rm D}(\mathbf{k}) + P^{\rm S}(\mathbf{k}) = \int {\rm d}^3r e^{i\mathbf{k}\cdot\mathbf{r}}\left\langle[1+\delta(\mathbf{x})][1+\delta(\mathbf{x}')]e^{ik\mu[u_\parallel(\mathbf{x})-u_\parallel(\mathbf{x}')]}\right\rangle. \qquad (3.11)
$$

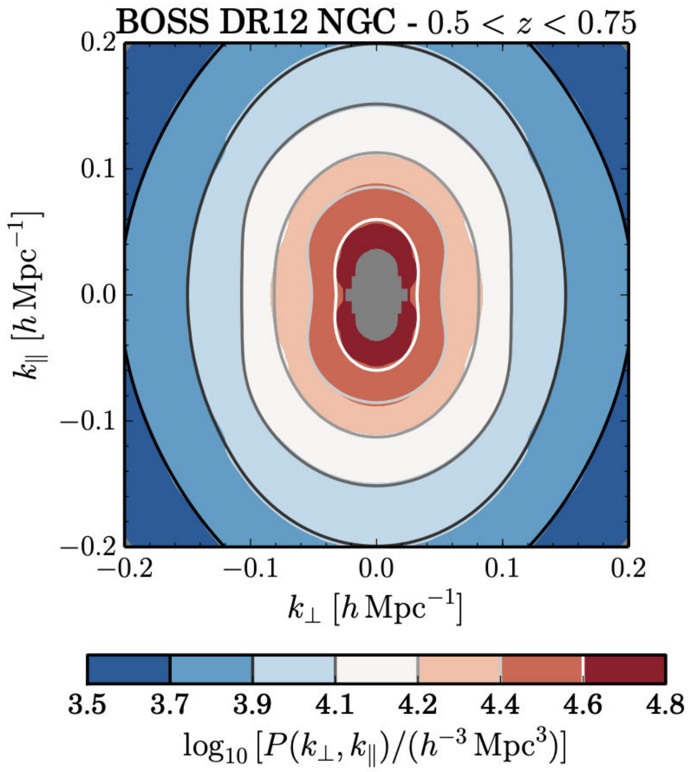

Figure 3.1: The galaxy power specrtrum measured in the SDSS-III Baryon Oscillatio Spectroscopic Survey [2], as a function of $(k_{\perp}, k_{\parallel})$. Cited from Ref. [19].

This power spectrum $P^{\mathrm{S}}(\mathbf{k})$ is expressed as a function of the wave number k and the cosine angle μ. It is symmetric with respect to the wave vector lying in the two-dimensional plane perpendicular to the line-of-sight, denoted as $\mathbf{k}_{\perp}$. Hence the redshift-space power spectrum is given as a function of two variables that specify the wave vector $\mathbf{k}$; (k, μ) or $(k_{\perp}, k_{\parallel})$, where $k_{\perp} = k\sqrt{1-\mu^2}$ and $k_{\parallel} = k\mu$ (see Fig. 3.1).

From Eq. (3.11), we also see that the redshift-space power spectrum reduces to the real-space one at $\mu = 0$, i.e., $P^{\mathrm{S}}(k, \mu = 0) = P(k)$. Throughout this chapter, we employ the global plane-parallel approximation in which we assume that the line-of-sight direction is parallel to one axis of the Cartesian coordinate, for which we take the x_3-axis direction, $\hat{\mathbf{n}} \parallel x_3$.

3.2.2 Linear theory treatment

So far we have discussed a highly general formulation of the redshift-space distortions. In this section, we provide the linear-theory treatment of the redshift-space galaxy power spectrum, first derived by Nick Kaiser [8]. Assuming the plane-parallel approximation along the x_3 axis, we calculate the Jacobian of the coordinate transformation between the real and redshift space,

$$J = \left| \frac{\partial \mathbf{s}}{\partial \mathbf{x}} \right| = 1 + \frac{\partial}{\partial x_3} \left(\frac{v_3}{aH} \right), \tag{3.12}$$

where v_3 is the x_3-component of velocity. Using this Jacobian, the redshift-space galaxy density field is related to the real-space galaxy density and velocity field,

$$\delta_{\mathrm{g}}^{\mathrm{S}}(\mathbf{s}) \simeq \delta_{\mathrm{g}}^{\mathrm{S}}(\mathbf{x}) = \delta_{\mathrm{g}}(\mathbf{x}) - \frac{1}{aH} \frac{\partial v_3}{\partial x_3}, \tag{3.13}$$

where we dropped the higher-order terms of the perturbations. We next move on to the Fourier space,

$$\delta_{\mathrm{g}}^{\mathrm{S}}(\mathbf{k}) = \delta_{\mathrm{g}}(\mathbf{k}) - \frac{ik_3}{aH} v_3(\mathbf{k}). \tag{3.14}$$

By using Eq. (2.59), we can write the redshift-space density field of galaxies in terms of real-sapce galaxy and matter density field,

$$\delta_{\mathrm{g}}^{\mathrm{S}}(\mathbf{k}) = \delta_{\mathrm{g}}(\mathbf{k}) + f \left(\frac{k_3}{k} \right)^2 \delta(\mathbf{k}) = \delta_{\mathrm{g}}(\mathbf{k}) + f\mu^2 \delta(\mathbf{k}), \tag{3.15}$$

where f is the linear growth rate defined in Eq. (2.57). Assuming the linear galaxy bias b_{g}, we obtain

$$\delta_{\mathrm{g}}^{\mathrm{S}}(\mathbf{k}) = (b_{\mathrm{g}} + f\mu^2)\delta(\mathbf{k}) = b_{\mathrm{g}}(1 + \beta\mu^2)\delta(\mathbf{k}), \tag{3.16}$$

where we define $\beta = f/b_{\mathrm{g}}$, which is called the redshift-space distortion parameter. The multiplicative factor $b_{\mathrm{g}} + f\mu^2$ is often called the Kaiser factor. The strength of the RSD effect is completely determined by this factor within the linear theory. The power spectrum in redshift space is of a quite simple form:

$$P_{\mathrm{g}}^{\mathrm{S}}(k, \mu) = (1 + \beta\mu^2)^2 b_{\mathrm{g}}^2 P(k) = (1 + \beta\mu^2)^2 P_{\mathrm{g}}(k). \tag{3.17}$$

This formula has a μ dependence in the form of a fourth-order polynomial without odd-order terms.

3.2.3 Multipole moment of redshift-space power spectrum

The redshift-space power spectrum given as a function of (k, μ) contains the full information in the galaxy distribution at the level of two-point statistics. However, in galaxy redshift surveys, measuring the power spectrum in the form of $P(k, \mu)$ can lead to a huge dimension of data vector, and the analysis would be computationally expensive; e.g., a calibration of the covariance matrix requires a large number of simulations that should be much larger than the dimension of data vector. For this reason, a dimensional reduction of data vector is useful.

It is common to expand the redshift-space power spectrum using the Legendre polynomials:

$$P^{\mathrm{S}}(k,\mu) = \sum_{\ell=0}^{\infty} P_\ell^{\mathrm{S}}(k)\,\mathcal{L}_\ell(\mu), \tag{3.18}$$

where $\mathcal{L}_\ell(\mu)$ is the ℓth order Legendre polynomials. Here $P_\ell^{\mathrm{S}}(k)$ is the ℓth order multipole moments of the power spectrum, which is given as a function of $|\mathbf{k}|$. Using the orthogonality of the Legendre polynomials, the multipole moment of the power spectrum is defined as

$$P_\ell^{\mathrm{S}}(k) \equiv \frac{2\ell+1}{2}\int_{-1}^{1} \mathrm{d}\mu\, P^{\mathrm{S}}(k,\mu)\,\mathcal{L}_\ell(\mu). \tag{3.19}$$

Note that the odd-ℓ moments vanish due to the rotational symmetry of the redshift-space clustering around the line-of-sight.

In the Kaiser's linear theory we presented in Sec. 3.2.2, the redshift-space power spectrum has the nonvanishing moments of $\ell = 0$ (monopole), $\ell = 2$ (quadrupole) and $\ell = 4$ (hexadecapole), and the higher-order moments vanish. The concrete expression for the linear-theory multipole moment of galaxy power spectrum is

$$\begin{pmatrix} P^{\mathrm{S}}_{0,\mathrm{Kaiser}}(k) \\ P^{\mathrm{S}}_{2,\mathrm{Kaiser}}(k) \\ P^{\mathrm{S}}_{4,\mathrm{Kaiser}}(k) \end{pmatrix} = \begin{pmatrix} 1 + \frac{2}{3}\beta + \frac{1}{5}\beta^2 \\ \frac{4}{3}\beta + \frac{4}{7}\beta^2 \\ \frac{8}{35}\beta^2 \end{pmatrix} b_{\mathrm{g}}^2 P_{\mathrm{m}}^{\mathrm{lin}}(k) \tag{3.20}$$

where $P_{\mathrm{m}}^{\mathrm{lin}}(k)$ is the linear matter power spectrum.

The monopole ($\ell = 0$) and the quadrupole ($\ell = 2$) moments are dominant terms of the anisotropic power spectrum at least on scales up to the quasi-nonlinear regime we are interested in. The current-generation galaxy redshift surveys such as the SDSS survey enable a significant detection of these two dominant moments [18, 45].

3.3 Alcock-Paczyński effect

In galaxy redshift surveys, another useful information can be extracted from an apparent geometrical distortion in the observed galaxy clustering; the Alcock-Paczyński (AP) effect [37, 38]. This effect arises from the discrepancy between the underlying true cosmology and the "reference" cosmological model, where the latter needs to be assumed in a clustering analysis when mapping direct observables of galaxy positions, i.e. its redshift and angular positions, to the comoving coordinates. The AP effect can be described by the coordinate transformation, and in Fourier space it is given as

$$k_{\perp,\mathrm{ref}} = \frac{D_{\mathrm{A}}(z)}{D_{\mathrm{A,ref}}(z)}k_\perp, \quad k_{\parallel,\mathrm{ref}} = \frac{H_{\mathrm{ref}}(z)}{H(z)}k_\parallel, \tag{3.21}$$

where $D_{\rm A}(z)$ is the angular diameter distance to redshift z given in Eq. (2.17) and $H(z)$ is the Hubble parameter at z, and quantities with and without subscript "ref" hereafter denote those in the reference (assumed) cosmological model and the true (unknown) cosmology, respectively. For convenience of our discussion, we define two parameters to characterize the AP distortion, following Ref. [46], as

$$\alpha_\perp \equiv \frac{D_{\rm A}(z)}{D_{\rm A,ref}(z)}, \quad \alpha_\parallel \equiv \frac{H_{\rm ref}(z)}{H(z)}. \tag{3.22}$$

Hence the observed redshift-space power spectrum can be expressed in terms of the underlying true power spectrum as

$$P^{\rm S}_{\rm gg,ref}(k_{\parallel,\rm ref}, k_{\perp,\rm ref}) = \frac{1}{\alpha_\perp^2 \alpha_\parallel} P^{\rm S}_{\rm gg}(k_\parallel, k_\perp), \tag{3.23}$$

In the following, we will often omit the subscript "ref" for notational simplicity. The baryon acoustic oscillation (BAO) features in the galaxy power spectrum makes the AP effect very powerful to constrain $D_{\rm A}(z)$ and $H(z)$ [47, 48, 49] (here note that the BAO peak location is almost unaffected by the RSD effect). The AP effect can also be utilized to constrain the cosmological parameters which are relevant to the cosmic expansion (see e.g. [50]).

The multipole power spectrum is defined from the observed spectrum as

$$P^{\rm S}_{\rm gg,ref,\ell}(k_{\rm ref}) = \frac{2\ell+1}{2\alpha_\perp^2\alpha_\parallel} \int_{-1}^{1} {\rm d}\mu_{\rm ref} \ \left\{ P^{\rm S}_{\rm gg}\left[k(k_{\rm ref}, \mu_{\rm ref}), \mu(\mu_{\rm ref})\right]\right\} \mathcal{L}_\ell(\mu_{\rm ref}), \tag{3.24}$$

where $\mathcal{L}_\ell(x)$ is the ℓ-th order Legendre polynomial and

$$k(k_{\rm ref}, \mu_{\rm ref}) \equiv \sqrt{k_\parallel^2 + k_\perp^2} = k_{\rm ref}\frac{1}{\alpha_\perp}\left[1 + \mu_{\rm ref}^2\left(\frac{\alpha_\perp^2}{\alpha_\parallel^2} - 1\right)\right]^{1/2}, \tag{3.25}$$

$$\mu(\mu_{\rm ref}) \equiv \frac{k_\parallel}{k} = \mu_{\rm ref}\frac{\alpha_\perp}{\alpha_\parallel}\left[1 + \mu_{\rm ref}^2\left(\frac{\alpha_\perp^2}{\alpha_\parallel^2} - 1\right)\right]^{-1/2} \tag{3.26}$$

As we will show in Chapter 6, the monopole moment of power spectrum is sensitive to the "dilation" parameter, $\alpha_\perp^2\alpha_\parallel$ whose variation causes an isotropic shift of the BAO peak locations and a change in the power spectrum amplitudes. On the other hand, the quadrupole moment is sensitive to the "warping" parameter $\alpha_\perp/\alpha_\parallel$, or $F_{\rm AP}$ in Ref. [19] whose variation causes an anisotropic distortion in the redshift-space power spectrum (therefore a change in the quadrupole moment).

3.4 Halo model formalism of galaxy power spectrum

In this section, we describe the halo model formalism [35, 34, 51, 52], which we will employ as the basic formalism to model the galaxy power spectrum in this thesis.

The comprehensive review of this approach is presented in Ref. [53].

In the halo model formalism, we assume that all matter is associated with halos, and then the matter correlation function is described by the contribution from pairs of mass elements in the same halo and those in two distinct halos, which are referred to as the one-halo and two-halo terms, respectively. Both terms can be modeled by assuming a halo density profile, i.e., the density distribution inside halos, such as the Navarro-Frenk-White profile [54]. This approach can also be applied to the galaxy distribution, as we describe below.

3.4.1 Halo occupation distribution model

First, we introduce the halo occupation distribution (HOD; [33, 52]) model, which is a phenomenological model for the number distribution of galaxies sitting in halos of a given mass. In this thesis, we adopt the HOD model proposed by Ref. [36]. It decomposes the galaxies into the central and satellite galaxies: the central galaxy is assumed to reside at the center of its host halo, and satellite galaxies are surrounding it. In this HOD model, the mean number of central and satellite galaxies are given separately:

$$\langle N\rangle(M) = \langle N_{\rm c}\rangle(M) + \langle N_{\rm s}\rangle(M), \tag{3.27}$$

where the notation $\langle\quad\rangle(M)$ denotes the average of a quantity for halos of a given mass M. We employ the mean HOD for central galaxies given by the following form:

$$\langle N_{\rm c}\rangle(M) = \frac{1}{2}\left[1 + {\rm erf}\left(\frac{\log M - \log M_{\rm min}}{\sigma_{\log M}}\right)\right], \tag{3.28}$$

where ${\rm erf}(x)$ is the error function and $M_{\rm min}$ and $\sigma_{\log M}$ are model parameters. Note $\langle N_{\rm c}\rangle \leq 1$. The mean central HOD, $\langle N_{\rm c}\rangle(M)$, can be interpreted as the probability that a halo with mass M hosts a central galaxy. The mean central HOD considered here has properties that $\langle N_{\rm c}\rangle \to 0$ for halos with $M \ll M_{\rm min}$, while $\langle N_{\rm c}\rangle \to 1$ for halos with $M \gg M_{\rm min}$. In our fiducial model we assume that halos host central galaxies following a Bernoulli process with the probability solely determined by the halo mass, or equivalently we ignore a possible extra dependence of the central HOD, often referred to as the *halo assembly bias*, on other physical properties such as large-scale environments or internal structures of halos (density profile, formation epoch, etc.) for our default choice. We will discuss the impact of assembly bias effect in Chapter 6.

For the mean HOD of satellite galaxies, we employ the following parametrized model:

$$\langle N_{\rm s}\rangle(M) \equiv \langle N_{\rm c}\rangle(M)\lambda_{\rm s}(M) = \langle N_{\rm c}\rangle(M)\left[\frac{M - \kappa M_{\rm min}}{M_1}\right]^{\alpha_{\rm sat}} \tag{3.29}$$

where M_1, $\alpha_{\rm sat}$, and κ are model parameters, and we have defined

$$\lambda_{\rm s}(M) \equiv \left[\frac{M - \kappa M_{\rm min}}{M_1}\right]^{\alpha_{\rm sat}}, \tag{3.30}$$

for convenience of our following discussion. For our default prescription, we assume that satellite galaxies reside only in a halo that already hosts a central galaxy. Hence, in the above equation, $N_{\rm c} = 1$ for a halo where satellite galaxy(ies) can reside. Then we assume that the number distribution of satellite galaxies in a given host halo follows the Poisson distribution with mean $\lambda_{\rm s}$: $P(N_{\rm s}|N_{\rm c} = 1) = (\lambda_{\rm s})^{N_{\rm s}} \exp(-\lambda_{\rm s})/(N_{\rm s}!)$ and $P(N_{\rm s}|N_{\rm c} = 0) = \delta^{\rm K}_{N_{\rm s},0}$, where $\delta^{\rm K}_{i,j}$ stands for the Kronecker's delta. Thus a host halo of satellite galaxies has in total $1 + N_{\rm s}$ galaxies. Under this setting, the mean number of galaxy pairs living in the same halo with mass M, which is relevant for the one-halo term calculation, can be computed as

$$\begin{aligned}\langle N(N-1)\rangle &= P(N_{\rm c} = 1)\,\langle N(N-1)|N_{\rm c} = 1\rangle + P(N_{\rm c} = 0)\,\langle N(N-1)|N_{\rm c} = 0\rangle \\ &= \langle N_{\rm c}\rangle \sum_{N_{\rm s}=0}^{\infty} \frac{(\lambda_{\rm s})^N_{\rm s}}{N_{\rm s}!} \exp(-\lambda_{\rm s})\; N_{\rm s}(1 + N_{\rm s}) \\ &= \langle N_{\rm c}\rangle(M)\left[2\lambda_{\rm s}(M) + \lambda_{\rm s}(M)^2\right].\end{aligned} \tag{3.31}$$

Note that the second term in the first line is zero following our assumption that no satellite galaxies reside in a halo without a central galaxy. This treatment is the same as in Ref. [36].

The central and satellite HOD models we use in this thesis are specified by five parameters $\{M_{\rm min}, \sigma_{\log M}, M_1, \alpha_{\rm sat}, \kappa\}$. In Chapter 6, however, we will adopt another notation by $M_{\rm sat} = \kappa M_{\rm min}$, and it also leads to the five-parameter HOD model.

3.4.2 Position distribution

To model the galaxy clustering in the halo model formalism, we need to model the (redshift-space) position distribution of satellite galaxies inside a halo. We assume, for simplicity, that satellite galaxies follow the spatial distribution of matter in the host halo. The number density profile of satellite galaxies is given as

$$\mathcal{H}(\mathbf{x}; M) = \frac{\rho(\mathbf{x}; M)}{M}, \tag{3.32}$$

where $\rho(\mathbf{x}; M)$ is the mass density profile for halo of mass M. This profile satisfies the normalization condition, $\int \mathrm{d}^3\mathbf{x}\; \mathcal{H}(\mathbf{x}; M) = 1$. Since we can assume a spherically symmetric radial profile in the statistical average sense, this normalization condition reduces to $\int_0^R 4\pi r^2 \mathrm{d}r\; \mathcal{H}(r; M) = 1$, where R is the halo radius. In this thesis, we adopted the normalized Navarro-Frenk-White (NFW) profile [54]:

$$\mathcal{H}(r; M, c) = \frac{c^3}{4\pi R^3}\left[\ln(1 + c) - \frac{c}{1 + c}\right]^{-1} \frac{1}{(cr/R)(1 + cr/R)^2}, \tag{3.33}$$

for the galaxy radial profile. The NFW profile is specified by the concentration parameter c and mass M. For this we employed the median concentration-mass relation $c(M)$ calibrated in Refs. [55, 56]. To compute it we use the publicly available Python toolkit Colossus[1] [57]. For Chapter 6, we also introduce a nuisance parameter to model a possible uncertainty in the concentration parameter, $c(M,z) \to c_{\rm conc}c(M,z)$ ($c_{\rm conc}=1$ for the fiducial model).

3.4.3 Velocity distribution: Finger-of-God effect

To model the redshift-space distribution inside halos, we also need a model of the velocity distribution of satellite galaxies with respect to the halo center. In this thesis, we employ an isotropic Gaussian distribution for the velocity distribution for simplicity,

$$\mathcal{F}(\Delta r_\parallel;\sigma_{{\rm vir},M}) = \frac{1}{\sqrt{2\pi}\frac{\sigma_{{\rm vir},M}}{aH}}\exp\left[-\frac{(\Delta r_\parallel)^2}{2\frac{\sigma^2_{{\rm vir},M}}{a^2H^2}}\right], \tag{3.34}$$

where $\sigma_{\rm vir}(M)$ is the velocity dispersion for halos of M. In Chapter 5, we assume that the velocity dispersion is specified by the host halo mass as

$$\sigma^2_{{\rm vir},M} = \frac{GM}{2R_{\rm phy}}, \tag{3.35}$$

where $R_{\rm phy}$ is the *physical* halo radius (i.e. $R_{\rm phy}=aR$). In Chapter 6, we use a more complex model, following Ref. [58]:

$$\sigma^2_{{\rm vir},M}(r) = \frac{GM(<r)}{2r}, \tag{3.36}$$

where $M(<r)$ is the mass enclosed within the radius r (it is also in the physical scale) from the center of the halo, and can be calculated by assuming the density profile. Similarly to the concentration parameter, we also introduce a nuisance parameter to model the uncertainty in the velocity dispersion, $\sigma_{{\rm vir},M}(r) \to c_{\rm vel}\sigma_{{\rm vir},M}(r)$ ($c_{\rm vel}=1$ for the fiducial model).

Eq. (3.34) denotes the distribution of the line-of-sight component of velocity, and we expressed the velocity function in terms of the positional displacement by the RSD effect due to the line-of-sight velocity component: $\Delta r_\parallel \equiv v_\parallel/(aH)$. The velocity function [Eq. (3.34)] satisfies the normalization condition $\int_{-\infty}^{\infty}{\rm d}(\Delta r_\parallel)\ \mathcal{F}(\Delta r_\parallel)=1$.

The RSD effect due to this internal virial motions of satellite galaxies inside host halos is called the Finger-of-God (FoG) effect [59] (also see [60, 61] for the halo model approach of the FoG effect). This is a highly nonlinear effect in the redshift-space galaxy clustering. The redshift-space distribution of satellite galaxies in a given host halo is stretched by the FoG effect along the line-of-sight direction. It can be

---

[1] `http://www.benediktdiemer.com/code/colossus/`

expressed by a convolution of the distributions of real-space spatial distribution and the velocity function of satellite galaxies (also see [58, 62]),

$$\mathcal{H}^{\mathrm{S}}(\mathbf{s}; M, \sigma_{\mathrm{vir},M}) = \int_{-\infty}^{\infty} \mathrm{d}y \; \mathcal{H}(\mathbf{s} - y\hat{\mathbf{n}}; M)\, \mathcal{F}(y; \sigma_{\mathrm{vir},M}), \tag{3.37}$$

where $\hat{\mathbf{n}}$ denotes the unit vector along the line-of-sight direction. Equation (3.37) reduces to a simple multiplicative form in Fourier space:

$$\tilde{\mathcal{H}}^{\mathrm{S}}(\mathbf{k}; M, \sigma_{\mathrm{vir},M}) = \tilde{\mathcal{H}}(\mathbf{k}; M)\, \tilde{\mathcal{F}}(k_{\parallel}; \sigma_{\mathrm{vir},M}). \tag{3.38}$$

Note that in this work we consider only the specific model based on the NFW profile and the Gaussian velocity distribution, but actually Eq. (3.38) can be constructed from any other models of the real-space position distribution $\tilde{\mathcal{H}}(\mathbf{k}; M)$ and displacement (velocity) distribution $\tilde{\mathcal{F}}(k_{\parallel}; \sigma_{\mathrm{vir},M})$.

3.4.4 Galaxy power spectrum

With all the building blocks we described above, we can calculate the galaxy power spectrum.

Once the HOD model is given, the mean number density of galaxies under consideration is given as

$$\bar{n}_{\mathrm{g}} = \int \mathrm{d}M \; \frac{\mathrm{d}n}{\mathrm{d}M} \left[\langle N_{\mathrm{c}}\rangle(M) + \langle N_{\mathrm{s}}\rangle(M)\right], \tag{3.39}$$

where $\mathrm{d}n/\mathrm{d}M$ is the halo mass function which gives the mean number density of halos in the mass range $[M, M + \mathrm{d}M]$. The redshift-space power spectrum of galaxies can be decomposed into two contributions within the halo model framework:

$$P_{\mathrm{gg}}^{\mathrm{S}}(\mathbf{k}) = P_{\mathrm{gg}}^{\mathrm{S,1h}}(\mathbf{k}) + P_{\mathrm{gg}}^{\mathrm{S,2h}}(\mathbf{k}), \tag{3.40}$$

where $P_{\mathrm{gg}}^{\mathrm{S,1h}}$ and $P_{\mathrm{gg}}^{\mathrm{S,2h}}$ are the one- and two-halo terms, respectively. The one-halo term arises from pairs of galaxies that reside in the same halo, while the two-halo term arises from those in different halos.

The two terms can be expressed as

$$\begin{aligned} P_{\mathrm{gg}}^{\mathrm{S,1h}}(\mathbf{k}) = \frac{1}{\bar{n}_{\mathrm{g}}^{2}} \int & \mathrm{d}M \; \frac{\mathrm{d}n}{\mathrm{d}M} \, \langle N_{\mathrm{c}}\rangle(M) \\ & \times \left[2\lambda_{\mathrm{s}}(M)\tilde{\mathcal{H}}^{\mathrm{S}}(\mathbf{k}; M, c, \sigma_{\mathrm{vir},M}) + \lambda_{\mathrm{s}}(M)^{2}\tilde{\mathcal{H}}^{\mathrm{S}}(\mathbf{k}; M, c, \sigma_{\mathrm{vir},M})^{2}\right], \end{aligned} \tag{3.41}$$

and

$$
\begin{aligned}
P^{\mathrm{S,2h}}_{\mathrm{gg}}(\mathbf{k}) = \frac{1}{\bar{n}_{\mathrm{g}}^2} \int \mathrm{d}M \frac{\mathrm{d}n}{\mathrm{d}M} & \left[\langle N_{\mathrm{c}}\rangle(M) + \langle N_{\mathrm{s}}\rangle(M) \tilde{\mathcal{H}}^{\mathrm{S}}(\mathbf{k}; M, c, \sigma_{\mathrm{vir},M})\right] \\
\times \int \mathrm{d}M' \frac{\mathrm{d}n}{\mathrm{d}M'} & \left[\langle N_{\mathrm{c}}\rangle(M') + \langle N_{\mathrm{s}}\rangle(M') \tilde{\mathcal{H}}^{\mathrm{S}}(\mathbf{k}; M', c', \sigma'_{\mathrm{vir},M'})\right] P^{\mathrm{S}}_{\mathrm{hh}}(\mathbf{k}; M, M').
\end{aligned}
\tag{3.42}
$$

Here $P^{\mathrm{S}}_{\mathrm{hh}}(\mathbf{k}; M, M')$ is the redshift-space power spectrum of two halos that have masses M and M', respectively. The above one-halo term has an asymptotic behavior $P^{\mathrm{S,1h}}_{\mathrm{g}} \to 1/\bar{n}_{\mathrm{gg}}$ for the limit $k \to 0$ because $\tilde{\mathcal{H}}^{\mathrm{S}} \to 1$.

Our overall approach in this thesis is to model the redshift-space galaxy power spectrum based on the halo power spectrum, $P^{\mathrm{S}}_{\mathrm{hh}}(\mathbf{k}; M, M')$, which is in the two-halo term. The halo model formalism described above takes an essential role in this approach.

3.4.5 Off-centering effect

Furthermore, we include a possible effect of "off-centered" central galaxies in our modeling. Since dark matter halo is not a well-defined object and experiences mergers of progenitor halos, galaxies selected by specific ways based on a spectroscopic sample (e.g. color and magnitude cuts) might be off-centered (i.e. satellite) galaxies, as indicated in the results of Ref. [62]. Even if a halo contains a single target galaxy in the sample and if the galaxy is off-centered from the true halo center, the galaxy is categorized as a "central" galaxy in a naive HOD picture. We explicitly include effects of these off-centered galaxies on redshift-space galaxy power spectrum. To do this, we follow the methods in Ref. [62] (also see [62, 63, 64, 65]) and we introduce a parameter p_{off} $(0 \le p_{\mathrm{off}} \le 1)$, which represents the probability that each central galaxy is off-centered from the center of its host halo. In addition we assume a Gaussian distribution for the radial distribution of the off-centered galaxy in each host halo:

$$
\mathcal{P}(r_{\mathrm{off}}) = \frac{1}{(2\pi)^{3/2}(r_{\mathrm{s}}\mathcal{R}_{\mathrm{off}})^3} \exp\left[-\frac{(r_{\mathrm{off}})^2}{2(r_{\mathrm{s}}\mathcal{R}_{\mathrm{off}})^2}\right], \tag{3.43}
$$

where r_{s} is the scale radius of each halo with mass M and we include additional dimensionless parameter $\mathcal{R}_{\mathrm{off}}$ which models a typical off-centering radius in units of the scale radius. Under this formulation, in Eqs. (3.41) and (3.42) we can replace the central HOD as

$$
\langle N_{\mathrm{c}}\rangle(M) \to \left[(1 - p_{\mathrm{off}}) + p_{\mathrm{off}} \exp\left\{-\frac{1}{2}k^2(r_{\mathrm{s}}\mathcal{R}_{\mathrm{off}})^2\right\} \tilde{\mathcal{F}}(\mathbf{k}; \sigma_{\mathrm{vir},\mathcal{M}})\right] \langle N_{\mathrm{c}}\rangle(M). \tag{3.44}
$$

Chapter 4

Measurement of Galaxy Power Spectrum

In this chapter, we describe the measurement techniques of the Fourier-space clustering statistics, focusing on the power spectrum. After we explain the basic treatment of the Fourier-space density field, we introduce the well-known estimator for the galaxy power spectrum proposed in Ref. [66]. We further describe the FFT-based estimator for the multipole monents of the redshift-space power spectrum [67], which we used in the power spectrum measurement on the survey galaxy catalogs in Chapter 7. In addition, we show the formulation of the survey window function effect which needs to be taken into account in galaxy redshift surveys.

4.1 Fourier-space statistics

4.1.1 Fourier series expansion of the fluctuation fields

When we calculate the clustering statistics of some field $f(\mathbf{x})$ in N-body simulations or galaxy surveys, we have only finite-volume information of the field. Therefore, in the case that we want the Fourier-space counterpart of the field, we impose the periodic boundary condition, i.e., the field satisfies

$$f(\mathbf{x}) = f(\mathbf{x} + L\mathbf{n}), \tag{4.1}$$

where L is the one-side length of the simulation box (in the case of real survey it is taken to be the side length of the FFT box to contain the whole survey footprints) and $\mathbf{n}$ is an arbitrary integer vector. The Fourier-space field, $\tilde{f}(\mathbf{k})$, is obtained by expanding $f(\mathbf{x})$ in Fourier series:

$$f(\mathbf{x}) = \sum_{\mathbf{k}=\frac{2\pi}{L}\mathbf{n}} \tilde{f}(\mathbf{k}) e^{i\mathbf{k}\cdot\mathbf{x}}, \tag{4.2}$$

where all wave vectors $\mathbf{k}$ are not continuous but discrete quantities. The Fourier component $\tilde{f}(\mathbf{k})$ is given by

$$\tilde{f}(\mathbf{k}) = \frac{1}{V}\int_V \mathrm{d}^3x f(\mathbf{x}) e^{-i\mathbf{k}\cdot\mathbf{x}}, \tag{4.3}$$

where $V = L^3$ is the volume we consider as above. We can calculate the Fourier-space statistics from this field. For instance, the power spectrum is given by

$$\begin{aligned}\left\langle \tilde{\delta}(\mathbf{k}_i)\tilde{\delta}^*(\mathbf{k}_j)\right\rangle &= \left\langle \int_V \frac{\mathrm{d}^3x}{V} e^{-i\mathbf{k}_i\cdot\mathbf{x}}\delta(\mathbf{x}) \int_V \frac{\mathrm{d}^3x'}{V} e^{i\mathbf{k}_j\cdot\mathbf{x}'}\delta(\mathbf{x}')\right\rangle \\ &= \int_V \frac{\mathrm{d}^3x}{V}\int_V \frac{\mathrm{d}^3x'}{V} e^{-i\mathbf{k}_i\cdot\mathbf{x}} e^{i\mathbf{k}_j\cdot\mathbf{x}'}\left\langle\delta(\mathbf{x})\delta(\mathbf{x}')\right\rangle \\ &= \int_V \frac{\mathrm{d}^3x}{V} e^{-i(\mathbf{k}_i-\mathbf{k}_j)\cdot\mathbf{x}} \int_V \frac{\mathrm{d}^3r}{V} e^{-i\mathbf{k}_j\cdot\mathbf{r}}\xi(\mathbf{r}) \\ &= \delta^K_{ij}\frac{1}{V}\left[\int_V \mathrm{d}^3r e^{-i\mathbf{k}_i\cdot\mathbf{r}}\xi(\mathbf{r})\right] \equiv \delta^K_{ij}\frac{\hat{P}(\mathbf{k}_i)}{V},\end{aligned} \tag{4.4}$$

where δ^K_{ij} is the Kronecker's delta, and $\xi(\mathbf{r}) = \langle\delta(\mathbf{x})\delta(\mathbf{x}')\rangle$ ($\mathbf{r} = \mathbf{x}-\mathbf{x}'$) is the two-point correlation function we defined in Sec. 2.3. In the last line, we used

$$\int_V \frac{\mathrm{d}^3x}{V} e^{-i(\mathbf{k}_i-\mathbf{k}_j)\cdot\mathbf{x}} = \delta^K_{ij}. \tag{4.5}$$

4.1.2 Direct summation method

To calculate the power spectrum from some discete particle distribution, there is a direct method with any artifact due to the Fourier transform. Suppose we have the distribution of N_p particles (e.g., N-body simulation particles or galaxies observed in surveys) in the spatial volume V. We define the number density field as

$$\rho(\mathbf{x}) = \sum_{i=1}^{N_\mathrm{p}} m\delta_\mathrm{D}(\mathbf{x}-\mathbf{x}_i), \tag{4.6}$$

where m is the mass of particles, or we can set $m = 1$ when we consider the number density field. Then, we write down the field of density contrast as

$$\delta(\mathbf{x}) \equiv \frac{\rho(\mathbf{x})}{\bar{\rho}} - 1 = \frac{1}{\bar{n}}\sum_{i=1}^{N_\mathrm{p}}\delta_\mathrm{D}(\mathbf{x}-\mathbf{x}_i) - 1, \tag{4.7}$$

where $\bar{\rho}$ is the mean mass density, $\bar{n} = \bar{\rho}/m = N_\mathrm{p}/V$ is the mean number density. Assuming the periodic boundary condition, we can derive the Fourier series component of $\delta(\mathbf{x})$,

$$\begin{aligned}\tilde{\delta}(\mathbf{k}) &= \frac{1}{\bar{n}}\sum_{i=1}^{N_\mathrm{p}}\frac{1}{V}\int_V \mathrm{d}^3x\delta_\mathrm{D}(\mathbf{x}-\mathbf{x}_i)e^{-i\mathbf{k}\cdot\mathbf{x}} - \frac{1}{V}\int_V \mathrm{d}^3x e^{-i\mathbf{k}\cdot\mathbf{x}} \\ &= \frac{1}{N_\mathrm{p}}\sum_{i=1}^{N_\mathrm{p}} e^{-i\mathbf{k}\cdot\mathbf{x}_i} - \delta^K_{\mathbf{k}},\end{aligned} \tag{4.8}$$

where $\delta^K_{\mathbf{k}}$ is unity when $\mathbf{k} = \mathbf{0}$ and otherwise zero (note that $\mathbf{k}$ is the discrete vector). When we calculate the power spectrum by averaging $\left|\tilde{\delta}(\mathbf{k})\right|^2$, the self-correlation of particles should be subtracted as the shot noise. This contribution amounts to $\frac{1}{N_{\rm p}^2}\sum_{i=1}^{N_{\rm p}} = \frac{1}{N_{\rm p}}$, and hence, the power spectrum is calculated using

$$
\begin{aligned}
\left\langle \tilde{\delta}(\mathbf{k}_i)\tilde{\delta}(\mathbf{k}_j) \right\rangle &= \delta^K_{ij}\left[\frac{P(\mathbf{k}_i)}{V} + \frac{1}{N_{\rm p}}\right] = \frac{\delta^K_{ij}}{V}\left[P(\mathbf{k}_i) + \frac{1}{\bar{n}}\right], \\
P(\mathbf{k}_i) &= V\left|\tilde{\delta}(\mathbf{k}_i)\right|^2 - \frac{1}{\bar{n}}.
\end{aligned}
\tag{4.9}
$$

This estimator is clean in the sense that it is free from the aliasing problem arising from the discrete Fourier transform. However, it is computationally expensive, because it requires $N_{\rm p} \times N_{\rm k}$ calculations, where $N_{\rm k}$ is the number of wave vector for which $\tilde{\delta}(\mathbf{k})$ is evaluated.

4.2 Fast Fourier transform-based method

To accelerate the measurement of the Fourier-space clustering statistics, we commonly resort to the fast Fourier Transform (FFT), an efficient algorithm of the discrete Fourier transform (DFT). It can compute the DFT of a function on the rectangular grid by $\mathcal{O}(N_{\rm g}\log N_{\rm g})$ calculations, where $N_{\rm g}$ is the number of grid points.

4.2.1 Interpolation of the particle distribution on the FFT grid

Since the discrete Fourier transform requires the field evaluated on each point of a rectangular grid, we need to interpolate the field calculated from the discrete particle distribution on the grid as follows.

First, each particle is assigned a "shape", which is represented by the shape function $S(\mathbf{x})$ centered on the particle position. This function is symmetric, positively defined and separable as $S(\mathbf{x}) = S_{\rm 1D}(x)S_{\rm 1D}(y)S_{\rm 1D}(z)$. This separability makes the calculations simply applicable to the arbitrary dimensional field. It also satisfies the normalization

$$
\int_V {\rm d}^3x S(\mathbf{x}) = 1. \tag{4.10}
$$

From this setting, we can calculate the field which is constructed from the particle distribution, e.g., the density contrast field $\delta(\mathbf{x})$. The density contrast field of $N_{\rm p}$ particles is

$$
\delta(\mathbf{x}) = \frac{1}{\bar{n}}\sum_{i=1}^{N_{\rm p}} S(\mathbf{x} - \mathbf{x}_i) - 1, \tag{4.11}
$$

and we obtain the grid-interpolated field of it as

$$\delta_{\mathrm{w}}(\mathbf{x}_j^{\mathrm{G}}) \equiv \frac{1}{H^3}\int_{\mathbf{x}_j^{\mathrm{G}}} \mathrm{d}^3x\delta(\mathbf{x}) = \frac{1}{\bar{n}}\sum_{i=1}^{N_{\mathrm{p}}}\left[\frac{1}{H^3}\int_{\mathbf{x}_j^{\mathrm{G}}} \mathrm{d}^3xS(\mathbf{x}-\mathbf{x}_i)\right] - 1, \tag{4.12}$$

where H is the grid spacing along one dimension. By defining the grid interpolation kernel as the grid-averaged shape of a particle,

$$W(\mathbf{x}_j^{\mathrm{G}} - \mathbf{x}_i) \equiv \frac{1}{H^3}\int_{\mathbf{x}_j^{\mathrm{G}}} \mathrm{d}^3xS(\mathbf{x}-\mathbf{x}_i), \tag{4.13}$$

Eq. (4.12) reduces to

$$\delta_{\mathrm{w}}(\mathbf{x}_j^{\mathrm{G}}) = \frac{1}{\bar{n}}\sum_{i=1}^{N_{\mathrm{p}}} W(\mathbf{x}_j^{\mathrm{G}} - \mathbf{x}_i) - 1. \tag{4.14}$$

By the separability of $S(\mathbf{x})$, $W(\mathbf{x})$ is also separable into each dimension, and it is sufficient if we use a one-dimensional function to construct the arbitrary dimensional interpolation kernel. As such grid interpolation kernels, the basis functions of B-spline curves are commonly used. The functional shapes for the lowest-order basis functions are as follows [68]:

- Nearest Grid Point (NGP)

$$W^{(1)}(x) = \begin{cases} 1 & (|x| < \frac{1}{2}) \\ 0 & (\text{otherwise}) \end{cases} \tag{4.15}$$

- Cloud In Cells (CIC)

$$W^{(2)}(x) = \begin{cases} 1 - |x| & (|x| < 1) \\ 0 & (\text{otherwise}) \end{cases} \tag{4.16}$$

- Triangular-Shaped Cloud (TSC)

$$W^{(3)}(x) = \begin{cases} \frac{3}{4} - x^2 & (|x| < \frac{1}{2}) \\ \frac{1}{2}\left(\frac{3}{2} - |x|\right)^2 & (\frac{1}{2} \le |x| < \frac{3}{2}) \\ 0 & (\text{otherwise}) \end{cases} \tag{4.17}$$

- Piecewise Cubic Spline (PCS)

$$W^{(3)}(x) = \begin{cases} \frac{1}{6}\left(4 - 6x^2 + 3|x|^3\right)^2 & (0 \le |x| < 1) \\ \frac{1}{6}\left(2 - |x|\right)^3 & (1 \le |x| < 2) \\ 0 & (\text{otherwise}) \end{cases} \tag{4.18}$$

In this thesis, we use the CIC in Chapters 5 and 6, and the PCS in Chapter 7.

4.2.2 Fourier-space field in FFT

After assigning the particles to each grid point, we perform the FFT to go to the Fourier space.

Since the discrete Fourier transform lose the high-frequency signals, the grid-interpolated field Eq. (4.12) can be mathematically described in terms of the comb function $\mathrm{III}(\mathbf{x}) \equiv \sum_{\mathbf{n}} \delta_{\mathrm{D}}(\mathbf{x}-\mathbf{n})$. We can define the field on the discrete grid as a sampling on the continuous space $\mathbf{x}$,

$$\delta^{\mathrm{G}}_{\mathrm{w}}(\mathbf{x}) = \mathrm{III}\left(\frac{\mathbf{x}}{H}\right)\delta_{\mathrm{w}}(\mathbf{x}), \tag{4.19}$$

where $\delta_{\mathrm{w}}(\mathbf{x})$ is underlying (continuous) interpolated field, which is given by

$$\begin{aligned}\delta_{\mathrm{w}}(\mathbf{x}) &= \int \mathrm{d}^3x' W(\mathbf{x}-\mathbf{x}')\delta(\mathbf{x}') = \int \mathrm{d}^3x' W(\mathbf{x}-\mathbf{x}') \left[\frac{1}{\bar{n}}\sum_{i=1}^{N_{\mathrm{P}}}\delta_{\mathrm{D}}(\mathbf{x}'-\mathbf{x}_i) - 1\right] \\ &= \frac{1}{\bar{n}}\sum_{i=1}^{N_{\mathrm{P}}} W(\mathbf{x}-\mathbf{x}_i) - 1. \end{aligned} \tag{4.20}$$

The discretely-sampled field $\delta^{\mathrm{G}}_{\mathrm{w}}(\mathbf{x})$ satisfies $\delta^{\mathrm{G}}_{\mathrm{w}}(\mathbf{x}^{\mathrm{G}}_j) = \delta_{\mathrm{w}}(\mathbf{x}^{\mathrm{G}}_j)$ on each grid point $\mathbf{x}^{\mathrm{G}}_j$, and becomes zero elsewhere. The Fourier-series coefficient of the comb function $\mathrm{III}(\mathbf{x})$ is $\tilde{\mathrm{III}}(\mathbf{k}) = \sum_{\mathbf{n}} \delta^{K}_{\mathbf{k},k_{\mathrm{s}}\mathbf{n}}$, where $k_{\mathrm{s}} = 2\pi/H$ is the sampling frequency. Hence the Fourier-series coefficient of $\delta^{\mathrm{G}}_{\mathrm{w}}(\mathbf{x})$ is

$$\begin{aligned}\tilde{\delta}^{\mathrm{G}}_{\mathrm{w}}(\mathbf{k}) &= \tilde{\mathrm{III}}(\mathbf{k}) * \tilde{\delta}_{\mathrm{w}}(\mathbf{k}) = \sum_{\mathbf{k}'} \tilde{\mathrm{III}}(\mathbf{k}')\tilde{\delta}_{\mathrm{w}}(\mathbf{k}-\mathbf{k}') = \sum_{\mathbf{n}}\sum_{\mathbf{k}'} \delta^{K}_{\mathbf{k}',k_{\mathrm{s}}\mathbf{n}}\tilde{\delta}_{\mathrm{w}}(\mathbf{k}-\mathbf{k}') \\ &= \sum_{\mathbf{n}} \tilde{\delta}_{\mathrm{w}}(\mathbf{k}-k_{\mathrm{s}}\mathbf{n}). \end{aligned} \tag{4.21}$$

The terms of $\mathbf{n} \neq 0$ are the aliasing contributions which arise from the discrete sampling. Since the sampling wavenumber of the grid k_{s} is much larger than the wavenumbers $\mathbf{k}$ we are interested in, the aliasing terms are typically from the higher-frequency region than $\mathbf{k}$. The field $\delta_{\mathrm{w}}(\mathbf{x})$ is a convolution of the interpolation window $W(\mathbf{x})$ and the true field $\delta(\mathbf{x})$, and hence we can remove the effect of the interpolation window from the main ($\mathbf{n}=0$) contribution by simply dividing by $\tilde{W}(\mathbf{k})$,

$$\tilde{\delta}^{\mathrm{G}}(\mathbf{k}) \equiv \frac{\tilde{\delta}^{\mathrm{G}}_{\mathrm{w}}(\mathbf{k})}{\tilde{W}(\mathbf{k})} = \tilde{\delta}(\mathbf{k}) + \sum_{\mathbf{n}\neq 0} \tilde{w}_{\mathbf{n}}(\mathbf{k})\tilde{\delta}(\mathbf{k}-k_{\mathrm{s}}\mathbf{n}), \tag{4.22}$$

where we define the "corrected" window function $\tilde{w}_{\mathbf{n}}(\mathbf{k}) \equiv \tilde{W}(\mathbf{k}-k_{\mathrm{s}}\mathbf{n})/\tilde{W}(\mathbf{k})$.

4.3 Feldman-Kaiser-Peacock estimator

4.3.1 Basic formalism

On the practical measurement of the power spectrum form galaxy redshift surveys, the selection effect due to the survey geometry needs to be taken into account. To this end, we introduce the so-called Feldman-Kaiser-Peacock estimator [66], which is commonly used in the measurement of galaxy clustering statistics.

Following Ref. [66], we define the weighted density field as

$$\delta_W(\mathbf{x}) \equiv \frac{w(\mathbf{x})\left[n_{\mathrm{g}}(\mathbf{x}) - \alpha n_{\mathrm{r}}(\mathbf{x})\right]}{\left[\int \mathrm{d}^3x \bar{n}^2(\mathbf{x}) w^2(\mathbf{x})\right]^{1/2}} = \frac{w(\mathbf{x})\left[n_{\mathrm{g}}(\mathbf{x}) - \alpha n_{\mathrm{r}}(\mathbf{x})\right]}{I_{22}^{1/2}}, \tag{4.23}$$

where $n_{\mathrm{g}}(\mathbf{x})$ and $n_{\mathrm{r}}(\mathbf{x})$ are the galaxy and random number density fields. Note that they already include the incompleteness weight due to the observational systematics. We denote the expected mean number density of galaxies as $\bar{n}(\mathbf{x})$, which depends on the position $\mathbf{x}$ due to the nontrivial survey geometry. The denominator, $I_{22} \equiv \int \mathrm{d}^3x \bar{n}^2(\mathbf{x}) w^2(\mathbf{x})$, is a normalization that assures the measured power spectrum becomes the true values when the survey geometry is trivial so that $\bar{n}(\mathbf{x})$ is the global mean density. It means that $\delta_W(\mathbf{x})$ does not represent the density contrast itself but is normalized for the power spectrum. Using $n_{\mathrm{g}}(\mathbf{x}) = \bar{n}(\mathbf{x})[1+\delta(\mathbf{x})]$ and $\alpha n_{\mathrm{s}}(\mathbf{x}) = \bar{n}(\mathbf{x})$, we calculate the correlations of the number density fields of galaxies and randoms as follows:

$$\langle n_{\mathrm{g}}(\mathbf{x}_1) n_{\mathrm{g}}(\mathbf{x}_2)\rangle = \bar{n}(\mathbf{x}_1)\bar{n}(\mathbf{x}_2)[1+\xi(\mathbf{x}_1,\mathbf{x}_2)] + \bar{n}(\mathbf{x}_1)\delta_{\mathrm{D}}(\mathbf{x}_1-\mathbf{x}_2), \tag{4.24}$$

$$\langle n_{\mathrm{r}}(\mathbf{x}_1) n_{\mathrm{r}}(\mathbf{x}_2)\rangle = \alpha^{-2}\bar{n}(\mathbf{x}_1)\bar{n}(\mathbf{x}_2) + \alpha^{-1}\bar{n}(\mathbf{x}_1)\delta_{\mathrm{D}}(\mathbf{x}_1-\mathbf{x}_2), \tag{4.25}$$

$$\langle n_{\mathrm{g}}(\mathbf{x}_1) n_{\mathrm{r}}(\mathbf{x}_2)\rangle = \alpha^{-1}\bar{n}(\mathbf{x}_1)\bar{n}(\mathbf{x}_2), \tag{4.26}$$

where $\xi(\mathbf{x}_1,\mathbf{x}_2)$ is the galaxy two-point correlation function and the terms of Dirac's delta functions represent the shot noises arising from the self-correlations of galaxies and randoms. Using these relations, we obtain

$$\begin{aligned}\langle \delta_W(\mathbf{x}_1)\delta_W(\mathbf{x}_2)\rangle &= \frac{1}{I_{22}}\left\langle w(\mathbf{x}_1)\left[n_{\mathrm{g}}(\mathbf{x}_1) - \alpha n_{\mathrm{r}}(\mathbf{x}_1)\right] w(\mathbf{x}_2)\left[n_{\mathrm{g}}(\mathbf{x}_2) - \alpha n_{\mathrm{r}}(\mathbf{x}_2)\right]\right\rangle \\ &= \frac{w(\mathbf{x}_1)w(\mathbf{x}_2)}{I_{22}}\left\{\bar{n}(\mathbf{x}_1)\bar{n}(\mathbf{x}_2)\xi(\mathbf{x}_1,\mathbf{x}_2) + (1+\alpha)\bar{n}(\mathbf{x}_1)\delta_{\mathrm{D}}(\mathbf{x}_1-\mathbf{x}_2)\right\},\end{aligned} \tag{4.27}$$

and hence, the (window-convolved) galaxy power spectrum $P_W(\mathbf{k})$ can be estimated as

$$\begin{aligned}\hat{P}_W(\mathbf{k}) = \left\langle|\tilde{\delta}_W(\mathbf{k})|^2\right\rangle &= \int \mathrm{d}^3x_1 e^{-i\mathbf{k}\cdot\mathbf{x}_1}\int \mathrm{d}^3x_2 e^{i\mathbf{k}\cdot\mathbf{x}_2}\left\langle\delta_W(\mathbf{x}_1)\delta_W(\mathbf{x}_2)\right\rangle \\ &= \frac{1}{I_{22}}\int\frac{\mathrm{d}^3k'}{(2\pi)^3}P(\mathbf{k}')\left|\int \mathrm{d}^3x\bar{n}(\mathbf{x})w(\mathbf{x})e^{-i(\mathbf{k}-\mathbf{k}')\cdot\mathbf{x}}\right|^2 + (1+\alpha)\frac{1}{I_{22}}\int \mathrm{d}^3x\bar{n}(\mathbf{x})w^2(\mathbf{x}),\end{aligned} \tag{4.28}$$

where the latter term is the shot noise which should be subtracted.

4.3.2 Multipole moment of power spectrum

In galaxy redshift surveys, we typically measure the multipole moments of the redshif-space galaxy power spectrum. The redshift-space power spectrum is translational-invariant only when the global plane-parallel approximation is assumed (i.e., all galaxies share the same line-of-sight direction), and in the absence of this the redshift-space power spectrum depends on the line-of-sight direction;

$$\hat{P}(\mathbf{k},\mathbf{x}) = (2\ell+1)\left[\int \mathrm{d}^3x_1 e^{-i\mathbf{k}\cdot\mathbf{x}_1}\delta(\mathbf{x}_1)\int \mathrm{d}^3x_2 e^{i\mathbf{k}\cdot\mathbf{x}_2}\delta(\mathbf{x}_2)\mathcal{L}_\ell(\hat{\mathbf{k}}\cdot\hat{\mathbf{x}})\right], \tag{4.29}$$

where we take $\mathbf{x}$ to be on the representative line-of-sight between the two positions $\mathbf{x}_1$ and $\mathbf{x}_2$, e.g., $\mathbf{x} = (\mathbf{x}_1+\mathbf{x}_2)/2$.

Including the survey window function, we can write the estimator of redshift-space power spectrum multipoles by averaging over the wave vectors within the k bins,

$$\hat{P}_{W,\ell}(k) = (2\ell+1)\int\frac{\mathrm{d}\Omega_k}{4\pi}\left[\int \mathrm{d}^3x_1 e^{-i\mathbf{k}\cdot\mathbf{x}_1}\delta_W(\mathbf{x}_1)\int \mathrm{d}^3x_2 e^{i\mathbf{k}\cdot\mathbf{x}_2}\delta_W(\mathbf{x}_2)\mathcal{L}_\ell(\hat{\mathbf{k}}\cdot\hat{\mathbf{x}}) - P_\ell^{\mathrm{shot}}(\mathbf{k})\right], \tag{4.30}$$

where $P_\ell^{\mathrm{shot}}(\mathbf{k})$ is the subtracted shot noise terms, defined as

$$P_\ell^{\mathrm{shot}}(\mathbf{k}) = (1+\alpha)\frac{1}{I_{22}}\int \mathrm{d}^3x\bar{n}(\mathbf{x})w^2(\mathbf{x}). \tag{4.31}$$

The shot noise contributions for the quadrupole or higher-order multipoles are negligible, and we subtract the shot noise only for the monopole momemt in the power spectrum measurement in Chapter 7.

We then use the local plane-parallel approximation, i.e., the vector from the observer to the either of two pair galaxies is taken as the line-of-sight direction:

$$\hat{P}_{W,\ell}(k) = (2\ell+1)\int\frac{\mathrm{d}\Omega_k}{4\pi}\left[\int \mathrm{d}^3x_1 e^{-i\mathbf{k}\cdot\mathbf{x}_1}\delta_W(\mathbf{x}_1)\int \mathrm{d}^3x_2 e^{i\mathbf{k}\cdot\mathbf{x}_2}\delta_W(\mathbf{x}_2)\mathcal{L}_\ell(\hat{\mathbf{k}}\cdot\hat{\mathbf{x}}_2) - P_\ell^{\mathrm{shot}}(\mathbf{k})\right], \tag{4.32}$$

This is called the Yamamoto estimator [69], which decompose the integration by $\mathbf{x}_1$ and $\mathbf{x}_2$ into the separable form.

In the Yamamoto estimator, the integration including the Legendre polynomial,

$$\int \mathrm{d}^3 x_2 e^{i\mathbf{k}\cdot\mathbf{x}} \delta_W(\mathbf{x}) \mathcal{L}_\ell(\hat{\mathbf{k}}\cdot\hat{\mathbf{x}}), \tag{4.33}$$

cannot be done by using FFTs. The solution to this issue has recently been proposed by several authors [70, 71, 67]. Among this, we will use the most recent method proposed in Ref. [67], This method decomposes the Legendre polynomial using the spherical harmonic addition theorem:

$$\mathcal{L}_\ell(\hat{\mathbf{x}}_1, \hat{\mathbf{x}}_2) = \frac{4\pi}{2\ell+1} \sum_{m=-\ell}^{\ell} Y_{\ell m}(\hat{\mathbf{x}}_1) Y^*_{\ell m}(\hat{\mathbf{x}}_2), \tag{4.34}$$

where $Y_{\ell m}(\hat{\mathbf{x}})$ is the sperical harmonics and $\hat{\mathbf{x}}_i$ denotes the unit vector along the direction of $\mathbf{x}_i$. With this decomposition, we can compute Eq. (4.32) by purely using FFTs.

$$\hat{P}_{W,\ell}(k) = (2\ell+1) \int \frac{\mathrm{d}\Omega_k}{4\pi} \delta_{W,0}(\mathbf{k}) \delta_{W,\ell}(-\mathbf{k}), \tag{4.35}$$

where we define

$$\begin{aligned} \delta_{W,\ell}(\mathbf{k}) &\equiv \int \mathrm{d}^3 x e^{-i\mathbf{k}\cdot\mathbf{x}} \delta_W(\mathbf{x}) \mathcal{L}_\ell(\hat{\mathbf{k}}\cdot\hat{\mathbf{x}}) \\ &= \frac{4\pi}{2\ell+1} \sum_{m=-\ell}^{\ell} Y_{\ell m}(\hat{\mathbf{k}}) \int \mathrm{d}^3 x e^{-\mathbf{k}\cdot\mathbf{x}} \delta_W(\mathbf{x}) Y^*_{\ell m}(\hat{\mathbf{x}}). \end{aligned} \tag{4.36}$$

This implies that, we can compute the ℓth-order power spectrum multipole by $2\ell+1$ FFTs. Thus is a huge reduction of computational complexity compared to a naive integration of Eq. (4.33).

4.4 The effect of survey window function

In the above formalism, we measure the power spectrum convolved with the survey window function. Here we take a closer look at this effect on the power spectrum. We start from the weighted density field [Eq. (4.23)],

$$\begin{aligned} \delta_W(\mathbf{x}) &= \frac{\bar{n}(\mathbf{x}) w(\mathbf{x})}{I_{22}^{1/2}} \left\{ \frac{n_\mathrm{g}(\mathbf{x})}{\bar{n}(\mathbf{x})} - \alpha \frac{n_\mathrm{r}(\mathbf{x})}{\bar{n}(\mathbf{x})} \right\} = \frac{\bar{n}(\mathbf{x}) w(\mathbf{x})}{I_{22}^{1/2}} \left\{ [1+\delta(\mathbf{x})] - \alpha \frac{n_\mathrm{r}(\mathbf{x})}{\bar{n}(\mathbf{x})} \right\} \\ &\equiv W(\mathbf{x}) \left\{ [1+\delta(\mathbf{x})] - \alpha \frac{n_\mathrm{r}(\mathbf{x})}{\bar{n}(\mathbf{x})} \right\}, \end{aligned} \tag{4.37}$$

where we define the survey window function (or selection function)

$$W(\mathbf{x}) \equiv \frac{\bar{n}(\mathbf{x}) w(\mathbf{x})}{I_{22}^{1/2}}. \tag{4.38}$$

Note that this window function satisfies the normalization condition $\int \mathrm{d}^3x|W(\mathbf{x})|^2 = 1$. The last term in the bracket of Eq. (4.37) is proceeded as

$$\alpha\frac{n_{\mathrm{g}}(\mathbf{x})}{\bar{n}(\mathbf{x})} = \frac{\int \mathrm{d}^3x\bar{n}(\mathbf{x})[1+\delta(\mathbf{x})]}{\int \mathrm{d}^3x\bar{n}(\mathbf{x})} = 1 + \frac{\int \mathrm{d}^3x\bar{n}(\mathbf{x})\delta(\mathbf{x})}{\int \mathrm{d}^3x\bar{n}(\mathbf{x})}, \tag{4.39}$$

and thus we have

$$\delta_W(\mathbf{x}) = W(\mathbf{x})\left\{\delta(\mathbf{x}) - \frac{\int \mathrm{d}^3x\bar{n}(\mathbf{x})\delta(\mathbf{x})}{\int \mathrm{d}^3x\bar{n}(\mathbf{x})}\right\}. \tag{4.40}$$

The second term in this equation leads to the term called integral constraint, but its contribution to the measured power spectrum in SDSS-III galaxies affects the signals only on very large scales $k \lesssim 0.005\,h\,\mathrm{Mpc}^{-1}$ [18], hence we ignore this term.

Neglecting the integral constraint, the window convolved power spectrum is

$$P_W(\mathbf{k}) = \int \frac{\mathrm{d}^3k'}{(2\pi)^3}P(\mathbf{k}')\left|\tilde{W}(\mathbf{k}-\mathbf{k}')\right|^2, \tag{4.41}$$

where $P(\mathbf{k})$ is the true power spectrum. $\tilde{W}(\mathbf{k})$ is the Fourier transform of the window function, and

$$\begin{aligned}\left|\tilde{W}(\mathbf{k})\right|^2 &= \left|\int \mathrm{d}^3xW(\mathbf{x})e^{i\mathbf{k}\cdot\mathbf{x}}\right|^2 = \int \mathrm{d}^3x\int \mathrm{d}^3x'W(\mathbf{x})W(\mathbf{x}')e^{i\mathbf{k}\cdot(\mathbf{x}-\mathbf{x}')}\\ &\simeq \sum_{i\neq j}^{N_{\mathrm{ran}}} w(\mathbf{x}_i)w(\mathbf{x}_j)e^{i\mathbf{k}\cdot(\mathbf{x}_i-\mathbf{x}_j)}\end{aligned} \tag{4.42}$$

This can be transformed as

$$\left|\tilde{W}(\mathbf{k})\right|^2 = \int \mathrm{d}^3s\left[\int \mathrm{d}^3xW(\mathbf{x})W(\mathbf{x}+\mathbf{s})\right]e^{i\mathbf{k}\cdot\mathbf{s}} \equiv \int \mathrm{d}^3s\left[W^2\right](\mathbf{s})\,e^{i\mathbf{k}\cdot\mathbf{s}}, \tag{4.43}$$

and the configuration-space window function $\left[W^2\right](\mathbf{s})$ can be estimated by thew (weighted) pair count of the random particles in the survey catalogs.

In Chapter 7, we will implement the survey window function in the theoretical template, by using the following method [17]. The multipole moments of the window-convolved power spectrum is written as

$$\begin{aligned}P_{W,\ell}(k) &= \frac{2\ell+1}{2}\int\frac{\mathrm{d}\phi}{2\pi}\int \mathrm{d}\mu\,P_W(\mathbf{k})\,\mathcal{L}_\ell(\mu)\\ &= \frac{2\ell+1}{2}\int\frac{\mathrm{d}\phi}{2\pi}\int \mathrm{d}\mu\int \mathrm{d}^3k'P(\mathbf{k}')\left|\tilde{W}(\mathbf{k}-\mathbf{k}')\right|^2\mathcal{L}_\ell(\mu)\\ &= \int \mathrm{d}^3k'P(\mathbf{k}')\left[\frac{2\ell+1}{2}\int\frac{\mathrm{d}\phi}{2\pi}\int \mathrm{d}\mu\left|\tilde{W}(\mathbf{k}-\mathbf{k}')\right|^2\mathcal{L}_\ell(\mu)\right]\\ &= \int_0^\infty k'^2\mathrm{d}k'\int_{-1}^1\mathrm{d}\mu'\int_0^{2\pi}\mathrm{d}\phi'P(k',\mu')\left[\frac{2\ell+1}{2}\int_0^{2\pi}\frac{\mathrm{d}\phi}{2\pi}\int_{-1}^1\mathrm{d}\mu\left|\tilde{W}(\mathbf{k}-\mathbf{k}')\right|^2\mathcal{L}_\ell(\mu)\right].\end{aligned} \tag{4.44}$$

Expanding the true redshift-space power spectrum as $P(k', \mu') = \sum_L P_L(k')\mathcal{L}_L(\mu')$ ($\mu' = \hat{\mathbf{k}}' \cdot \hat{\mathbf{x}}_h$), and using the formulae

$$\begin{aligned} e^{ikx\mu} &= \sum_\ell i^\ell (2\ell+1) j_\ell(kx)\mathcal{L}_\ell(kx) \\ \frac{2\ell+1}{2}\int_{-1}^{1}\mathrm{d}\mu \int_0^{2\pi}\frac{\mathrm{d}\phi}{2\pi}&\mathcal{L}_\ell(\hat{\mathbf{k}}\cdot\Delta\hat{\mathbf{x}})\mathcal{L}_{\ell'}(\hat{\mathbf{k}}\cdot\hat{\mathbf{x}}_h) = \mathcal{L}_\ell(\hat{\mathbf{x}}_h\cdot\Delta\hat{\mathbf{x}})\delta_{\ell\ell'}, \end{aligned} \tag{4.45}$$

where $j_\ell(x)$ is the spherical Bessel function, we have

$$\begin{aligned} P_{W,\ell}(k) &= \int_0^\infty k'^2 \mathrm{d}k' \int_{-1}^{1}\mathrm{d}\mu' \int_0^{2\pi}\mathrm{d}\phi' \sum_L P_L(k')\mathcal{L}_L(\mu') \\ &\quad\times \frac{2\ell+1}{2}\int_0^{2\pi}\frac{\mathrm{d}\phi}{2\pi}\int_{-1}^{1}\mathrm{d}\mu\,\mathcal{L}_\ell(\mu)\sum_{i\neq j}^{N_{\mathrm{ran}}} w(\mathbf{x}_i)w(\mathbf{x}_j)e^{i\mathbf{k}\cdot\Delta\mathbf{x}}e^{-i\mathbf{k}'\cdot\Delta\mathbf{x}} \\ &= 2\pi\int_0^\infty k'^2\mathrm{d}k'\sum_L P_L(k')2i^\ell(-i)^L(2\ell+1) \\ &\quad\times\left[\sum_{i\neq j}^{N_{\mathrm{ran}}} w(\mathbf{x}_i)w(\mathbf{x}_j)j_\ell(k\left|\Delta\mathbf{x}\right|)j_L(k'\left|\Delta\mathbf{x}\right|)\mathcal{L}_\ell(\hat{\mathbf{x}}_h\cdot\Delta\hat{\mathbf{x}})\mathcal{L}_L(\hat{\mathbf{x}}_h\cdot\Delta\hat{\mathbf{x}})\right] \\ &\equiv 2\pi\int_0^\infty k'^2\mathrm{d}k'\sum_L P_L(k')\left|\tilde{W}(k,k')\right|^2_{\ell L}, \end{aligned} \tag{4.46}$$

where we define the "multipoles" of the window function in Fourier space,

$$\left|\tilde{W}(k,k')\right|^2_{\ell L} \equiv 2i^\ell(-i)^L(2\ell+1)\left[\sum_{i\neq j}^{N_{\mathrm{ran}}} w(\mathbf{x}_i)w(\mathbf{x}_j)j_\ell(k\left|\Delta\mathbf{x}\right|)j_L(k'\left|\Delta\mathbf{x}\right|)\mathcal{L}_\ell(\hat{\mathbf{x}}_h\cdot\Delta\hat{\mathbf{x}})\mathcal{L}_L(\hat{\mathbf{x}}_h\cdot\Delta\hat{\mathbf{x}})\right] \tag{4.47}$$

Thus, we can calculate the window-convolved power specrtrum multipoles by combining the theoretical model of the true power spectrum with the $\left|\tilde{W}(k,k')\right|^2_{\ell L}$ estimated using the random catalogs.

Chapter 5

Accurate Emulator for the Redshift-Space Power Spectrum of Halos and Galaxies

In this chapter, we develop an N-body simulation-based theoretical template, so-called the *emulator*, for the redshift-space power spectrum of massive halos. To avoid the difficulty of analytic approaches in the nonlinear regime, we employ a machine learning technique to interpolate the N-body simulation data set.

There have been several previous works on the emulator approach for the large-scale structure probes. As a pioneering work on the emulator construction, the Coyote Universe [72, 73, 74] employed the Gaussian process regression [75] on 1000 N-body simulations covering 38 wCDM cosmologies to construct an emulator for the nonlinear matter power spectrum in the redshift range $0 \leq z \leq 1$, which can predict the matter power spectrum at $k \lesssim 1\,h\,\mathrm{Mpc}^{-1}$ to within about 1% accuracy. In recent years, the *Euclid* collaboration constructs the EuclidEmulator [76, 77], which emulates the nonlinear correction of the matter power spectrum at $k \lesssim 10\,h\,\mathrm{Mpc}^{-1}$. In the context of the galaxy clustering, the Aemulus Project [78, 79, 80] constructed an emulator for the monopole and quadrupole moments of the redshift-space galaxy correlation function, as well as the halo mass function. It used 47 wCDM cosmologies and a specific form of the halo occupation distribution (HOD) to produce the mock galaxy catalogs, and constructed an emulation of the galaxy correlation function, which has about 1% accuracy in the redshift-space separations of $1 \lesssim s/(h^{-1}\,\mathrm{Mpc}) \lesssim 10$.

These works suggest that it is possible to construct the simulation-based emulator which can be used to extract the cosmological information. In this work, we develop an emulator for the redshift-space power spectrum of halos, instead of galaxies. This approach is unique in that we can include the bias at the level of halos, and then can implement the galaxy bias by using phenomenological halo model formalism, depending on the user-specific settings of the halo-galaxy connection. Also, we emulate the redshift-space power spectrum as a function of (k, μ), in stead of its multipole moments as in the Aemulus emulator, and it enables us to straightforwardly implement the Alcock-Paczynski effect, which is enevitable in galaxy redshift surveys.

5.1 Emulation Design

We present our overall strategy to develop an "emulator" of redshift-space power spectrum of "halos", and describe the relation of the halo power spectrum to the galaxy power spectrum in redshift space, which is a direct observable from galaxy surveys.

Under the halo model picture (also see Sec. 3.4), without loss of generality, the redshift-space power spectrum of galaxies is generally given by the sum of the one- and two-halo terms,

$$\begin{aligned} P^{\mathrm{S}}_{\mathrm{gg}}(\mathbf{k}) &= P^{\mathrm{S}}_{\mathrm{gg,1h}}(\mathbf{k}) + P^{\mathrm{S}}_{\mathrm{gg,2h}}(\mathbf{k}) \\ &= P^{\mathrm{S}}_{\mathrm{gg,1h}}(\mathbf{k}) + \int \mathrm{d}M_1 \mathcal{G}(\mathbf{k};M_1) \int \mathrm{d}M_2 \mathcal{G}(\mathbf{k};M_2) P^{\mathrm{S}}_{\mathrm{hh}}(\mathbf{k};M_1,M_2). \end{aligned} \tag{5.1}$$

The first term is the one-halo term arising from the contribution of correlations between galaxies inside the same halo, while the second term is the two-halo term arising from those between galaxies that reside in different halos. $P^{\mathrm{S}}_{\mathrm{hh}}(\mathbf{k};M_1,M_2)$ is the redshift-space power spectrum for halos of masses M_1 and M_2. Other functions, $P^{\mathrm{S}}_{\mathrm{gg,1h}}$ and $\mathcal{G}$, are needed to model the relation of halos to galaxies and therefore depend on galaxy physics. The halo emulator approach in this study is motivated by the fact that the redshift-space power spectrum of halos can be accurately modeled using N-body simulations, as done in Ref. [29]. On the other hand, since it is still quite challenging to model the formation and evolution of galaxies from the first principles, one has to employ an empirical prescription to describe characteristics of a target galaxy sample, by employing a sufficient number of nuisance parameters to model the effects due to properties and physics of galaxies. Then, the nuisance parameters have to be marginalized over to obtain unbiased and robust constraints on cosmological parameters at the price of conservative confidence intervals. In summary, we assume that $P^{\mathrm{S}}_{\mathrm{hh}}$ carries cosmological information, while the galaxy-related functions are treated as theoretical errors/uncertainties that lead to degradation of the cosmological parameter constraints,

$$\begin{aligned} \text{Halos (cosmology):} &\quad P^{\mathrm{S}}_{\mathrm{hh}}(\mathbf{k};z,M_1,M_2,\mathbf{p}_{\mathrm{cosmo}}) \\ \text{Galaxies (errors and nuisance):} &\quad \left\{P^{\mathrm{S}}_{\mathrm{gg,1h}}(\mathbf{k}), \mathcal{G}(\mathbf{k};M)\right\}, \end{aligned} \tag{5.2}$$

where $\mathbf{p}_{\mathrm{cosmo}}$ is a set of cosmological parameters.

Hence, we use an ensemble of high-resolution N-body simulations to develop an emulator that allows for fast and accurate computation of the redshift-space halo power spectrum, $P^{\mathrm{S}}_{\mathrm{hh}}(\mathbf{k};z,M_1,M_2,\mathbf{p}_{\mathrm{cosmo}})$, as a function of redshift, halo masses (M_1 and M_2), and cosmological parameters ($\mathbf{p}_{\mathrm{cosmo}}$). Since we use N-body simulations, the halo power spectrum we emulate includes all complicated effects in the nonlinear regime: nonlinear clustering, nonlinear redshift-space distortion, nonlinear bias, and so on. This is complementary to perturbation theory-based approaches. On the other hand, galaxy-related functions ($P^{\rm S}_{\rm gg,1h}$, $\mathcal{G}$) need to be provided by a user. In this chapter, as a working example, we use the specific halo model and HOD functions described in Sec. 3.4 to implement the galaxy power spectrum based on the halo emulator.

5.2 Dark Quest N-body Simulations

In this section we describe the DARK QUEST, a suite of cosmological N-body simulations that we use to develop the emulator. We will also create mock galaxy catalogs from this simulation suite, which are mainly used in Chapters 6 and 7. This simulation suite targets primarily on the development of halo and matter clustering emulator named DARK EMULATOR, and our work in this chapter is a part of this emulation project. Detailed descriptions on the DARK QUEST and DARK EMULATOR can be found in Ref. [29]. Here we briefly describe the main properties of these simulations.

5.2.1 N-body simulations

All the simulations in DARK QUEST [29] were executed by using the Tree-Particle Mesh hybrid code GADGET2 [81]. The initial conditions of each simulation are generated assuming the adiabatic Gaussian initial conditions based on the linear matter power spectrum for each cosmology. DARK QUEST consists of the simulations with two different particle resolutions: high-resolution (HR) and low-resolution (LR) runs. The side lengths of the simulation boxes in the HR and LR runs are 1 and $2\,h^{-1}\,{\rm Gpc}$, respectively, and both adopt $N_{\rm p} = 2048^3$ particles. Thus the particle mass for the fiducial *Planck* 2015 TT,TE,EE+lowP best-fit cosmology [32] (we will refer it simply as *Planck* cosmology in this and the next chapters) is $m_{\rm p} = 1.02$ and $8.16 \times 10^{10}\,h^{-1}\,M_\odot$ for HR and LR runs, respectively. In this work, we utilize only the LR simulations to create the training and validation data sets to keep the sufficient statistics, since we need only the positions, velocities, and masses of halos to measure the redshift-space power spectrum of halos (for different mass thresholds) and we do not use N-body particles. For LR simulations, the initial conditions are generated at redshift around 30, using the second-order Lagrangian perturbation theory (2LPT; [82, 83]) based on the implementation by Refs. [84, 85]. Note that the initial redshifts are slightly varied depending on the input cosmology according to the criterion in Ref. [29]. We also use the HR simulations to assess the effects of Fourier resolution on the power spectrum measurements in Appendix 1.

The DARK QUEST simulations employ the flat-geometry wCDM cosmology framework that is characterized by the six cosmological parameters as follows. The set of cosmological parameters for which the simulations are run is defined using the optimal maximin-distance sliced Latin hypercube design [86], which enables an efficient sampling from a high-dimensional parameter space with a hierarchical structure among the samples. Our purpose is to construct an emulator from the simulations each of which requires very high computational cost, and thus such an efficient simulation design is of great importance. Following this scheme, the Dark Quest contains five disjoint subgroups of cosmological parameters (referred to as "slice" in the following), each of which satisfies a homogeneous sampling from the parameter space. The cosmological parameters are sampled from the following ranges (also see Fig. 2 in [29]):

$$\begin{aligned}
&0.0211375 < \omega_\mathrm{b} < 0.0233625,\\
&0.10782 < \omega_\mathrm{cdm} < 0.13178,\\
&0.54752 < \Omega_\mathrm{de} < 0.82128,\\
&2.4752 < \ln(10^{10}A_\mathrm{s}) < 3.7128,\\
&0.916275 < n_\mathrm{s} < 1.012725,\\
&-1.2 < w < -0.8,
\end{aligned} \tag{5.3}$$

where $\omega_\mathrm{b} \equiv \Omega_\mathrm{b}h^2$ and $\omega_\mathrm{cdm} \equiv \Omega_\mathrm{cdm}h^2$ are the physical density parameters of baryon and cold dark matter, respectively; h is the dimensionless Hubble constant defined as $h \equiv H_0/(100\,\mathrm{km\,s^{-1}\,Mpc^{-1}})$; Ω_de is the dark energy density parameter, A_s and n_s are the amplitude and spectral tilt of the power spectrum of primordial curvature perturbations, defined at the pivot scale, $k_\mathrm{p} = 0.05\,\mathrm{Mpc}^{-1}$; w denotes the equation-of-state parameter of dark energy. The parameter range above Eq. (5.3) is defined to be centered at the best-fit ΛCDM model for the *Planck* 2015 TT,TE,EE+lowP data [32], i.e., $\omega_\mathrm{b} = 0.02225, \omega_\mathrm{cdm} = 0.1198, \Omega_\mathrm{de} = 0.6844, \ln(10^{10}A_\mathrm{s}) = 3.094, n_\mathrm{s} = 0.9645,$ and $w = -1$. For the neutrino abundance, we assume $\omega_\nu \equiv \Omega_\nu h^2 = 0.00064$ to include the effect on the initial linear power spectrum alone, and neglect the dynamical effect of massive neutrinos in the N-body simulations. The Hubble constant is computed from the total energy budget condition assuming flatness, i.e., $\Omega_\mathrm{m}h^2 = \omega_\mathrm{b} + \omega_\mathrm{cdm} + \omega_\nu$ and $\Omega_\mathrm{m} + \Omega_\mathrm{de} = 1$. Aside from the *Planck* cosmology, each of the five slices has 20 sets of cosmological parameters, and we have one realization for each of 100 cosmological models. Hence we sample $100 + 1$ models in total for our emulator construction. We note that the ranges of cosmological parameters are broad enough, e.g., to cover the current constraints of the large-scale structure probes such as those from the Subaru Hyper Suprime-Cam [87].

The Dark Quest stored outputs of each N-body simulation realization at 21 redshifts, given by $z = 1.48$, 1.35, 1.23, 1.12, 1.02, 0.932, 0.846, 0.765, 0.689, 0.617, 0.549, 0.484, 0.422, 0.363, 0.306, 0.251, 0.198, 0.147, 0.0967, 0.0478, and 0. These redshifts are evenly stepped by the linear growth factor for the fiducial *Planck* cosmology.

In addition it has 15 random realizations for the fiducial *Planck* cosmology each of which has a volume of 8 $(h^{-1}\,\mathrm{Gpc})^3$, which is larger than the volume of SDSS-III BOSS survey that has about 5.7 $(h^{-1}\,\mathrm{Gpc})^3$. We will often use these simulations to estimate statistical errors such as the errors expected for the power spectrum measurements.

5.2.2 Halo catalogs

Halo catalogs from each simulation output in this simulation suite are produced based on the following procedure. First, halos are identified using the friends-of-friends halo finder in six-dimensional phase space, ROCKSTAR, developed in Ref. [88]. The center of each halo is defined as the center-of-mass of the "core particles," a subset of member particles in the inner part of that halo, which is considered as a proxy of the mass density maximum or the location of central galaxy if forms. Similarly, the velocity of each halo is given as the center-of-mass velocity of the core particles.

The DARK QUEST employ the halo mass definition given by $M_{200} = (4\pi/3)200\bar{\rho}_{\mathrm{m}0}R_{200}^3$, where R_{200} is the spherical halo boundary radius within which the interior mass is equal to 200 times the mean mass density $\bar{\rho}_{\mathrm{m}0}$. Note that the use of the mean mass density today $\bar{\rho}_{\mathrm{m}0}$ is due to the use of the comoving coordinates, meaning that R_{200} is also in comoving length units. This definition of halo mass includes all the N-body particles within the boundary R_{200} around the halo center, including those not gravitationally bound by the halo. After identifying halo candidates, all the halos are split into either central or satellite halos. When the separation between the centers of different halos is closer than R_{200} of any other halo, the most massive halo is marked as a central halo, and the other halo(s) as a satellite subhalo(s). Only the central halos with mass $M_{200} > 10^{12}\,h^{-1}\,M_\odot$ are kept in the final catalogs.

5.3 Construction of the emulator for the redshift-space halo power spectrum

In this section, we describe details of the emulator development. The goal is to develop an emulator which allows for fast, accurate computation of the redshift-space power spectrum of halos for an input cosmological model within wCDM framework, given as a function of wave vector (k, μ), redshift (z), and halo masses (M_1 and M_2).

5.3.1 Problem setting and emulation scheme

Before going to details of the emulator development, we here describe several important aspects of our problem and discuss the machine learning scheme to meet the requirements from the problem setting.

The problem that we are dealing with falls in the category of regression, i.e., to find a reasonable function that reacts to the input parameters smoothly and predicts the outcome for new sets of inputs. In particular, we construct a data set of the redshift-space power spectrum corresponding to different cosmologies, redshifts and number densities. Our goal is to implement the regression of the power spectrum data set in the input parameter space. As we will describe later, the number of combinations of the input parameter values is quite large (more than 10^5), and for each of these inputs, a quite high-dimensional data vector of the redshift-space power spectrum, each component of which corresponds to each (k, μ) bin, needs to be output. Such a regression of (i) a *multi-output* (or equivalently, vector-valued) function in (ii) a *multi-dimensional* input parameter space on (iii) a *large data set* is a highly nontrivial task, and furthermore we need to realize it in (iv) a small computational time. To meet these requirements, we need to pay a special attention to select an efficient machine learning algorithm.

Traditionally, the Gaussian process (GP) regression [75] has been applied to the emulator constructions. This is because of some advantages of the GP; it enables a nonparametric regression, i.e., we need not assume any specific function shape to fit the data set, it works well even in a relatively high-dimensional input space, it is robust against the overfitting, and it can provide predictions in a probabilistic manner which accounts for the errors in the data set (though we do not necessarily regard the last point as important in cosmology applications, since the physical interpretation of the predicted variance is somewhat unclear). However, the GP has a drawback that it is difficult to apply to large data sets (specifically, the data size of order of 10^4 or more) due to its high computational cost, unless we introduce some sparse approximation. In addition, current typical GP applications mainly focus on the problems with a single scalar output, and the multi-output GP schemes are not straightforward to apply. Therefore, in previous works on the emulator constructions using GPs, multiple single-output GPs were independently built so that each of them corresponds to each component of the multi-dimensional output data vector. When the dimensionality of the output data vector is quite high (as in our problem), this can lead to a large computational time due to the call of each GP in the resultant emulator, as well as a quite large data size of the emulator code set. Thus, in the application of GPs to the emulator construction, it is almost inevitable to employ some scheme to reduce the dimensionality of the output data, e.g., the principal component analysis. However, to find a successful scheme of the dimensionality reduction for a given target quantity, i.e., the scheme by which we can precisely reconstruct the high-dimensional data vector from the reduced data encoded in a low-dimensional space, would be also a nontrivial task. It is highly desirable, if possible, to build a learning pipeline that we can easily apply to almost any target quantities.

In this work, we choose a feed-forward neural network as a hopeful candidate for such a scheme of high versatility. The neural network provides a smooth interpolation of the data set in the multi-dimensional input space, and a relatively easy scheme for the multi-output regression without the necessity of dimensionality reduction, and it can be applied to a large data set. This approach was previously applied to cosmology (e.g., [89, 90, 91]), and its performance was shown to be competitive or sometimes better than other existing methods, when the network architecture was appropriately designed. In addition, as we would extend the data size by additional simulation runs in the future, this scalability for larger data sets would be advantageous. This is opposed to the $\mathcal{O}(N^3)$ scaling of the popular Gaussian process regression with N training samples. On the other hand, the neural network has a drawback that it is more susceptible to the overfitting compared to GPs. Hence we need to carefully check the emulation performance using the validation data set and tune the network architecture so that the generalization error is successfully suppressed.

5.3.2 Data set

Our aim is to develop a machine-learning pipeline that optimally finds the correspondence between the input parameters (cosmology, redshift, and two halo masses M_1 and M_2) and the output power spectrum $P^{\mathrm{S}}_{\mathrm{hh}}(k,\mu)$ from the training data set. Following the procedure in Ref. [29], we set two distinct number density bins n_1 and n_2, instead of mass bins, to make the learning process easier. This choice is intended to have similar error levels over the data vector among different cosmologies. If we had specified a halo sample by its mass instead, the shot noise level could be quite different among different cosmologies especially in high-mass bins, reflecting the strong dependence of the halo mass function (i.e., the exponential damping as a function of the mass variance) on some of the cosmological parameters. In Appendix 2 we see that the two distinct number density bins, n_1 and n_2, are necessary to cover the full mass dependence of the halo power spectrum, and hence irreducible to a single set of bins.

For each number density bin n, we pick up the halos from top of the ranked list in which we sort all the halos in descending order of mass, to reach the given number density. Such number density bins correspond to the halo mass threshold (minimum mass in the halo sample) derived from the halo mass function,

$$n_{\mathrm{h}}(M > M_{\mathrm{min}}) = \int_{M_{\mathrm{min}}}^{\infty} \mathrm{d}M \, \frac{\mathrm{d}n}{\mathrm{d}M}(M), \tag{5.4}$$

where M_{min} denotes the halo mass threshold and $\mathrm{d}n/\mathrm{d}M$ is the halo mass function in the range $[M, M+\mathrm{d}M]$ which depends on the cosmology and redshift. In the prediction stage, the emulator outputs the predictions (redshift-space power spectrum) as a function of mass by taking the numerical derivative at the target masses M_1, M_2,

$$P^{\mathrm{S}}_{\mathrm{hh}}(\mathbf{k}; M_1, M_2) = \frac{\frac{\partial^2}{\partial M \partial M'} \left[n_{\mathrm{h}}(M) n_{\mathrm{h}}(M') P^{\mathrm{S}}_{\mathrm{hh}}(\mathbf{k}; n(M), n(M')) \right] \Big|_{\substack{M=M_1, \\ M'=M_2}}}{\frac{\mathrm{d}n}{\mathrm{d}M}(M_1) \frac{\mathrm{d}n}{\mathrm{d}M}(M_2)}, \tag{5.5}$$

where $n(M)$ is the halo number density corresponding to the mass threshold M.

We employ nine logarithmic bins for the number density ranging from 10^{-7} to $10^{-3}\,(h^{-1}\,\mathrm{Mpc})^{-3}$, and add one *mass* threshold bin $M_{\mathrm{min}} = 10^{12}\,h^{-1}\,M_{\odot}$ for each cosmology and redshift. Since we adopt the (logarithm of) number density as the actual input argument to the neural network, the mass threshold $M_{\rm min} = 10^{12}\,h^{-1}\,M_\odot$ for each cosmology and redshift is converted to the number density through Eq. (5.4), i.e., we have a slightly heterogeneous sampling of the number density over different cosmologies and redshifts.

We measure the halo power spectra from the halo catalogs by using the FFT-based method described in Chapter. 4. Each halo catalog in the DARK QUEST simulations contains the positions, velocities, and masses of halos. We construct the number density field of halos in redshift space by shifting the halo positions along the x_3 axis according to their velocities and assigning each halo to the FFT grid using the Cloud-In-Cell (CIC) interpolation kernel. We then mitigate the aliasing contaminations in Fourier space by using the interlacing scheme in Ref. [92]. We adopt 1024^3 grids on the $2\,h^{-1}$ Gpc cubic box, which corresponds to the Nyquist wave number $k_{\rm Ny} = 1.61\,h\,{\rm Mpc}^{-1}$. We use the k-bin width $\Delta k = 0.02\,h\,{\rm Mpc}^{-1}$ and define the k value for each bin as its central value. In Appendix 1 we show a resolution study on this measurement procedure, where we find that our specific choice of the number of grids and the k-bin width has almost no significant impact on the measured power spectrum.

In the measurement, we assume the Poisson shot noise and subtract it from the measured power spectrum, but note that this procedure requires a slightly careful treatment as follows. Suppose we measure the power spectrum between the halo samples of two different number densities, n_1 and n_2 ($n_1 < n_2$), defined by the procedure above (we call these two samples "sample 1" and "sample 2," respectively). By construction, sample 1 is a subsample of the sample 2, and hence the cross power spectrum between these two samples is decomposed into the auto and cross power spectra, respectively, for the overlapping and the exclusive subsamples:

$$P_{1,2}(\mathbf{k}) = f P_{1,1}(\mathbf{k}) + (1-f) P_{1,2\setminus 1}(\mathbf{k}), \tag{5.6}$$

where $f = n_1/n_2$, $P_{1,2}(\mathbf{k})$ is the cross power spectrum between samples 1 and 2, $P_{1,1}(\mathbf{k})$ is the auto power spectrum of the sample 1, and $P_{1,2\setminus 1}(\mathbf{k})$ is the cross power spectrum between the sample 1 and the subsample of the sample 2 which has no overlap with the sample 1. The Poisson noise that should be subtracted from the auto power spectrum $P_{1,1}(\mathbf{k})$ is simply $1/n_1$, and this is equivalent to the subtraction of $f/n_1 = 1/n_2$ from $P_{1,2}(\mathbf{k})$. On the other hand, the second term in the right-hand side does not have a contribution from shot noise by construction.

5.3.3 Data preprocessing

The power spectrum signals measured in (k, μ) bins from each simulation are noisy due to the small number of modes averaged within each (k, μ) bin. This inaccuracy is particularly problematic for low number density samples. To overcome this obstacle, we use the lowest four multipole moments to approximate the two-dimensional power

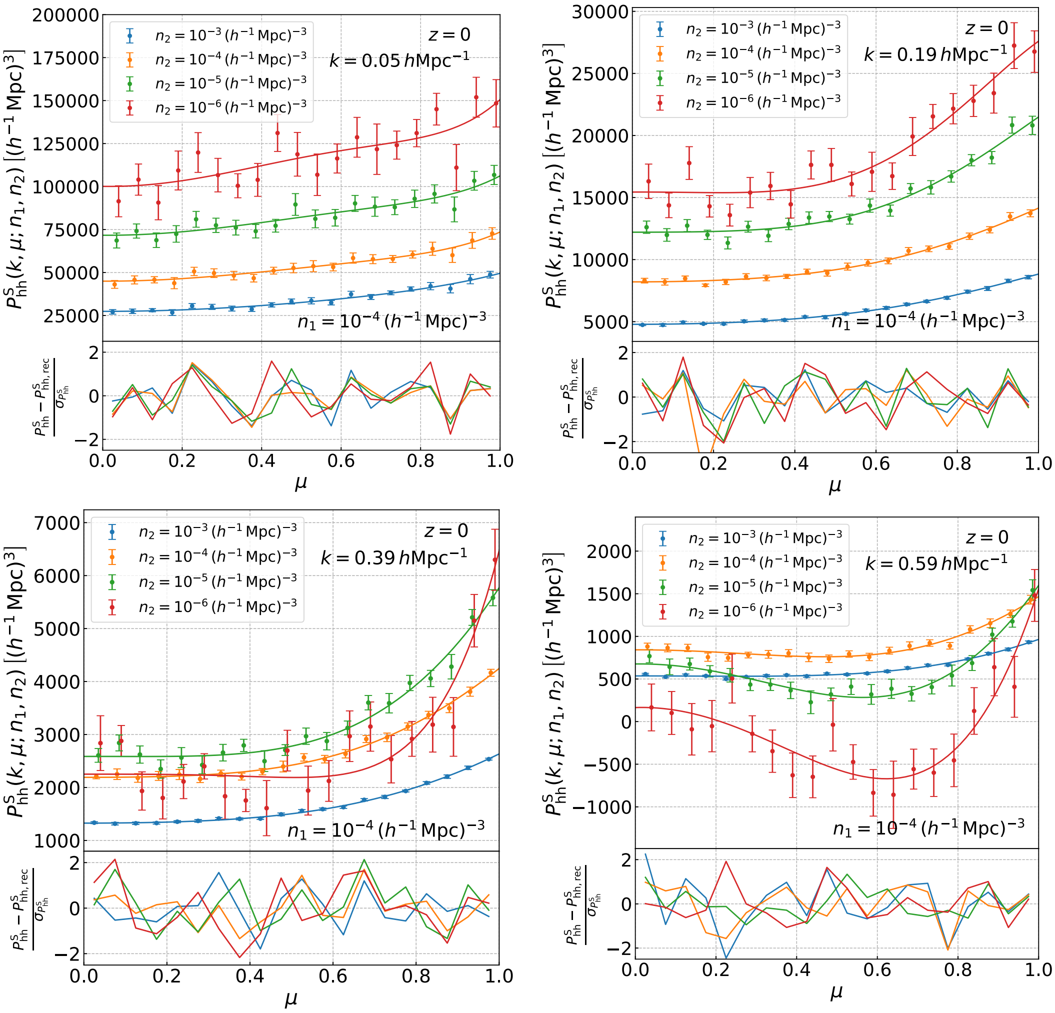

Figure 5.1: An assessment of the approximation, Eq. (5.7), to model the redshift-space power spectrum $P^{\mathrm{S}}_{\mathrm{hh}}(k,\mu)$ in terms of the lowest four multipole moments. In the upper panel in each plot, the symbols with error bars are the cross power spectrum between the halo samples of number densities (n_1 and n_2), $P^{\mathrm{S}}_{\mathrm{hh}}(k,\mu;n_1,n_2)$, measured from one simulation realization at $z = 0$ for the *Planck* cosmology, where we consider the fixed number density for one sample, $n_1 = 10^{-4}\,(h^{-1}\,\mathrm{Mpc})^{-3}$ and consider the other sample of different number densities, $n_2 = 10^{-3}$ (blue), 10^{-4} (orange), 10^{-5} (green), or 10^{-6} (red) $(h^{-1}\,\mathrm{Mpc})^{-3}$, respectively. The error bars are the standard deviation among 15 realizations for the *Planck* cosmology, corresponding to the statistical errors in the band power measurement for a volume of 8 $(h^{-1}\,\mathrm{Gpc})^3$. The solid lines are the results of Eq. (5.7), i.e., the power spectrum reconstructed from the multipole moments up to degree $\ell = 6$ that are measured from the same halo samples in the same realization. We show the results at $k = 0.05, 0.19, 0.39,$ and $0.59\,h\,\mathrm{Mpc}^{-1}$, from upper left to lower right plots. We also show, in each lower panel, the differences between the reconstructed spectra and the simulation results in (k,μ) bins, relative to the scatter in the bin.

spectrum as

$$P^{\mathrm{S}}_{\mathrm{hh}}(k,\mu) \simeq \sum_{\ell=0,2,4,6} P^{\mathrm{S}}_{\mathrm{hh},\ell}(k)\,\mathcal{L}_\ell(\mu), \tag{5.7}$$

Here we ignore contributions from the higher-order multipoles of $\ell \geq 8$. Since the hexadecapole ($\ell = 4$) and tetra-hexadecapole ($\ell = 6$) moments are highly noisy and have almost zero amplitudes at low k for most cosmological models, we avoid to directly learn the individual multipoles, and instead choose to feed the reconstructed two-dimensional power spectrum, based on Eq. (5.7), into the neural network. Using Eq. (5.7), we reconstruct the approximated power spectrum in 31 linearly spaced bins of k in the range $[0.01, 0.61]\,h\,\mathrm{Mpc}^{-1}$ and 20 linearly spaced bins of μ in the range $[0.025, 0.975]$. We use 620 (k,μ) bins in total.

A validation of the approximation [Eq. (5.7)] is given by Fig. 5.1. The symbols show the power spectrum $P^{\mathrm{S}}_{\mathrm{hh}}(k,\mu)$ as a function of μ in some representative bins of k, directly measured from a particular realization of the fiducial *Planck* cosmology. On the other hand, the solid lines are the results obtained using Eq. (5.7), where we used the multipole moments of $\ell = 0, 2, 4$ and 6 measured from the same realization. The solid lines show a good agreement with the direct measurements and do not show any systematic deviation for any value of (k,μ), confirming that the higher-order multipoles do not give a significant contribution to the two-dimensional power spectrum.

In addition to the approximation [Eq. (5.7)], we employ the following linear transformation to reduce the dynamic range of data vector. For every sampling point of (k,μ), we transform the data vector so that the mean and variance of data over all the inputs (cosmology, redshift and two distinct number densities) are reduced to zero and unity, respectively:

$$P^{\mathrm{S}}_{\mathrm{hh}}(k,\mu) \mapsto \frac{P^{\mathrm{S}}_{\mathrm{hh}}(k,\mu) - \bar{P}^{\mathrm{S}}_{\mathrm{hh}}(k,\mu)}{\sqrt{\mathrm{Var}\left[P^{\mathrm{S}}_{\mathrm{hh}}(k,\mu)\right]}}, \tag{5.8}$$

where $\bar{P}^{\mathrm{S}}_{\mathrm{hh}}(k,\mu)$ and $\mathrm{Var}\left[P^{\mathrm{S}}_{\mathrm{hh}}(k,\mu)\right]$ are the mean and variance among all the power spectra in each (k,μ) bin over all the training and validation data sets. We feed these transformed data into the neural network.

5.3.4 Regression using a neural network

The machine learning using neural networks has been rapidly developed on the back of the recent progress of machine power and the success of the back-propagation method, in addition to the vast increase of available data. Its applicability to a broad range of learning tasks has already been recognized in the community of cosmology as well as astrophysics. For regression tasks, feed-forward neural networks perform accurately serving as a “universal function approximator” [93], i.e., it can

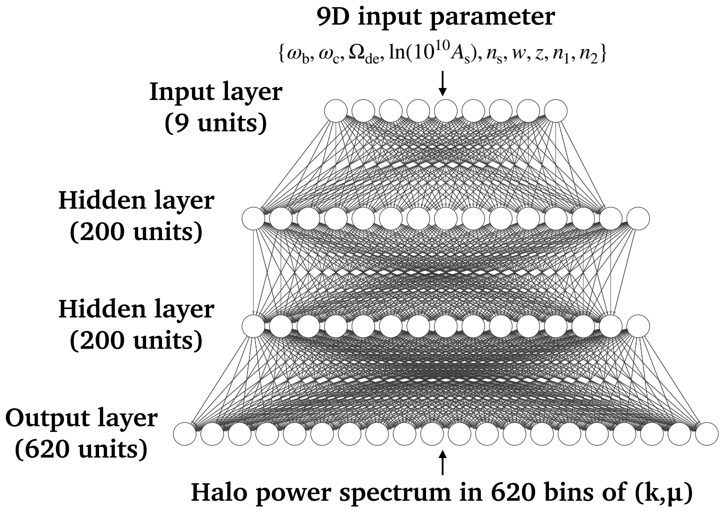

Figure 5.2: The architecture of the feed-forward neural network which we adopt for the regression of the input power spectrum data (training data set). The input layer has nine units corresponding to the nine-dimensional input parameters [Eq. (5.9)]. We adopt two hidden layers that contain 200 units to give a large flexibility to the mapping from the input to output vectors. Finally the output layer has 620 units, which is equal to the number of the (k, μ) bins we use.

approximate almost any continuous functions $f(\mathbf{x})$ with high precision, provided that it has a sufficiently large number of parameters. As we mentioned above, another strength of neural networks is their relatively easy handle on multi-output functions.

In this work we found that a feed-forward neural network with a simple architecture enables us to perform a multi-dimensional regression of the power spectrum data measured from the simulations. Figure 5.2 shows the network architecture we adopt for the regression. We adopt the fully-connected network with two hidden layers; the input layer takes the nine input parameters, i.e., six wCDM cosmological parameters, redshift z and two distinct number densities, n_1, n_2:

$$\mathbf{p}_{\rm in} = \{\omega_{\rm b}, \omega_{\rm cdm}, \Omega_{\rm de}, \ln(10^{10}A_{\rm s}), n_{\rm s}, w, z, n_1, n_2\}. \tag{5.9}$$

On the other hand, the network output layer corresponds to the vector of $P^S_{\rm hh}(k, \mu)$ values, i.e., the output dimension is equal to the number of (k, μ) bins, $N_{\rm bin} = 620$. We set two hidden layers which have a large number (200 for each) of hidden units. In Appendix 3, we describe how we chose the optimal number of hidden units. As the activation function, we impose the Gaussian Error Linear Units (as known as GELUs) [94], which is a smooth variant of the Rectified Linear Units (ReLUs) that are typically used in various machine learning tasks, to both two hidden layers. This is because we expect that the response (i.e., the derivative) of the power spectrum to any of the input variables is smooth without discontinuity from which the standard ReLU function often suffers. Through these activation functions, the input parameter vectors are nonlinearly transformed to represent the target quantities, i.e., the data of the halo power spectrum.

We implement the neural network and the training procedure by using PyTorch (`https://pytorch.org/`) [95], which is an open-source Python framework for the deep learning. The training of the network is done by using the adaptive stochastic optimization algorithm Adam [96]. The training performance is highly sensitive to the learning rate for the Adam optimizer. We set the learning rate to 10^{-3}, which we found is the best choice among $10^{-4}, 5\times10^{-4}, 10^{-3}, 5\times10^{-3},$ and 10^{-2}.

We train the neural network to *learn* the correspondence between the input and output variables,

$$\mathbf{p}_{\rm in} \mapsto P^{\rm S}_{\rm hh}(k,\mu|\mathbf{p}_{\rm in}), \tag{5.10}$$

where $\mathbf{p}_{\rm in}$ is a set of nine parameters [Eq. (5.9)], and $P^{\rm S}_{\rm hh}(k,\mu|\mathbf{p}_{\rm in})$ is the redshift-space halo power spectrum, based on the transformation of Eq. (5.8). The training data set consists of the power spectrum data for combinations of 80 cosmologies, 21 redshifts, and 10 number density bins for each of n_1 and n_2; hence, the size of the training data amounts to 168,000 instances. Through the training procedure, we optimize the neural network so that the network output $P^{\rm S}_{\rm emu}(k,\mu)$ precisely approximates the simulation data $P^{\rm S}_{\rm sim}(k,\mu)$. In the optimization, we obtain the network parameters by minimizing the loss function that we define as

$$\tilde{\chi}^2_m \equiv \frac{1}{m}\sum_{i=1}^{m}\frac{1}{N_{\rm bin}}\sum_{(k,\mu)}^{N_{\rm bin}}\left[\frac{P^{\rm S}_{\rm sim}(k,\mu|\mathbf{p}_i)-P^{\rm S}_{\rm emu}(k,\mu|\mathbf{p}_i)}{\sigma_{P^{\rm S}_{\rm fid}}(k,\mu|\mathbf{p}_i)}\right]^2, \tag{5.11}$$

where $N_{\rm bin}$ is the number of (k,μ) bins ($N_{\rm bin}=620$ in our case), m is the number of training data in one "mini-batch" (see below), and $\sigma_{P^{\rm S}_{\rm fid}}(k,\mu|\mathbf{p}_i)$ is the error of the power spectrum in the (k,μ) bin for the ith training data set. The mini-batch is a subset of the training data set that is used to train the network parameters. The training of neural network is done by feeding data into the network in the form of mini-batch, and repeatedly updating the network parameters according to the derivative of the loss function back-propagated to each unit until the loss function is sufficiently minimized. The use of mini-batches is beneficial because it is not only memory efficient, but also leads to an improved optimization performance compared to feeding all the training data all at once, as it adds a certain degree of stochasticity to the parameter updates and this helps to escape from local minima in the high-dimensional network parameter space. The training period during which all the mini-batches in the training data set are fed into the network is called as an "epoch." At the beginning of each epoch, we set up the mini-batches by randomly shuffling the whole training data set and dividing it into the mini-batches each of which contains 2000 instances, i.e., $m=2000$ in Eq. (5.11). For the error $\sigma_{P^{\rm S}_{\rm fid}}$, we use the standard deviation of the power spectra, for a given set of redshift, n_1 and n_2 in the ith parameter ($\mathbf{p}_i$), computed from the 15 realizations for the *Planck* cosmology. That is, we ignore the dependence of the power spectrum error on cosmological models, as we have only one realization for each cosmological model in the training sets. Note that the simulations for the *Planck* cosmology is not included in the training data set.

We use 1000 epochs to train the neural network, and after the training we obtain the optimized network parameters that give a parametrized fitting formula of the redshift-space power spectrum, $P^{\mathrm{S}}_{\mathrm{emu}}(k,\mu)$. We design the loss function [Eq. (5.11)] to approximately correspond to the χ^2 value between the data and "model" (network output in this case), averaged over all the (k,μ) bins of all the instances in the mini-batch. Hence, we expect that the loss function roughly goes to unity when the training successfully converges to the optimal result. In fact, the trained network we obtain shows the loss function value to be about 2 for *both* the training and validation data set (while the validation data set is not used for the training itself), and this value is sufficiently saturated by the end of the training. With the trained network we can compute the redshift-space power spectrum, $P^{\mathrm{S}}_{\mathrm{hh}}(k,\mu)$, for an arbitrary input set of the model parameters that are covered within the ranges of nine parameters. From the neural network output which has $N_{\mathrm{bin}} = 620$ values, we can obtain the prediction at any point of (k,μ) within the range that we consider, by using the bivariate cubic spline interpolation.

5.3.5 Large-scale limit: Stitching with linear theory prediction

The redshift-space power spectrum measured from simulations is considerably noisy on very large scales due to the lack of large-scale Fourier modes or the significant sample variance of a finite volume, 8 $(h^{-1}\,\mathrm{Gpc})^3$. Thus, the power spectrum predicted by the neural network output does not meet our requirements at roughly $k \lesssim 0.02\,h\,\mathrm{Mpc}^{-1}$. To overcome this inaccuracy, we stitch the linear theory prediction with the neural network output to obtain the emulator predictions over a wide range of scales. Specifically, we smoothly stitch the neural network output and the linear theory prediction as

$$P^{\mathrm{S}}_{\mathrm{hh}}(k,\mu) = P^{\mathrm{S}}_{\mathrm{hh,lin}}(k,\mu)e^{-(k/k_{\mathrm{switch}})} + P^{\mathrm{S}}_{\mathrm{hh,NN}}(k,\mu)\left[1 - e^{-(k/k_{\mathrm{switch}})}\right], \tag{5.12}$$

where $P^{\mathrm{S}}_{\mathrm{hh,NN}}(k,\mu)$ is the neural network output we have described above, and $P^{\mathrm{S}}_{\mathrm{hh,lin}}(k,\mu)$ is the linear theory prediction. For the latter, we employ the following model:

$$P^{\mathrm{S}}_{\mathrm{hh,lin}}(k,\mu;n_1,n_2) = \left[b_{\mathrm{h}}(n_1) + f\mu^2\right]\left[b_{\mathrm{h}}(n_2) + f\mu^2\right]P_{\mathrm{lin}}(k), \tag{5.13}$$

where $f = \mathrm{d}\ln D_+/\mathrm{d}\ln a$ is the linear growth rate, and $b_{\mathrm{h}}(n)$ is the linear bias for the halo sample of a given number density n. We use the Dark Emulator developed in [29] for real-space halo statistics to compute the halo bias for the halo sample

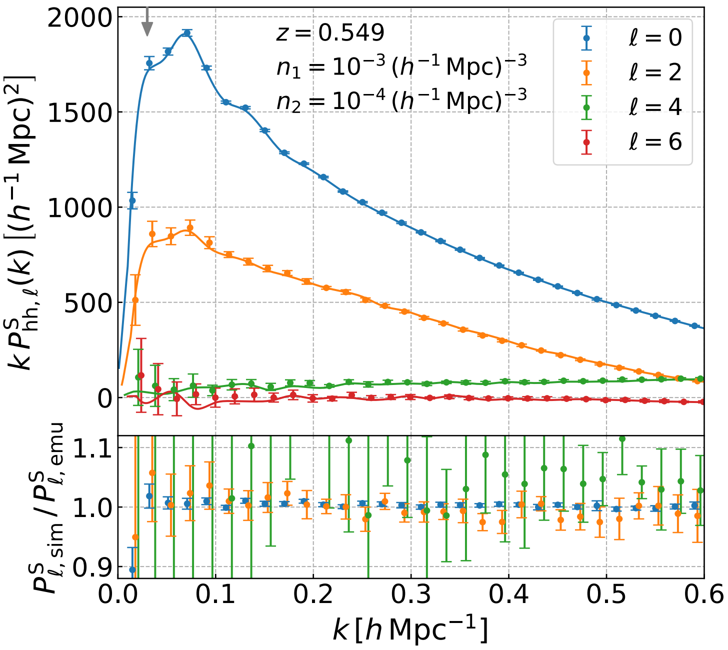

Figure 5.3: An example of the emulator prediction for the multipole moments of the redshift-space cross power spectrum between the halo samples with number densities, $n_1 = 10^{-3}$ and $n_2 = 10^{-4}$ $(h^{-1}\mathrm{Mpc})^3$ at $z = 0.549$, for the *Planck* cosmology that is not used in the training data set. The blue, orange, green and red lines show the predictions for the monopole ($\ell = 0$), quadrupole ($\ell = 2$), hexadecapole ($\ell = 4$), and tetra-hexadecapole ($\ell = 6$) moments, respectively. The symbols with error bars denote the moments measured from one realization for the *Planck* cosmology, where the errors are the statistical errors for a volume of 8 $(h^{-1}\,\mathrm{Gpc})^3$, as in the previous figure. The gray down arrow on the upper horizontal axis denotes the scale $k_{\mathrm{switch}} = 0.03\,h\,\mathrm{Mpc}^{-1}$ that is the switching scale between the linear theory prediction and the emulator output [see around Eq. (5.12) for details].

of a given number density. Throughout this chapter, we adopt the switching scale $k_{\mathrm{switch}} = 0.03\,h\,\mathrm{Mpc}^{-1}$ for all cosmological models. Including this stitching, our emulator implementation can compute $P^{\mathrm{S}}_{\mathrm{hh}}(k, \mu)$ in a few of 10^{-2} CPU seconds on a 2.8 GHz quad-core Intel Core i7 processor, for given input parameters.

5.3.6 Emulator performance

We below discuss the validation and performance of the emulator that we have explained in the preceding section.

Figure 5.3 shows an example of the emulator predictions, for the *Planck* cosmology that is not used in the training set. Here we consider the multipole moments of the redshift-space cross power spectrum between the halo samples of number densities, $n_1 = 10^{-3}$ $(h^{-1}\,\mathrm{Mpc})^{-3}$ and $n_2 = 10^{-4}$ $(h^{-1}\,\mathrm{Mpc})^{-3}$, which can be obtained by

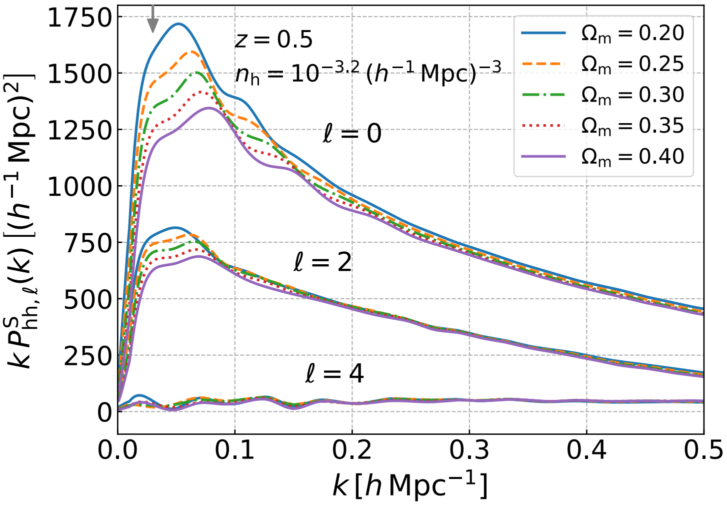

Figure 5.4: A demonstration of the emulator predictions in the cosmological parameter space. We vary Ω_m in the range $[0.2, 0.4]$ while other cosmological parameters are fixed to the values for the *Planck* cosmology. We show the predictions for the halo sample with $n_\mathrm{h} = 10^{-3.2}\,(h^{-1}\,\mathrm{Mpc})^{-3}$ at $z = 0.5$, which are not at the sampling points of redshift and number density in the training data set.

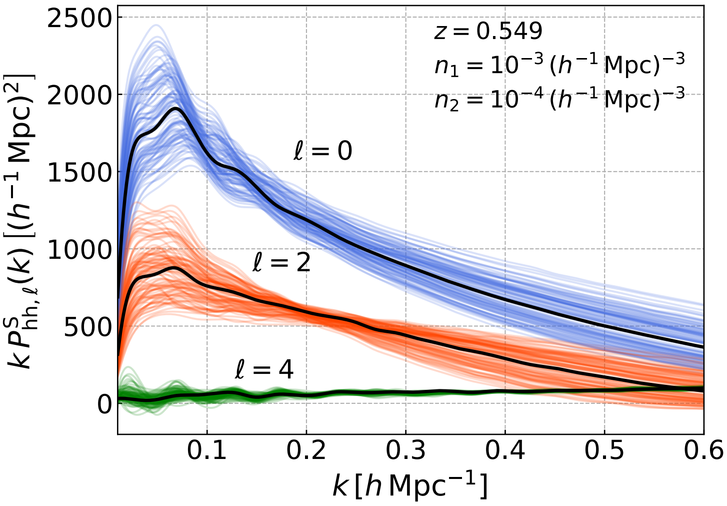

Figure 5.5: The emulator predictions for all the 101 cosmologies covered by the DARK QUEST simulation suite. We show the moments for the halo samples with $(n_1, n_2) = (10^{-3}, 10^{-4})\,(h^{-1}\,\mathrm{Mpc})^{-3}$ at $z = 0.549$. For comparison the black thick lines show the predictions for the *Planck* cosmology.

numerically integrating the emulator output, $P^{\rm S}_{\rm hh}(k,\mu)$, over μ, weighted by the Legendre polynomials corresponding to the multipole order. The figure shows that the monopole and quadrupole from the simulations are reproduced well by our network, by better than 5% in the fractional difference (even over the range of k scales where the quadrupole moment has small amplitudes). The $\ell = 4$ and 6 moments have smaller amplitudes and noisy, but the emulator still explains the overall trend with wave number k fairly well, especially in large k bins compared to the statistical errors for a volume of 8 $(h^{-1}\,{\rm Gpc})^3$. The gray arrow on the upper axis denotes the switching scale between the linear theory and the direct neural network prediction as discussed in Sec. 5.3.5.

In Fig. 5.4, we show how we can use the emulator to study variations in the monopole, quadrupole and hexadecapole moments for cosmological models with different $\Omega_{\rm m}(= 1 - \Omega_{\rm de})$. Note that we assumed the flat-geometry universe, and the other five parameters, i.e., $\{\omega_{\rm b}, \omega_{\rm cdm}, \ln(10^{10}A_{\rm s}), n_{\rm s}, w\}$, are kept to their values for the *Planck* cosmology. The figure shows a clear dependence of the moments on $\Omega_{\rm m}$, including variations in the feature originating from the baryonic acoustic oscillations (BAO). The changes in the quadrupole and hexadecapole are not so prominent compared to the monopole because of their smaller amplitudes.

Figure 5.5 gives another demonstration of the emulator. We here show variations in the multipole moments of the redshift-space power spectrum for all the 101 cosmological models that are sampled in the Dark Quest simulation suite. Here we consider the halo samples with different number densities of $n_1 = 10^{-3}$ and 10^{-4} $(h^{-1}\,{\rm Mpc})^{-3}$ at $z = 0.549$, as an example of general cases. The figure shows that the emulator covers a wide dynamic range for each multipole moment, and describes the cosmological dependence of the BAO features.

Figure 5.6 gives an assessment of the emulator outputs. We consider the multipole moments of redshift-space power spectra for the halo sample with number density $n_{\rm h} = 10^{-4}\,(h^{-1}\,{\rm Mpc})^{-3}$ at redshifts $z = 1.48$, 0.549, and 0.0 from left to right panels, respectively. The sample at $z = 0.549$ roughly corresponds to host halos of the SDSS BOSS galaxies. The upper panel of each plot shows that the emulator well recovers the input power spectrum data, meaning that the neural network does not degrade the accuracy after the regression. The lower panel gives a validation of the emulator, which shows the comparison of the emulator predictions with the multipole moments directly measured from simulations for each of 20 validation cosmological models in slice 5, which are not used in the training. The neural network reproduces equally well the simulation results for each of the validation models. The accuracy of the emulator predictions is comparable between the training and validation data sets. It implies that the neural network successfully avoids the overfitting. We also emphasize that our emulator can predict the monopole and quadrupole moments of halo power spectrum with the number density $n_{\rm h} = 10^{-4}\,(h^{-1}\,{\rm Mpc})^{-3}$ with about 1 and 5% accuracies, respectively, in the fractional errors. For comparison the blue and red shaded regions denote the statistical errors expected for measurements of the

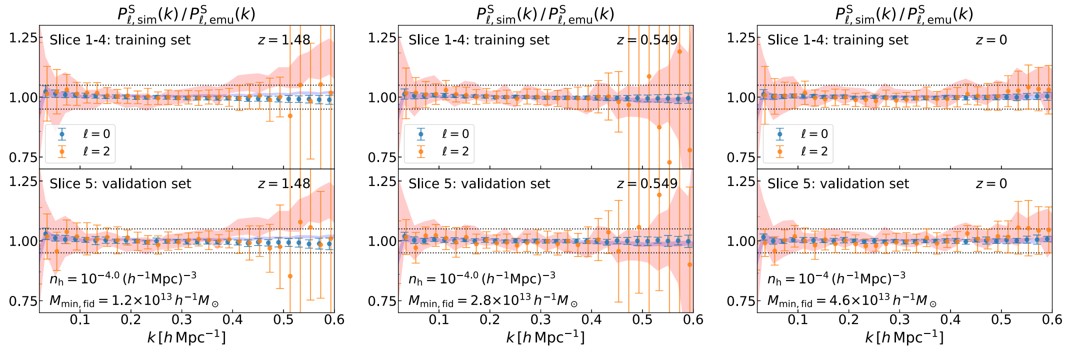

Figure 5.6: A validation of the emulator predictions. We compare, by the ratio, the emulator predictions with the simulation results for the monopole and quadrupole moments, for the halo sample with $n_{\rm h} = 10^{-4}\,(h^{-1}\,{\rm Mpc})^{-3}$ at three representative redshifts $z = 1.48$, 0.549, and 0.0, respectively. The upper panel in each plot shows the comparison for 80 cosmological models in the training data set, while the lower panel shows the comparison for 20 cosmological models in the validation data set. The symbols and error bars are the mean and standard deviation among 80 or 20 results, respectively. For comparison the blue and red shaded regions are the statistical errors around the ratio for the fiducial *Planck* cosmology, where the errors are for $V = 8\ (h^{-1}\,{\rm Gpc})^3$. $M_{\rm min,fid}$ in the legend denotes the halo mass threshold corresponding to the number density $n_{\rm h} = 10^{-4}\,(h^{-1}\,{\rm Mpc})^{-3}$, for the *Planck* cosmology at each redshift. The black dotted lines indicate ±5% fractional errors.

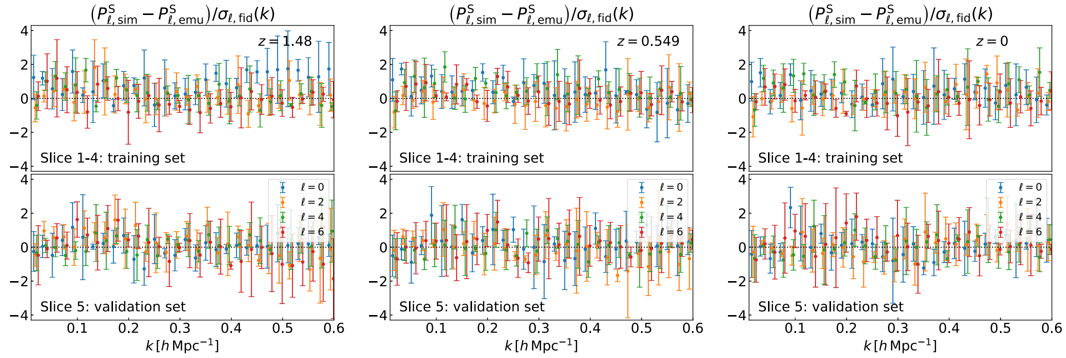

Figure 5.7: Similar to the previous figure, but another validation of the emulator predictions using the quantify to evaluate the accuracy of the emulator prediction (Eq. 5.14), which is defined by the difference between the emulator predictions and the simulation results relative to the statistical errors in each multipole moment for a volume of 8 $(h^{-1}\,{\rm Gpc})^3$. We here show the results up to the multipole moments of $\ell = 6$. The symbols and error bars are the mean and standard deviation among 80 and 20 realizations for the training and validation sets, respectively.

monopole and quadrupole moments, respectively, for a volume of 8 $(h^{-1}\,\mathrm{Gpc})^3$, which are estimated from the standard deviations among 15 realizations for the *Planck* cosmology, where the simulation volume is larger than that of the SDSS BOSS survey, $V_s \simeq 5.7\ (h^{-1}\,\mathrm{Gpc})^3$. The quadrupole moment for the *Planck* cosmology (red shaded region) at $z = 1.48$ shows a deviation at high k. It should be by chance due to the inaccuracy of learning, since we do not see the same behavior at other redshifts or number densities. One might notice relatively larger variances in the quadrupole moment (i.e., orange error bars) at $z = 1.48$ and 0.549 for both the training and validation sets at $k \gtrsim 0.4\,h\,\mathrm{Mpc}^{-1}$. This is due to the fact that the quadrupole moments happen to have a transition from positive to negative values around these scales for some of the cosmological models, for the halo sample at these redshifts and number density. In Appendix 4, we show the prediction accuracy for the monopole and quadrupole moments for the halo samples of different number densities.

For the hexadecapole ($\ell = 4$) and tetra-hexadecapole ($\ell = 6$) moments, it is tricky to make a similar fractional comparison of the emulator predictions with the simulation results, especially at large scales, because the higher-order moments are noisy in the simulation measurements, and have small (almost zero-consistent) amplitudes. Instead, we perform another comparison as shown in Fig. 5.7. In this figure we compare the differences between the emulator predictions and the simulation data (both in the training and validation sets), relative to the standard deviation among 15 realizations for the fiducial *Planck* cosmology; we use the following quantity to evaluate the accuracy of the emulator predictions:

$$\frac{P^{\mathrm{S}}_{\ell,\mathrm{sim}}(k) - P^{\mathrm{S}}_{\ell,\mathrm{emu}}(k)}{\sigma_{P^{\mathrm{S}}_{\ell,\mathrm{fid}}}(k)}, \tag{5.14}$$

where $P^{\mathrm{S}}_{\ell,\mathrm{sim}}(k)$ and $P^{\mathrm{S}}_{\ell,\mathrm{emu}}(k)$ are the power spectrum multipole of degree ℓ measured from the simulation halo catalogs and predicted by our emulator, respectively, and $\sigma_{P^{\mathrm{S}}_{\ell,\mathrm{fid}}}(k)$ is the standard deviation among 15 realizations for the *Planck* cosmology. We show the results for the same halo samples of three redshifts and number density as in Fig. 5.6. The four color (blue, orange, green, and red) symbols with error bars are their mean and standard deviation over 80 or 20 cosmologies in the training (upper) or validation (lower) sets, respectively. The figure shows that the accuracies of the emulator predictions for the higher-order moments are roughly comparable between the training and validation sets as well as among different multipole moments, over all the k range that our emulator covers. This means that the training of neural network has been successfully done so that the all the terms in the loss function [Eq. (5.11)] are on average equally minimized, and the training procedure did not cause a serious overfitting.

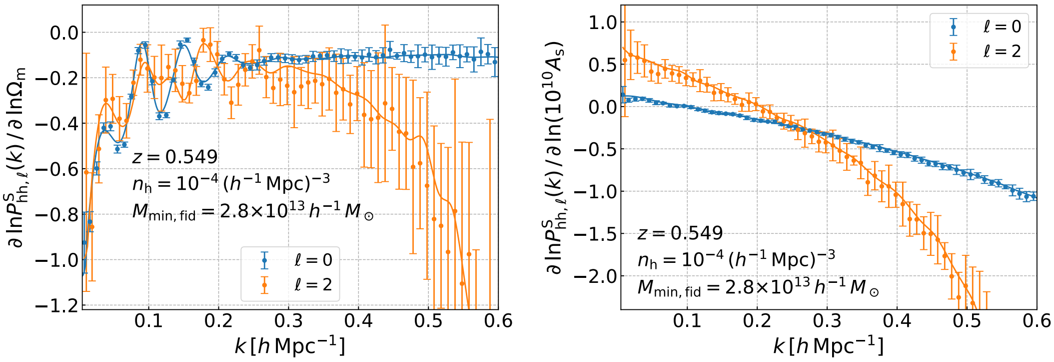

Figure 5.8: The logarithmic derivatives of the halo power spectrum with respect to Ω_{m} (left) and A_{s} (right), around the fiducial *Planck* cosmology. We show the derivatives of the monopole (blue) and quadrupole (orange) moments. The solid lines are the emulator predictions, while the symbols are the signals measured from the N-body simulations. For the latter, we used the additional N-body simulations, with varying Ω_{m} or A_{s} from its *Planck* cosmology value, to numerically evaluate the derivatives from the measured power spectra in different simulations (see text for details). The error bars are the standard deviation among the 10 realizations each of which has a volume of 8 $(h^{-1}\,\mathrm{Gpc})^3$.

5.3.7 Derivatives of the the power spectrum with respect to cosmological parameters

Figure 5.8 shows the derivatives of the halo power spectrum with respect to two cosmological parameters, Ω_{m} (left) and A_{s} (right). While our training procedure of the neural network is such that it minimizes the differences between the training data and the network outputs, the *rate* of change in the data in response to changes in the input parameters is not explicitly taken into account. Hence there is no guarantee that the emulator gives accurate predictions on the derivatives. In this figure, we focus on the derivatives with respect to the cosmological parameters around the fiducial *Planck* cosmology. We show the case of the halo sample with number density $n_{\mathrm{h}} = 10^{-4}\,(h^{-1}\,\mathrm{Mpc})^{-3}$ at $z = 0.549$, which corresponds to the halo mass threshold $M_{\mathrm{min}} = 2.8 \times 10^{13}\ h^{-1}\,M_\odot$ for the *Planck* cosmology. For the monopole (blue) and quadrupole (orange) moments, the emulator predictions (solid lines) and the measured derivative signals (symbols) show a good agreement with each other. For the measured signals, we used the additional N-body simulations to numerically evaluate the derivatives, where we used a shifted value of $\Omega_{\mathrm{de}} = 1 - \Omega_{\mathrm{m}}$ or $\ln(10^{10}A_{\mathrm{s}})$ by ±5% from the fiducial value of *Planck* cosmology to run the simulations (the other five parameters in Eq. (5.3) are kept to their fiducial values). We will describe the details of this additional runs later in Chapter 6. The error bars are the standard deviation among 10 realizations (we have two different simulations of +5% and −5% to take the two-sided derivative with respect to each of Ω_{m} and A_{s}, and thus we used in total 40 realizations for this study). We compute the emulator predictions by the

Class	Function	Description
Primary	$P^{\mathrm{S}}_{\mathrm{hh}}(\mathbf{k}; z, M_1, M_2, \mathbf{p})$	Redshift-space power spectrum for halos of mass thresholds M_1 and M_2, given as a function of redshift (z), wave vector ($\mathbf{k}$), and cosmological parameters $\mathbf{p} = \{\omega_{\mathrm{b}}, \omega_{\mathrm{cdm}}, \Omega_{\mathrm{de}}, \ln(10^{10}A_{\mathrm{s}}), n_{\mathrm{s}}, w\}$
Nuisance	$\langle N_{\mathrm{c}}\rangle(z, M)$	HOD for central galaxies
	$\langle N_{\mathrm{s}}\rangle(z, M)$	HOD for satellite galaxies
	$\tilde{\mathcal{H}}(\mathbf{k}; z, M, ...)$	Real-space position distribution of galaxies in host halos of mass M
	$\tilde{\mathcal{F}}(k_{\parallel}; z, M, ...)$	Velocity distribution of galaxies inside halos of mass M

Table 5.1: A summary of the functions that we use in this chapter. "Primary" function is the redshift-space power spectrum for halos, $P^{\mathrm{S}}_{\mathrm{hh}}(\mathbf{k})$. It is the primary output of the emulator we develop in this chapter. "Nuisance" functions are needed to model the relation between halos and target galaxies in redshift space. These functions need to be flexible enough to model the range of effects of galaxy physics in the redshift-space galaxy power spectrum.

two-sided numerical derivatives in which we shift Ω_{m} or $\ln(10^{10}A_{\mathrm{s}})$ by $\pm 1\%$, while changing this rate in the range of 1%–5% gives almost no change in the predictions.

5.4 Galaxy power spectrum

We have so far described the construction and validation of the emulator for the halo power spectrum. Our primary aim is to have accurate model predictions for the redshift-space galaxy power spectrum, a direct observable in galaxy redshift surveys. In this section we describe how we can use the emulator output to make model predictions for the galaxy power spectrum, and demonstrate that it has a sufficient functionality to give the theoretical templates for a cosmological analysis of actual galaxy redshift surveys.

5.4.1 Galaxy power spectrum based on the halo model formalism

To compute the redshift-space galaxy power spectrum, we combine the halo model formalism described in Sec. 3.4 with the emulator output analytically at the level of equations (also see [29] for the similar method for the real-space galaxy clustering statistics). In doing so, we keep a large flexibility by providing a dedicated functionality module so that a user can adopt a desired HOD model for a sample of target galaxies. The requirement for an application of our emulator to the halo model formalism is that target galaxies reside in host halos with masses $M \geq 10^{12}\ h^{-1}M_{\odot}$ at a redshift for a cosmological model within the ranges covered by our training set.

We here summarize representative model ingredients of HOD that we already implemented in the emulator modules. Once again, a user can extend the model to include other effects, so the following items should be considered as a working example:

- $\langle N_{\rm c}\rangle(M)$ — The HOD for central galaxies that model the average number of "central" galaxies in the host halos of mass M.
- $\langle N_{\rm s}\rangle(M)$ — The HOD for satellite galaxies.
- $\mathcal{H}(r;M)$ — The normalized radial profile of satellite galaxies in the host halo of mass M. One can employ the spherically-symmetric profile in the average sense, and the profile needs to be defined so as to satisfy the normalization condition of $\int_0^{R_{200}} 4\pi r^2 {\rm d}r\ \mathcal{H}(r;M) = 1$.
- $\mathcal{F}(\Delta r_\parallel; r, M)$ — The distribution function of the relative line-of-sight displacement due to the RSD effect caused by the internal (virial) velocities of satellite galaxies in the host halos of mass M [61, 60, 58]. This leads to the FoG effect [59]. We can assume a spherically symmetric profile with a dependence only on the radial distance from the halo center, in the average sense, but the radial and tangential velocity dispersions with respect to the halo center can be different. The velocity function satisfies the normalization condition $\int_{-\infty}^{\infty} {\rm d}\Delta r_\parallel\ \mathcal{F}(\Delta r_\parallel) = 1$.
- $\mathcal{P}(r_{\rm off}; M)$ — Some of central galaxies can have an off-centering effect with respect to the halo center (the density maximum) as a consequence of merger or accretion in the hierarchical structure formation, as indeed indicated by the actual data [62] or by the simulation study [64]. We can assume the spherically symmetric distribution for $\mathcal{P}$ in the average sense, and the profile satisfies the normalization condition, $\int_0^{\infty} 4\pi r_{\rm off}^2 {\rm d}r_{\rm off}\ \mathcal{P}(r_{\rm off}) = 1$. The off-centered galaxies would have internal motions with respect to the halo center, so the velocity distributions of the off-centered galaxies need to be given if one wants to include the RSD effect, as we do for satellite galaxies using $\mathcal{F}$.

Note that the above functions depend on redshift z, but we omit z in the argument for notational simplicity. One can employ parametrized functions to model these ingredients or inject a numerical table into the emulator modules to implement the halo-galaxy connection. In Table 5.1, we summarize the functions that we use in this chapter.

We should emphasize that the form of $P^{\rm S}_{\rm hh}(k,\mu;M_1,M_2)$ in the emulator output makes it straightforward to include the FoG effect due to the virial motions of galaxies in the host halo and the AP geometrical distortion effect (see below) to obtain the redshift-space power spectrum of galaxies. This is not the case if the emulator output is in the form of the multipole moments. This is one of the requirements to which we stick when building the emulator.

We note that, strictly speaking, our standard implementation of the one-halo term in Eq. (3.41) behaves as a shot-noise-like term of k^0 at the limit of $k \to 0$ and this violates the mass and momentum conservation at this limit [97]. Nevertheless, for the tests in the next subsection, we did not find any signature of failure caused by our implementation of the one-halo term over the range of k we consider, so we ignore this limitation for now. For further improvement, one can introduce an empirical function to give a cutoff of the one-halo term at very small k, e.g., following the method in Ref. [98] (see also [85]).

Our default implementation implicitly assumes that the halo-galaxy connection is determined solely by the host halo mass. This would be violated if more complicated conditions apply to the target galaxies, which is often referred to as the assembly bias, i.e., the existence of additional parameter, beyond halo mass, in the halo-galaxy connection such as the halo mass concentration, the halo ellipticity, and environments in more general terms. The previous studies discussed that the assembly bias hardly affects the RSD effect due to bulk motions of host halos, partly because the RSD effect is a gravitational effect [99, 100, 31]. The assembly bias effect should be carefully taken into account when one performs the cosmological parameter estimation. We will discuss this issue in Chapter 6.

5.4.2 Implementation of galaxy power spectrum

We now present a demonstration of the application of our emulator to predicting the redshift-space power spectrum of galaxies. To do this, we consider galaxy samples from the SDSS-III Baryon Oscillation Spectroscopic Survey (BOSS) as a working example, and compare the emulator prediction to the mock measurement from the mock galaxy catalogs. We will put the detailed description of the mock catalog creation in Chapter 6. In this chapter, we used mocks that mimic the LOWZ sample at $z = 0.251$ and the CMASS (we refer it as "CMASS1" in Chapter 6) sample at $z = 0.484$ [2]. The survey volumes for these samples $V_s \simeq 1.0\ (h^{-1}\,\mathrm{Gpc})^3$ for the fiducial *Planck* cosmology. Although details of the model ingredients are not essential for the demonstration, we use up to 18 model parameters for each galaxy sample: six cosmological parameters, two parameters to model the AP effect, and 10 parameters to model the halo-galaxy connection (see Table 6.2 in Chapter 6). Among these, 12 parameters (the parameters besides the cosmological parameters) are different for the LOWZ and CMASS galaxy samples. Even for this fairly complex model, our emulator enables one to compute the redshift-space power spectrum of galaxies in about 0.35 seconds on a 2.8 GHz quad-core Intel Core i7 processor including a two-dimensional integral for the two mass variables.

In Fig. 5.9, we compare the emulator predictions for the multipole moments of the redshift-space galaxy spectrum with those measured from the mock catalogs for SDSS LOWZ- and CMASS-like samples. Note that, for this result, we did not include the off-centering effect, and will discuss it below separately. The figure clearly

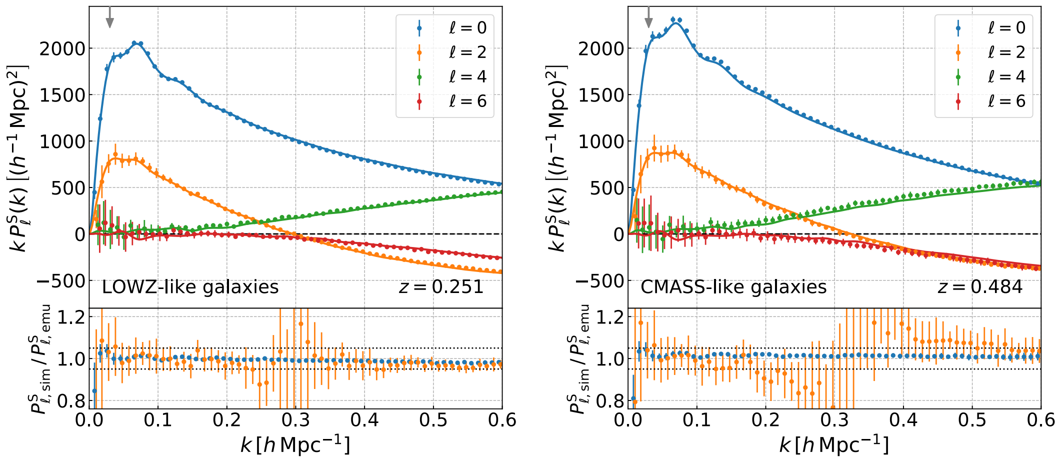

Figure 5.9: The solid lines show the emulator predictions for the multipole moments of redshift-space power spectrum for galaxies that mimic the SDSS BOSS LOWZ- and CMASS-like galaxies at $z = 0.251$ and $z = 0.484$, respectively, for the *Planck* cosmology. Here we adopt the HOD method to combine with the emulator outputs to compute the redshift-space galaxy power spectra for the BOSS-like galaxies. The symbols with error bars are the spectra measured from the mock catalogs, where we employ the same HOD to populate galaxies into halos in each simulation realization, include the RSD effect, and then measure the multipole moments from the mocks. The mock results are for one particular realization, and the errors are for a volume of 8 $(h^{-1}\,\mathrm{Gpc})^3$. The lower panels show the ratio for the monopole and quadrupole moments.

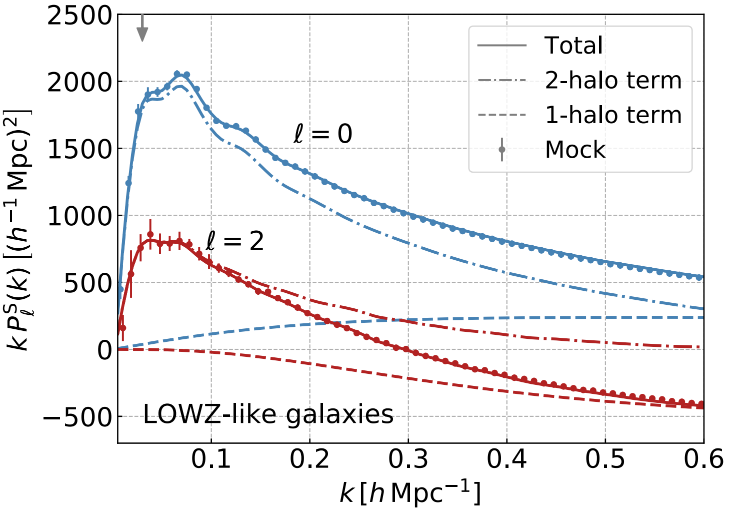

Figure 5.10: The data points with error bars and the solid curves are the same as those for the LOWZ-like sample in Fig. 5.9. The dashed and dot-dashed lines are the one- and two-halo term contributions to the total power for the monopole and quadrupole moments, respectively.

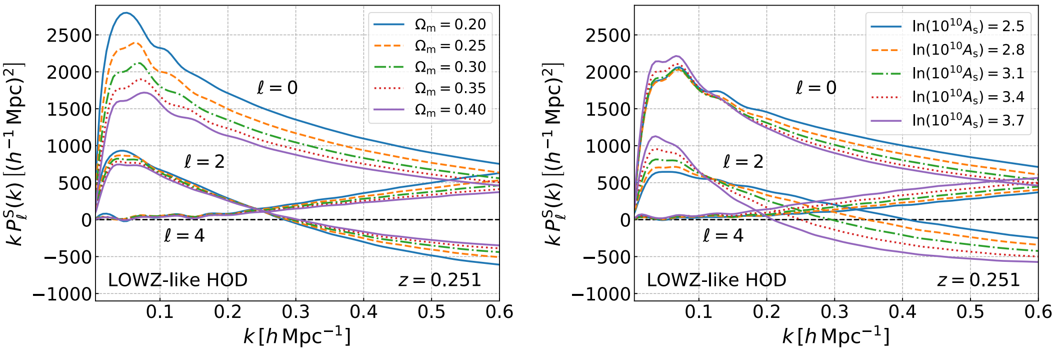

Figure 5.11: A demonstration for the use of the emulator. Here we use the emulator to study variations in the multipole moments of redshift-space galaxy power spectrum for cosmological models with varying $\Omega_{\rm m}$ or $A_{\rm s}$ for LOWZ-like galaxies as in Fig. 5.9. Other model parameters, besides a varied parameter ($\Omega_{\rm m}$ or $A_{\rm s}$), are kept to their fiducial values.

shows that the emulator fairly well reproduces the mock measurements over all scales up to $k = 0.6\ h\,\mathrm{Mpc}^{-1}$. To be more quantitative the lower panels show the ratio, compared to the statistical errors for a volume of 8 $(h^{-1}\,\mathrm{Gpc})^3$. The agreement is well within the errors, definitely within the expected errors for an actual survey volume of $V_s \simeq 1\ (h^{-1}\,\mathrm{Gpc})^3$, which have a factor of 3 larger errors than those plotted in the figure. The lower panel displays a relatively large discrepancy (bias) around $k \simeq 0.3\ h\,\mathrm{Mpc}^{-1}$ for the quadrupole moments due to the zero-crossing in the amplitude. The mock measurements are quite computationally expensive; run high-resolution simulations (a few days for each with multiple processors), identify halos, populate galaxies into halos, and then measure the redshift-space power spectrum and the moments. The emulator enables a computation of these galaxy spectra in $\mathcal{O}(0.1)$ CPU second, and allows for huge improvements in the computation time, more than 6 orders of magnitudes (at least days time scale with multiple CPUs vs. 0.1 seconds with a single CPU).

In Fig. 5.10, we show respective contributions of the one- and two-halo terms [Eqs. (3.41) and (3.42)] to the total power of the multipole moments for the LOWZ sample in Fig. 5.9. The one-halo term gives a non-negligible or even significant contribution to each of the moments, starting from quite small-k scales, around $k \simeq 0.05\ h\,\mathrm{Mpc}^{-1}$ for the monopole, and from $k \simeq 0.1\ h\,\mathrm{Mpc}^{-1}$ for the quadrupole, respectively. The nice agreements between the emulator predictions and the mock measurements cannot be realized unless we include the one-halo term contributions even on such large scales. Hence, this means that we have to marginalize over the halo-galaxy connection parameters, which preferentially affect the one-halo term, to obtain robust constraints on cosmological parameters.

We can easily use the emulator to study the dependence of the galaxy power spectrum on cosmological parameters. Figure 5.11 shows how the multipole moments of the galaxy power spectrum vary with changes in either $\Omega_{\rm m}$ or $A_{\rm s}$. Here again

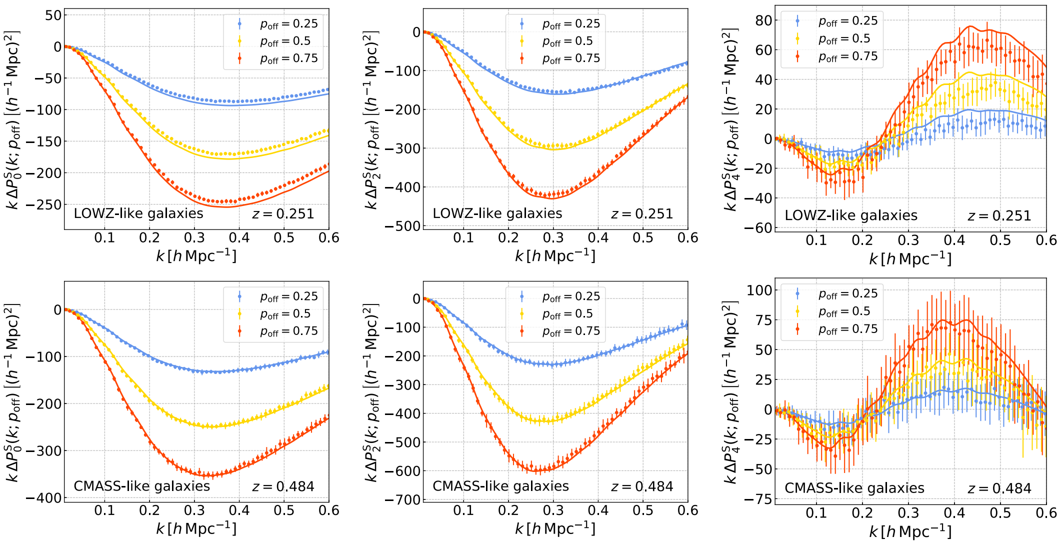

Figure 5.12: Shown is how the off-centering effects of central galaxies affect the monopole, quadrupole and hexadecapole moments for the LOWZ- and CMASS-like galaxies as in Fig. 5.9. Here we quantify the effects by the differences between the power spectra with and without the off-centering effects [see Eq. (5.15)]. The solid lines are the emulator predictions, while the symbols with the error bars are the results measured from the mock catalogs. We model the off-centering effects by the two parameters, $p_{\rm off}$ and $\mathcal{R}_{\rm off}$, where $p_{\rm off}$ is a fraction of central galaxies that are off-centered in host halos of a given mass (here we assume the constant fraction across all halo masses), and $\mathcal{R}_{\rm off}$ is a characteristic radius relative to the scale radius of NFW profile for the host halo (see text for details). We consider three cases for $p_{\rm off}$, as indicated in the legend, and consider $\mathcal{R}_{\rm off} = 2$. The case without the off-centering effect corresponds to $p_{\rm off} = 0$.

we vary $\Omega_{\rm m}$ through $\Omega_{\rm de}$ using the spatial flatness ($\Omega_{\rm m} = 1 - \Omega_{\rm de}$), and the other cosmological parameters in Eq. (5.3), besides a varied parameter ($\Omega_{\rm de}$ or $A_{\rm s}$), and the halo-galaxy connection parameters are kept fixed to their fiducial values. Thus our emulator quite easily enables us to evaluate the sensitivity of the galaxy power spectrum to cosmological parameters, which would be useful to explore an optimal survey design for a galaxy survey.

Since dark matter halos are not relaxed nor in dynamical equilibrium and have no clear boundary, there is no unique definition of the halo center. Common choices include the potential minimum, the mass density peak, the center of mass of member particles, or the position of massive subhalos. Throughout this chapter we employ the mass density maximum traced by the center-of-mass position of a certain fraction of innermost particles as a proxy of halo center, as provided as the Rockstar output. In addition, central galaxies might have an offset from the halo center (any of the above centers) as a consequence of merger and accretion (e.g., see Fig. 11 in

[64]). If a galaxy-galaxy weak lensing measurement is available for spectroscopic galaxies used in the redshift-space power spectrum measurements, it might be possible to observationally constrain the off-centering effects [58, 62]. In any case, the off-centering effect is uncertain or difficult to accurately model, so a conservative approach would be to include the possible contamination in the model template, which should be marginalized over. We here use the emulator to study the impact of off-centering effects on the redshift-space galaxy power spectrum. To quantify the impact, we study the differences between the multipole moments of redshift-space power spectrum with and without the off-centering effects, defined as

$$\Delta P_\ell^{\mathrm{S}}(k;p_{\mathrm{off}}) \equiv P_\ell^{\mathrm{S}}(k;p_{\mathrm{off}}) - P_\ell^{\mathrm{S}}(k;p_{\mathrm{off}}=0), \tag{5.15}$$

where p_{off} is a parameter to specify the fraction of central galaxies in halos of a given mass M that are off-centered. Here we do not consider the halo mass dependence of p_{off}; that is, we assumed the same fraction of off-centered galaxies across different host-halo masses. For a characteristic off-centering radius, we adopt $\mathcal{R}_{\mathrm{off}} = 2$, where $\mathcal{R}_{\mathrm{off}}$ is the parameter to specify the characteristic off-centering radius relative to the scale radius r_{s} of the Navarro-Frenk-White (NFW) profile [54], i.e., we use $R_{\mathrm{off}} = \mathcal{R}_{\mathrm{off}} r_{\mathrm{s}}$ in Eq. (3.43).

Figure 5.12 shows variations in the multipole moments with the different p_{off} values, for the LOWZ- and CMASS-like galaxies. We also implemented the same off-centering effects into the mock galaxy catalogs, and then measured the multipole moments from the varied mocks. The figure shows that the off-centering effects affect the multipole moments at $k \gtrsim 0.1\,h\,\mathrm{Mpc}^{-1}$, by more than the statistical errors of 8 $(h^{-1}\,\mathrm{Gpc})^3$ volume. Our emulator nicely captures the variations in the monopole, quadrupole and hexadecapole moments due to the off-centering effect, although there still remain subtle differences between the predictions and the mock measurements. We checked that the subtle difference can be resolved by slightly changing the off-centering parameters. Hence, we would like to suggest that the off-centering parameters need to be included, and then be marginalized over the uncertainties in cosmological analyses, rather than precisely fixing them from theoretical considerations.

5.4.3 Alcock-Paczyński effect

Finally, we implemented the AP distortion in our emulator. Figure 5.13 shows how the AP distortion affects the monopole, quadrupole, and hexadecapole moments of the galaxy power spectrum, for the LOWZ- and CMASS-like galaxies. We compare the emulator predictions with the measurements from the mock catalogs. To create the mock power spectrum including the AP effect, we artificially distorted the Fourier-space coordinates according to Eq. (3.21), in the measurement code. For illustrative purpose, we here study the differences between the emulator predictions and the mock measurements, defined in a similar way to Eq. (5.15). The AP effect has 2 degrees of freedom in the dependences of the galaxy power spectrum, e.g., the angular

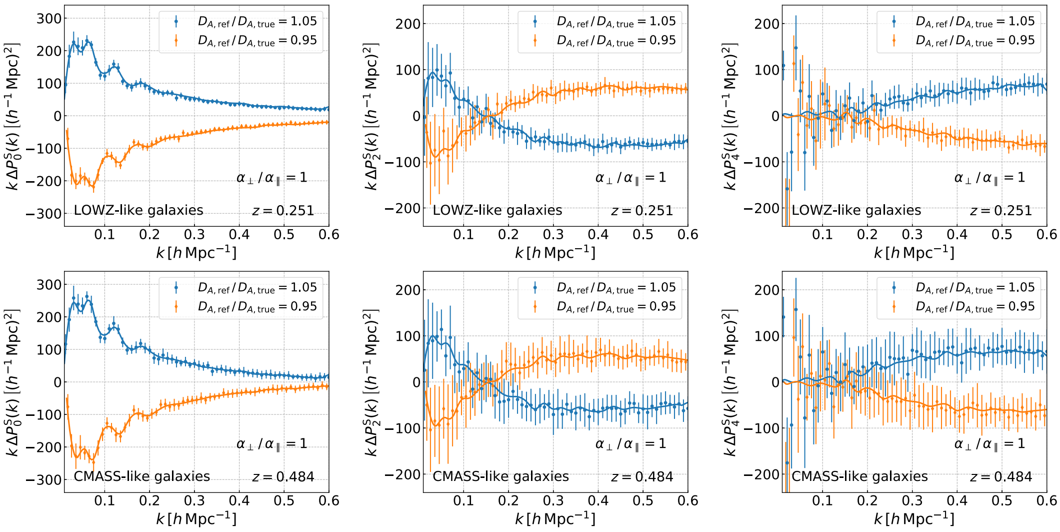

Figure 5.13: The AP distortion effect on the monopole and quadrupole moments in the galaxy power spectrum for the LOWZ- and CMASS-like galaxies. Here we vary either the angular diameter distance $D_{A,\mathrm{ref}}(z)$ or the Hubble expansion rate $H_\mathrm{ref}(z)$ at the redshift of galaxy sample by ±5%, keeping the AP distortion parameter $\alpha_\perp/\alpha_\| \propto D_A(z)H(z)$ to their true value (i.e. $\alpha_\perp/\alpha_\| = 1$), where $D_{A,\mathrm{ref}}$ and H_ref are the quantities for the reference cosmology that is adopted in the clustering analysis. The blue and orange solid lines are the emulator predictions, while the symbols with error bars are the results measured from the simulations including the AP distortion. The errors are the statistical errors expected for measurements of each moment for a volume of 8 $(h^{-1}\,\mathrm{Gpc})^3$.

diameter distance D_A and the Hubble parameter H. Here we focus on variations in the moments with varying either of D_A or H with keeping the AP parameter $(\alpha_\perp/\alpha_\|)$ fixed to the fiducial value (its true value). The figure clearly shows that our emulator well describes the AP distortions in the monopole, quadrupole, and hexadecapole moments at equal accuracies to the mock measurements. Our emulator allows for the computation of these moments in $\mathcal{O}(0.1)$ CPU second.

All the evaluations of our emulator for the galaxy power spectrum in comparison with the mock measurements are quite encouraging. We conclude that our emulator is ready to apply to actual measurements from galaxy redshift surveys such as the BOSS surveys.

Chapter 6

Cosmological Parameter Forecasts on SDSS-III Galaxy Power Spectrum

In the previous chapter, we have developed a fast and accurate emulator to predict the halo and galaxy power spectrum in redshift space. The strategy we adopt to model the galaxy power spectrum is the halo model-based approach employing an HOD model. As we mentioned above, the halo model formalism is highly phenomenological prescription which can include a number of nuisance parameters concerning the poorly-understood halo-galaxy connection. Hence, we are interested in what cosmological information would be held after the marginalization of such nuisance parameters.

In this work, we delve into this issue by using the Fisher matrix forecast. We for the first time calculate the Fisher matrix for the redshift-space galaxy power spectrum at the quasi-nonlinear scales up to $k = 0.3\,h\,\mathrm{Mpc}^{-1}$. By using the N-body simulation-based mock galaxy catalogs, we evaluate the parameter derivatives of the power spectrum in an non-perturbative way. Our main focus is on what cosmological parameter constraints will be obtained from these quasi-nonlinear scales which has never been included in the cosmological analysis of the galaxy power spectrum, in the halo model framework.

6.1 N-body simulation-based mock galaxy power spectrum

In this work, we compute the Fisher matrix on the redshift-space galaxy power spectrum for the model parameters, i.e., the cosmological and halo-galaxy connection parameters. To this end we compute the derivative factors evaluated from the N-body simulations. In this section we describe details of our procedure to create the mock catalogs which mimic the Sloan Digital Sky Survey (SDSS)-III galaxies and compute the sensitivity of the redshift-space galaxy power spectrum to each model parameter, and the way to compute the covariance matrix.

6.1.1 N-Body Simulations and Halo Catalogs

To create the mock galaxy catalogs in this work, we again used the Dark Quest N-body simulations and some additional runs we prepared using the same code set

Model	# of sim.	Ω_m	$\ln(10^{10}A_\mathrm{s})$	σ_8	Response ($\partial P^\mathrm{S}_\ell/\partial p_\alpha$) w.r.t.
Planck	16	0.3156	3.094	0.831	AP/HOD/galaxy
$\Omega_{\mathrm{m}+}$	10	0.350	-	0.820	Ω_m, σ_8
$\Omega_{\mathrm{m}-}$	10	0.281	-	0.841	Ω_m, σ_8
$A_{\mathrm{s}+}$	10	-	3.249	0.897	σ_8
$A_{\mathrm{s}-}$	10	-	2.939	0.769	σ_8

Table 6.1: Summary of N-body simulations used in this study. Each simulation employs a box size of 2 h^{-1}Gpc and 2048^3 N-body particles (see text for details). We use 16 realizations for the fiducial *Planck* cosmology to compute the response functions of redshift-space galaxy power spectrum, $\partial P^\mathrm{S}_{\mathrm{gg},\ell}(k)/\partial p_\alpha$, with respect to each of the halo-galaxy connection parameters (see text) and the cosmological distances at a given redshift, $D_\mathrm{A}(z)$ and $H(z)$, via a hypothetical clustering analysis taking into account an apparent geometrical distortion due to the Alcock-Paczyński effect. In addition, we use 10 realizations for each of the varied cosmological models where either of Ω_m or the parameter of primordial curvature perturbations, $\ln(10^{10}A_\mathrm{s})$, is shifted by about ±11% or ±5%, respectively, but other cosmological parameters are kept fixed. We use these varied cosmology simulations to compute the response functions with respect to either of Ω_m or σ_8. The element denoted as "-" means the same parameter value as the fiducial *Planck* cosmology.

as the Dark Quest. We briefly review the details of the N-body simulations we used, as summarized in Table 6.1.

We use different sets of simulations. The first set is 16 realizations for the fiducial *Planck* cosmology that are contained in the Dark Quest simulations. These correspond to the total volume of $16 \times 8 = 128$ $(\mathrm{Gpc}/h)^3$ which is much larger than the volume of SDSS-III survey with area 8000 $\deg^2$ and over the redshift range we consider in this chapter, $V_\mathrm{SDSS} \simeq 6.2$ $(h^{-1}\mathrm{Gpc})^3$ (see Table 6.3). Hence the *Planck* realizations allow for a precision measurement of redshift-space galaxy power spectra due to the large statistics.

In this work, we use the halo catalogs at output redshifts $z = 0.251, 0.484$ and 0.617 that represent the redshifts of the LOWZ galaxy sample and low-z and high-z sides of the CMASS galaxies in the SDSS-III DR11 survey, respectively. Table 6.3 gives a summary of these survey parameters.

The purpose of this chapter is to evaluate cosmological information contents in the galaxy power spectrum after marginalization over various nuisance parameters that model halo-galaxy connection. To do this, we numerically evaluate a response function of the redshift-space galaxy power spectrum to each model parameter, $\partial P^\mathrm{S}_{\mathrm{gg},\ell}(k)/\partial p_\alpha$, which quantifies how a change in the α-th parameter, p_α, alters the multipole power spectrum $P^\mathrm{S}_{\mathrm{gg},\ell}(k)$. More precisely we use the two-sided finite difference to numerically evaluate the partial derivative:

$$\frac{\partial P^{\rm S}_{{\rm gg},\ell}(k)}{\partial p_\alpha} \equiv \frac{P^{\rm S}_{{\rm gg},\ell}(k; p_{\alpha,{\rm fid}}+\Delta p_\alpha) - P^{\rm S}_{{\rm gg},\ell}(k; p_{\alpha,{\rm fid}}-\Delta p_\alpha)}{2\Delta p_\alpha} \tag{6.1}$$

where $P^{\rm S}_{{\rm gg},\ell}(k; p_{\alpha,{\rm fid}} \pm \Delta p_\alpha)$ is the ℓ-th multipole power spectrum of galaxies where the parameter is shifted to $p_{\alpha,{\rm fid}} \pm \Delta p_\alpha$ by a small amount Δp_α (see below), but other parameters are fixed to their fiducial values. To compute this we use the mock catalog of galaxies to evaluate the power spectrum $P^{\rm S}_{{\rm gg},\ell}(k)$ for each of varied models. For the derivatives $\partial P^{\rm S}_{{\rm gg},\ell}(k)/\partial p_\alpha$, with respect to the halo-galaxy connection parameters, we use the mock catalogs of SDSS galaxies that are constructed from 16 N-body simulation realizations at target redshifts for the fiducial *Planck* cosmology (see below for details).

To compute the other derivatives with respect to cosmological parameters we run different sets of N-body simulations to estimate the dependence of the galaxy power spectrum. In this chapter we focus on $\Omega_{\rm m}$ and σ_8 to which the galaxy power spectrum is sensitive within the flat ΛCDM model. Other cosmological parameters are fixed to their values for the fiducial *Planck* model. To do this we run 10 paired realizations of N-body simulations by varying either of $\Omega_{\rm m}$ or $A_{\rm s}$ on either positive or negative side from their fiducial value, with other parameters being kept to the fiducial values (actually we use $\ln(10^{10}A_{\rm s})$ rather than $A_{\rm s}$ itself, as the parameter for which the numerical derivatives are evaluated, but we simply refer to as $A_{\rm s}$ to avoid the complexity of the description). For each paired realizations, we use the same initial seed of initial conditions to run the N-body simulations. Table 6.1 summarizes details of the N-body simulations we use in this chapter. The reason we use $A_{\rm s}$ instead of σ_8 is that we use $A_{\rm s}$ for the normalization parameter of the initial power spectrum for the fiducial *Planck* model in Ref. [29]. Using the chain rule we compute the numerical derivative with respect to σ_8 as

$$\begin{aligned}
\left.\frac{\partial P^{\rm S}_{{\rm gg},\ell}(k)}{\partial \Omega_{\rm m}}\right|_{A_{\rm s}} &= \left.\frac{\partial P^{\rm S}_{{\rm gg},\ell}(k)}{\partial \sigma_8}\right|_{\Omega_{\rm m}} \left.\frac{\partial \sigma_8}{\partial \Omega_{\rm m}}\right|_{A_{\rm s}} + \left.\frac{\partial P^{\rm S}_{{\rm gg},\ell}(k)}{\partial \Omega_{\rm m}}\right|_{\sigma_8}, \\
\left.\frac{\partial P^{\rm S}_{{\rm gg},\ell}(k)}{\partial A_{\rm s}}\right|_{\Omega_{\rm m}} &= \left.\frac{\partial P^{\rm S}_{{\rm gg},\ell}(k)}{\partial \sigma_8}\right|_{\Omega_{\rm m}} \left.\frac{\partial \sigma_8}{\partial A_{\rm s}}\right|_{\Omega_{\rm m}}.
\end{aligned} \tag{6.2}$$

We use the mock catalog of galaxies that are constructed from N-body simulations with varying either of $\Omega_{\rm m}$ or $A_{\rm s}$ (see Table 6.1), and then evaluate the numerical derivative, $\partial P^{\rm S}_{{\rm gg},\ell}(k)/\partial A_{\rm s}\big|_{\Omega_{\rm m}}$ or $\partial P^{\rm S}_{{\rm gg},\ell}(k)/\partial \Omega_{\rm m}\big|_{A_{\rm s}}$, using Eq. (6.1), where we fix the halo-galaxy connection parameters to their fiducial values. Then we use the above equation to compute $\partial P^{\rm S}_{{\rm gg},\ell}/\partial \sigma_8\big|_{\Omega_{\rm m}}$ and $\partial P^{\rm S}_{{\rm gg},\ell}/\partial \Omega_{\rm m}\big|_{\sigma_8}$, where we use CAMB to evaluate $\partial \sigma_8/\partial \Omega_{\rm m}|_{A_{\rm s}}$ and $\partial \sigma_8/\partial A_{\rm s}|_{\Omega_{\rm m}}$ around the fiducial *Planck* cosmology.

Parameter	Fiducial value			$\sigma_{\rm prior}$
	LOWZ	CMASS1	CMASS2	
$D_{\rm A}(z)\,[h^{-1}\,{\rm Mpc}]$	564.6	861.5	971.5	-
$H(z)\,[h\,{\rm km\ s^{-1}\ Mpc^{-1}}]$	114.1	131.0	142.1	-
$\log M_{\rm min}$	13.62	13.94	14.19	2.0
$\sigma_{\log M}$	0.6915	0.8860	0.7919	1.0
$\log M_1$	14.42	14.46	14.85	2.0
$\log M_{\rm sat}$	13.33	13.72	13.01	2.0
$\alpha_{\rm sat}$	0.9168	1.192	0.9826	2.0
$c_{\rm conc}$	1.0	1.0	1.0	2.0
$c_{\rm vel}$	1.0	1.0	1.0	2.0
$p_{\rm off}$	0.30	0.30	0.30	1.0
$\mathcal{R}_{\rm off}$	2.0	2.0	2.0	2.0
$P_{\rm SN}$	0	0	0	$0.1/\bar{n}_{\rm g}$

Table 6.2: The fiducial values of model parameters in our Fisher matrix analysis for a hypothetical galaxy survey that resembles the LOWZ galaxy sample and two subsamples of CMASS galaxies at lower and higher redshift sides in the SDSS-BOSS surveys (see Table 6.3). Here we consider 12 parameters for each galaxy sample: the angular and radial distances, $D_{\rm A}(z_n)$ and $H(z_n)$, 9 parameters to model the halo-galaxy connection, and the residual shot noise parameter. In addition we include the cosmological parameters $\Omega_{\rm m}$ and σ_8 for the background cosmological model. Using these fiducial values and the slightly-varied value for each parameter (with other parameters being kept fixed), we generate the mock catalogs of these galaxies from the halo catalogs in N-body simulations for the fiducial *Planck* cosmology, make a hypothetical measurement of the redshift-space power spectrum from each mock and then compute the Fisher matrix elements from the measured power spectra. The column denoted as "$\sigma_{\rm prior}$" is the value for a Gaussian prior of each parameter. For a prior of the residual shot noise, we employ 10% of the shot noise for the fiducial mock of each sample.

Sample	Redshift range	$V_{\rm S}\ [h^{-1}{\rm Gpc}]^3$	$\bar{n}_{\rm g}\ [h\,{\rm Mpc}^{-1}]^3$	linear bias $b_{\rm g}$
LOWZ	$[0.15, 0.30]$ (0.251)	1.98	2.173×10^{-4}	1.78
CMASS1	$[0.47, 0.55]$ (0.484)	2.26	9.251×10^{-5}	2.12
CMASS2	$[0.55, 0.70]$ (0.617)	3.8	5.336×10^{-5}	2.28

Table 6.3: The parameters of galaxy samples that resemble the LOWZ, CMASS1 and CMASS2 galaxies in the BOSS survey. Each sample is defined to be a volume-limited sample which is defined to be luminosity-limited, rather than flux-limited, for a given redshift range (see text for details). The mean number density of galaxies ($\bar{n}_{\rm g}$) is computed from the mock catalogs using the fiducial HOD parameters for the fiducial *Planck* model (Tables 6.1 and 6.2). The linear bias ($b_{\rm g}$) is determined from comparison of the galaxy power spectrum with the matter power spectrum in the same mock realization at low-k bins.

6.1.2 Mock catalogs of SDSS LOWZ and CMASS galaxies

We consider models of halo-galaxy connection that mimic spectroscopic galaxies in the SDSS survey [2]. We consider the "LOWZ" galaxies in the redshift range $z = [0.15, 0.30]$ and two subsamples of "CMASS" galaxies that are divided into two redshift bins of $z = [0.47, 0.55]$ and $[0.55, 0.70]$, respectively. Hereafter we call the two CMASS samples in the lower and higher redshift bins, CMASS1 and CMASS2, respectively. We employ the HOD and other parameters that roughly resemble the SDSS galaxies for the *Planck* cosmology, as given in Table 6.2. To generate mock catalogs of these galaxies we use the halo catalogs produced from N-body simulation outputs at redshifts $z = 0.251, 0.484$ and 0.617, which are close to the median redshifts of the LOWZ, CMASS1, and CMASS2, respectively (see Table 6.3). We ignore the redshift evolution of the galaxy clustering within each redshift bin. The following is the details of procedures to populate SDSS-like galaxies into halos identified in each N-body simulation realization:

(i) *Central galaxies* – We employ the central HOD, $\langle N_{\rm c}\rangle(M)$, with the form given by Eq. (3.28). We select halos to populate central galaxies assuming a Bernoulli distribution with mean $\langle N_{\rm c}\rangle(M)$. We assume that each central galaxy has the same peculiar velocity as the bulk velocity of its host halo measured as the center-of-mass velocity of particles in the core region.

(ii) *Off-centering effect of central galaxies* – As our default model we include a population of off-centered "central" galaxies. We select off-centered galaxies from all the central galaxies selected in the procedure (i), following the prescription described in Sec. 3.4: each central galaxy to be off-centered is selected with a probability $p_{\rm off}$, and its displacement from its host halo center is drawn from the isotropic 3D Gaussian distribution given by Eq. (3.43). The scale radius $r_{\rm s}$ of each halo is computed from the fitting formula of halo mass-concentration relation, $c(M, z)$, in Ref. [55], where we assume an NFW profile for the host halo mass M and redshift z for the *Planck* cosmology. Once an off-centered radius $r_{\rm off}$ is given, we assign a "sloshing" velocity of the off-centered galaxy around the halo center, assuming it follows a Gaussian distribution with the typical velocity dispersion given by Eq. (3.36). The total velocity of each "off-centered" central galaxy is given as the sum of the assigned internal velocity and the bulk velocity of its host halo.

(iii) *Satellite galaxies* – To populate satellite galaxies into halos we employ the satellite HOD with the form given by Eq. (3.29). As described in Sec. 3.4 we assume that satellite galaxies reside in halos which already host a "central" galaxy inside, including the off-centered galaxy in the procedure (ii). For each of such host halos with mass M, we determine the number of satellite galaxies, randomly drawn from the Poisson distribution with mean $\lambda_{\rm s}$ defined in Eq. (3.29). For each satellite galaxy we determine its position within r_{200}

of the halo, by randomly drawing from the NFW profile. As we do for the off-centered galaxy in the procedure (ii), we assign an internal velocity to each satellite galaxy using the interior mass $M(<r)$ at the satellite position. Likewise the total velocity is given as a sum of the internal motion and the host halo's bulk velocity.

These are the procedures to populate central and satellite galaxies in the halos found in N-body simulation realizations including the RSD effect. These are an empirical approach, and the properties of true galaxies would be more complicated because of the dependence on complicated physics inherent in galaxy formation/evolution processes as well as on non-trivial selection effects, e.g., color and magnitude cuts. Hence these mock galaxy catalogs should be considered as a working example for the following discussion, and we will discuss the impact of other effects that we ignore on our results, e.g., the assembly bias separately.

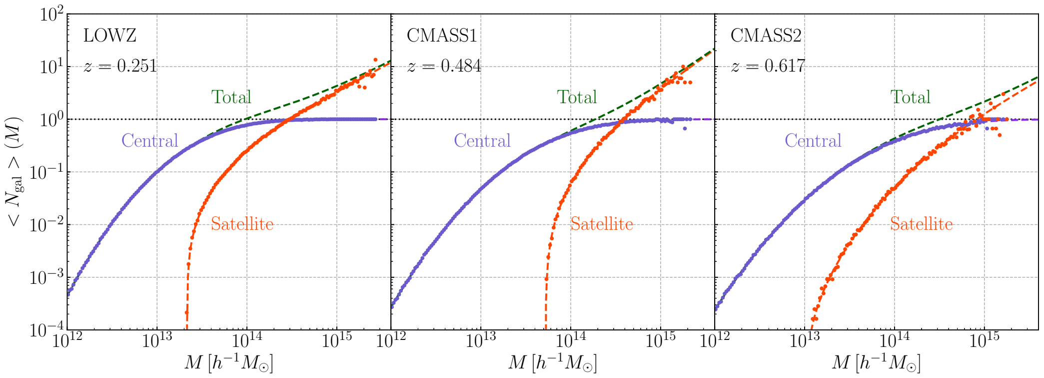

Figure 6.1: The halo occupation distribution (HOD), measured from one realization of the galaxy mock catalogs of LOWZ, CMASS1 and CMASS2 for the fiducial *Planck* cosmology (Table 6.2). Here we show the central (blue) and satellite (orange) HODs. Note that we use the halos with mass $M_{200} \geq 10^{12}\,h^{-1}M_\odot$ as host halos of the mock galaxies in the simulation. For comparison the dashed curves show the input mean HODs in Table 6.2.

Fig. 6.1 shows the HODs for the LOWZ, CMASS1, and CMASS2-like galaxies that we employ when building the mock catalogs in this chapter. The three dashed curves in each panel show the central and satellite HODs and the total HOD, respectively. The points show the respective HODs that are measured from the mock catalogs for the fiducial *Planck* cosmology. The SDSS galaxies are passively-evolving early-type galaxies that are selected based on color and magnitude cuts [101, 2]. These galaxies typically reside in halos with masses $\sim 10^{13}M_\odot$, while cluster-scale halos with $\gtrsim 10^{14}M_\odot$ host these galaxies as satellite galaxies. The average number density $\bar{n}_{\rm g} = 2.173 \times 10^{-4}, 9.251 \times 10^{-5}$ or $5.336 \times 10^{-5}\ [h{\rm Mpc}^{-1}]^3$ for the LOWZ, CMASS1, or CMASS2 for the *Planck* cosmology, respectively (see Table 6.3). These number densities are smaller than that of the full LOWZ and CMASS galaxies, because we mimic the luminosity-limited subsample, not the flux-limited all galaxies (see [102] for a similar discussion). The detailed shape of HOD is not essential for our purpose. We employ these HODs as a working example.

6.1.3 Measurements of redshift-space power spectra from mock galaxy catalogs

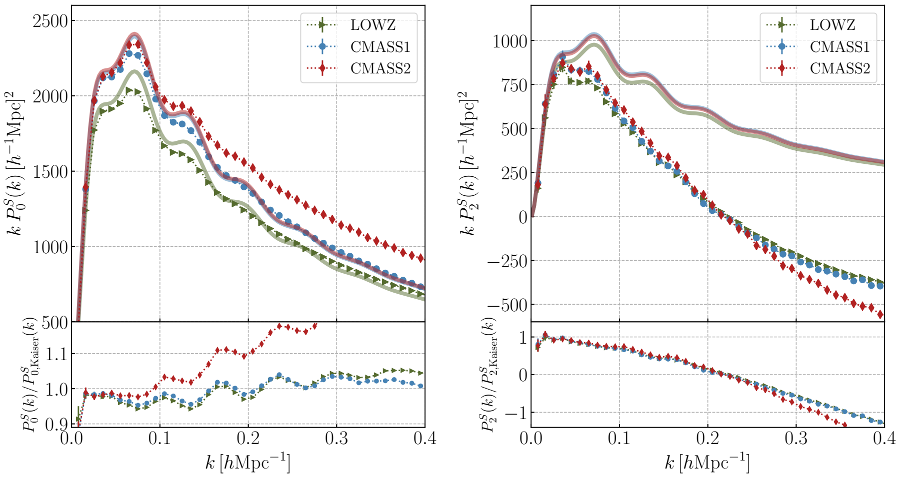

Figure 6.2: The symbols show the monopole (left panel) and quadrupole (right) power spectra measured from the galaxy mocks that resemble LOWZ, CMASS1 and CMASS2 galaxies, respectively. For illustrative purpose we multiply the power spectrum by k so that the power spectrum shown is in a narrow range of this amplitude (therefore y axis is in a linear, rather than logarithmic, scale). Since the power spectra are estimated from the 16 realizations of 2 h^{-1}Gpc cubic box corresponding to volume of 128 $(h^{-1}\mathrm{Gpc})^3$ in total, the error bar of the mean of band power measurements at each k bin, although shown, is not visible. For comparison, the solid curves show the predictions of Kaiser formula [Eq. (3.20)], where we used the linear matter power spectrum, the linear bias parameter (b_g in Table 6.1), and the redshift-space distortion parameter $\beta = (1/b_\mathrm{g})\mathrm{d}\ln D_+/\mathrm{d}\ln a$ for the *Planck* model (D_+ is the linear growth rate). Note that the plotting ranges of y-axis in the monopole and quadrupole spectra are different from each other because of their different amplitudes (see text for details). The lower panel shows the ratio. The Kaiser formula ceases to be accurate at $k \gtrsim 0.05\ h\,\mathrm{Mpc}^{-1}$, especially for the quadrupole spectrum.

We measure the power spectrum from each realization of the galaxy mocks constructed according to the method in the preceding subsection, using FFT-based method (see Chapter 4). First we map the real-space positions of mock galaxies and their velocities to the redshift-space positions using Eq. (3.4), under the plane-parallel approximation where the line-of-sight is taken to be along the z-axis direction. The number density field of mock galaxies is defined on 1024^3 3D mesh grids using the Cloud-in-Cell (CIC) interpolation. Since our simulations' box size is 2000 h^{-1} Mpc, the Nyquist wave number is $k_\mathrm{Ny} = 1.608\ h\,\mathrm{Mpc}^{-1}$, which is sufficiently smaller than

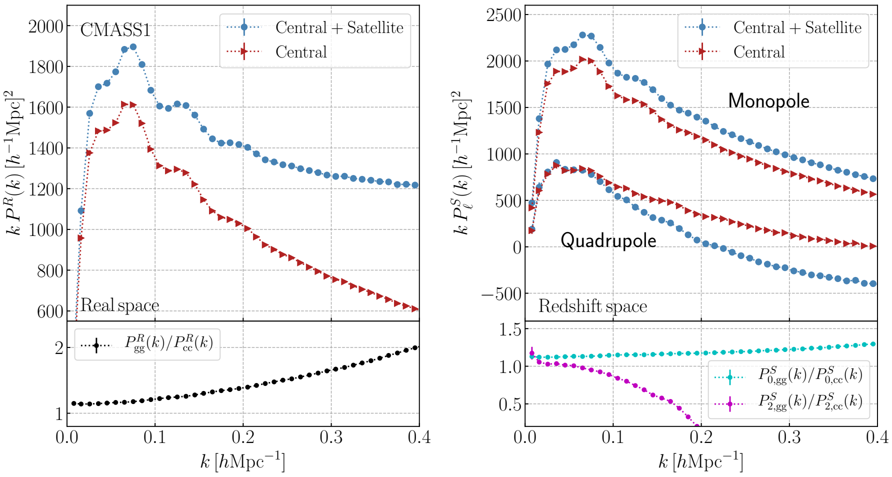

Figure 6.3: The impact of satellite galaxies on the real-space (left panel) and redshift-space (right) power spectra. To study this, the triangle symbols with error bars show the power spectra when using central galaxies alone in each galaxy mock (i.e., removing satellite galaxies from the mock), while the circle symbols are the same as in Fig. 6.2. The lower panels show the ratio.

the scales we are interested in. We then implement the FFT method to the number density field of galaxies to obtain the Fourier-transformed field, where we reduce the aliasing contamination arising from the grid interpolation, using the interlacing scheme described in [92]. We split each Fourier mode into linearly-spaced k-bins ranging $k = [0, 2]$ $h\,\mathrm{Mpc}^{-1}$, and obtain the power spectrum signals by averaging the modes that enter into each bin of k. We adopt the bin width $\Delta k = 0.01$ $h\,\mathrm{Mpc}^{-1}$that is sufficiently narrow compared to the BAO features in the power spectrum. We assume the Poisson shot noise $P_{\mathrm{Poisson}} = 1/\bar{n}_{\mathrm{g}}$ and subtract it from the measured power spectrum.

Fig. 6.2 shows the monopole and quadrupole power spectra measured from the 16 realizations of mock catalogs of LOWZ, CMASS1 and CMASS2-like galaxies for the *Planck* cosmology. The error bar at each k bin denotes an estimate of the error on the mean of power spectrum amplitude, estimated as $\sigma/\sqrt{16}$, where σ is the standard deviation of band power at each k bin. Hence the error represents the statistical error when the band power at each k bin is measured from a volume of 128 $(h^{-1}\mathrm{Gpc})^3$. For comparison we also show the linear theory predictions for each galaxy sample, which are computed using the Kaiser formula, Eq. (3.20). We determine the linear bias b_{g} from a comparison of the real-space power spectra of galaxies and matter measured from the galaxy mocks and N-body simulations, respectively, at the lowest 5 k-bins (corresponding to $k \lesssim 0.05$ $h\,\mathrm{Mpc}^{-1}$) that are considered to be well in the linear regime. The linear bias value estimated based on this method is given in Table 6.3. The Kaiser formula predicts that the ratio of the quadrupole power spectrum to the monopole spectrum is given as $P^{\mathrm{S}}_{2,\mathrm{Kaiser}}/P^{\mathrm{S}}_{0,\mathrm{Kaiser}} = (4\beta/3+4\beta^2/7)/(1+2\beta/3+\beta^2/5)$

independently of the linear matter power spectrum and the wave number k. Galaxies with greater bias parameter has a smaller ratio of $P_2^{\rm S}/P_0^{\rm S}$. The redshift and linear bias parameter in Table 6.3 give about 0.43–0.45 for the ratio for the LOWZ, CMASS1 and CMASS2 samples.

Fig. 6.2 shows that the linear-theory prediction moderately matches the simulation result for the monopole power spectrum up to $k \simeq 0.1\ h\,{\rm Mpc}^{-1}$. However, the Kaiser formula ceases to be accurate very quickly at $k \gtrsim 0.05\ h\,{\rm Mpc}^{-1}$for the quadrupole power spectrum, indicating that nonlinearities in the RSD effect become significant from the relatively small k compared to the nonlinear effect on the real-space or monopole power spectrum. In particular the nonlinear quadrupole power spectra have smaller amplitudes than the linear theory predicts at $k \gtrsim 0.05\ h\,{\rm Mpc}^{-1}$because of the smearing effect due to streaming motions of halos or virial motions of galaxies [103, 104, 13]. Hence it is of critical importance to properly take into account the nonlinear effects in the galaxy power spectra in order to accurately estimate the power of redshift-space galaxy power spectra for constraining cosmological parameters.

In the halo model picture, the underlying halo power spectrum contains the cosmological information, while the effects arising from the halo-galaxy connection are considered as a source of systematic effects. To study this, in Fig. 6.3 we plot the power spectra of the central galaxies alone; i.e., we repeat the measurement after we remove the satellite galaxies from each mock realization.The galaxy power spectrum including the satellite galaxies is quite different from the power spectrum of central galaxies. The satellite galaxies alter the galaxy clustering in several ways (also see [105] for a similar discussion). First, the inclusion of the satellite galaxies leads to a boost in the large-scale (small-k) amplitude of galaxy power spectrum, because the satellite galaxies tend to reside in massive halos, which have a greater linear bias, and including the satellite galaxies upweights the contribution of massive halos leading to the greater band power at small k bins in the 2-halo term regime. Secondly, as is clear from the real-space power spectrum, the satellite galaxies boost the power spectrum amplitude at small scales due to the 1-halo term contribution, which arises from clustering of (central-satellite or satellite-satellite) galaxies in the same host halo. Thirdly, the satellite galaxies cause a suppression in the power spectrum amplitude at small scales due to the FoG effect, as can be found from the redshift-space power spectra in the right panel. Hence the 1-halo term contribution and the FoG effect are somewhat compensated. Thus, the satellite galaxies, more generally the halo-galaxy connection parameters, cause complex, scale-dependent changes in the galaxy power spectrum at small scales compared to the power spectrum of the host halos or the central galaxies.

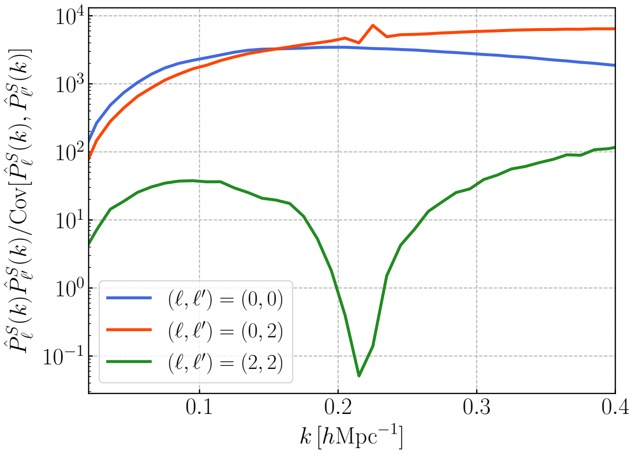

Figure 6.4: The Gaussian covariance of the monopole and quadrupole galaxy power spectra. Note that, to estimate the covariance matrices, we used the redshift-space galaxy power spectrum, $P^{\rm S}_{\rm gg}(k,\mu)$, measured from the 16 realizations of CMASS1 mocks for the *Planck* model [see Eq. (6.3)]. For illustrative purpose, we show the ratio $P^{\rm S}_{{\rm gg},\ell}(k)P^{\rm S}_{{\rm gg},\ell'}(k)/{\rm Cov}[P^{\rm S}_{{\rm gg},\ell}(k),P^{\rm S}_{{\rm gg},\ell'}(k)]$ as a function of k. Since the quadrupole power spectrum amplitude has a zero crossing at $k\simeq 0.2\,h\,{\rm Mpc}^{-1}$, the curves involving the quadrupole power spectrum displays a discontinuity around the wave number.

6.1.4 Covariance matrix of redshift-space power spectra

To compute the Fisher matrix, we need to estimate the covariance matrix for the multipole power spectra of galaxies, which is defined as

$$\mathrm{Cov}\left[\hat{P}^{\rm S}_{{\rm gg},\ell}(k_i),\hat{P}^{\rm S}_{{\rm gg},\ell'}(k_j)\right]\equiv\left\langle\hat{P}^{\rm S}_{{\rm gg},\ell}(k_i)\hat{P}^{\rm S}_{{\rm gg},\ell'}(k_j)\right\rangle-\left\langle\hat{P}^{\rm S}_{{\rm gg},\ell}(k_i)\right\rangle\left\langle\hat{P}^{\rm S}_{{\rm gg},\ell'}(k_j)\right\rangle. \quad (6.3)$$

In this chapter we employ the Gaussian covariance matrix as given in Appendix A in Ref. [106] (also see [47, 107]), which is given by

$$\mathrm{Cov}\left[\hat{P}^{\rm S}_{{\rm gg},\ell}(k_i),\hat{P}^{\rm S}_{{\rm gg},\ell'}(k_j)\right]=$$
$$\delta^K_{ij}\frac{1}{N_{\rm mode}(k_i)}\int_{-1}^{1}{\rm d}\mu\,(2\ell+1)\mathcal{L}_\ell(\mu)(2\ell'+1)\mathcal{L}_{\ell'}(\mu)\left[P^{\rm S}_{\rm gg}(k_i,\mu)+\frac{1}{\bar{n}_{\rm g}}\right]^2, \quad (6.4)$$

where δ^K_{ij} is the Kronecker delta function, defined so as to satisfy $\delta^K_{ij}=1$ if $i=j$, otherwise $\delta^K_{ij}=0$; $N_{\rm mode}(k_i)$ is the number of independent Fourier modes, determined by the fundamental Fourier mode for a given survey, in the spherical shell of radius k_i with width Δk; $N_{\rm mode}(k_i)\simeq 4\pi k_i^2\Delta k/[(2\pi)^3/V_{\rm S}]$ for $k_i\gg 2\pi/(V_{\rm S})^{1/3}$, and $V_{\rm S}$ is the survey volume; $[P^{\rm S}_{\rm gg}(k_i,\mu)+1/\bar{n}_{\rm g}]$ is the "observed" redshift-space power spectrum given as a function of (k_i,μ), including the shot noise contamination. For the survey volume, we adopt $V_{\rm S}=1.98, 2.26$ or $3.80\,[h^{-1}{\rm Gpc}]^3$ for the redshift slice of LOWZ, CMASS1 or CMASS2-like galaxies, respectively (see Table 6.3). For the redshift-space power spectrum $P^{\mathrm{S}}(k,\mu)$ (including the shot noise term) in the above equation, we use the power spectrum directly measured from the 16 realizations of mock catalogs for the fiducial *Planck* cosmology. Note that, for the real-space power spectrum $P_{\mathrm{gg}}(k)$ (i.e., no μ-dependence), the above formula reproduces the standard covariance formula, $\mathrm{Cov}[P_{\mathrm{gg}}(k_i),P_{\mathrm{gg}}(k_j)]=[2\delta^K_{ij}/N_{\mathrm{mode}}(k_i)]\times[P_{\mathrm{gg}}(k_i)+1/\bar{n}_{\mathrm{g}}]^2$.

In Fig. 6.4 we show the Gaussian covariance matrices for the monopole and quadrupole power spectra for the CMASS1-like galaxies. For illustrative purpose, we plot $P^{\mathrm{S}}_{\mathrm{gg},\ell}(k_i)P^{\mathrm{S}}_{\mathrm{gg},\ell'}(k_i)/\mathrm{Cov}[P^{\mathrm{S}}_{\mathrm{gg},\ell}(k_i),P^{\mathrm{S}}_{\mathrm{gg},\ell'}(k_i)]$, which roughly gives a signal-to-noise ratio for the band power measurement at each k_i bin, $(S/N)^2|_{k_i}$. The figure clearly shows that the signal-to-noise ratio for the quadrupole spectrum is much smaller than that of the monopole spectrum, by up to a factor of 100. This large-factor reduction is due to the two facts. First, the quadrupole power spectrum has a smaller band power than the monopole spectrum by a factor of 4 (see Fig. 6.2), which explains a factor of 16 in $(S/N)^2|_{k_i}$ that scales as the square of band power. Second, the covariance of the quadrupole power spectrum also arises from the monopole. This explains the remaining factor in the factor of 100. Nevertheless, as we will show below, the quadrupole spectrum is quite powerful to constrain cosmological parameters, as it purely arises from the RSD effect and cosmological AP distortion both of which are cosmological effects. The figure also shows a significant cross-covariance between the monopole and quadrupole spectra. Note that, in this study we consider only the diagonal, Gaussian contribution, but in reality there should be the off-diagonal covariance. As has been recently shown in [108], such non-Gaussian contribution is relatively small for SDSS galaxies because of the relatively large shot noise contribution to the total covariance matrix. We postpone the evaluation of this impact on the cosmological parameter inference in realistic galaxy surveys and we will further investigate this point using the SDSS galaxy clustering data in the future work.

6.2 Results

In this section we show the main results of this chapter; we show parameter forecasts that are obtained from measurements of the redshift-space power spectra of SDSS-like galaxies.

6.2.1 Fisher information matrix

To perform the parameter forecast, we employ the Fisher information formalism [109, 110]. We include, as observables, the monopole and quadrupole power spectra of LOWZ, CMASS1 and CMASS2-like galaxies. The Fisher matrix for the ℓ- and

ℓ'-th multipole power spectra is defined as

$$F_{\alpha\beta}^{\ell\ell'} = \sum_{z_n} \sum_{k_i,k_j} \frac{\partial P^{\rm S}_{{\rm gg},\ell}(k_i;z_n)}{\partial p_\alpha} {\rm Cov}^{-1}\left[\hat{P}^{\rm S}_{{\rm gg},\ell}(k_i;z_n), \hat{P}^{\rm S}_{{\rm gg},\ell'}(k_j;z_n)\right] \frac{\partial P^{\rm S}_{{\rm gg},\ell'}(k_j;z_n)}{\partial p_\beta} \tag{6.5}$$

where the ${\rm Cov}^{-1}\left[\hat{P}^{\rm S}_{{\rm gg},\ell}(k_i;z_n), \hat{P}^{\rm S}_{{\rm gg},\ell'}(k_j;z_n)\right]$ is the inverse of the covariance matrix [Eq. (6.4)], and p_α is the α-th parameter. Here we use the Gaussian covariance assumption, and hence the covariance matrix is diagonal in wave number bins; the summation over k_i and k_j reduces to a single summation $\sum_{k_i}$. To combine the Fisher information for different samples of the LOWZ, CMASS1 and CMASS2-like galaxies, we simply sum the Fisher matrices for the three galaxy samples. In other words, we ignore a possible cross-covariance between the different galaxy samples at different redshift slices. When computing the Fisher information for a combined measurement of the monopole and quadrupole power spectra, we properly take into account the cross-covariance. When computing the Fisher matrix, we set $k_{\rm min} = 0.02\ h\,{\rm Mpc}^{-1}$for the minimum wave number in the k-bin summation $\sum_{k_i}$, and then study how the Fisher information content varies with a maximum wave number, $k_{\rm max}$, for which we mainly consider $k_{\rm max} = 0.1$, 0.2 or 0.3 $h\,{\rm Mpc}^{-1}$, respectively. We consider the following set of model parameters:

$$\begin{aligned}\mathbf{p} \equiv \{&\Omega_{\rm m}, \sigma_8, D_{\rm A}(z_n), H(z_n),\\ &\log M_{\rm min}(z_n), \sigma_{\log M}(z_n), \log M_1(z_n), \log M_{\rm sat}(z_n), \alpha_{\rm sat}(z_n),\\ &c_{\rm conc}(z_n), c_{\rm vel}(z_n), p_{\rm off}(z_n), \mathcal{R}_{\rm off}(z_n), P_{\rm SN}(z_n)\}\,,\end{aligned} \tag{6.6}$$

where quantities including z_n in the argument indicate that they can take different values for the three galaxy samples at different redshifts (either of LOWZ, CMASS1 or CMASS2). When we include the information from the galaxy samples of three redshift bins, we consider 38 model parameters in total. Among those, 8 cosmological parameters; $(\Omega_{\rm m}, \sigma_8)$ and $\{D_{\rm A}(z_n), H(z_n)\}$ for each of the three redshifts, where $D_{\rm A}(z_i)$ are $H(z_i)$ are the parameters to model the AP effect (see Section 3.3). On the other hand, we include 10 nuisance parameters that model the halo-galaxy connection and the residual shot noise for each of the three redshifts. Table 6.2 gives the fiducial values as well as the prior for the nuisance parameters. Note that the prior we employ is a very weak one, and we use it only to have a stable calculation of the Fisher matrix (e.g., its inversion).

The most important model ingredient for the Fisher calculation is the response function $\partial P^{\rm S}_{{\rm gg},\ell}(k)/\partial p_\alpha$, which quantifies how a change in the α-th model parameter alters the ℓ-th multipole moment of the power spectrum, or equivalently a sensitivity of the ℓ-th multipole moment to the α-th parameter. Fig. 6.5 shows the response functions for the monopole and quadrupole moments. As described we use the realizations of galaxy mock catalogs to numerically evaluate the response function for each parameter up to the nonlinear scales (high k) (see Table 6.1 and Section 6.1). We also discuss a validation of the measured responses using the linear theory prediction in Appendix 5. As shown in the appendix, the k-dependence of the response function at relatively small k bins is fairly well captured by variations in the underlying linear matter power spectrum, the linear galaxy bias (via the small-k behavior of 2-halo term) and the linear RSD effect. These are all useful cosmological information, while the 1-halo term causes a complex k-dependent effect on the response functions.

We first focus on the results for cosmological parameters $\Omega_{\rm m}$ and σ_8 to which large-scale structure probes are most sensitive within the flat ΛCDM model. As expected, the cosmological parameter, $\Omega_{\rm m}$ or σ_8, causes characteristic changes in the amplitude and shape of the redshift-space power spectra over all the scales we consider. Note that when we change $\Omega_{\rm m}$ the baryon and CDM density parameters, $\omega_{\rm b} = \Omega_{\rm b}h^2$ and $\omega_{\rm cdm} = \Omega_{\rm cdm}h^2$, are kept unchanged, since these parameters are well constrained from the CMB experiments. Also note all the responses are measured at every k bin in units of $h\,{\rm Mpc}^{-1}$, although a change of $\Omega_{\rm m}$ leads to a change of h.

The responses to $\Omega_{\rm m}$ display oscillatory behaviors of the BAO, which however is not due to the shift of BAO peak itself (in physical unit) but the change in the Hubble constant h, since $\omega_{\rm b}$ and $\omega_{\rm cdm}$ are kept unchanged. For fixed σ_8 and HOD parameters, increasing $\Omega_{\rm m}$ leads to a decrease in the power spectrum amplitude at the redshifts of the galaxy samples. The change in $\Omega_{\rm m}$ also alters the RSD strength. Such a kind of behavior is also seen on the linear matter power spectrum, and is further confirmed by the linear theory prediction using the halo bias model in Appendix 5.

Next let us consider the responses to σ_8. First, increasing σ_8, for a fixed $\Omega_{\rm m}$, leads to a greater normalization of the linear matter power spectrum by definition. In addition, increasing σ_8 leads to an increase in the abundance of massive halos, which boosts a clustering contribution from satellite galaxies in massive halos that have greater linear bias. This yields the greater amplitude of galaxy power spectrum, even at small k bins in the linear regime (also see discussion around Fig. 1 in Ref. [105]). However these boosts are to some extent compensated by a smaller halo bias due to the increased σ_8, because halos of a fixed mass scale become less biased and therefore have smaller linear bias compared to the fiducial *Planck* model (again see Fig. 1 in Ref. [65]). Furthermore, an increase of σ_8 causes larger random or streaming motions of halos, yielding a greater suppression in the clustering amplitude at larger k in the nonlinear regime. Thus increasing σ_8 causes a scale-dependent response for the monopole and quadrupole power spectra, causing positive to negative responses from small to large k. We will below study how changes in $\Omega_{\rm m}$ and σ_8 alter the power spectra of central galaxies, i.e., removing satellite galaxies, which helps to gain a clearer understanding of these behaviors.

The AP effect distorts the BAO peak locations, and consequently the response functions display oscillatory behaviors. As described in Sec.3.3 and later in this text, since the redshift-space power spectrum includes two different combinations of the AP distortion, the effects of $D_{\rm A}$ and H are distinguishable. Note that the responses of the monopole power spectrum to D_A and H have behaviors quite similar to that to Ω_m, which is not true of the quadrupole power spectrum. This indicates that the effects of Ω_m and distance parameters on the monopole spectrum are highly degenerated, and hence combining the monopole and quadrupole spectra is of critical importance to break the degeneracies.

The middle-row panels of Fig. 6.5 show the responses to the five HOD parameters. As can be found from Eq. (3.28), the parameters $\log M_\mathrm{min}$ and $\sigma_{\log M}$ determine the cutoff and shape of the mean central HOD at the low-mass end. When $\log M_\mathrm{min}$ is decreased or when $\sigma_{\log M}$ is increased, less massive halos, which are below the cutoff mass scale in the fiducial HOD model, become to be included in the sample. Such halos have smaller bias, leading to the smaller amplitudes of the power spectra. Hence the response functions of the monopole power spectrum with respect to $\log M_\mathrm{min}$ or $\sigma_{\log M}$ are positive or negative, respectively. On the other hand, such less massive halos have smaller random motions, and therefore cause a less suppression at small scales. For this reason, the response of the quadrupole power spectrum changes its sign at $k \simeq 0.1\ h\,\mathrm{Mpc}^{-1}$.

The HOD of satellite galaxies is characterized by the parameters, $\log M_1$, $\log M_\mathrm{sat}$ and α_sat. Here $\log M_1$ determines the normalization of the mean satellite HOD; e.g., decreasing the mass scale M_1 leads to a higher normalization, thereby yielding more satellites to be in the sample. Increasing M_1 leads to a smaller clustering amplitude at small k bins due to a less contribution from massive halos, while it leads to a smaller FoG effect. For this reason, the monopole response to M_1 is negative, while the quadrupole response is negative at very small k bins and then becomes positive at larger k. The parameter M_sat determines a cut-off mass scale; $\langle N_\mathrm{s} \rangle \to 0$ at $M \to M_\mathrm{sat}$. The increase of M_sat confines the mass scale of the host halos to higher mass, which results in the decrease of the large-scale galaxy bias. The parameter α_sat determines the slope of halo mass dependence of the mean satellite HOD. Its increase leads to two different effects on the power spectrum amplitude at large scales: one is the enhancement of the number of satellite galaxies hosted by high-mass halos, and another is the suppression of the number of those living in low-mass halos. The typical mass at this enhancement/suppression transition is $M - M_\mathrm{sat} \sim M_1$. In addition, at small scales, an increase of the satellite population causes an enhancement of the FoG smearing, so the behavior of the response to α_sat would be subtle.

Other nuisance parameters, c_conc, c_vel, p_off and $\mathcal{R}_\mathrm{off}$, model distributions of galaxies inside their host halos, and therefore affect the redshift-space power spectrum at k bins of our interest due to the FoG effect (because the real-space changes due to variations of galaxy distribution in the same halo are all at scales below a few h^{-1} Mpc, which are outside the k-range we consider). The bottom-row panels of Fig. 6.5 display similar shapes for the responses to these parameters due to the changes in the amount of FoG effect. These responses would be approximately described by a k^2 dependence at small k bins [58, 62]. Hence, as long as a FoG function, which has a k^2-dependent term with free amplitude parameter, is introduced, one might be able to take into account variations in the FoG contamination.

For completeness, in Fig. 6.6 we study the responses of the power spectra of the central galaxies to the model parameters. We numerically evaluate the response functions from the power spectra of the central galaxies. These power spectra are measured from the central galaxies in the same mock catalogs as used in the mocks in Fig. 6.5. Comparison of Figs. 6.5 and 6.6 manifests the role of satellite galaxies in these response functions. For example, the σ_8 response for the monopole power spectrum of the central galaxies changes its sign at small k bins, compared to Fig. 6.5, and is negative over all the k-scales. Since the multipole power spectra are expressed as $P_0(k) \sim (b^2 + 2bf/3 + f^2/5)(\sigma_8)^2$ and $P_2(k) \sim (4bf/3 + 4f^2/7)(\sigma_8)^2$ [see Eq. (3.20)], the sign change at small k is due to the fact that a decrease in the linear bias overcomes an increase in σ_8 in the monopole response; the leading term $b^2(\sigma_8)^2$ has a negative response to an increase in σ_8. On the other hand, the σ_8-response of the quadrupole power spectrum is still positive at small k bins, because of the weaker dependence on b as the leading term has a dependence of $b(\sigma_8)^2$. All these complicated dependences of the power spectra on cosmological parameters are contained in the halo power spectrum.

6.2.2 Cosmological parameter forecasts

Signal-to-noise ratio of multipole power spectra

Before showing cosmological parameter forecasts, we first study, in Fig. 6.7, the cumulative signal-to-noise ratio $(S/N)^2$ expected for a measurement of the monopole and quadrupole power spectrum for the SDSS-like survey (Table 6.3), which is defined as

$$\left(\frac{S}{N}\right)^2 = \sum_{i,j}^{k_{\rm max}} P_\ell^{\rm S}(k_i)\,{\rm Cov}^{-1}\left[P_\ell^{\rm S}(k_i), P_\ell^{\rm S}(k_j)\right] P_\ell^{\rm S}(k_j), \tag{6.7}$$

The inverse of $(S/N)^2$ gives a precision in estimating the amplitude parameter of power spectrum, if the power spectrum up to a given maximum wave number, $k_{\rm max}$, is measured from an assumed galaxy survey (here the SDSS-like survey), assuming that the power spectrum shape is perfectly known. Fig. 6.7 shows the results of S/N for the monopole and quadrupole power spectra as a function of $k_{\rm max}$. Here we consider the LOWZ, CMASS1, and CMASS2-like samples. If the power spectrum measurement is in the sample-variance-limited regime and the Gaussian covariance is valid, $S/N \propto k_{\rm max}^{3/2}$. The figure shows that (S/N) keep increasing with increasing $k_{\rm max}$ up to $k_{\rm max} \sim 0.2\ h\,{\rm Mpc}^{-1}$. However, at the larger $k_{\rm max}$ the covariance is dominated by the shot noise for the SDSS-like galaxies which have the number density of about 10^{-4} $(h{\rm Mpc}^{-1})^3$ (see Table 6.3), and the S/N is saturated in the shot noise regime. The figure also shows that S/N for the quadrupole has a smaller amplitude than the monopole by a factor of 10. Nevertheless the quadrupole spectrum carries a significant information on cosmological parameters thanks to its sensitivity to the RSD effect and the AP effect, and therefore helps break the parameter degeneracies when combined with the monopole spectrum, as we will show below.

Geometrical constraints and cosmological parameter forecasts

We now show the forecasts for cosmological constraints, which are the main results of this chapter. A notable advantage of the redshift-space galaxy clustering method, compared to other large-scale structure probes, is that it enables us to simultaneously constrain the growth of matter clustering (usually $f\sigma_8$) as well as the cosmological distances via the AP effect. As we have described above, in this study we treat these parameters independently, $\Omega_{\rm m}$, σ_8, $D_{\rm A}(z_n)$, and $H(z_n)$ in our parameter forecasts, even though the cosmological distances can be specified for a given $\Omega_{\rm m}$ at a given redshift for a flat ΛCDM model. Thus the redshift-space galaxy clustering method enables a stringent geometrical test of the cosmological distances free of uncertainties in the large-scale structure growth or galaxy bias [111] (also see [112] for a similar discussion). We keep this advantage for our parameter forecasts, and then will discuss how the $\Omega_{\rm m}$ constraint is improved if we use the $\Omega_{\rm m}$-dependence of distances for a flat ΛCDM model.

The BAO peak position and shape in the galaxy power spectrum is measured anisotropically if a reference cosmological model, which needs to be assumed in converting the observed angular scales and redshifts to the comoving coordinates in the analysis, differs from the underlying true cosmology. Fig. 6.8 shows the 68% CL error ellipses in determination of $D_{\rm A}(z_n)$ and $H(z_n)$, including marginalization over other 32 parameters including nuisance parameters to model the halo-galaxy connection. The left, middle and right panels in each row show the results when using either of the monopole or quadrupole power spectrum alone or when combining the two spectra, respectively. The top-, middle- and bottom-row panels are the results for the LOWZ, CMASS1 and CMASS2-like galaxy samples, respectively. First of all, each panel shows that the geometrical constraints are improved as the information up to the higher $k_{\rm max}$ is included. The monopole power spectrum gives a tighter constraint on the combination of "$D_{\rm A}(z)^2/H(z) (\propto \alpha_\perp^2\alpha_\parallel)$", where $\alpha_\parallel = H/H_{\rm fid}$ and $\alpha_\perp = D_{\rm A,fid}/D_{\rm A}$ ($D_{\rm A}$ and H are model parameters, and the quantities with "fid" are the values for the *Planck* cosmology, i.e., the true values). The value of "$\alpha_\perp^2\alpha_\parallel$" is varying along the direction perpendicular to "$\alpha_\perp^2\alpha_\parallel = \text{const.}$" shown in each panel, which is close to the direction of the constant warping parameter ($\alpha_\parallel/\alpha_\perp = \text{const.}$). A change in $H(z)$ and $D_{\rm A}(z)$ while keeping $\alpha_\parallel/\alpha_\perp$ fixed, causes an "isotropic" distortion in the monopole spectrum, or causes an isotropic shift in the BAO peak locations and the broad-band k-dependent shape as a function of k. It means that the distance constraints in the monopole power spectrum are from the isotropic distortion (sometimes called the "dilation" effect). On the other hand, the quadrupole spectrum gives a tighter constraint on the combination of $\alpha_\perp/\alpha_\parallel$. Again the direction of varying the value of $\alpha_\perp/\alpha_\parallel$ is close to the direction of $\alpha_\perp^2\alpha_\perp =$ constant. While the monopole power spectrum amplitude is kept fixed along this direction of $\alpha_\perp^2\alpha_\perp =$ const., it causes an anisotropic distortion in the redshift-space power spectrum and therefore alters the quadrupole power spectrum. Fig. 6.9 explicitly shows how a change in either of $\alpha_\parallel/\alpha_\perp$ or $\alpha_\perp^2\alpha_\parallel$, keeping the other fixed, alters either of the monopole or quadrupole power spectra, while the other is almost unchanged. Interestingly, even though the signal-to-noise (S/N) in the quadrupole power spectrum is smaller than that of the monopole spectrum by a factor of 10 (see Fig. 6.7), the quadrupole carries a better precision of the distance measurements than that of the monopole. This would be explained by the fact that a change of Ω_m has a strong degeneracy with that of $D_\mathrm{A}(z)$ and $H(z)$ in the monopole power spectrum (see Fig. 6.5). On the contrary, the quadrupole has distinct behaviors in the responses to Ω_m and AP parameters, as well as to another cosmological parameters σ_8.

Fig. 6.10 shows the 68% CL error ellipses in the $(\Omega_\mathrm{m}, \sigma_8)$-subspace, including marginalization over other 36 parameters (the cosmological distances and the halo-galaxy connection parameters). Here we include the information for the three redshift slices of the LOWZ-, CMASS1- and CMASS2-like surveys (Table 6.3). For comparison, we here show the results when using either of the monopole or quadrupole power spectrum alone, or combining the monopole and quadrupole signals up to a given maximum wave number, $k_\mathrm{max} = 0.1, 0.2$ or $0.3\ h\,\mathrm{Mpc}^{-1}$, respectively. As we have shown in Fig. 6.8, variations in the BAO peak locations and anisotropic features in the power spectrum are captured by the cosmological distance parameters, $D_\mathrm{A}(z)$ and $H(z)$. The constraints on Ω_m and σ_8 shown here are from the RSD effect and the amplitude information in the power spectrum. Similarly to the previous figure, this figure shows that the quadrupole power spectrum carries a similar-level information on these cosmological parameters to that of the monopole power spectrum. Thus the RSD effect to which the quadrupole power spectrum is sensitive carries useful cosmological information. Hence, combining the monopole and quadrupole power spectra improves the cosmological constraints compared to the constraints from either of the two power spectra alone. The figure also shows that including the power spectrum information up to the higher k_max, from 0.1 to $0.3\ h\,\mathrm{Mpc}^{-1}$, continues to improve the cosmological constraints, even after marginalization over other nuisance parameters. This implies that changes in Ω_m and σ_8 cause quite different scale-dependent changes in the redshift-space power spectra from the dependences of other parameters, as quantified by the response functions in Fig. 6.5. Therefore the cosmological parameters are distinguishable from other parameters such as the halo-galaxy connection parameters in the measured redshift-space power spectrum. Table 6.4 summarizes the marginalized 68% CL error of Ω_m or σ_8. The table shows that including the information up to $k_\mathrm{max} = 0.3\ h\,\mathrm{Mpc}^{-1}$from $0.1\ h\,\mathrm{Mpc}^{-1}$leads to an improvement in the constraint on Ω_m or σ_8 by a factor of 3.15 or 3.63, respectively.

	$\sigma(\Omega_\mathrm{m})/\Omega_\mathrm{m}$		
k_max [$h\,\mathrm{Mpc}^{-1}$]	0.1	0.2	0.3
P_0^S	0.40 (0.060)	0.16 (0.023)	0.10 (0.020)
P_2^S	0.71 (0.29)	0.18 (0.11)	0.12 (0.085)
$P_0^\mathrm{S}+P_2^\mathrm{S}$	0.18 (0.052)	0.083 (0.020)	0.058 (0.018)
	$\sigma(\sigma_8)/\sigma_8$		
k_max [$h\,\mathrm{Mpc}^{-1}$]	0.1	0.2	0.3
P_0^S	0.23 (0.17)	0.13 (0.12)	0.087 (0.085)
P_2^S	0.51 (0.27)	0.15 (0.10)	0.096 (0.062)
$P_0^\mathrm{S}+P_2^\mathrm{S}$	0.12 (0.071)	0.078 (0.040)	0.056 (0.030)

Table 6.4: The 68% fractional error of Ω_m or σ_8, including marginalization over other parameters. Shown here is the fractional error when using either of the monopole (P_0^S) or quadrupole (P_2^S) power spectrum information or using the joint measurement ($P_0^\mathrm{S}+P_2^\mathrm{S}$) up to a given maximum wave number, $k_\mathrm{max}=0.1$, 0.2 or 0.3 $h\,\mathrm{Mpc}^{-1}$, respectively. The number in the parentheses gives the error if including the Ω_m information in the angular diameter distance D_A and the Hubble expansion rate H for the flat ΛCDM model (see Fig. 6.11 for details).

This would be compared to a factor of $5.2(=27^{1/2})$, which corresponds to a naive improvement if the parameter error scales with the inverse of Fourier volume, $1/k_\mathrm{max}^{3/2}$ in a case that all the parameters are totally independent and the information is in the sample-variance-limited regime. The results in Fig. 6.10 and Table 6.4 are quite encouraging.

An alternative approach one might want to employ is to use the measured redshift-space galaxy power spectrum to make a most stringent test or even falsify the flat ΛCDM paradigm. Within the flat ΛCDM model, the cosmological distances, $D_\mathrm{A}(z)$ and $H(z)$, are specified by a given Ω_m, and hence one could obtain an even tighter constraint on Ω_m than the case where $D_\mathrm{A}(z)$ and $H(z)$ are treated as free parameters. Fig. 6.11 shows the marginalized errors of Ω_m and σ_8 based on this approach, where we used 32 parameters in the Fisher analysis; 38 minus 6 parameters ($D_\mathrm{A}(z)$ and $H(z)$ for each of the three redshift slices). The figure clearly shows that including the geometrical information significantly improves the constraint on Ω_m, while the constraint on σ_8 is almost unchanged. This implies that most of the information in Ω_m is from the geometrical constraints, the BAO peak locations and the AP effect, if assuming the flat ΛCDM model, while the constraint on σ_8 is mainly from the RSD and amplitude information. Table 6.4 gives a summary of the marginalized 1D error in Ω_m and σ_8, and shows that we could achieve about 2% or 3% accuracy in Ω_m or σ_8, respectively, if we can use the information up to $k_\mathrm{max}=0.3\ h\,\mathrm{Mpc}^{-1}$, even after including marginalization over the halo-galaxy connection parameters.

What is the impact of nuisance parameters such as the halo-galaxy connection parameters on the cosmological parameter inference? To address this question, in

Fig. 6.12, we show the results if we fix the halo-galaxy connection parameters to their fiducial values by the thin lines on top of the results after marginalization (thick), which were already shown in Fig. 6.10. Here we used only 8 parameters in the Fisher analysis; $\Omega_{\rm m}$, σ_8 and 6 distance parameters (3 $D_{\rm A}$'s and H's parameters). First of all, if we use the information up to $k_{\rm max} = 0.1\ h\,{\rm Mpc}^{-1}$, we cannot obtain any meaningful constraint on either of $\Omega_{\rm m}$ or σ_8 due to strong degeneracies between the power spectrum amplitudes and the halo-galaxy connection parameters, where the latter controls the overall galaxy bias at small k limit. If we use either of the monopole or quadrupole information up to $k_{\rm max} = 0.2$ or $0.3\ h\,{\rm Mpc}^{-1}$, the halo-galaxy connection parameters degrade the accuracy of $\Omega_{\rm m}$ or σ_8 by a similar amount. In the case of the joint constraints using both of the monopole and quadrupole, the error of $\Omega_{\rm m}$ is not largely changed when $k_{\rm max} \geq 0.2\ h\,{\rm Mpc}^{-1}$, because $\Omega_{\rm m}$ is mainly determined by the AP effect as we discussed. On the other hand, the σ_8 constraint is largely degraded by the halo-galaxy connection parameters. Hence, an accuracy of σ_8 estimation from the redshift-space galaxy power spectrum largely depends on a level of our understanding of the halo-galaxy connection in the nonlinear regime.

To quantify the constraining power of the BOSS-like galaxy survey on the cosmological parameters, we compute the following figure of merit (FoM), defined in terms of the Fisher matrix as

$$\mathrm{FoM} = \frac{1}{\sqrt{|\det{(\mathbf{F}^{-1})_{\rm sub}}|}}, \tag{6.8}$$

where $\mathbf{F}^{-1}$ is the inverse of Fisher matrix, "sub" in $(\mathbf{F}^{-1})_{\rm sub}$ means (8×8) sub-matrix elements containing only $\Omega_{\rm m}$, σ_8 and 6 distance parameters, and "det" denotes the determinant of the sub-matrix. The FoM quantifies a volume of the marginalized ellipsoid in the 8-dimensional space of cosmological parameters.

Fig. 6.13 shows that the FoM of the quadrupole power spectrum is comparable to that of the monopole power spectrum. What is remarkable is that the quadrupole gets a larger FoM than the monopole when the HOD and other halo-galaxy connection parameters are marginalized. This is ascribed to huge degeneracies between the cosmological parameters and the HOD parameters in the monopole power spectrum (see Fig. 6.5). By combining the two information, the impact of halo-galaxy connection parameters, i.e., uncertainties in galaxy physics or small-scale structures, is mitigated, which boosts the FoM by a factor of over 1000 compared to either of the two alone. In addition, the power spectrum information in the quasi nonlinear regime is useful; including the information up to $k_{\rm max} = 0.3\ h\,{\rm Mpc}^{-1}$leads to about factor of 6 gain in the information content compared to $k_{\rm max} = 0.2\ h\,{\rm Mpc}^{-1}$. This gain is larger than a naive expectation, $(0.3/0.2)^{3/2} \simeq 1.8$, and is ascribed to the fact that the nonlinear information helps efficiently break the parameter degeneracies. This result clearly demonstrates that the redshift-space power spectrum in mildly nonlinear regime is quite powerful to constrain the cosmological parameters.

6.3 Discussion

6.3.1 A model-independent measurement of the RSD effect

The uniqueness of the redshift-space power spectrum method is it enables to measure the cosmological distances ($D_{\rm A}$ and H) and the strength of peculiar velocities via the RSD effect. Because peculiar velocities of galaxies arise from the gravitational field in large-scale structure, it can be used to test gravity theory on cosmological scales. Here we more explicitly address the power of the redshift-space galaxy power spectrum for making a "model-independent" test of the RSD effect ([also see [113, 114] for similiar discussion). To do this, when generating a mock catalog of galaxies in redshift space, we modify the radial displacement of each halo by an amount of model parameter $f_{\rm RSD}$, from Eq. (3.4), as

$$\begin{aligned}\Delta\mathbf{s} &= \frac{v'_{\parallel}(\mathbf{x})}{aH(z)}\hat{\mathbf{n}},\\ v'_{\parallel} &= f_{\rm RSD}v_{{\rm h},\parallel} + v_{{\rm vir},\parallel},\end{aligned} \tag{6.9}$$

where $v_{{\rm h},\parallel}$ and $v_{{\rm vir},\parallel}$ are the line-of-sight components of the halo bulk velocity and of the virial velocity of galaxies inside the halo, respectively, and $f_{\rm RSD}$ is a model parameter; if $f_{\rm RSD} = 1$, the RSD displacement is the same as that for the fiducial *Planck* ΛCDM cosmology. If we assume $f_{\rm RSD} \neq 1$, the amount of RSD effect is artificially modified. When we consider LOWZ, CMASS1, and CMASS2, we employ the same constant factor $f_{\rm RSD}$ in generating the mock catalogs of the galaxies. Note that the RSD effect in the linear regime is proportional to $f\sigma_8$. The standard RSD analyses to constrain the parameter combination $f\sigma_8$ to test gravity theories are usually based on the nonlinear templates of the spectra constructed for ΛCDM cosmology within the GR framework but float $f\sigma_8$ as an independent parameter. Our test here is exactly along this line. Assuming a constant $f_{\rm RSD}$ across the three redshifts of galaxies, it gives a simplest model of the RSD modification. However, due to large uncertainties in internal random motions of galaxies inside the host halo, we do not modify the RSD displacement due to the relative motion of galaxies to the halo bulk velocity, i.e., the FoG effect. Thus the following forecast on an estimation of $f_{\rm RSD}$ is purely from the effect on the halo power spectrum. However note that velocities of these random motions are actually modified according to the details of the modified gravity model, e.g., [115], which shows using simulations that the Hu-Sawicki $f(R)$ [116] and the Symmetron [117] gravity model affect the velocity profiles inside halos in a model-dependent way.

Fig. 6.14 shows how a change in $f_{\rm RSD}$ alters the monopole and quadrupole power spectra as a function of k. Note that the real-space power spectra are independent of $f_{\rm RSD}$ and the same for all these cases. As expected, the parameter $f_{\rm RSD}$ alters the monopole and quadrupole spectra, and is different from the AP distortion (Fig. 6.9). The effect at small k is as expected by the Kaiser formula, but the effect at large

k changes its sign. This is because the RSD effect at large k is dominated by the smearing effect due to streaming motions of different halos. This effect is enhanced or reduced respectively by changing $f_{\rm RSD} > 1$ or < 1 from the fiducial value of $f_{\rm RSD} = 1$, which explains the sign change at large k in Fig. 6.14.

In Fig. 6.15, we show the marginalized error ellipses in the two-dimensional subspace of $D_{\rm A}$, H or $f_{\rm RSD}$. To do this, we fix $\Omega_{\rm m}$ and σ_8 to their fiducial values; that is, we do not include these parameters in the Fisher matrix. Hence we use 37 model parameters in the Fisher analysis; $f_{\rm RSD}$ and 3 $D_{\rm A}$'s and H's parameters for three redshift slices, and 30 nuisance parameters of the halo-galaxy connection. Because we fix $\Omega_{\rm m}$ and σ_8 to their fiducial values, all the real-space power spectra are the same for models varying either of $f_{\rm RSD}, D_{\rm A}$ or H, and the changes in the redshift-space power spectrum are due to variations in the RSD effect (via $f_{\rm RSD}$) or the AP distortion. Therefore this forecast for $f_{\rm RSD}$ assesses the power of the redshift-space power spectrum for constraining the RSD effect strength, or more generally a deviation of the RSD effect from the ΛCDM prediction. If we can find $f_{\rm RSD} \neq 1$ from this kinds of analysis, that would be a smoking gun evidence of non-GR gravity. The figure shows that the SDSS-like galaxy survey would allow for a 10% accuracy of $f_{\rm RSD}$ determination, even after marginalization over the AP effects and other parameters.

6.3.2 Galaxy assembly bias

We have so far employed the HOD method to model the biased relation between distributions of galaxies and matter, i.e., galaxy bias, in an N-body simulation realization. One critical assumption employed in the HOD method is it assumes that a probability of populating galaxies in halos is solely described by halo masses, $\langle N\rangle(M)$. Even if halos have the same mass, the halos have various assembly histories due to the nature of hierarchical structure formation in a CDM scenario. For this reason halos, even with the same mass, could have a different large-scale bias. That is, the large-scale bias of halos could depend on another parameter besides the halo mass – this effect is usually referred to as an assembly bias [118, 119, 120, 121, 122].

Therefore we here study a possible impact of assembly bias on the cosmological parameter forecast. To include the assembly bias effect in the mock galaxy catalog, we used the following method. First, using the member N-body particles of each halo in a given N-body simulation realization, we compute the mass enclosed within the sphere of radius of $0.5r_{200}$ and use the mass fraction to the whole halo mass M_{200} as a proxy of the mass concentration. We then make a ranked list of all the halos in the ascending order of the inner-mass fraction at each halo mass bin ranging $M = [10^{12}, 10^{16}]h^{-1}M_\odot$ with width $\Delta\log_{10} M = 0.02$, and populate central galaxies into halos from the top of the list (from the lowest-concentration halo), according to the number fraction specified by the central HOD $\langle N_{\rm c}\rangle(M)$ [Eq. (3.28)]. Finally we populate satellite galaxies into the halos which already host a central galaxy using the fiducial satellite HOD. Thus this method does not change the mean HOD as a function of mass, but would change clustering properties of galaxies by preferentially selecting host halos with low concentration. We then measure the redshift-space power spectrum from these modified mocks, in the same way as we do for the fiducial mocks.

Fig. 6.16 shows the power spectra measured from the mocks including the assembly bias effect. The real-space power spectrum, measured from the mocks with assembly bias, displays greater amplitudes than that in the fiducial mocks by 20%, over all the scales we consider. Thus, halos with low mass concentrations have greater clustering amplitudes than the average, displaying a physical connection between inner-structure of halos and the large-scale environments. This is consistent with the claims in the previous work [119], for relatively massive halos with $M \gtrsim M_*$, where M_* is a typical nonlinear halo mass satisfying $\delta_{\rm collap}/\sigma(M_*) \simeq 1$ ($\delta_{\rm collap} = 1.67$), because BOSS galaxies reside in such massive halos. This result should be considered as an extreme case, because we completely followed the ranked list of the halo mass concentration when populating central galaxies in a fully deterministic manner, and did not include any scatter in the galaxy-halo concentration. Hence a more realistic case would be in between the fiducial model and the assembly bias result even if the assembly bias exists in the real galaxy catalog. The right panel shows the effect of assembly bias on the monopole and quadrupole power spectra. The assembly bias amplifies the monopole spectrum by a similar amount to that of the real-space power spectrum. The effect on the quadrupole power spectrum is less significant. The lower panel shows the comparison with the predictions of Kaiser formula, if we change the linear bias by an amount of the assembly bias effect (about factor of 1.1), but do not change $f\sigma_8$. The figure shows that the modified Kaiser prediction fairly well reproduces the simulation results, although the quadrupole power spectrum has a zero-crossing at $k \simeq 0.2\,h\,{\rm Mpc}^{-1}$, so the results look noisy around the scale. This means that the assembly bias mainly affects the halo bias, and does not change the RSD effect. Or equivalently the peculiar velocity field of low-concentration halos is not so different from that of halos with the same mass – i.e., little assembly bias effect on the velocity field (see [99, 100] for similar discussion).

To quantify the impact of assembly bias on cosmological parameter estimation, we estimate a possible bias on the cosmological parameters due to the ignorance of the dependence on the concentration in the model, using the formula [123, 124]

$$\delta p_\alpha = \sum_\beta \left(F^{\ell\ell'}\right)^{-1}_{\alpha\beta} \sum_{ij} \left[P_\ell^{\rm S+AB}(k_i) - P_\ell^{\rm S}(k_i)\right] {\rm Cov}^{-1}\left[\hat{P}_\ell^{\rm S}(k_i), \hat{P}_{\ell'}^{\rm S}(k_j)\right] \frac{\partial P_{\ell'}^{\rm S}(k_j)}{\partial p_\beta}, \tag{6.10}$$

where $P_\ell^{\rm S+AB}(k_i)$ is the power spectrum measured from the mocks with assembly bias, and $P_\ell^{\rm S}(k)$ without superscript "+AB" is the fiducial power spectrum. The quantity δp_α estimated from the above equation quantifies a bias in the parameter

p_α due to the assembly bias effect, if the model predictions do not include the effect. Fig. 6.17 shows the results for a possible bias in Ω_m or σ_8 if the assembly bias affects the redshift-space power spectra for all the LOWZ, CMASS1, CMASS2-like galaxies. Since the assembly bias we consider is an extreme case and the assembly bias, even if exists, unlikely affects all the SDSS galaxies at different redshifts, this can be considered as a worst case scenario. The figure shows that the assembly bias does not cause an amount of bias in these parameter greater than the marginalized error. This is because the assembly bias changes only the overall amplitudes of the real-space power spectrum, i.e., a change in the apparent galaxy bias, and does not affect the RSD effect, as shown in Fig. 6.16. We have actually confirmed that this assembly bias effect causes a significant bias in the forecast on Ω_m and σ_8 when we do not include any uncertainty in the halo-galaxy connection, but can be absorbed by the changes in HOD parameters, even if all the other nuisance parameters, c_conc, c_vel, p_off, $\mathcal{R}_\mathrm{off}$ and P_SN, are fixed to their fiducial values.

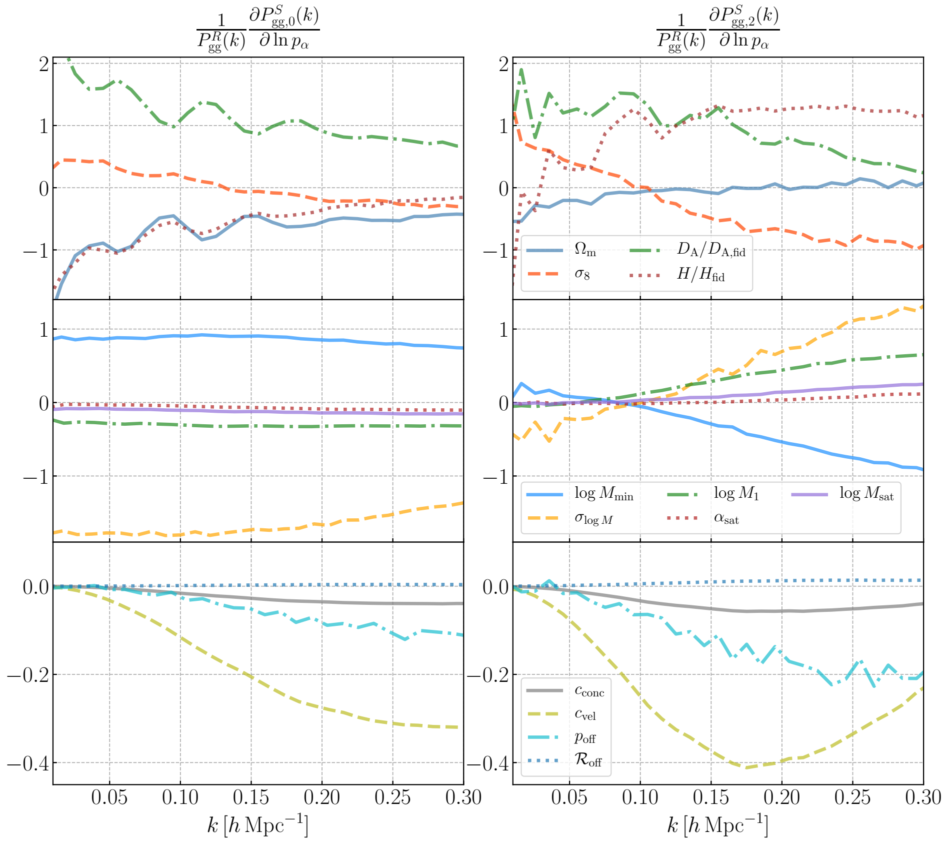

Figure 6.5: The partial derivative of the monopole (left panels) or quadrupole (right) power spectrum with respect to each model parameter (p_α), which we refer to as the "response" function, for the CMASS1 sample. To compute the response function, we first generate the mock catalogs where we slightly varied a parameter but fixed other parameters to their fiducial values, and then numerically compute the partial derivative. Note that we compute the response functions for $D_{\rm A}$ and H from the AP distortion effect in a hypothetical clustering analysis; we assume a slightly shifted value in $D_{\rm A}$ or H from the fiducial value when mapping the real-space positions of galaxies to the comoving coordinates in each mock for the fiducial *Planck* model, and then measure the monopole and quadrupole spectra from the mock. For illustrative purpose, we show the fractional response function relative to the real-space power spectrum for the fiducial mocks, $[1/P^{\rm R}_{\rm gg}(k)]\partial P^{\rm S}_{{\rm gg},\ell}(k)/\partial \ln p_\alpha$. Note that we employ the parameters $\log M_{\rm min}$, $\log M_1$ and $\log M_{\rm sat}$ rather than the physical quantities $M_{\rm min}$, M_1 and $M_{\rm sat}$ in units of $h^{-1}M_\odot$ for numerical convenience. We multiply the response functions for these parameters by 1/20 so that the functions are in the similar range of y-axis.

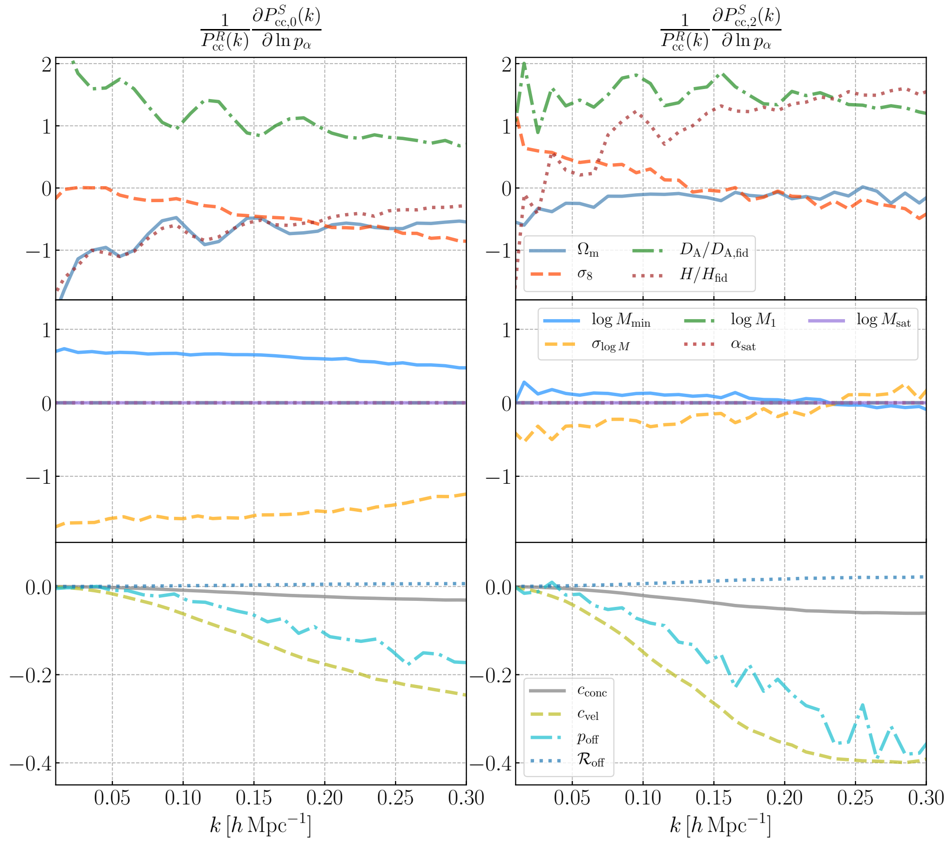

Figure 6.6: The similar to Fig. 6.5, but the results for the power spectra of central galaxies that are computed from the mocks including only the central galaxies as in Fig. 6.3.

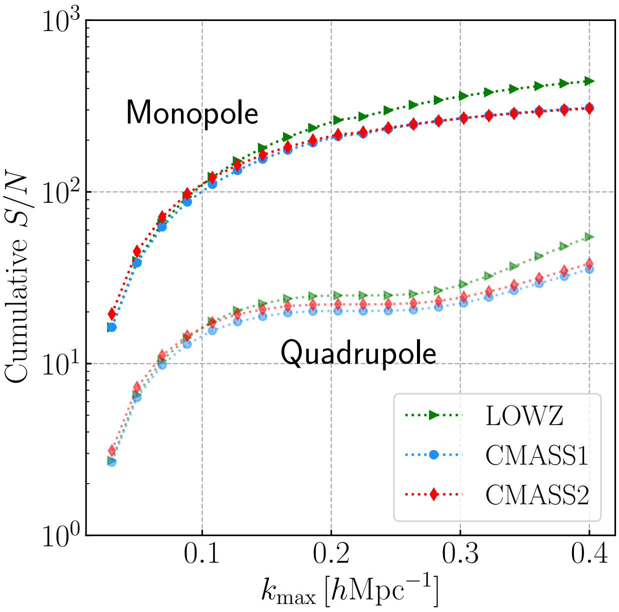

Figure 6.7: The cumulative signal-to-noise ratio, S/N [defined by Eq. (6.7)] for a hypothetical measurement of the monopole and quadrupole power spectra for each of the LOWZ, CMASS1 and CMASS2 samples, respectively. The cumulative S/N is the information content of the power spectrum amplitude, obtained by integrating the signal-to-noise at each k bin from the minimum wave number, set to $k_{\rm min} = 0.02\ h\,{\rm Mpc}^{-1}$here, up to a given maximum wave number $k_{\rm max}$ shown in the x-axis.

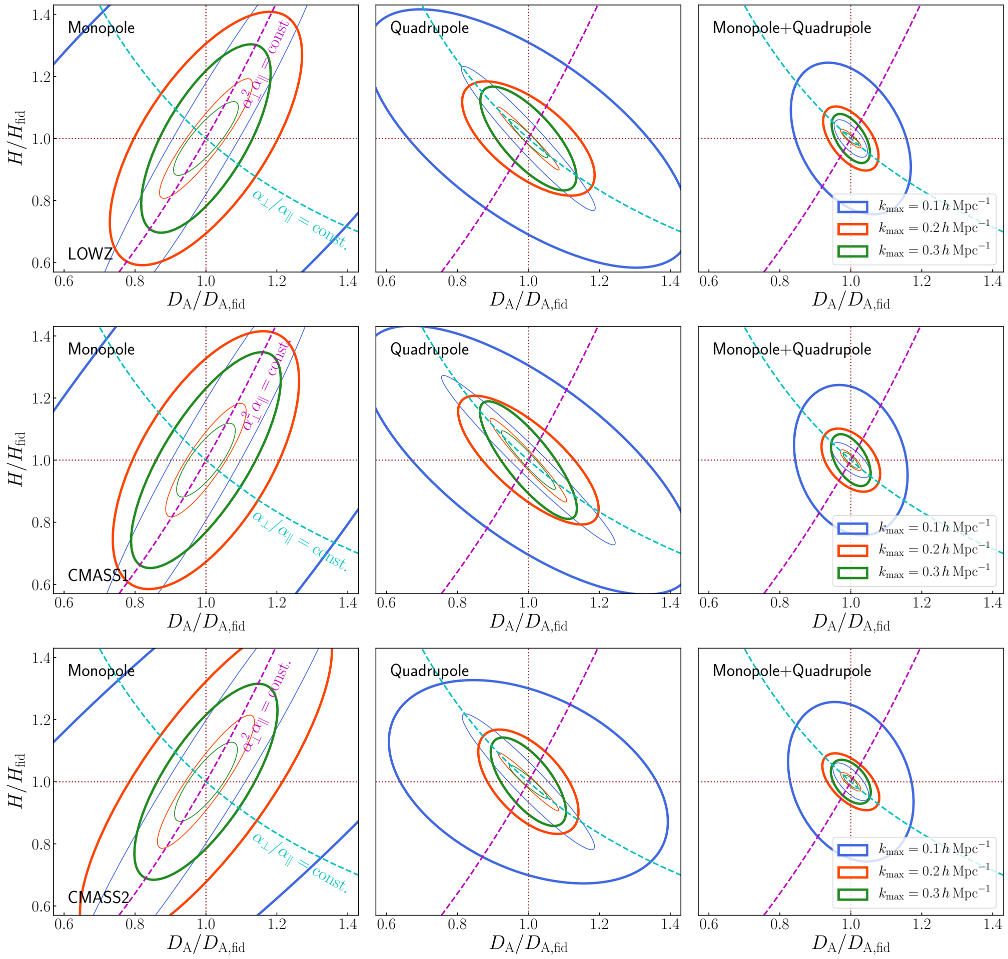

Figure 6.8: The Fisher-forecasted 68% CL error ellipse in the sub-space of angular diameter distance $D_{\rm A}(z_n)$ and the Hubble expansion rate $H(z_n)$ at each redshift of the LOWZ (top-row panels), CMASS1 (middle-row) and CMASS2 (bottom-row) samples, respectively, including marginalization over other parameters. The left, middle or right panel in each row shows the result when using either of the monopole or quadrupole power spectrum alone or using the joint measurement of monopole and quadrupole spectra, respectively. The three contours in thick lines in each panel show the results when using the power spectrum information up to $k_{\rm max} = 0.1$, 0.2 or 0.3 $h\,{\rm Mpc}^{-1}$, respectively. These constraints are from measurements of the geometrical AP distortion of the BAO peak locations and broad-band shape in the redshift-space power spectra. For comparison, the magenta or cyan dashed curve shows the direction where the isotropic "dilation" parameter, $\alpha_\perp^2\alpha_\parallel$ or the anisotropic "warping" parameter $\alpha_\perp/\alpha_\parallel$ in the geometrical AP distortion is kept constant; $\alpha_\perp^2\alpha_\parallel = $ const. or $\alpha_\perp/\alpha_\parallel = $ const, respectively. Here $\alpha_\perp$ and $\alpha_\parallel$ are the ratio of the assumed cosmological distances (i.e., the assumed values) to the true values (i.e., the values for the *Planck* model as given in Table 6.2): $\alpha_\perp \equiv D_{\rm A,fid}/D_{\rm A}$ and $\alpha_\parallel = H/H_{\rm fid}$ that are shown in the x- and y-axes, respectively. We also put the thin solid-line contours, which denote the error ellipses in the case where the halo-galaxy connection parameters are fixed to their fiducial values.

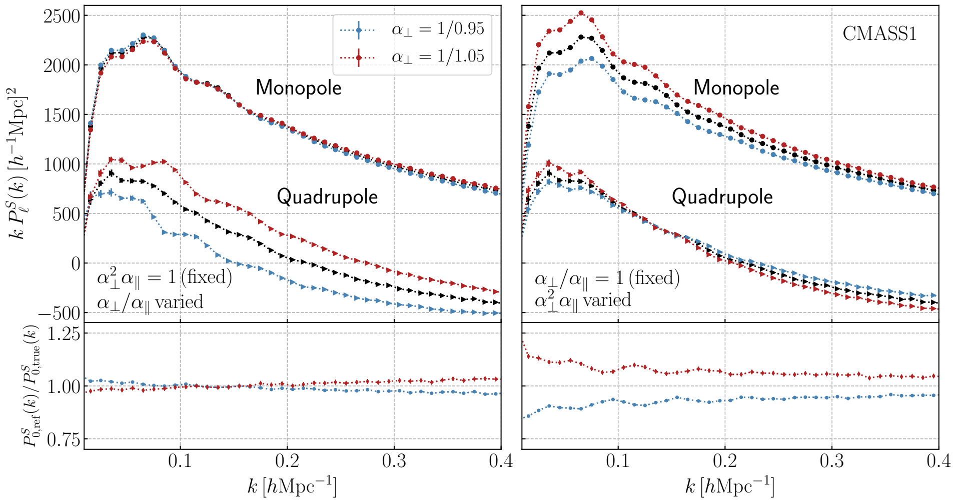

Figure 6.9: The geometrical AP effect on the monopole and quadrupole power spectra for the fiducial CMASS1 mocks. To study this, we focus on the two components of AP effect: the isotropic dilation effect "$\alpha_\perp^2\alpha_\parallel$" and the anisotropic warping effect "$\alpha_\perp/\alpha_\parallel$" (see the caption in the previous figure). The left panel shows the spectra when the warping parameter $\alpha_\perp/\alpha_\parallel$ is varied by $\alpha_\perp = 1/0.95$ or $1/1.05$, while the dilation parameter $\alpha_\perp^2\alpha_\parallel$ is kept fixed. While the monopole power spectrum amplitude and the BAO peak locations are almost unchanged, this variation alters the relative amplitude of the quadrupole power spectrum. The right panel shows the spectra when the dilation parameter $\alpha_\perp^2\alpha_\parallel$ is varied by the same amount of $\alpha_\perp$ as in the left panel, while the warping parameter $\alpha_\perp/\alpha_\parallel$ is kept fixed. In this case, while the monopole power spectrum is largely changed, the change of the quadrupole is relatively moderate.

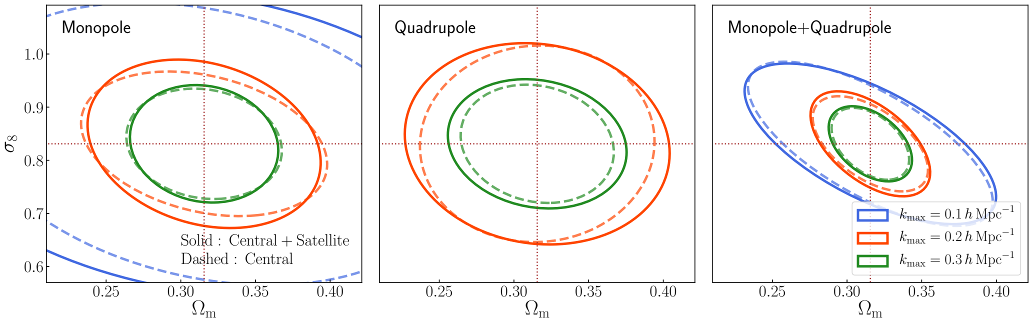

Figure 6.10: The marginalized error ellipses in the sub-space of parameters, Ω_m and σ_8, as in Fig. 6.12. To derive this, we used the Fisher matrix jointly combining the power spectrum information for the LOWZ, CMASS1, and CMASS2 samples. Since we treated the geometrical information in the galaxy power spectrum by $D_\mathrm{A}(z_n)$ and $H(z_n)$ at each redshift, the constraints on Ω_m and σ_8 are mainly from the RSD effect and the amplitude information in the redshift-space galaxy power spectrum. The dashed-line contours represent the constraints from the power spectra that are measured from the mocks including central galaxies alone (i.e., removing satellite galaxies from each mock). Comparison of the solid and dashed contours shows that the constraining power of Ω_m and σ_8 is mainly from the redshift-space power spectra of central galaxies.

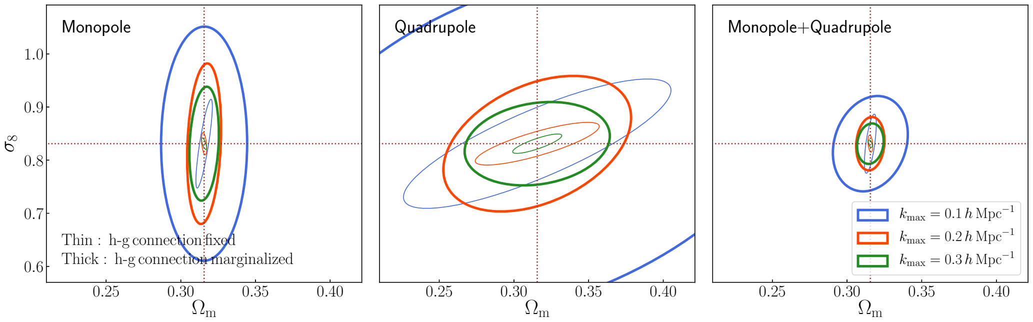

Figure 6.11: Similar results to the previous figure, but show the expected errors on Ω_m and σ_8 for the flat ΛCDM framework. Here we include the Ω_m information in $D_\mathrm{A}(z_n)$ and $H(z_n)$ at each redshift of the LOWZ, CMASS1 and CMASS2 samples, since these quantities at each redshift is specified by an assumed Ω_m if a flat ΛCDM model is *a priori* assumed. Consequently the error of Ω_m is significantly tightened. The thin solid-line contours are the error ellipses when we fix the halo-galaxy connection parameters to their fiducial values, i.e., unmarginalized errors.

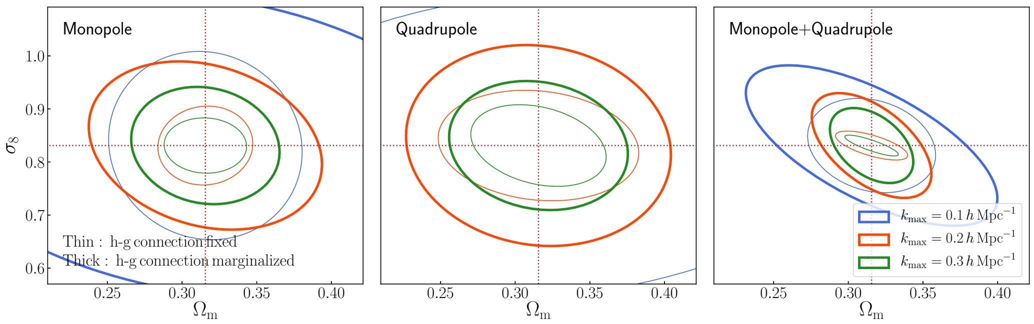

Figure 6.12: The impact of uncertainties in halo-galaxy connection on the errors of Ω_m and σ_8. Similar plot to Fig. 6.10, but shows the results when fixing the halo-galaxy connection parameters to their fiducial values as the thin solid-line contours. To compute this, we use (8×8) sub-matrix elements of the full Fisher matrix that contain only Ω_m and σ_8 and the two distances, D_A and H, for each of the three redshift bins.

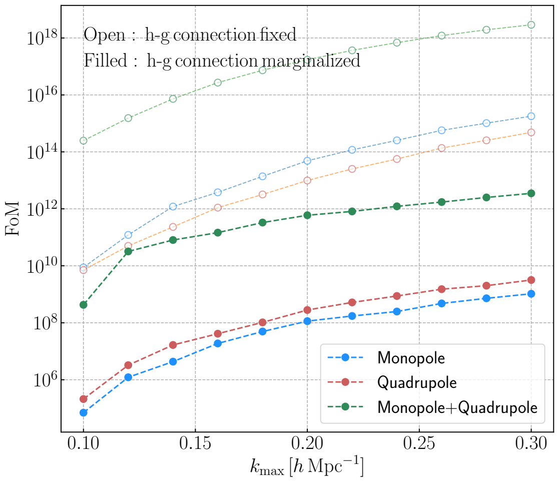

Figure 6.13: The figure-of-merit (FoM) of cosmological information, $\{\Omega_\mathrm{m}, \sigma_8, D_\mathrm{A}(z_n)/D_\mathrm{A,fid}, H(z_n)/H_\mathrm{fid}\}$ (8 parameters in total), in the redshift-space galaxy power spectra for the LOWZ, CMASS1 and CMASS2 samples. The FoM quantifies a volume of the error ellipsoid in the eight-dimensional space of the cosmological parameters. The filled symbols show the results when including the power spectrum information up to a given maximum wave number k_max shown in the x-axis. Here we show the results for the monopole or quadrupole power spectrum alone or when combining measurements of the two spectra. The open symbols show the results when other halo-galaxy connection parameters are kept fixed to their fiducial values.

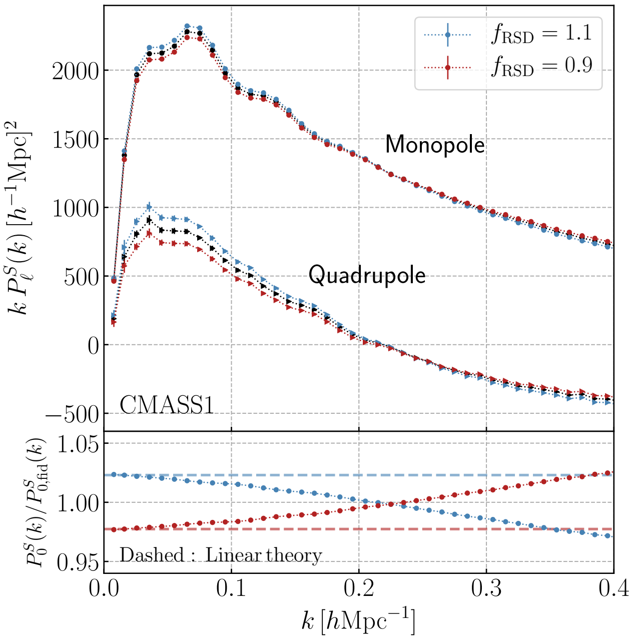

Figure 6.14: The effect of RSD control parameter, $f_{\rm RSD}$, on the monopole and quadrupole power spectra; when generating the mocks of of CMASS1 galaxies in redshift space, we modified the RSD displacement of host halos by the amount of $f_{\rm RSD}$, and then computed these multipole power spectra from the mocks (we did not change the RSD effects due to internal motions of galaxies inside the host halo). Note that $f_{\rm RSD} = 1$ corresponds to the ΛCDM model, and all the models shown here have the same real-space power spectrum. A change in the RSD parameter $f_{\rm RSD}$ alters these power spectra depending on k. The lower panel shows the fractional ratio relative to the fiducial model. The dashed curve shows the Kaiser formula prediction [Eq. (3.20)] that is computed by replacing $\beta_{\Lambda{\rm CDM}}$ in the formula with $f_{\rm RSD}\beta_{\Lambda{\rm CDM}}$, and fairly well reproduce the mock results at small k limit.

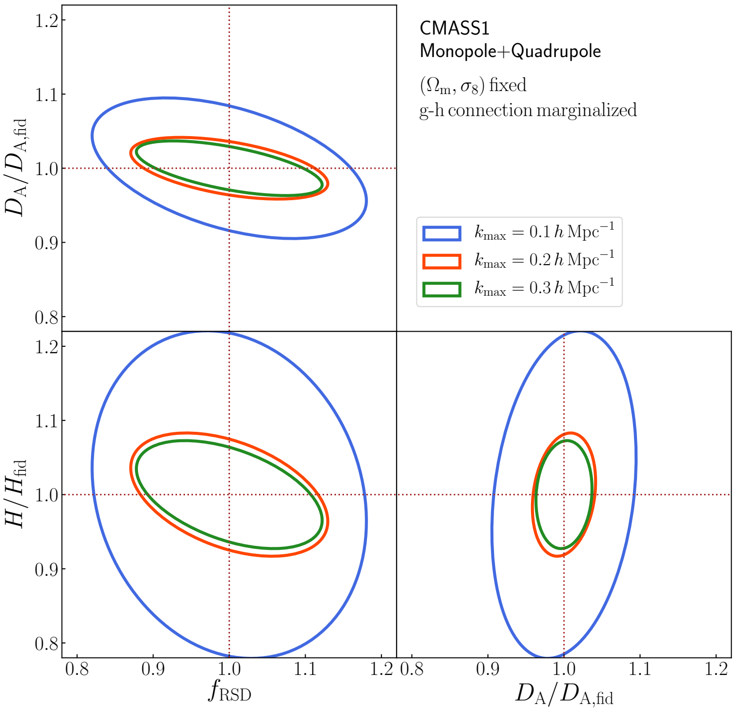

Figure 6.15: The marginalized error ellipse in each of the two-dimensional subspaces of D_A, H or f_RSD, where we consider the distance constraints for the CMASS1 sample and the constraint on f_RSD is from the information of all the three redshift slices (i.e., we use the same parameter for the RSD modification of all the three slices by the same amount f_RSD). To obtain these forecasts, we use f_RSD, and 3 D_A and H parameters for the three redshift slices, instead of Ω_m and σ_8, and include other 30 nuisance parameters of the halo-galaxy connection. These constraints are purely from the RSD, the BAO peak locations and the AP effects. The constraint f_RSD (its fiducial value $f_\mathrm{RSD} = 1$) corresponds to a fractional error of $f\sigma_8$ in the linear regime.

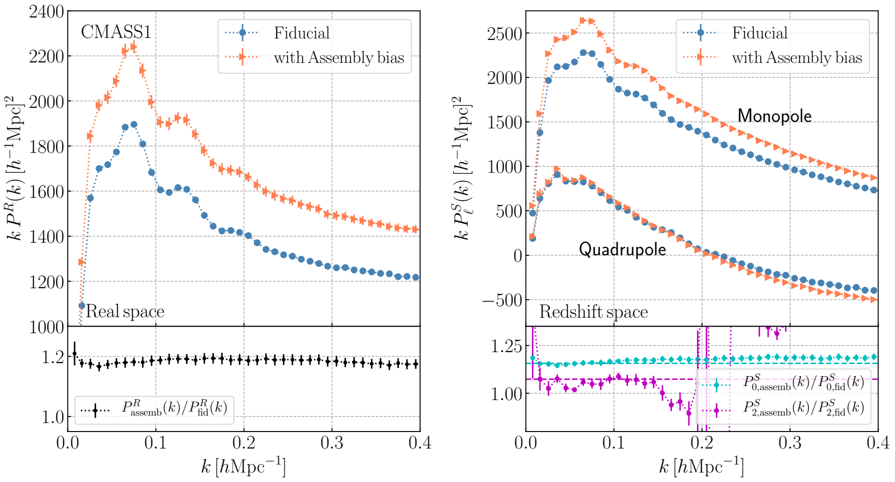

Figure 6.16: Comparison of the fiducial signals with those that included the effect of halo assembly bias (see text for details). The result for CMASS1-like galaxies is shown. Here we implemented the assembly bias effect by populating galaxies into halos according to the ranked list of mass concentration at each halo mass bin (from the lowest mass concentration). The left panel shows that the real-space power spectrum is amplified by almost constant factor, 1.2, over all the scales we consider. The right panel shows the redshift-space power spectrum, while the lower panel shows the comparison with the Kaiser formula, where the linear bias is modified by the factor that matches the real-space power spectrum amplitude. The modified Kaiser formula fairly well reproduces the monopole and quadrupole spectra. Thus the assembly bias appears to be mainly from the density field around mock galaxies, while the velocity field is not largely changed by the assembly bias.

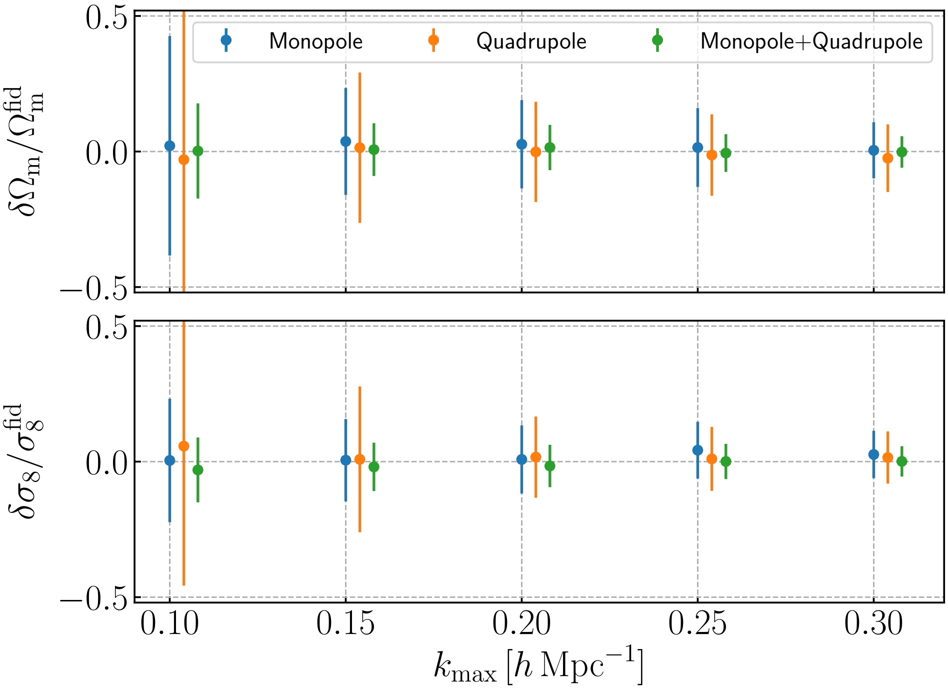

Figure 6.17: An estimation of a possible bias in Ω_{m} (upper panels) or σ_8 (lower panels) due to the effect of assembly bias on the redshift-space power spectrum, if the effect is ignored in the model prediction. We here assume that the assembly bias, which is implemented in the same way as in Fig. 6.16, affects the redshift-space power spectra for all the LOWZ, CMASS1, and CMASS2-like galaxies, and then estimate the parameter bias using the Fisher method (Eq.6.10). We show the results, relative to the fiducial value (true value) of each parameter, as a function of the maximum wave number k_{max}, and also show the marginalized error for comparison.

Chapter 7

Cosmological Analysis of SDSS-III Galaxy Power Spectrum

So far, we have constructed the theoretical template for the redshift-space galaxy power spectrum based on the halo-model formalism and assessed the impact of marginalization of nuisance parameters on the cosmological parameter constraints. In this chapter, we employ our theoretical template in the cosmological analysis of a real galaxy survey, the Sloan Digital Sky Survey [125].

As we mentioned in Chapter 5, there are recent several works for the emulation of the large-scale structure probes, such as the nonlinear matter power spectrum [76, 77] and the two-point correlation function of the HOD galaxies [80]. Although the primary purpose for building simulation-based emulators is to extract the cosmological information from galaxy survey data, there has been no attempt to apply them to the cosmological analysis in the actual galaxy surveys. In this work, we, for the first time, analyze the full-shape power spectrum measured from a galaxy redshift survey by using an emulator-based analysis pipeline, and obtain the cosmological parameter inferences.

7.1 Sloan Digital Sky Survey-III: Baryon Oscillation Spectroscopic Survey

The Sloan Digital Sky Survey (SDSS) is the largest galaxy imaging and spectroscopic survey that has been already completed. In this work, we use the Final Data Release (Data Release 12; DR12) of the SDSS-III Baryon Oscillation Spectroscopic Survey (BOSS) [2]. The BOSS DR12 contains the spectroscpic redshifts of $1,198,006$ luminous red galaxies, lying over the redshift range $0.2 < z < 0.75$. The area of sky coverage is 10,252 deg^2, and it is divided into the two sky regions named the North Galactic Cap (NGC) and South Galactic Cap (SGC).

For the cosmological analysis, we use the publicly available large-scale structure catalog named `CMASSLOWZTOT`[1]. This catalog combines the two different selections of galaxies, LOWZ and CMASS into one galaxy sample, by correcting the systematic

---

[1] The BOSS DR12 public large-scale structure catalogs can be downloaded from `https://data.sdss.org/sas/dr12/boss/lss/`

Redshift bin	Redshift range	z_{eff}	Chunk	N_{gal}	N'_{gal}
Low-Z	$0.2 < z < 0.5$	0.38	NGC	429182	445260.72
			SGC	174819	182676.6
Mid-Z	$0.4 < z < 0.6$	0.51	NGC	500872	534722.44
			SGC	185498	197081.45
High-Z	$0.5 < z < 0.75$	0.61	NGC	435741	467502.47
			SGC	158262	169907.44

Table 7.1: Various properties of galaxy samples in the `CMASSLOWZTOT` catalog we used in this study. We listed the values of effective redshift z_{eff} and unweighted and weighted numbers of galaxies, N_{gal} and N'_{gal}, respectively.

weights (see Ref. [126] for detailed description of the catalog creation). We split the whole catalog into three overlapping bins of redshift, which we denote them as Low-Z ($0.2 < z < 0.5$), Mid-Z ($0.4 < z < 0.6$) and High-Z ($0.5 < z < 0.75$). It is the same partition as the public cosmological analysis of the BOSS DR12 full-shape power spectrum in Ref. [18].

Table 7.1 shows the parameters of galaxy samples in each redshift bin and angular data chunk (either NGC or SGC). N_{gal} is the unweighted number of galaxies, i.e., naive count of galaxies listed in the catalog. In reality, each galaxy has its own weights to take into account the correction of various observational artifacts. Using this correction weight, which we denote as w_{c}, we calculate the weighted number $N'_{\text{gal}} = \sum_{i=1}^{N_{\text{gal}}} w_{\text{c},i}$. Aside from the correction weight, each galaxy also has the FKP weight to improve the signal-to-noise ratio of the measured power spectrum. We use the FKP weight in the form of

$$w_{\text{FKP},i} = \frac{1}{1 + \bar{n}(z_i) P_0}, \tag{7.1}$$

where z_i is the spectroscopic redshift of the ith galaxy, $\bar{n}(z_i)$ is the expected number density, and we use $P_0 = 10^4\, h^{-3}\, \text{Mpc}^3$. z_{eff} is called the effective redshift, and is used to calculate the theoretical template of the power spectrum for each galaxy sample. We define it as the weighted mean redshift over the galaxy sample:

$$z_{\text{eff}} = \frac{\sum_{i=1}^{N_{\text{gal}}} w_{\text{tot},i} z_i}{\sum_{i=1}^{N_{\text{gal}}} w_{\text{tot},i}}, \tag{7.2}$$

where $w_{\text{tot},i}$ is the total weight of the ith galaxy, given by $w_{\text{tot},i} = w_{\text{c},i} w_{\text{FKP},i}$.

7.2 Power spectrum measurement

We measure the monopole, quadrupole, and hexadecapole moments of the redshift-space pwoer spectrum for each redshift bin and angular chunk. For the measurement,

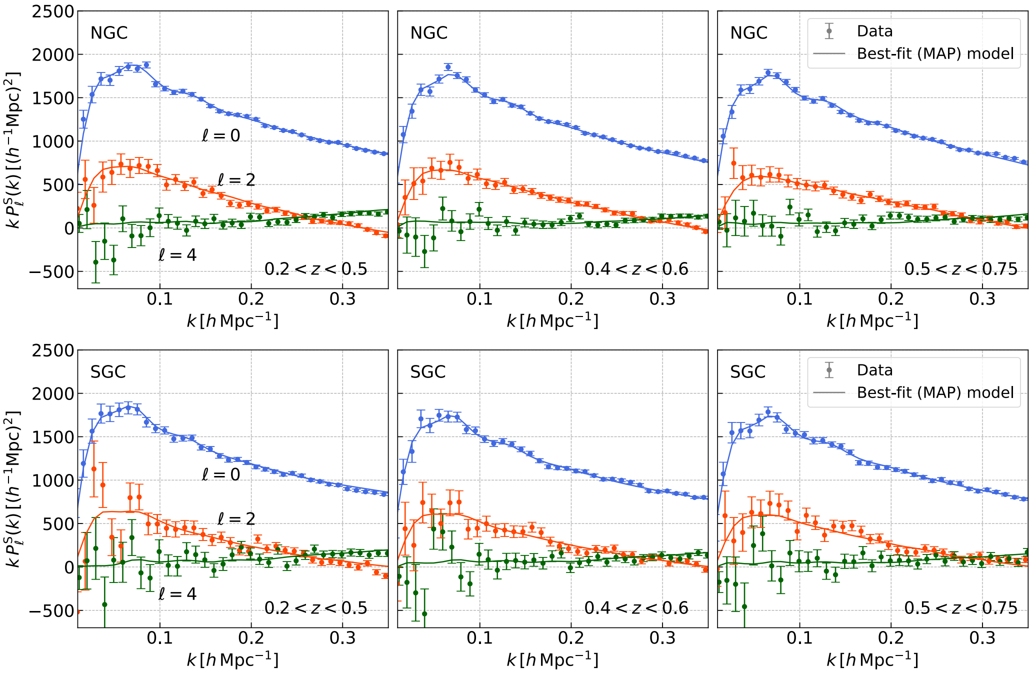

Figure 7.1: The multipole moments of the power spectrum measured from the `CMASSLOWZTOT` catalogs, for both NGC (upper) and SGC (lower) and three redshift bins. We measured the monopole (blue), quadrupole (red), and hexadecapole (green) moments, and also show the best-fit (MAP) model predictions for each redshift and angular chunk as solid lines. The error bars of data are the square root of the diagonal elements of the covariance matrices we estimated using the MultiDark-Patchy mock catalogs (see Sec. 7.3).

we adopt the FFT-based estimator of the power spectrum multipoles, described in Ref. [67] and in Chapter 4.

In the measurement, we create the FKP weighted density field by assigning the galaxy and random catalogs into cubic FFT boxes, using the Piecewise Cubic Spline (PCS) interpolation scheme (see Chapter 4). The FFT boxes are set so that they contain all the galaxies and random particles in them and zero-padding regions not less than 200 h^{-1} Mpc. We determine the grid spacing for each FFT box according to the Nyquist wave number $k_{\mathrm{Ny}} = 1.2\ h\,\mathrm{Mpc}^{-1}$. We also use the interlacing scheme to mitigate the aliasing contaminations, as well as the decomposition of the PCS interpolation window in Fourier space. Each wave vector mode is split into the linearly-spaced bins of k with width $\Delta k = 0.01\,h\,\mathrm{Mpc}^{-1}$.

As the fiducial (or reference) cosmology for which we computed the three-dimensional comoving coordinates of galaxies and randoms in the real survey data, we assumed the flat-geometry ΛCDM model with $\Omega_{\mathrm{m}} = 0.31$, following Ref. [18].

Fig. 7.1 shows the multipole moments of the power spectrum we measured from the `CMASSLOWZTOT` catalogs. Symbols with error bars are the measured spectra, and solid lines are the best-fit (maximum a posteriori; MAP) models computed with our emulator-based theoretical template. Note that we fit the model independently to the power spectra for each redshift bin and angular chunk, and in this figure we show the case that we used all of three multipoles up to $k_{\mathrm{max}} = 0.3\,h\,\mathrm{Mpc}^{-1}$. The error bars of the data are from diagonal elements of the covariance matrices estimated using the MultiDark-Patchy mock catalogs, as we describe in Sec. 7.3.

In the measurement, we found that our measured power spectra is slightly different from those provided by the SDSS collaboration, which is also reported in Ref. [127]. We did a cross check of the measurement by using a publicly available PYTHON toolkit NBODYKIT[2] [128], and confirmed that the power spectrum measured with it and with our code well agree to each other.

7.3 Covariance matrix using MultiDark-Patchy mock catalogs

To infer the cosmological parameters by the comparison of the theoretical prediction and measured power spectrum data, we need the covariance matrix. In this work, we estimate the power spectrum covariance using 2048 realizations of the MultiDark-Patchy mock catalogs created in Refs. [129, 130]. These mock catalogs are created using an approximate N-body solver which combines the Lagrangian perturbation theory and a small-scale halo collapse model, and a semi-analytical galaxy biasing scheme, with calibration to a reference large-volume N-body simulation sample selected from the BigMultiDark simulations [131]. The input cosmological parameters are as follows: $\Omega_{\mathrm{b}} = 0.048$, $\Omega_{\mathrm{m}} = 0.307115$, $h = 0.6777$, $M_\nu = 0.06$ (neutrino mass), $n_{\mathrm{s}} = 0.9611$, and $\sigma_8 = 0.8288$, and we derive $\omega_{\mathrm{b}} = 0.02205$, $\omega_{\mathrm{cdm}} = 0.1184$, $\ln(10^{10}A_{\mathrm{s}}) = 3.1$.

To measure the power spectrum from these mock catalogs, we employed the same estimator as applied to the data power spectrum, including the interpolation kernel (PCS) and zero-padding size (at least $200\,h^{-1}\,\mathrm{Mpc}$), but we set slightly smaller Nyquist wave number $k_{\mathrm{Ny}} = 1.0\,h\,\mathrm{Mpc}^{-1}$ to suppress the computational time. We estimate the power spectrum covariance matrix as

$$\mathrm{Cov}\left[\hat{P}^{\mathrm{S}}_{\ell}(k_i), \hat{P}^{\mathrm{S}}_{\ell'}(k_j)\right] = \frac{1}{N_{\mathrm{r}} - 1} \sum_{n=1}^{N_{\mathrm{r}}} \left[\hat{P}^{\mathrm{S}}_{\ell}(k_i) - \bar{P}^{\mathrm{S}}_{\ell}(k_i)\right] \left[\hat{P}^{\mathrm{S}}_{\ell'}(k_j) - \bar{P}^{\mathrm{S}}_{\ell'}(k_j)\right], \tag{7.3}$$

where $N_{\mathrm{r}} = 2048$ is the number of realizations of mock catalogs, and we define the mean power spectrum as

$$\bar{P}^{\mathrm{S}}_{\ell}(k_i) = \sum_{n=1}^{N_{\mathrm{r}}} \hat{P}^{\mathrm{S}}_{\ell}(k_i). \tag{7.4}$$

---

[2] `https://nbodykit.readthedocs.io/en/latest/`

We estimate the covariance matrix from the finite number of mock realizations and invert to obtain the estimate of the inverse covariance matrix. However, it leads to the biased estimation of the inverse covariance, even though the estimator of the covariance Eq. (7.3) is unbiased. To approximate the unbiased estimator of the inverse covariance, we simply multiplied to the inverse of the estimated covariance the so-called Hartlap factor [132] defined as

$$f_{\mathrm{Hartlap}} = \frac{N_{\mathrm{r}} - n_{\mathrm{bin}} - 2}{N_{\mathrm{r}} - 1}, \tag{7.5}$$

where n_{bin} is the number of bins we use in the parameter inference. For example, in the case that we use the monopole, quadrupole, and hexadecapole moments up to $k_{\mathrm{max}} = 0.3\,h\,\mathrm{Mpc}^{-1}$, the number of bins amounts to $n_{\mathrm{nin}} = 30 \times 3 = 90$, which means $f_{\mathrm{Hartlap}} = 0.9555$.

7.4 Theoretical model and methodology

7.4.1 Survey window function

We take into account the survey window function in the theoretical model. We put the detailed description of this in Sec. 4.4. Acturally, a measurement of the window functions using the random catalogs is computationally difficult. Hence, in this study, we approximated the Fourier-space window functions introduced in Sec. 4.4 by transforming the BOSS DR12 configuration-space window functions (see Ref. [18]) provided by the SDSS collaboration. We confirmed this approximation works well using the linear power spectrum.

Fig. 7.2 is an illustration to show how the survey window function affects the power spectrum, in the case of Low-Z SGC galaxies. The window function basically alters the power spectrum only at large scales, $k \lesssim 0.1\,h\,\mathrm{Mpc}^{-1}$.

7.4.2 Model parameters and priors

In this subsection, we describe the model parameters that we infer, as well as their prior settings.

Cosmological parameters

Since we want to infer the cosmological parameters within the flat-geometry ΛCDM framework, we sample all of five parameters:

$$\mathbf{p}_{\mathrm{cosmo}} = \left\{\omega_{\mathrm{b}}, \omega_{\mathrm{cdm}}, \Omega_{\mathrm{de}}, \ln(10^{10}A_{\mathrm{s}}), n_{\mathrm{s}}\right\}. \tag{7.6}$$

For ω_{b} and n_{s}, we impose priors that are inferred from the *Planck* 2018 cosmology. More precisely, we impose the Gaussian priors given in Table 1 of Ref. [133] for the

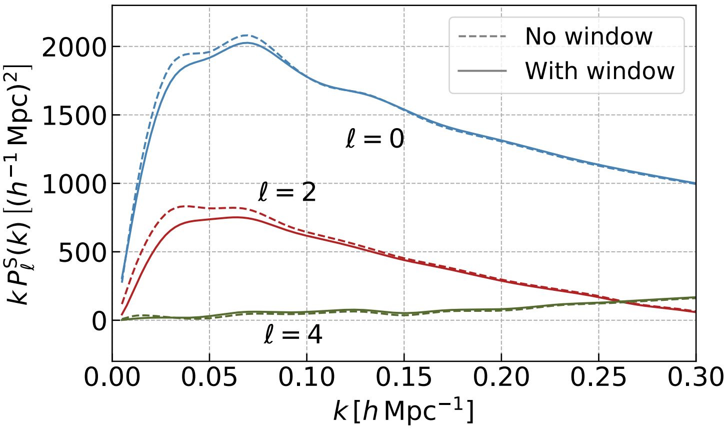

Figure 7.2: A demonstration of the window function effects on the power spectrum multipoles for the Low-Z SGC galaxies. The dashed lines are the power spectrum multipoles computed by the emulator, which roughly mimic the Low-Z SGC power spectrum. The solid lines are those including the window function effects following the scheme we described in Sec. 4.4.

Parameter	Prior
Cosmology	
$\omega_{\rm b}$	$\mathcal{N}(\mu = 0.02237, \sigma = 0.00015)$
$\omega_{\rm cdm}$	$\mathcal{U}(0.10782, 0.13178)$
$\Omega_{\rm de}$	$\mathcal{U}(0.54752, 0.82128)$
$\ln(10^{10} A_{\rm s})$	$\mathcal{U}(2.4752, 3.7128)$
$n_{\rm s}$	$\mathcal{N}(\mu = 0.9649, \sigma = 0.0042)$
Nuisance	
$\log M_{\rm min}$	$\mathcal{U}(12.0, 15.0)$
$\sigma^2_{\log M}$	$\mathcal{U}(0.0001, 2.0)$
$\log M_1$	$\mathcal{U}(12.0, 16.0)$
$\alpha_{\rm sat}$	$\mathcal{U}(0.01, 5.0)$
κ	$\mathcal{U}(0.01, 5.0)$
$P_{\rm shot}$	$\mathcal{U}(-10^4, 10^4)\, h^{-3}\,{\rm Mpc}^3$
$c_{\rm vel}$	$\mathcal{U}(0.01, 10.0)$

Table 7.2: The parameter set we varied in the cosmological analysis within the flat ΛCDM cosmology. $\mathcal{N}(\mu, \sigma)$ denotes the Gaussian distribution with mean μ and standard deviation σ. $\mathcal{U}(a, b)$ denotes the uniform distribution between the minimum value a and the maximum value b. The flat priors for cosmological parameters are set to be within the parameter ranges on which the emulator is supported.

Planck 2018 TT, TE, EE+lowE+lensing. We treat $\Omega_\mathrm{m} = 1 - \Omega_\mathrm{de}$ and σ_8 as derived parameters.

Since we assumed the fiducial cosmology ($\Omega_\mathrm{m} = 0.31$) when we measured the power spectrum, we include the Alcock-Paczynski effect in the theoretical model, following Eq. (3.24) in Chapter 3.

Nuisance parameters

The model we use is basically the same as one we described in Chapter 5, but we include two additional nuisance parameters, as we consider in Chapter 6:

- P_shot, which represents the residual shot noise contribution apart from the simple Poisson shot noise. We add P_shot to the galaxy power spectrum $P_\mathrm{gg}(k, \mu)$, and hence it is relevant only to the monopole moment.

- c_vel, which represents the multiplicative coefficient to the galaxy velocity dispersion inside halos. This parameter regulates the uncertainty on the strength of FoG effect.

Since we use the five-parameter HOD model, we have seven nuisance parameters on the halo-galaxy connections:

$$\mathbf{p}_\mathrm{galaxy} = \{\log M_\mathrm{min}, \sigma^2_{\log M}, \log M_1, \alpha_\mathrm{sat}, \kappa, P_\mathrm{shot}, c_\mathrm{vel}\}, \tag{7.7}$$

for each redshift bin and angular chunk. We listed the parameter set used in the analysis in Table 7.2.

7.4.3 Bayesian inference of posterior distribution

To infer the cosmological parameters, we employ the Bayesian posterior inference. Using the power spectrum data vectors and the covariance matrix, we compute the log-likelihood function:

$$\begin{aligned}&\ln \mathcal{L}(\mathcal{D}|\mathbf{p}) = \\ &-\frac{1}{2}\sum_{\ell,\ell'}\sum_{i,j}^{k_\mathrm{max}} \left[P_\ell^\mathcal{D}(k_i) - P_\ell(k_i;\mathbf{p})\right] \mathrm{Cov}^{-1}\left[P_\ell(k_i), P_{\ell'}(k_j)\right] \left[P_{\ell'}^\mathcal{D}(k_j) - P_{\ell'}(k_j;\mathbf{p})\right],\end{aligned} \tag{7.8}$$

where we assume the Gaussian likelihood and omit the normalization factor. $P_\ell^\mathcal{D}(k_i)$ denotes the data of the ℓth-order power spectrun multipole at the ith bin, $P_\ell(k_i;\mathbf{p})$ is its theoretical model, and $\mathbf{p}$ is the model parameters. By combining with the priors we mentioned above, we sample the posterior disttributions by using the nested sampling.

All the parameter inference were done by using the publicly-available MontePython3[3] code [134, 135], and we employed the efficient nested sampling algorithm MultiNest [136] implemented in it, rather than the standard MCMC sampling.

7.5 Model validation on mock data

Although our theoretical model for the power spectrum is calibrated by the cosmological N-body simulations at the level of dark matter halos, we assume a specific form of the phenomenological prescription for the halo-galaxy connection, as discussed in Chapter 5. Therefore, we need to check that our emulator-based theoretical model can safely recover the true cosmological parameters in the mock galaxy power spectrum.

7.5.1 Validation using the HOD galaxy mocks

For this purpose, we created the mock galaxy catalogs which roughly mimic the BOSS DR12 galaxy power spectrum we consider, by using the HOD-based method used to create mock galaxy catalogs in Chapter 5 and 6. We created two kinds of mocks:

(i) `Fiducial` — The standard HOD galaxy mocks where the five parameters of central and satellite HOD models, Eqs. (3.28) and (3.29), are chosen to mimic the Mid-Z galaxy sample.

(ii) `Off-centering` — The galaxy mocks with the same HOD but also include the off-centered central galaxies with the off-centering probability $p_{\rm off} = 0.3$ and the typical off-centering radius with respect to the NFW scale radius, $\mathcal{R}_{\rm off} = 2.0$ (see Sec. 3.4 for the definitions of these two parameters).

For both settings, we created mocks by populating galaxies into halo catalogs from the Dark Quest LR simulations (i.e., the box side length is $2\,h^{-1}$ Gpc) run for the fiducial *Planck* 2015 ΛCDM cosmology. We use the mean power spectrum signals among 15 realizations as the mock signals.

Since we employ the HOD-based theoretical template, it can reproduce the same power spectrum as the `Fiducial` mock data, up to the prediction accuracy of the emulator itself. Thus, the fit on this mock takes on the role of a kind of sanity check of our analysis pipeline. Nevertheless, it is not entirely clear whether our model can recover the true cosmological parameters after marginalization over nuisance parameters of galaxy-halo connection. If any of cosmological parmaeters have severe degeneracies with the nuisance parameters, the posterior distribution could display a sizable bias compared to the true value (see e.g., Ref. [137]). On the other hand, for

---

[3] `https://github.com/brinckmann/montepython_public`

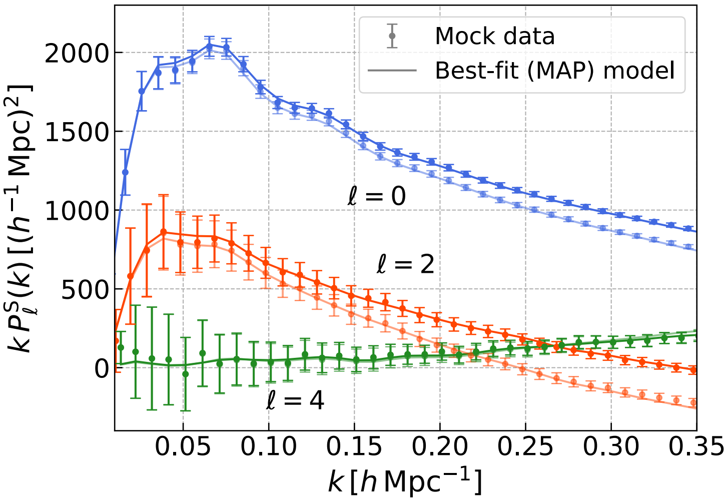

Figure 7.3: The mock data (symbols with error bars) we used in the model validation and the best-fit (MAP) model predictions (solid lines). Thick-colored symbols and solid lines correspond to the `Fiducial` mock, and thin-colored ones correspond to the `Off-centering` mock, respectively. We show the case of $k_{\mathrm{max}} = 0.3\,h\,\mathrm{Mpc}^{-1}$.

the test using the `Off-centering` mocks, our set of nuisance parameters employed in this analysis does not contain the off-centering parameters, p_{off} and $\mathcal{R}_{\mathrm{off}}$, and hence it is nontrivial whether our model can safely recover the true cosmological parameters for the `Off-centering` mocks. We perform the cosmological analysis on these mock signals using our analysis pipeline, with two slight differences from our analysis of the actual BOSS spectra: one is that we employ the Gaussian prior of with the mean values of $\omega_{\mathrm{b}} = 0.2225$ and $n_{\mathrm{s}} = 0.9645$, which are taken from the Planck 2015 cosmology instead of *Planck* 2018, because our mocks are built from N-body simulations assuming the *Planck* 2015 cosmology. Another is that we did not implement the survey window function as these mocks do not have the window function effect.

First, we show the mock signals as well as the corresponding best-fit model predictions in Fig. 7.3. In this figure, we show the results for both the `Fiducial` (thick-colored) and `Off-centering` (thin-colored) mocks together, to see the difference between these two. For both cases, our model well fits to the mock signals on scales up to $k = 0.3\,h\,\mathrm{Mpc}^{-1}$, which is the maximum wave number we considered in the analysis. Note that in the cases of smaller k_{max}, we also confirmed that the best-fit models well agree with the signals on scales up to that k_{max}.

Fig. 7.5 shows the parameter posterior distributions obtained by our mock analysis. The upper and lower panels are the results obtained by the analyses of `Fiducial` and `Off-centering` mock data, respectively. In both cases, we obtain highly similar posteriors, and our method successfully recovers the true input *Planck* cosmology (shown as gray horizontal and vertical solid lines in each subplot), when the power spectrum signals up to $k_{\rm max} = 0.2$ and $0.3\,h\,{\rm Mpc}^{-1}$ are used in the parameter inference. For the case of $k_{\rm max} = 0.1\,h\,{\rm Mpc}^{-1}$, our model tends to give the lower values than the truth for $\ln(10^{10}A_{\rm s})$ and σ_8. In addition, from the constraint on $\Omega_{\rm m} - \sigma_8$ plane, we see that the $\Omega_{\rm m}$ constraint shows almost no improvement by increasing $k_{\rm max} = 0.2$ to $0.3\,h\,{\rm Mpc}^{-1}$, while the σ_8 constraint is still improved to some extent. This behavior looks highly consistent with the Fisher forecast in Fig. 6.11 (or Fig. 8 in Appendix 6, where we show the forecasts using the same nuisance parameter set as we use in this work), which implies that $\Omega_{\rm m}$ is almost determined by the BAO feature alone. The fact that, we find no remarkable difference in the cosmological parameter constraints in spite of the significant difference in the power spectrum signals due to the off-centering effect, is thought to reflect that the flexibility of our model due to severe degeneracies between the nuisance parameters of halo-galaxy connection and the cosmological parameters. That is, even if we include the power spectrum information at $k > 0.2\,h\,{\rm Mpc}^{-1}$, the information does not much imporve the cosmological constraints, and is rather explained by the nuisance parameters.

Fig. 7.6 shows the impact of the inclusion of the hexadecapole moment in the cosmological parameter inference. The blue and red contours are the posterior distributions of $\{\Omega_{\rm m}, \ln(10^{10}A_{\rm s}, \sigma_8, H_0)\}$ in the case that we use only the monopole and quadrupole moments, or we use the three multipole moments up to the hexadecapole in the analysis. The upper and lower panels are the case of $k_{\rm max} = 0.2$ and $0.3\,h\,{\rm Mpc}^{-1}$. By including the hexadecapole moment, the estimated variances of $A_{\rm s}$ and σ_8 are marginally improved especially the case of $k_{\rm max} = 0.2\,h\,{\rm Mpc}^{-1}$, while it hardly affects the estimations of $\Omega_{\rm m}$ and H_0.

7.5.2 Nuisance parameters

In this subsection, we see the behaviors of the nuisance parameter constraints, focusing on the `Fiducial` HOD-based mock. Fig. 7.7 show how the parameter estimation including seven nuisance parameters changes by the increase of maximum wave number $k_{\rm max}$. We show the same settings of analysis as the upper panel of Fig. 7.5. As we use the power spectrum signals at the quasi-nonlinear scales $k > 0.1\,h\,{\rm Mpc}$, the estimation of almost all the nuisance parameters is significantly improved. It means that the information to break the degeneracies among the cosmological and nuisance parameters is contained in these regime. Fig. 7.8 shows the change of parameter estimation by the inclusion of hexadecapole moment, under the same setting of analysis as the upper panel of Fig. 7.6. From this figure, we see that the hexadecapole moment mainly contributes to the determination of $\log M_{\rm min}$ and $\sigma_{\log M}$, the HOD parmeters for central galaxies, and $c_{\rm vel}$, the multiplicative factor on the galaxy velocity variance inside halos. The marginal improvement in $A_{\rm s}$ (and σ_8) estimation seems to be arising from the degeneracy breaking among $A_{\rm s}$ and these nuisance parameters.

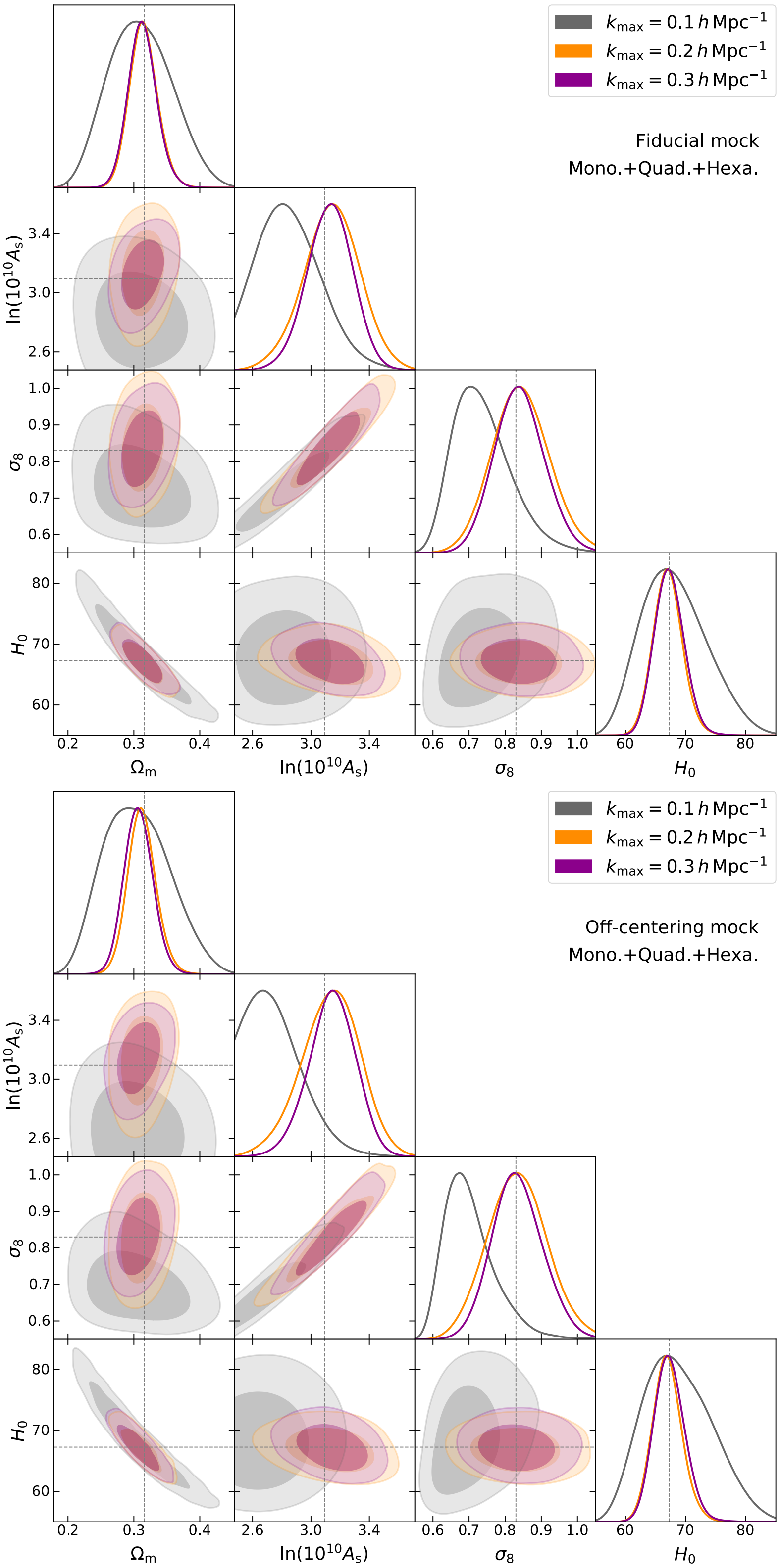

Figure 7.4: The marginalized one- and two-dimensional (1D and 2D) posterior distributions for $\{\Omega_{\rm m}, \ln(10^{10}A_{\rm s}), \sigma_8, H_0\}$ estimated on the `Fiducial` (upper) and `Off-centering` (lower) HOD-based mock catalogs. We show the results of the Mid-Z SGC mock signals. The gray, orange, and magenta curves and contours correspond to $k_{\rm max} = 0.1$, 0.2, and $0.3\ h\,{\rm Mpc}^{-1}$, respectively.

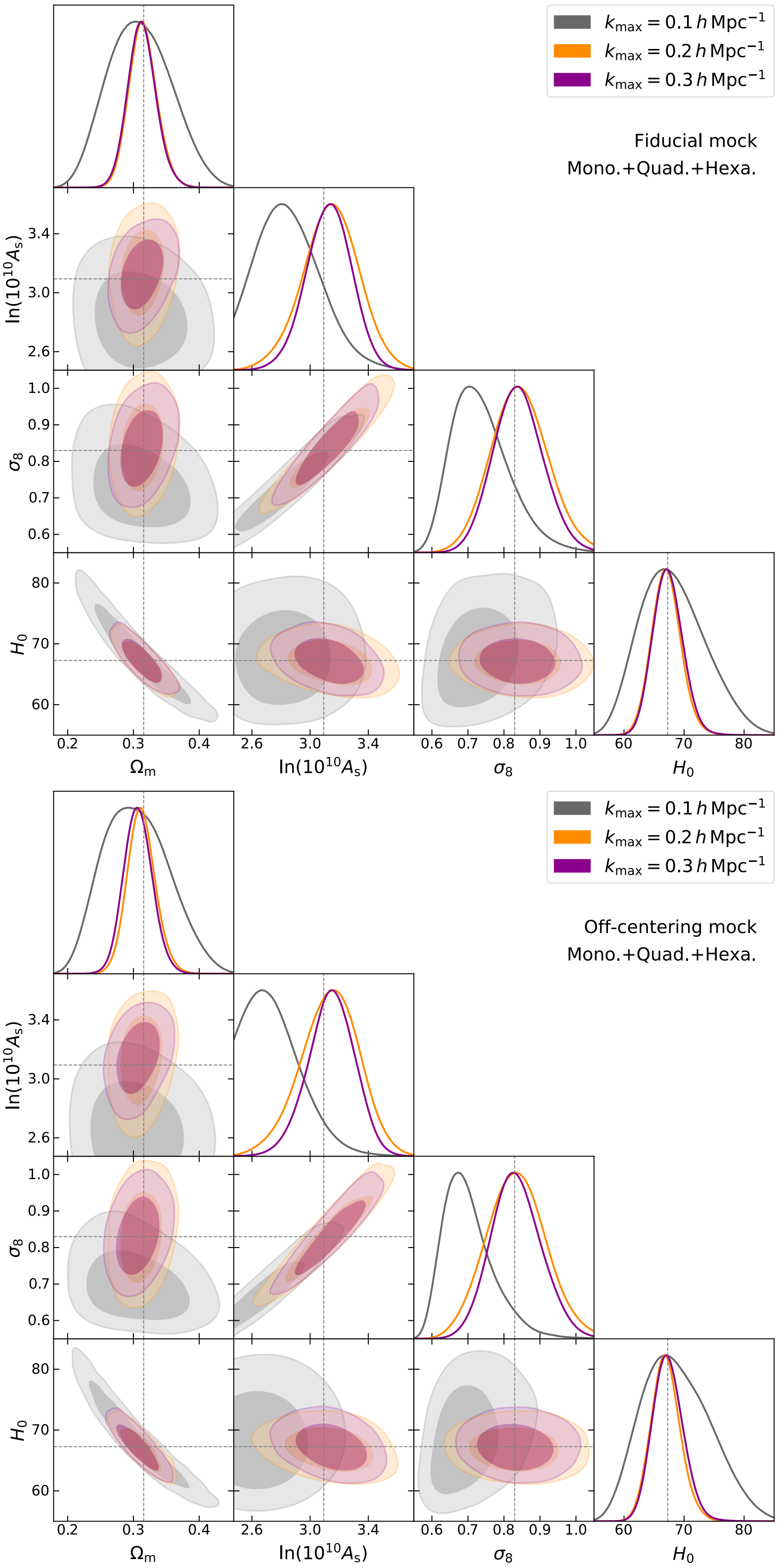

Figure 7.5: The marginalized one- and two-dimensional (1D and 2D) posterior distributions for $\{\Omega_{\rm m}, \ln(10^{10}A_{\rm s}), \sigma_8, H_0\}$ estimated on the `Fiducial` (upper) and `Off-centering` (lower) HOD-based mock catalogs. We show the results of the Mid-Z SGC mock signals. The gray, orange, and magenta curves and contours correspond to $k_{\rm max} = 0.1$, 0.2, and $0.3\ h\,{\rm Mpc}^{-1}$, respectively.

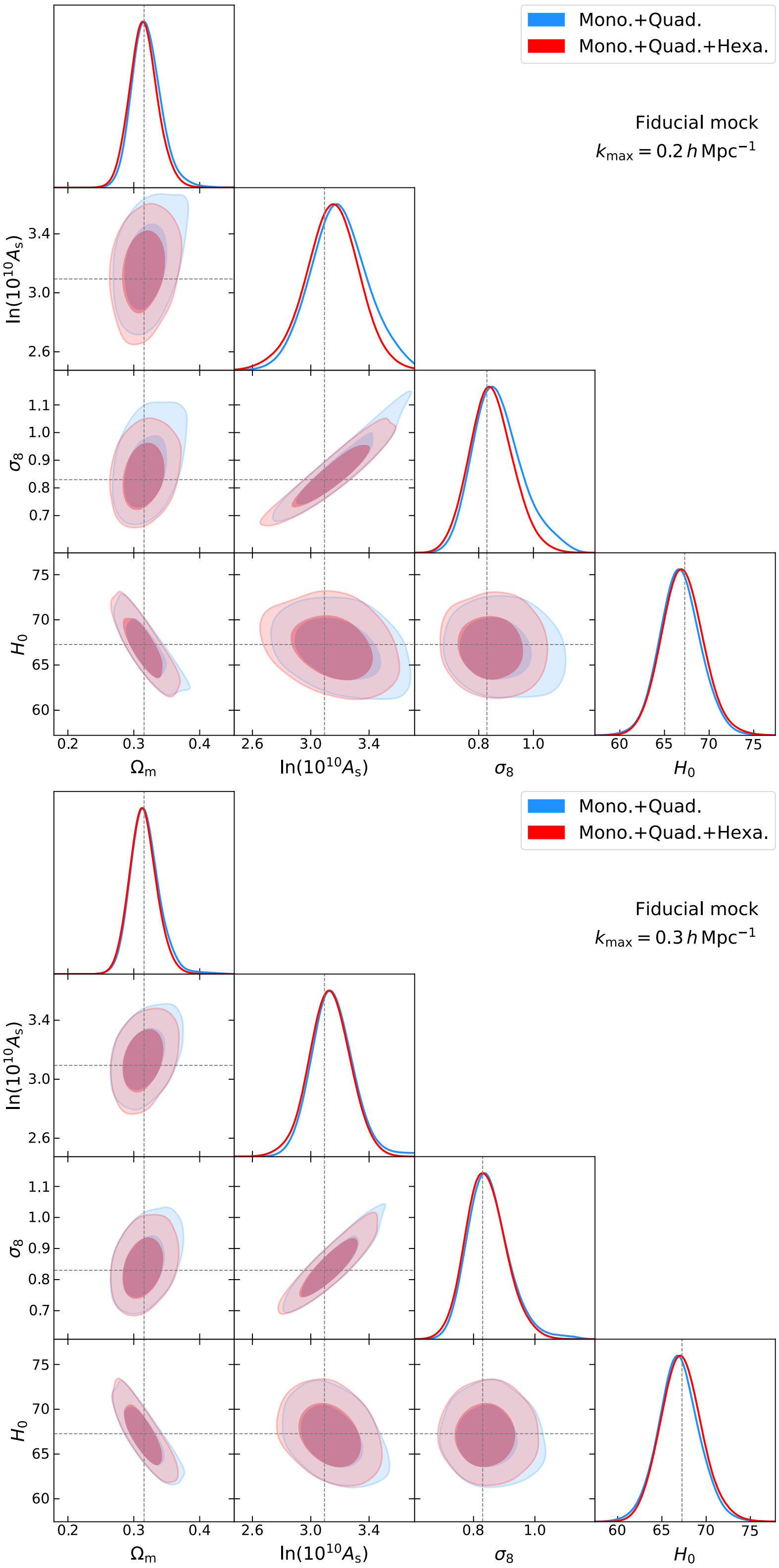

Figure 7.6: Comparison between the cosmological parameter inferences with and without the hexadecapole moment. We show the results of the Mid-Z SGC `Fiducial` mock signals, for the cases of $k_{\rm max} = 0.2$ (upper) and 0.3 (lower) $h\,{\rm Mpc}^{-1}$.

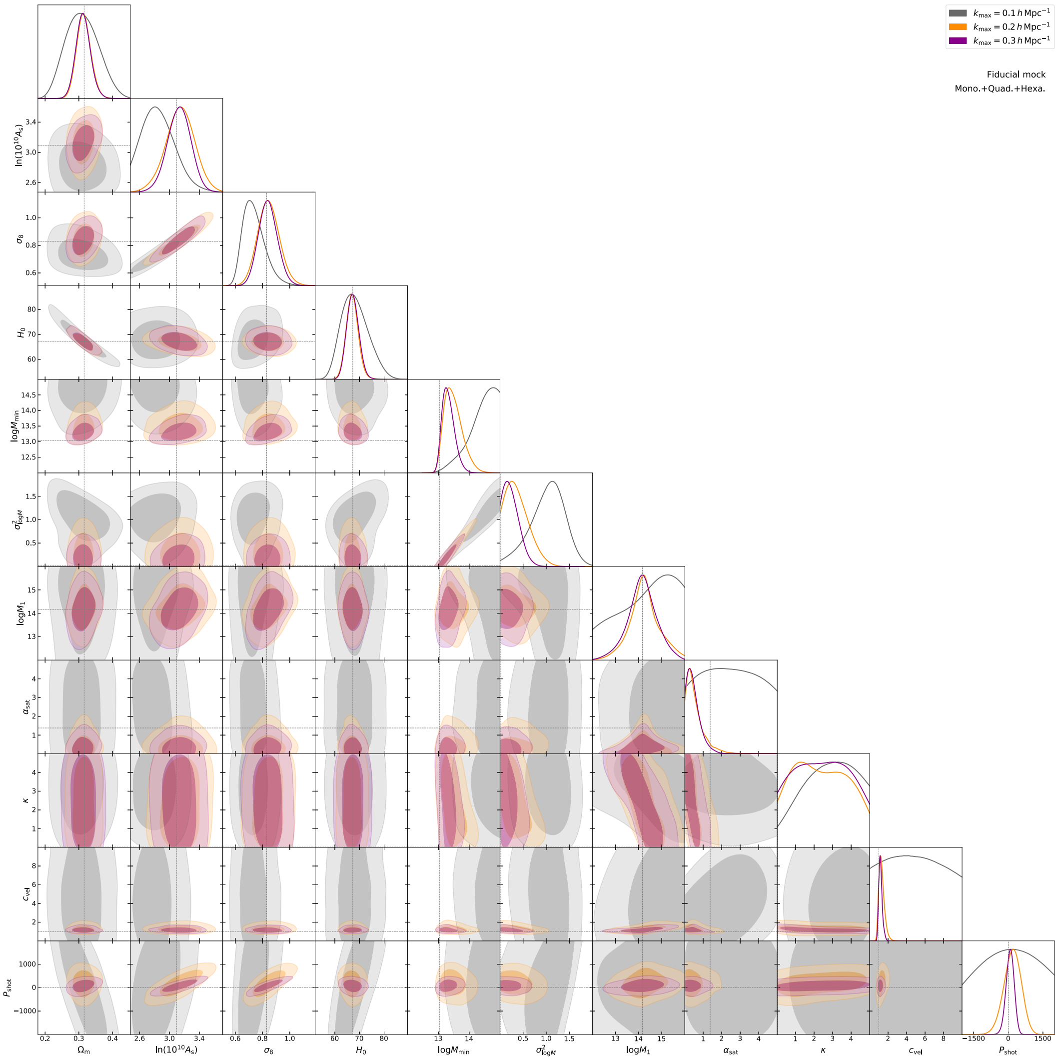

Figure 7.7: The parameter posteriors of $\{\Omega_{\mathrm{m}}, \ln(10^{10}A_{\mathrm{s}}), \sigma_8, H_0\}$ and seven nuisance parameters listed in Table 7.2. We use the monopole, quadrupole, and hecadecapole moments of the Mid-Z SGC `Fiducial` mock galaxies.

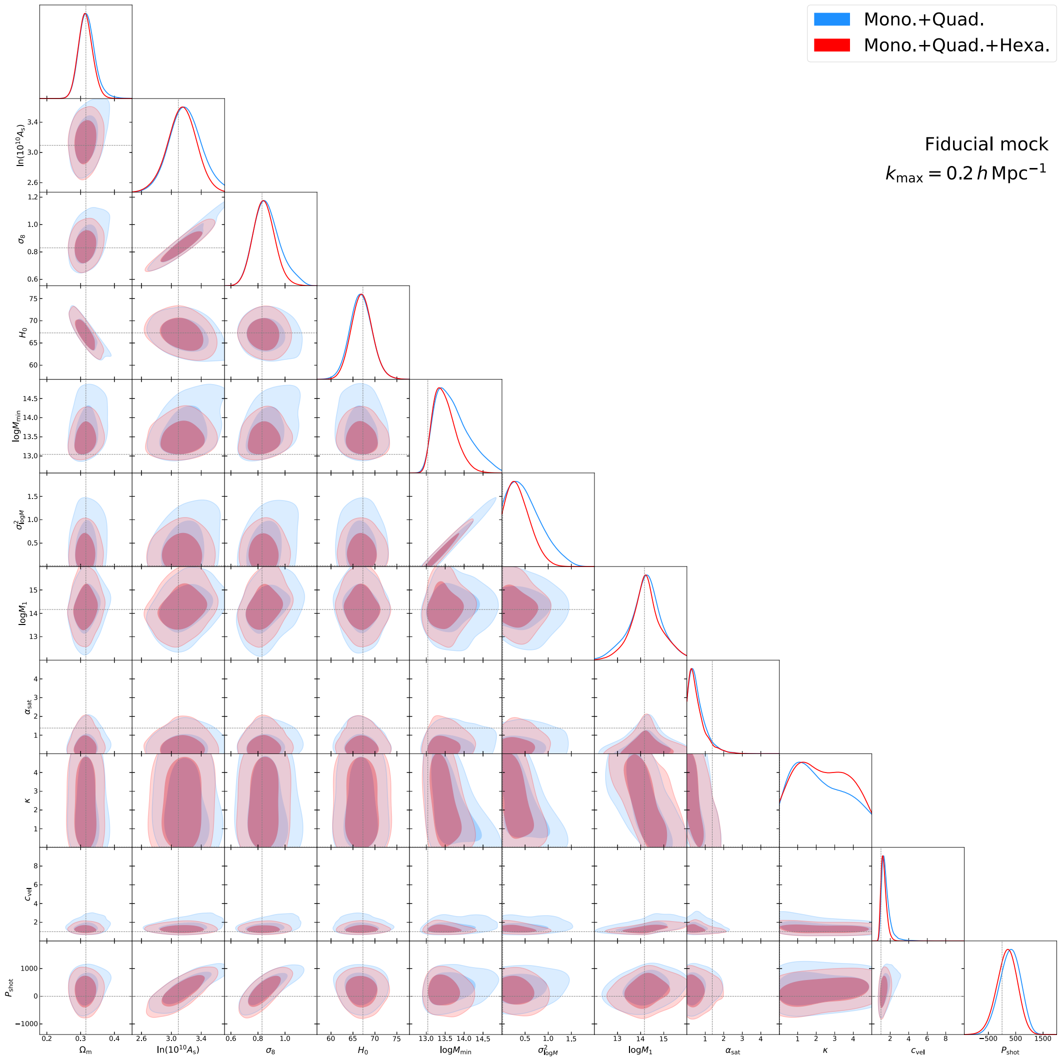

Figure 7.8: The same as Fig. 7.7, but we show the comparison between the analyses with and without the hexadecapole moment.

7.5.3 Validation using the MultiDark-Patchy mocks

We also applied our analysis pipeline to another set of mocks: MultiDark-Patchy mocks. While the MultiDark-Patchy mocks are not created from the full N-body simulations but are created using various phenomenological approximated schemes, they include the same survey window as the real galaxy catalogs. Hence we used our pipeline with only difference in the means of Gaussian priors on ω_b and n_s, which are set to be the input values of MultiDark-Patchy listed in Sec. 7.3.

Fig. 7.9 shows the resultant paramter posteriors. Again, we show the case for the monopole, quadrupole, and hexadecapole moments and the covariance of the Mid-Z SGC samples. It shows the same behavior with results on the HOD mock catalogs: the $k_\mathrm{m} = 0.1\,h\,\mathrm{Mpc}^{-1}$ case shows the significantly lower values for A_s and σ_8, while the increasing k_max to $0.2\,h\,\mathrm{Mpc}^{-1}$ improve both the estimated parameter variance and descripancy from the true values. However, the A_s and σ_8 estimates for $k_\mathrm{max} = 0.3\,h\,\mathrm{Mpc}^{-1}$ appear to again start to deviate from the truth. Thus, in the analysis below we mainly focus on the case of $k_\mathrm{max} = 0.2\,h\,\mathrm{Mpc}^{-1}$, while we show the case of $k_\mathrm{max} = 0.3\,h\,\mathrm{Mpc}^{-1}$ as well. The issue of robustness of the parameter estimation should be further investigated using more various mock catalogs. We will delved into this issue in more detail as a future work.

7.6 Analysis of BOSS DR12

In this section, we show the main results of cosmological parameter inference. In our baseline setting, we use the monopole, quadrupole, and hexadecapole moments, and show the results for the maximum wave number $k_\mathrm{max} = 0.2$ and $0.3\,h\,\mathrm{Mpc}^{-1}$. While we vary five cosmological parameters as we described in the previous section, we mainly focus on the results for $\{\Omega_\mathrm{m}, \ln(10^{10}A_\mathrm{s}), \sigma_8, H_0\}$, which are of particular interest in the large-scale structure probes.

7.6.1 Cosmological parameter constraints for single redshift and angular chunk

First we show the cosmological parameter inference results performed on the galaxy sample in the single redshift bin and either of the North or South survey fields.

Fig. 7.10 is the marginalized posterior distributions for the cosmological parameters $\{\Omega_\mathrm{m}, \ln(10^{10}A_\mathrm{s}), \sigma_8, H_0\}$, obtained from the analyses on each redshift bin and angular chunk. We show the cases of $k_\mathrm{max} = 0.2$ (upper) and $0.3\,h\,\mathrm{Mpc}^{-1}$ (lower). In both cases, we see that the contours for all of redshifts and angular chunks roughly mutually agree. The High-Z NGC case (shown in magenta) shows lower values of $\ln(10^{10}A_\mathrm{s})$ and σ_8, and the Low-Z SGC case (shown in green) shows lower Ω_m and higher H_0, than the other five cases, respectively. However, these values are consistent with the cosmmological analysis using the Effective Field Theory (EFT)-based modeling [20] (see Fig. 2 in Ref. [20]).

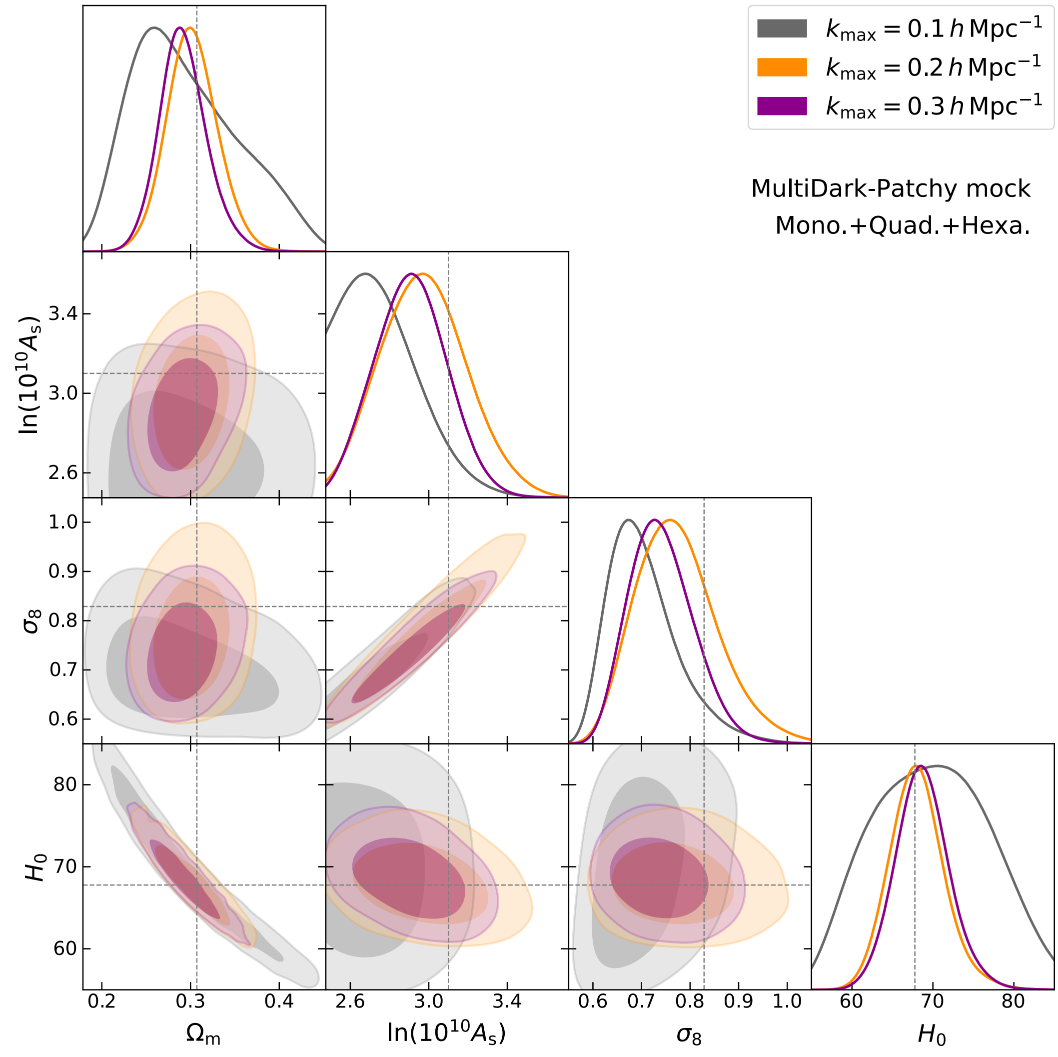

Figure 7.9: The same as Fig. 7.5, but we show the result on the MultiDark-Patchy mock catalogs.

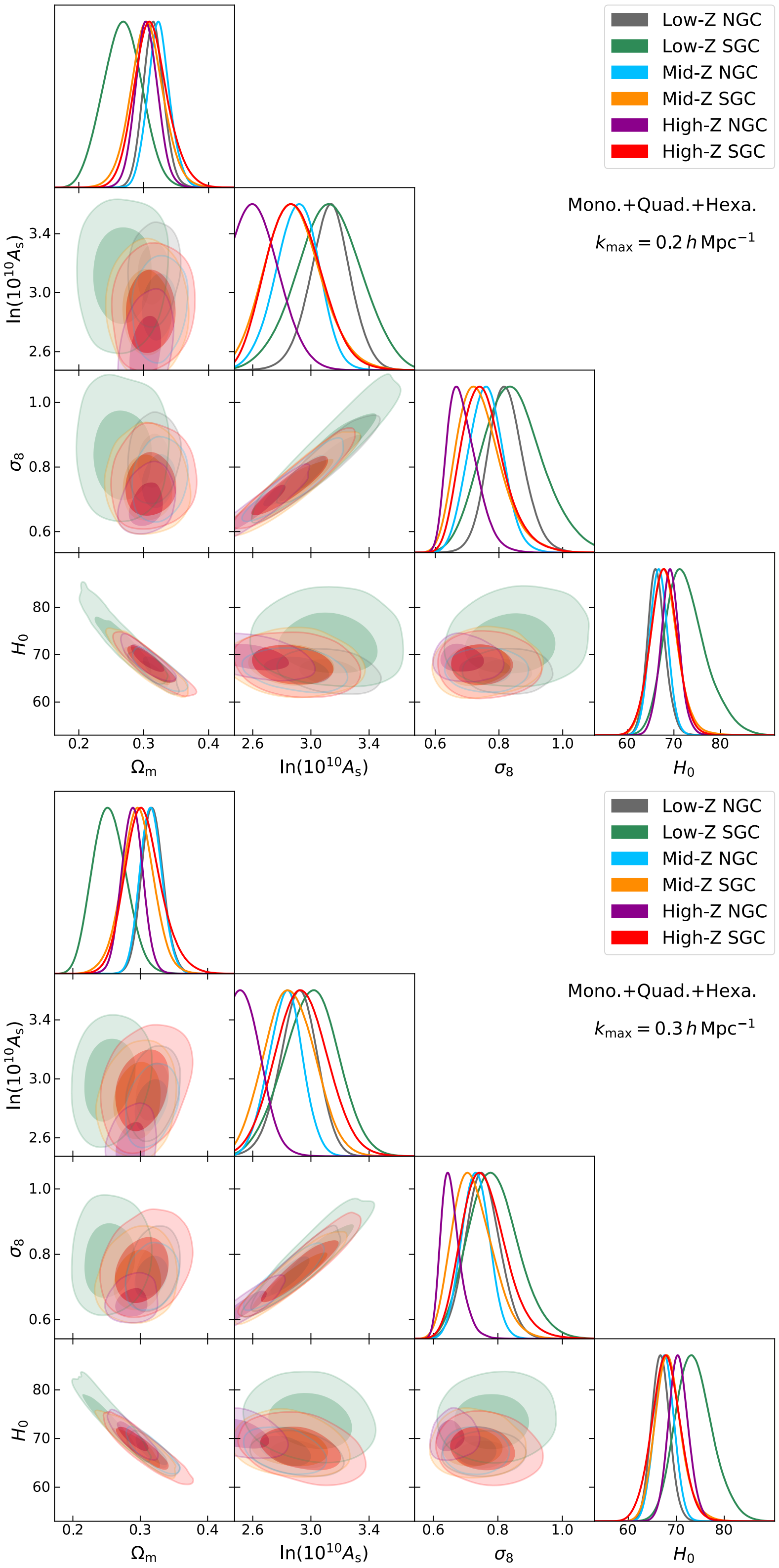

Figure 7.10: The marginalized 1D and 2D posterior distributions for $\{\Omega_{\rm m}, \ln(10^{10}A_{\rm m}), \sigma_8, H_0\}$, for each redshift and angular chunk. We show the cases of $k_{\rm max} = 0.2$ (upper) and $0.3\,h\,{\rm Mpc}^{-1}$ (lower). Different colors of contours correspond to different redshifts and chunks listed in the legend.

7.7 Discussion: future prospect on the systematics

In this work, we have the first step to the cosmological analysis of the redshift-space galaxy clustering based on the emulator. Although we saw that our methodology can be powerful in the cosmological parameter inference in actual galaxy spectroscopic surveys, we should enumerate the possible systematics which can affect the emulator-based cosmological analysis to suggest the wrong cosmology.

Since we assume the specific phenomenological model on the poorly-understood halo-galaxy connection, our model flexibility of galaxy power spectrum is inevitably restrictive, although it can provide the non-perturbative predictions of the power spectrum. To check the biases in the inferred cosmological parameters arising from the use of such a restrictive theoretical model, we need to test the inference pipeline on the mock catalogs with various settings of the halo-galaxy connection. In this work, we tested our method on two kinds of HOD mock catalogs, as the first step. However, there are further variations on how the galaxies can reside in their host halos, even if the same HOD is assumed. For example, in these two HOD-based mocks we assume that the spatial distributions of satellite galaxies follows the NFW profile, but in reality the galaxies do not faithfully trace the dark matter distribution inside halos. Furthermore, as we mentioned in Chapter 5, our emulator predicts the dependence of halo power spectrum only on one halo property, i.e., mass, and ignore the halo assembly bias. In reality, several simulation-based studies showed that the halo clustering does depend on the halo properties other than mass, and the population of galaxies targeted in surveys can correlate with such properties. In Sec. 6.3.2, we see that the difference between the galaxy power spectrum with and without a possible assembly bias due to the halo concentration can be safely absorbed by the marginalization over HOD parameters. We need to test the emulator-based analysis on such mock catalogs with the large degree-of-freedom of assembly bias. On this issue, there is a similar previous study for the investigation of the bias in the parameter inference from the lensing data of the Subaru Hyper Suprime-Cam and SDSS projected clustering [137].

Furthermore, to extend the maximum wave number of the power spectrum signals used in the cosmological analysis in galaxy redshift surveys, we will need to properly evaluate the observational systematics due to the fiber collision, which arises from the fact that the two spectroscopic fibers on the telescopes cannot be physically closer than some angular distance set by the hardware, and fails to measure the redshift of some target galaxies. Since the probability that the fiber collision happens depends on the angular number density of target galaxies at a local sky patch, it distorts the measured power spectrum, and this effect becomes severer at larger k (e.g., [138]). We need to quantify the influence of fiber collision, and mitigate its impact, e.g., by properly weighting the galaxies or, if possible, by implementing this effect in the theoretical model.

Chapter 8

Conclusion

In this thesis, we have delved into a newly-developed, simulation-based approach of cosmological inference from the redshift-space galaxy power spectrum from various aspects: the theoretical model building, the assessment of impact of nuisance parameters on cosmology constraints, and the cosmological analysis of actual survey data.

Emulator development

For the theoretical model building, we have developed an "emulator" of the redshift-space power spectrum of halos, based on the N-body simulations and a machine learning-based technique. A fast and accurate prediction of the power spectrum in a multi-dimensional input parameter space requires an efficient way to precisely interpolate the simulation data. To this end, we adopted a feed-forward neural network with a simple structure. In the six-dimensional parameter space of flat-geometry wCDM cosmology and the redshift range $0 \leq z \leq 1.48$ investigated in a large cosmological N-body simulation suite, the neural network can reproduce the halo power spectrum $P^{\mathrm{S}}_{\mathrm{hh}}(k, \mu)$ for a given halo mass threshold above $10^{12}\, h^{-1}\, M_{\odot}$, in several CPU milliseconds. The prediction accuracy of the emulator is shown to be about 1% (5%) for the monopole (quadrupole) moments of the power spectrum for halos with a mass threshold $\sim 10^{13}\, h^{-1}\, M_{\odot}$, which are likely to host the galaxies targeted in the current galaxy redshift survey.

We demonstrated that we can combine the emulator outputs with the halo model formalism to obtain the model predictions for the redshift-space galaxy power spectrum for a galaxy sample of interest. Since our emulator outputs the redshift-space power spectrum as a function of (k, μ), instead of its multipole moments, it allows one to easily incorporate various anisotropic effects: the so-called Finger-of-God effects due to the random motions of galaxies inside host halos, the off-centering effects, and the Alcock Paczynski distortions, where these effects generally mix contributions of different multipole moments to a given multipole. As a working example, we used a halo occupation distribution (HOD) model calibrated for the SDSS-III galaxies to compute the redshift-space galaxy power spectra based on the halo emulator. We showed that the emulator predictions well match the power spectra measured from the simulation-based mock catalogs that are generated using the same HOD and the same spatial and velocity distributions of galaxies inside halos. Our emulator can compute the galaxy power spectrum in $\mathcal{O}(0.1)$ CPU seconds, which corresponds to a huge reduction in the computation time compared to the full N-body simulations, which the emulator essentially reproduces.

Impact of the uncertainties in the halo-galaxy connection on cosmological constraints

In Chapter 6, we have studied the cosmological information content in the redshift-space power spectrum of galaxies over a range of wave number scales from the linear to quasi-nonlinear regimes. Using simulation-based mock galaxy catalogs, we studied how changes in cosmological parameters and the halo-galaxy connection parameters alter the redshift-space power spectrum of galaxies. Rather than galaxies whose formation and evolution processes remain uncertain, the redshift-space power spectrum of halos hosting the galaxies should carry the cosmological information accessible with our current knowledge. We presented theoretical forecasts on cosmological parameter constraints from the HOD galaxy power spectrum, using the Fisher information matrix. We studied how the power spectrum of SDSS-like galaxies can be used to constrain the cosmological parameters (Ω_m and σ_8) and the cosmological distances (D_A and H), even after marginalization over the halo-galaxy connection parameters.

We have seen that varying the cosmological parameters and the cosmological distances via the AP effect leads to characteristic variations in the monopole and quadrupole moments of galaxy power spectrum on scales $k \leq 0.3\ h\,\mathrm{Mpc}^{-1}$(Fig. 6.5). In particular, we found that the Baryon Acoustic Oscillation (BAO) features are quite useful to obtain robust measurements of the angular and radial cosmological distances D_A and H, even in the presence of uncertainties in the halo-galaxy connection (Fig. 6.8). Compared to this, the parameters $(\Omega_\mathrm{m}, \sigma_8)$, which control the amplitude of redshift-space power spectrum and the RSD strength, are more strongly affected by the halo-galaxy connection parameters, but the constraints can be improved by including the redshift-space power spectrum information on quasi-nonlinear scales up to $k_\mathrm{max} = 0.3\ h\,\mathrm{Mpc}^{-1}$. Though the signal-to-noise ratio of the quadrupole moment is smaller than that of the monopole moment by up to a factor of 100, the quadrupole moment has the sensitivity to cosmological parameters comparable to that of the monopole. By combining the two we can improve the cosmological constraints, mitigating the impact of halo-galaxy connection parameters. Our results imply that combining the monopole and quadrupole moments allows for a *self-calibration* of cosmological parameters, lifting the degeneracies among the cosmological and nuisance parameters, to some extent.

A uniqueness of the redshift-space power spectrum, compared to other large-scale structure probes, is that the anisotropic features allow one to measure the cosmological distances (also via the BAO peaks) as well as the RSD effect. Here the RSD effect is expected to be a powerful probe of the gravity theory on cosmological scales. We have also addressed this issue. By introducing a parameter $f_{\rm RSD}$ to control the amplitude of the RSD effect of halos hosting galaxies in the mocks, we assessed the power of the redshift-space power spectrum for making a model-independent estimation of the RSD parameter together with the distance parameters $D_{\rm A}$ and H. With this parameterization, the constraint on $f_{\rm RSD}$ comes purely from the anisotropic features in the redshift-space power spectrum, because it does not alter the real-space power spectrum. We found that the fractional accuracy of $f_{\rm RSD}$, corresponding to the fractional error of $f\sigma_8$ in the linear regime, is about 10% if we include the redshift-space power spectrum up to $k_{\rm max} = 0.3\ h\,{\rm Mpc}^{-1}$, after marginalization over the halo-galaxy connection parameters and uncertainties in the FoG effect due to virial motions of galaxies in their host halos. Our forecast might be considered as a conservative forecast, but generally implies that there are severe degeneracies between the RSD effect and the systematics due to the halo-galaxy connection.

Cosmological analysis on the SDSS-III galaxy catalog

As one of the main results of this thesis, we applied our theoretical model based on the emulator combining with halo model formalism to the cosmological parameter inference on the observed galaxy power spectrum. We used the redshift-space galaxy power spectrum from the completed SDSS-III BOSS Final Data Release galaxy catalog, which contains over 1,000,000 luminous red galaxies over the redshift range $0.2 < z < 0.75$, in total of North and South sky regions. We split the catalogs into three overlapping redshift bins, and measured the monopole, quadrupole, and hexadecapole moments of power spectrum from each redshift bin and sky region (North or South). Likewise, we also measured the covariance matrix of the power spectrum multipoles, using 2048 realizations of the MultiDark-Patchy mock galaxy catalogs.

On these measured power spectrum signals, we performed the cosmological parameter inference based on our emulator-based theoretical template, within the flat ΛCDM cosmology. Our main aim is to see how well we can estimate the cosmological parameters from the redshift-space galaxy power spectrum, on quasi-nonlinear scales up to $k_{\rm max} = 0.2$ or $0.3\,h\,{\rm Mpc}^{-1}$, for which our emulator-based theoretical template is fully valid at the level of halos.

Our approach includes various nuisance parameters phenomenologically describing the halo-galaxy connection, which is the main theoretical uncertainty. To see whether our method can robustly measure the cosmological parameters, we first tested the method using simulation-based mock galaxy catalogs. We prepared mock catalogs with different settings: the HOD-based mock catalogs with and without the off-centering effect (which causes the significant difference in the reshift-space power spectrum), and the MultiDark-Patchy mock catalogs. For two HOD-based mocks, our method successfully recovered the input cosmology, for both the cases of using the signals up to $k_{\rm max} = 0.2$ and $0.3\,h\,{\rm Mpc}^{-1}$. For MultiDark-Patchy mock catalogs, our method recovers the input cosmology in the $k_{\rm max} = 0.2\,h\,{\rm Mpc}^{-1}$ case, but in the $k_{\rm max} = 0.3\,h\,{\rm Mpc}^{-1}$ case, the estimation of $A_{\rm s}$ and σ_8 tend to present lower values. The issue of robustness of the parameter estimation should be further discussed using more various mock catalogs as a future work.

After the tests using the mock catalogs with different recipes to populate galaxies, we performed the cosmological parameter inferences on the real survey data, and see that our emulator-based method can present the reasonable cosmological parameter constraint, compared to the another analysis based on the perturbation theory-based theoretical model.

This is the first attempt in the world to measure the cosmological parameters from the redshift-space galaxy clustering based on the N-body simulation-based emulator. The method developed in this thesis should be useful for upcoming surveys such as the Subaru Prime Focus Spectrograph, Dark Energy Survey Instrument, *Euclid*, and Roman Space Telescope.

Future works

The emulator-based cosmological analysis of galaxy surveys is still a very premature method. The most important problem which should be investigated in the future works is the systematics on the cosmological parameter inference. As we mentioned in Sec. 7.7, our approach using the halo emulator and halo model formalism leads to the restrictive theoretical model prediction in the sense that it does not completely cover the all the possibility on how the galaxies targeted in galaxy redshift surveys reside in their host halos, including the correlation with the halo assembly bias. This fact can leads to the theoretical systematics which prevent us to unbiasedly estimate the cosmological parameters, even if we marginalize a lot of parameters which model the halo-galaxy connection. While it is highly difficult to perfectly resolve this issue, the state-of-the-art method to evaluate the robustness of the parameter inference is to test the analysis pipeline on the galaxy mock catalogs with different recipes to populate galaxies inside halos. As an immediate future work, we will need more detailed investigations on the parameter estimation bias, using further different mock catalogs, in particular the assembly bias mocks.

In this thesis, we show only the result for each redshift and sky region, and we do not present the combined results of different redshifts and sky regions. To obtain the stringent constraints of the cosmological parameters which are shared over different redshifts, combining the data in different redshift bins is highly essential. This is also our future work after the dissertation.

From the observation side, the influence of the fiber collision can become problematic. This effect correlates with the galaxy clustering and becomes severer on larger-k scales. Hence, when we try to use the large-k signals at e.g., $k \simeq 0.3\,h\,{\rm Mpc}$, we will need to properly handle this observational systematics, also possibly by using the mock catalogs with such a systematics.

Appendix

1 A resolution study on the power spectrum measurement

In Sec. 5.3.2, we described our settings used in measurements of the redshift-space power spectrum of halos that were in turn used as the datasets of emulator building. In this appendix, we present a resolution study in the power spectrum measurement.

First, we study how the grid assignment we used affects the power spectrum measurement. For this purpose we use the Dark Quest HR simulations, which have a box size of 1 h^{-1}Gpc, a halved size of our default simulations of 2 h^{-1} Gpc. Figure 1 compares the multipole moments of halo power spectrum using the CIC assignment with different number of grids: 512^3 grids and 1024^3, respectively. Here the former has the same Nyquist frequency in the FFT computation as that of our default setting (2 h^{-1} Gpc plus 1024^3). For both cases we use the interlacing scheme for the aliasing mitigation. Here we consider the auto power spectrum for two samples of halos with number densities, $n_\mathrm{h} = 10^{-3}$ and $10^{-4}\,(h^{-1}\,\mathrm{Mpc})^{-3}$, respectively, at $z = 0$ for the *Planck* cosmology. The error bars represent standard deviation among the 15 realizations. Although the systematics due to the grid assignment is below the errors for the quadrupole and tetra-hexadecapole ($\ell = 6$) moments, it significantly affects the monopole and hexadecapole moments at $k \gtrsim 0.7$ or $0.8\,h\,\mathrm{Mpc}^{-1}$. In this paper we use the power spectrum data at $k < 0.61\,h\,\mathrm{Mpc}^{-1}$ for the emulator construction, and in this range our default setting accurately estimates the multipole moments with the precision better than the statistical errors. Hence we conclude that the FFT resolution does not affect our emulator construction.

Second, we study the impact of a finite k binning in the power spectrum measurements. There is a trade-off in a choice of the bin width. For a finner bin width, the band power measurement in each k bin becomes noisier due to a smaller number of the Fourier modes, but it can well capture features in the power spectrum. For a wider bin width, the measurement becomes less noisy but might erase or smooth features in the power spectrum. For our emulator construction, we need less noisy datasets to avoid any failure of the machine learning due to too large sample variance. For this reason, we adopt the k-bin width $\Delta k = 0.02\,h\,\mathrm{Mpc}^{-1}$, although the analyses using the current-generation galaxy redshift surveys usually employ $\Delta k \simeq 0.01\,h\,\mathrm{Mpc}^{-1}$ for the k-bin width [18]. Hence it is important to check the effect of our binning on the power spectrum measurement. In Fig. 2, we compare the power spectrum measured with two different bin widths $\Delta k = 0.01$ and $0.02\,h\,\mathrm{Mpc}^{-1}$, respectively. In the upper panel, the solid line represents the spline interpolation of the power

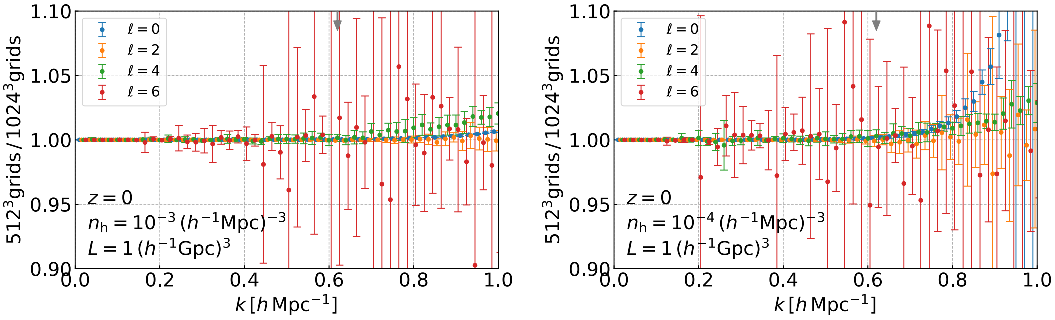

Figure 1: The effect of the FFT grid assignment on the multipole moments of halo power spectrum measured from the simulations. We compare four multipole moments of degrees $\ell = 0$, 2, 4, and 6 for the *Planck* cosmology, between the CIC assignments on 512^3 grids and on 1024^3 grids, respectively. Since we measure from the Dark Quest HR simulations with box size of $1\,h^{-1}\,\mathrm{Gpc}$, the Nyquist wave number for each setting is 1.61 and $3.22\,h\,\mathrm{Mpc}^{-1}$, respectively. The former FFT resolution is equivalent to our fiducial setting we used for the main results of this paper. The gray arrow in the upper horizontal axis indicates the maximum wave number of data, $k_{\max} = 0.61\,h\,\mathrm{Mpc}^{-1}$, which we adopt to construct the emulator.

spectrum measured at $\Delta k = 0.02\,h\,\mathrm{Mpc}^{-1}$, while the symbols are that measured at $\Delta k = 0.01\,h\,\mathrm{Mpc}^{-1}$ for the multipole moment of each order. The error bars show the variances among 15 realizations of the *Planck* cosmology. Over all the k range we are interested in, the power spectrum measured with finner bins shows almost no significant discrepancy from the case of the wider bins. A caveat is that the wider binning slightly smears out the BAO features. However, the primary purpose of this work is to accurately model the nonlinear clustering effects and the RSD effect in the redshift-space power spectrum, so we most care about an unbiased measurement of the power spectrum amplitudes. Thus, Fig. 2 shows that our binning scheme well captures the amplitudes of the multipole moments, with the precision better than the statistical errors, up to $k \simeq 0.7\ h\,\mathrm{Mpc}^{-1}$. Hence, we conclude that our choice $\Delta k = 0.02\,h\,\mathrm{Mpc}^{-1}$ meets the requirements.

2 Multiplication of the cross power spectrum of halos?

In our emulator, we choose to work on the power spectrum of halos with different number densities (masses): $P^{\mathrm{S}}_{\mathrm{hh}}(\mathbf{k}; n_1, n_2)$. In linear theory, the redshift-space power spectrum between halos with mass M_1 and M_2 can be expressed in the multiplicative form as

$$P^{\mathrm{S}}_{\mathrm{hh,lin}}(k, \mu; M_1, M_2) = \left[b_{\mathrm{h}}(M_1) + f\mu^2\right]\left[b_{\mathrm{h}}(M_2) + f\mu^2\right] P_{\mathrm{lin}}(k), \tag{1}$$

where $b_{\mathrm{h}}(M)$ is the linear bias of halos with mass M. The standard halo model also assumes that the two-halo term of the halo power spectrum is given by such

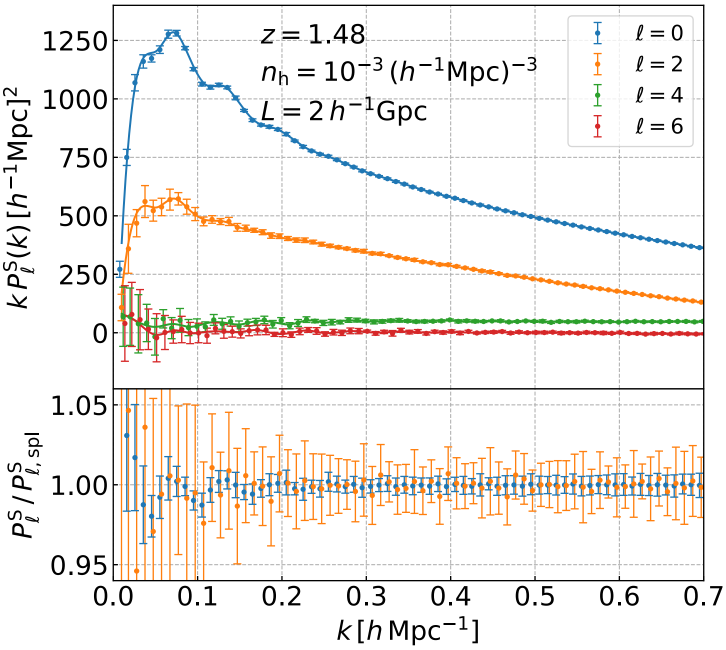

Figure 2: Effects of the k-bin width on the multipole moments (up to $\ell = 6$) of halo power spectrum. The symbols with error bars are the multipole moments measured using the bin width $\Delta k = 0.01\,h\,\mathrm{Mpc}^{-1}$. The solid lines are the results obtained by the spline interpolations of the moments using the bin width $\Delta k = 0.02\,h\,\mathrm{Mpc}^{-1}$. The error bars are estimated from the standard deviation among the 15 realizations of Dark Quest LR simulations (2 h^{-1}Gpc on a side) for the *Planck* cosmology.

a multiplicative form as $P^{\rm 2h}_{\rm hh}(k; M_1, M_2) = b(M_1)b(M_2)P^{\rm L}_{\rm hh}(k)$ [139, 140]. From this consideration, one might ask whether the power spectrum of halos in different mass bins can be approximated by the multiplicative form as

$$P^{\rm S}_{\rm hh,lin}(k, \mu; M_1, M_2) = \sqrt{P^{\rm S}_{\rm hh,lin}(k, \mu; M_1)P^{\rm S}_{\rm hh,lin}(k, \mu; M_2)}. \tag{2}$$

If the above approximation or ansatz was valid at nonlinear scales for all the halo mass range, it would be sufficient to study the auto power spectrum of halos in a single mass bin, which reduces the efforts and difficulty of the emulator development. Here we study whether the above ansatz is valid using the simulations.

In Fig. 3, we investigate a validity of the ansatz, Eq. (2). To this, we study the cross-correlation coefficient between the monopole moments of the redshift-space power spectrum for the halo samples of two number densities,

$$\frac{P^{\rm S}_{\rm hh,0}(k; n_1, n_2)}{\sqrt{P^{\rm S}_{\rm hh,0}(k; n_1)P^{\rm S}_{\rm hh,0}(k; n_2)}} \tag{3}$$

for the *Planck* cosmology at $z = 0$. We consider the cases of $n_2 = 10^{-3.5}, 10^{-4}, 10^{-4.5}$, and $10^{-5}\,(h^{-1}\,{\rm Mpc})^{-3}$, while keeping n_1 fixed to $10^{-3}\,(h^{-1}\,{\rm Mpc})^{-3}$. Note that the halo sample of n_2 is a subsample of the sample of n_1, and we subtracted the shot noise from each power spectrum in the numerator and the denominator. The figure clearly shows that the ansatz, Eq. (2), does not hold at nonlinear scales. As an overlap between the two samples decreases (the differences between n_1 and n_2 get larger), a deviation of the cross-correlation coefficient from unity becomes greater and starts from smaller k bins. With the results in this figure, we conclude that it is indispensable to use the halo power spectrum of two number density bins for the emulator construction.

3 An optimal choice of the number of hidden units in the neural network training

In our network architecture, we employed two hidden layers to give a large flexibility to the nonlinear mapping from the nine-dimensional input vector to the output power spectrum. The main factor which handles the model flexibility of neural network is the number of hidden units (hereafter, we call it as $N_{\rm hidden}$). We executed the following study to make an appropriate choice of $N_{\rm hidden}$ in our neural network.

Figure 4 shows how the loss function values after the training vary with $N_{\rm hidden}$. We employ the equal $N_{\rm hidden}$ for both the two hidden layers, and run the training for 1000 epochs as we described in Sec. 5.3.4, for the different $N_{\rm hidden}$ in the range of [20,1000]. In addition, to measure the goodness of choice of $N_{\rm hidden}$ in our network including its possible uncertainty due to the variations of dataset, we change the split of training/validation datasets; since we have five slices (slice 1–5) in the DARK QUEST

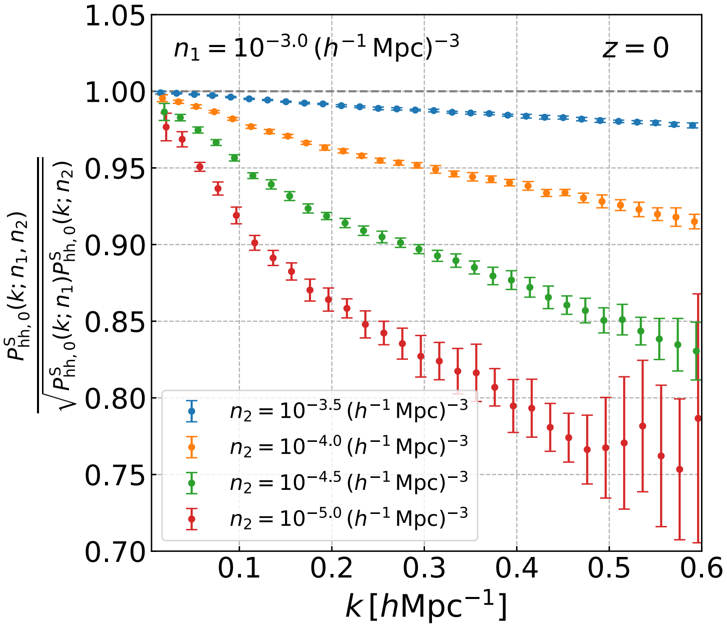

Figure 3: A test of multiplication of the redshift-space halo power spectrum; whether does the multiplication [Eq. (2)] hold? This identify holds for the linear theory prediction with the Kaiser RSD effect. If the above identity holds, the cross-correlation coefficients in the y axis should be unity. Here we consider the case that one halo sample has a fixed number density of $n_1 = 10^{-3}\,(h^{-1}\,\mathrm{Mpc})^{-3}$, and the other sample has varying number densities, n_2 to be $10^{-3.5}$ (blue), 10^{-4} (orange), $10^{-4.5}$ (green) and 10^{-5} (red) $(h^{-1}\,\mathrm{Mpc})^{-3}$, respectively. The error bars are the standard deviation among the 15 realizations for the *Planck* cosmology.

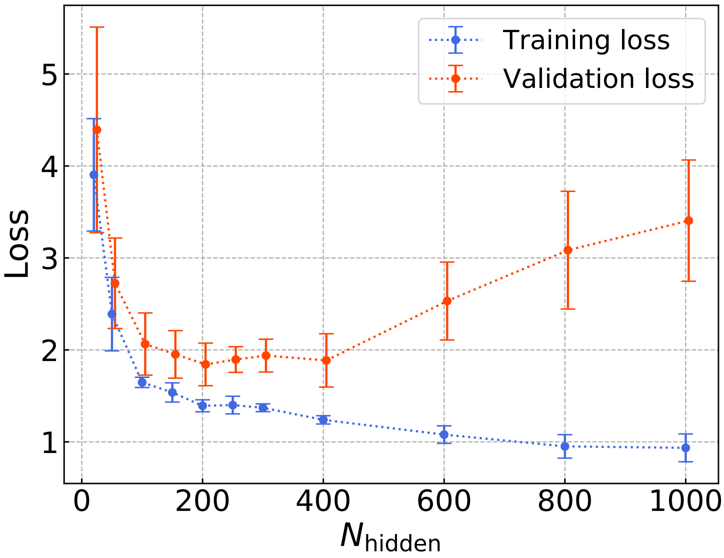

Figure 4: Shown is how the value of the loss function [Eq. (5.11)] after the training for 1000 epochs varies with the number of hidden units, N_{hidden}. Blue and red symbols with error bars are the training and validation loss, respectively. The error bars are the standard deviation among five different choices of the training/validation split (see text).

simulation suite, we can consider five different choices of the training/validation split, by choosing one of them as the validation set and remaining four slices as the training set. In this figure, we show the mean and standard deviation of the final loss function values among the five choices of the training/validation split, for each of the training (blue) and validation (red) losses. Note that, when we calculated the final training or validation loss, we followed the definition of Eq. (5.11), except that we averaged over the whole training or validation dataset, respectively.

The training loss decreases almost monotonically with the increase of N_{hidden}, because the enhanced flexibility of the neural network enables better fittings to the training dataset. However, this is not the case in the validation loss. When N_{hidden} is low, the validation loss decreases with the increase of N_{hidden}, similarly to the training loss. However, as we increase N_{hidden} more than about 400, the validation loss also increases, which leads to a worse emulation performance. It is due to that the neural network has too large flexibility to properly generalize to the validation data. Since our goal is to construct an emulator that can predict not only the training dataset but also the power spectrum for new inputs, we need to suppress the validation loss and avoid such an overfitting. The validation loss becomes the lowest when $N_{\mathrm{hidden}} \sim 200$. We use this value as an optimal choice of N_{hidden} for our emulator construction.

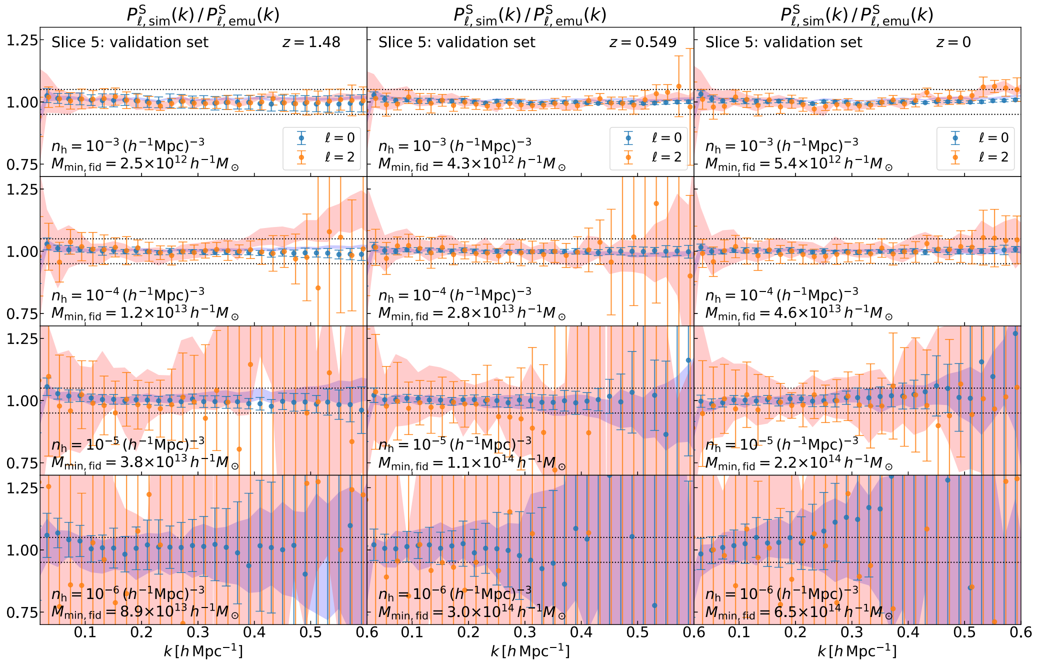

Figure 5: The accuracy of the emulator predictions for different values of halo number density. We focus on the cases of $n_1 = n_2 = n_\mathrm{h}$ presented in each subplots. The second row is identical to the lower panels in Fig. 5.6.

4 Dependence of the emulator accuracy on the halo number density

In this appendix, we study the accuracy/performance of the emulator predictions for other halo samples which we did not consider in the main text. Figures 5 and 6 show how the emulator accuracies for the monopole and quadrupole moments with the different halo samples. In Fig. 5 we show the results for the power spectrum of the single number density bin, n_h, where $n_\mathrm{h} = 10^{-3}, 10^{-4}, 10^{-5}$, and $10^{-6}\,(h^{-1}\,\mathrm{Mpc})^{-3}$, respectively. Due to the severe shot noise, the accuracy for the low number density such as $n_\mathrm{h} = 10^{-6}\,(h^{-1}\,\mathrm{Mpc})^{-3}$ is much worse than that for the higher number density sample. However, for each value of n_h, the discrepancies are roughly comparable to the variance estimated from 15 realizations for the fiducial *Planck* cosmology, indicated by shaded regions. This indicates that the training of the neural network reaches the limit determined from the noise levels of the training data. The same tendency is also presented in Fig. 6, which shows the cases in which n_1 and n_2 are different.

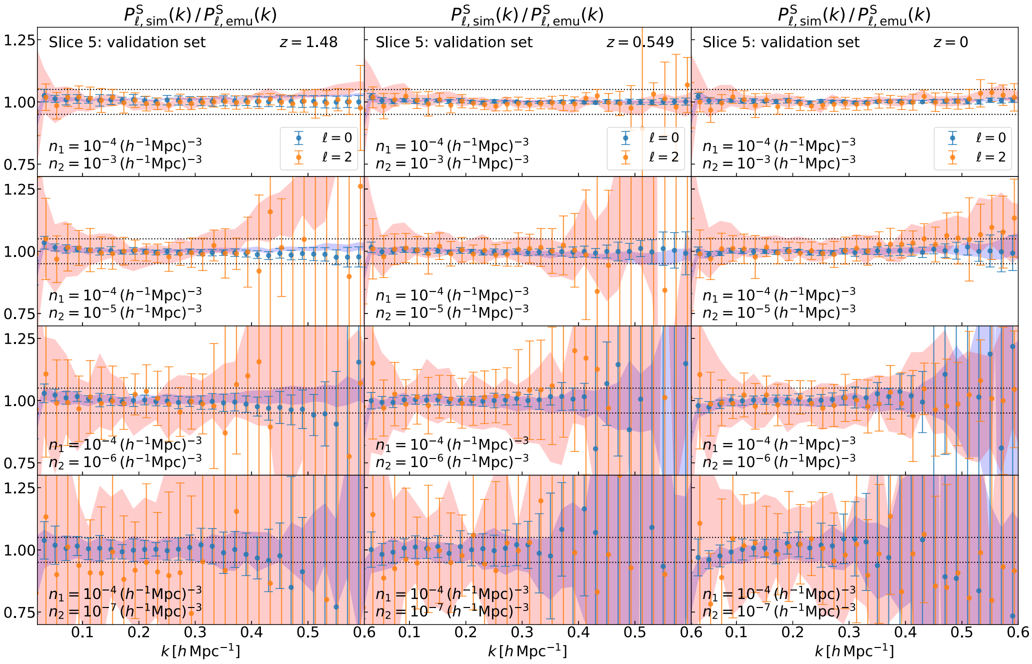

Figure 6: The same as Fig. 5, but we show the cases of $n_1 \neq n_2$.

5 Comparison of responses with simple theoretical prescriptions

In this paper we execute a Fisher matrix analysis using the response of the redshift-space power spectrum with respect to various parameters. For completeness, in this appendix we compare the estimation of these responses from our simulation-based galaxy mocks with their predictions based on the linear theory and the halo model formalism, which is presented in Eqs. (3.41) and (3.42). We predict the responses following two simple models.

(i) *The HOD power spectrum combined with the FoG damping* – Following Eqs. (3.41) and (3.42), we compute the real-space galaxy power spectrum based on the halo power spectrum, a NFW radial profile of galaxies and the HOD defined by Eqs. (**??**) and (**??**). The halo power spectrum is computed from the linear matter power spectrum and the large-scale halo bias $b_{\rm h}(M)$. To model the redshift-space distortions, we employ the well-known Kaiser's effect and the FoG damping factor:

$$P^{\rm S}_{\rm gg}(k,\mu) = \left(1+\beta\mu^2\right)^2 P^{\rm R}_{\rm gg}(k) D_{\rm FoG}(k\mu f\sigma_{\rm v}), \tag{4}$$

where $\beta = f/b_{\rm g}$ and $\sigma_{\rm v}$ is the parameter which represents the velocity dispersion of the virial velocities. For the FoG damping we assume the broadly-used Gaussian form, i.e., $D_{\rm FoG}(k\mu f\sigma_{\rm v}) = e^{-k^2\mu^2 f^2\sigma_{\rm v}^2}$, and we compute $\sigma_{\rm v}$ by simply using the linear theory expression:

$$\sigma^2_{\mathrm{v,lin}} = \frac{1}{3}\int \frac{\mathrm{d}^3q}{(2\pi)^3}\frac{P_{\mathrm{lin}}(q)}{q^2}. \tag{5}$$

(ii) *The linear power spectrum with the linear galaxy bias* – We compute the galaxy power spectrum following Kaiser's formula from the linear matter power spectrum and the linear galaxy bias. Note that the HOD parameters affect only on this galaxy bias in this model.

In both models above, we use the linear galaxy bias b_{g} given as

$$b_{\mathrm{g}} = \int \mathrm{d}M\ \frac{\mathrm{d}n}{\mathrm{d}M}\left[\langle N_{\mathrm{c}}\rangle(M) + \langle N_{\mathrm{s}}\rangle(M)\right] b_{\mathrm{h}}(M), \tag{6}$$

where $b_{\mathrm{h}}(M)$ is the linear halo bias. To compute the halo mass function and the linear halo bias in these models for an input cosmology, we employ Dark Emulator in Ref. [?]. Since the parameters to model the spatial and velocity distributions of galaxies in their host halos, c_{conc}, c_{vel}, p_{off} and $\mathcal{R}_{\mathrm{off}}$, are difficult to include in the linear theory prediction, we focus only on the cosmological and HOD parameters here.

Fig. 7 shows the comparison of the parameter responses measured from mocks to these two models. The three columns show the results for LOWZ, CMASS1 or CMASS2-like galaxies, respectively. The filled symbols are the measured responses with respect to each parameter, and the solid and dashed lines are the predictions given by the models (i) and (ii) described above, respectively. We see that behaviors of these responses at highly large scales are well described by both models, and the model (i) has a slightly better performance on reproducing the responses to the cosmological parameters than the simplest linear theory prediction (ii). However, the modification included in the model (i) gives little improvements on reproducing the HOD-responses. This means that the model (i) is still too naive to capture these behaviors and hence we must employ more complicated models in analyzing the galaxy power spectrum in the current galaxy surveys.

6 Fisher forecasts on cosmological parameters using the nuisance parameter set in Chapter 7

In this appendix, we present the Fisher matrix forecasts on the cosmological parameters $\{\Omega_{\mathrm{m}},\ \sigma_8\}$, when we use the same set of nuisance parameters used in the cosmological analysis described in Chapter 7. In Chapter 7, we reduce the number of nuisance parameters from the set used in Chapter 6, by fixing three parameters; $p_{\mathrm{off}}, \mathcal{R}_{\mathrm{off}}$, which handle the off-centering effect, and c_{conc}, the multiplicative factor on the mass-concentration relation.

Fig. 8 shows the Fisher matrix forecast on $\Omega_{\rm m}$ and σ_8 we investigated in Chapter 6. As in Chapter 7, we focus on the cosmological parameter constraints in the concordance ΛCDM framework. The solid-line contours correspond to the results in which we use the same set of nuisance parameters as used in the cosmology inference in Chapter 7. The dashed-line contours are the same as those we showed in Chapter 6. There is an only marginal deference between these two, especially for the case that the monopole and quadrupole moments are combined.

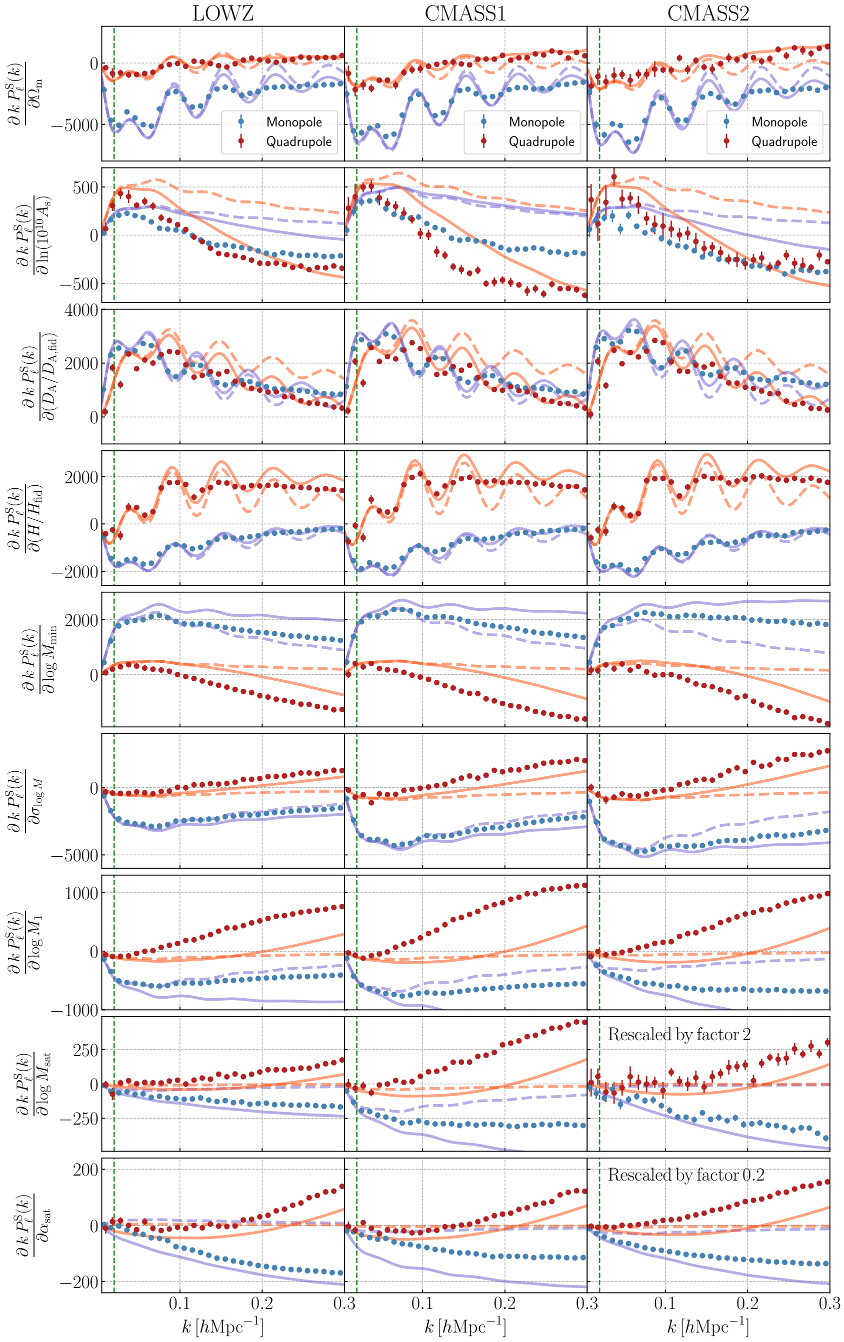

Figure 7: The comparison of the derivatives of the power spectrum computed from the SDSS-like galaxy mocks to the predictions by two simple models (see text for details). We compare the derivatives with respect to Ω_m, $\ln(10^{10}A_s)$, $D_A(z_n)$, $H(z_n)$ and five HOD parameters with the corresponding theoretical predictions. Blue and red lines are for the monopole and quadrupole moments, and the solid and dashed lines denote the model (i) and (ii), respectively. The green, vertical dashed line indicates the scale $k = 0.02$ $h\,\mathrm{Mpc}^{-1}$, which is adopted as the minimum wavenumber $k_{\min}$ in all the Fisher calculations in this study.

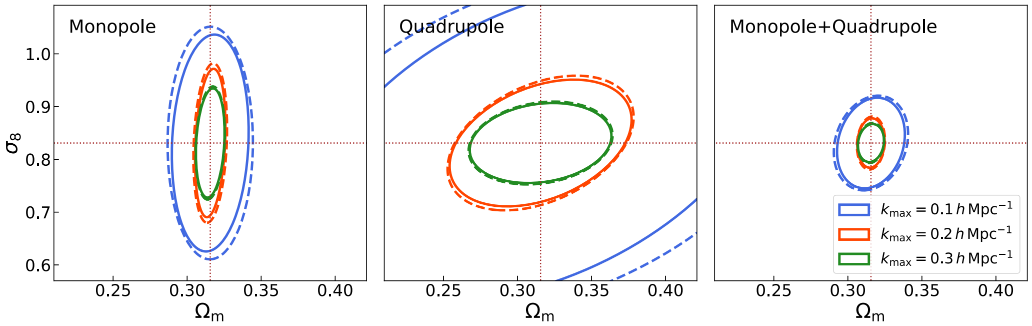

Figure 8: The 68% error ellipse on Ω_m and σ_8 for the flat ΛCDM framework. The solid-line contours are the error ellipses when we marginalize the nuisance parameters we used in Chapter 7. The dashed-line contours are the same as those in Fig. 6.11.

Bibliography

[1] J. P. Huchra, M. J. Geller, V. de Lapparent, and R. Burg. The CFA Redshift Survey. In J. Audouze, M. C. Pelletan, A. Szalay, Ya. B. Zel'dovich, and P. J. E. Peebles, editors, *Large Scale Structures of the Universe*, volume 130, page 105, January 1988.

[2] Kyle S. Dawson, David J. Schlegel, Christopher P. Ahn, Scott F. Anderson, Éric Aubourg, Stephen Bailey, Robert H. Barkhouser, Julian E. Bautista, Alessand ra Beifiori, Andreas A. Berlind, Vaishali Bhardwaj, Dmitry Bizyaev, Cullen H. Blake, Michael R. Blanton, Michael Blomqvist, Adam S. Bolton, Arnaud Borde, Jo Bovy, W. N. Brandt, Howard Brewington, Jon Brinkmann, Peter J. Brown, Joel R. Brownstein, Kevin Bundy, N. G. Busca, William Carithers, Aurelio R. Carnero, Michael A. Carr, Yanmei Chen, Johan Comparat, Natalia Connolly, Frances Cope, Rupert A. C. Croft, Antonio J. Cuesta, Luiz N. da Costa, James R. A. Davenport, Timothée Delubac, Roland de Putter, Saurav Dhital, Anne Ealet, Garrett L. Ebelke, Daniel J. Eisenstein, S. Escoffier, Xiaohui Fan, N. Filiz Ak, Hayley Finley, Andreu Font-Ribera, R. Génova-Santos, James E. Gunn, Hong Guo, Daryl Haggard, Patrick B. Hall, Jean-Christophe Hamilton, Ben Harris, David W. Harris, Shirley Ho, David W. Hogg, Diana Holder, Klaus Honscheid, Joe Huehnerhoff, Beatrice Jordan, Wendell P. Jordan, Guinevere Kauffmann, Eyal A. Kazin, David Kirkby, Mark A. Klaene, Jean-Paul Kneib, Jean-Marc Le Goff, Khee-Gan Lee, Daniel C. Long, Craig P. Loomis, Britt Lundgren, Robert H. Lupton, Marcio A. G. Maia, Martin Makler, Elena Malanushenko, Viktor Malanushenko, Rachel Mandelbaum, Marc Manera, Claudia Maraston, Daniel Margala, Karen L. Masters, Cameron K. McBride, Patrick McDonald, Ian D. McGreer, Richard G. McMahon, Olga Mena, Jordi Miralda-Escudé, Antonio D. Montero-Dorta, Francesco Montesano, Demitri Muna, Adam D. Myers, Tracy Naugle, Robert C. Nichol, Pasquier Noterdaeme, Sebastián E. Nuza, Matthew D. Olmstead, Audrey Oravetz, Daniel J. Oravetz, Russell Owen, Nikhil Padmanabhan, Nathalie Palanque-Delabrouille, Kaike Pan, John K. Parejko, Isabelle Pâris, Will J. Percival, Ismael Pérez-Fournon, Ignasi Pérez-Ràfols, Patrick Petitjean, Robert Pfaffenberger, Janine Pforr, Matthew M. Pieri, Francisco Prada, Adrian M. Price-Whelan, M. Jordan Raddick, Rafael Rebolo, James Rich, Gordon T. Richards, Constance M. Rockosi, Natalie A. Roe, Ashley J. Ross, Nicholas P. Ross, Graziano Rossi, J. A. Rubiño-Martin, Lado Samushia, Ariel G. Sánchez, Conor Sayres, Sarah J. Schmidt, Donald P. Schneider, C. G. Scóccola, Hee-

Jong Seo, Alaina Shelden, Erin Sheldon, Yue Shen, Yiping Shu, Anže Slosar, Stephen A. Smee, Stephanie A. Snedden, Fritz Stauffer, Oliver Steele, Michael A. Strauss, Alina Streblyanska, Nao Suzuki, Molly E. C. Swanson, Tomer Tal, Masayuki Tanaka, Daniel Thomas, Jeremy L. Tinker, Rita Tojeiro, Christy A. Tremonti, M. Vargas Magaña, Licia Verde, Matteo Viel, David A. Wake, Mike Watson, Benjamin A. Weaver, David H. Weinberg, Benjamin J. Weiner, Andrew A. West, Martin White, W. M. Wood-Vasey, Christophe Yeche, Idit Zehavi, Gong-Bo Zhao, and Zheng Zheng. The Baryon Oscillation Spectroscopic Survey of SDSS-III. *The Astronomical Journal*, 145:10, Jan 2013.

[3] Kyle S. Dawson, Jean-Paul Kneib, Will J. Percival, Shadab Alam, Franco D. Albareti, Scott F. Anderson, Eric Armengaud, Éric Aubourg, Stephen Bailey, Julian E. Bautista, Andreas A. Berlind, Matthew A. Bershady, Florian Beutler, Dmitry Bizyaev, Michael R. Blanton, Michael Blomqvist, Adam S. Bolton, Jo Bovy, W. N. Brandt, Jon Brinkmann, Joel R. Brownstein, Etienne Burtin, N. G. Busca, Zheng Cai, Chia-Hsun Chuang, Nicolas Clerc, Johan Comparat, Frances Cope, Rupert A. C. Croft, Irene Cruz-Gonzalez, Luiz N. da Costa, Marie-Claude Cousinou, Jeremy Darling, Axel de la Macorra, Sylvain de la Torre, Timothée Delubac, Hélion du Mas des Bourboux, Tom Dwelly, Anne Ealet, Daniel J. Eisenstein, Michael Eracleous, S. Escoffier, Xiaohui Fan, Alexis Finoguenov, Andreu Font-Ribera, Peter Frinchaboy, Patrick Gaulme, Antonis Georgakakis, Paul Green, Hong Guo, Julien Guy, Shirley Ho, Diana Holder, Joe Huehnerhoff, Timothy Hutchinson, Yipeng Jing, Eric Jullo, Vikrant Kamble, Karen Kinemuchi, David Kirkby, Francisco-Shu Kitaura, Mark A. Klaene, Russ R. Laher, Dustin Lang, Pierre Laurent, Jean-Marc Le Goff, Cheng Li, Yu Liang, Marcos Lima, Qiufan Lin, Weipeng Lin, Yen-Ting Lin, Daniel C. Long, Britt Lundgren, Nicholas MacDonald, Marcio Antonio Geimba Maia, Elena Malanushenko, Viktor Malanushenko, Vivek Mariappan, Cameron K. McBride, Ian D. McGreer, Brice Ménard, Andrea Merloni, Andres Meza, Antonio D. Montero-Dorta, Demitri Muna, Adam D. Myers, Kirpal Nandra, Tracy Naugle, Jeffrey A. Newman, Pasquier Noterdaeme, Peter Nugent, Ricardo Ogando, Matthew D. Olmstead, Audrey Oravetz, Daniel J. Oravetz, Nikhil Padmanabhan, Nathalie Palanque-Delabrouille, Kaike Pan, John K. Parejko, Isabelle Pâris, John A. Peacock, Patrick Petitjean, Matthew M. Pieri, Alice Pisani, Francisco Prada, Abhishek Prakash, Anand Raichoor, Beth Reid, James Rich, Jethro Ridl, Sergio Rodriguez-Torres, Aurelio Carnero Rosell, Ashley J. Ross, Graziano Rossi, John Ruan, Mara Salvato, Conor Sayres, Donald P. Schneider, David J. Schlegel, Uros Seljak, Hee-Jong Seo, Branimir Sesar, Sarah Shandera, Yiping Shu, Anže Slosar, Flavia Sobreira, Alina Streblyanska, Nao Suzuki, Donna Taylor, Charling Tao, Jeremy L. Tinker, Rita Tojeiro, Mariana Vargas-Magaña, Yuting Wang, Benjamin A. Weaver, David H. Weinberg, Martin White, W. M. Wood-Vasey, Christophe Yeche, Zhongxu Zhai, Cheng

Zhao, Gong-bo Zhao, Zheng Zheng, Guangtun Ben Zhu, and Hu Zou. The SDSS-IV Extended Baryon Oscillation Spectroscopic Survey: Overview and Early Data. *The Astronomical Journal*, 151(2):44, Feb 2016.

[4] M. Takada, R. S. Ellis, M. Chiba, J. E. Greene, H. Aihara, N. Arimoto, K. Bundy, J. Cohen, O. Doré, G. Graves, J. E. Gunn, T. Heckman, C. M. Hirata, P. Ho, J.-P. Kneib, O. Le Fèvre, L. Lin, S. More, H. Murayama, T. Nagao, M. Ouchi, M. Seiffert, J. D. Silverman, L. Sodré, D. N. Spergel, M. A. Strauss, H. Sugai, Y. Suto, H. Takami, and R. Wyse. Extragalactic science, cosmology, and Galactic archaeology with the Subaru Prime Focus Spectrograph. *Publications of the Astronomical Society of Japan*, 66:R1, February 2014.

[5] Amir Aghamousa et al. The DESI Experiment Part I: Science,Targeting, and Survey Design. 2016.

[6] R. Laureijs et al. Euclid Definition Study Report. 2011.

[7] Neil Gehrels and David N. Spergel. Wide-Field InfraRed Survey Telescope (WFIRST) Mission and Synergies with LISA and LIGO-Virgo. *Journal of Physics: Conference Series*, 610(1):012007, 2015.

[8] N. Kaiser. Clustering in real space and in redshift space. *Monthly Notices of the Royal Astronomical Society*, 227:1–21, July 1987.

[9] A. J. S. Hamilton. Measuring Omega and the Real Correlation Function from the Redshift Correlation Function. *The Astrophysical Journal Letters*, 385:L5, Jan 1992.

[10] A. J. S. Hamilton. Linear redshift distortions: A review. *The Evolving Universe*, page 185–275, 1998.

[11] F. Bernardeau, S. Colombi, E. Gaztañaga, and R. Scoccimarro. Large-scale structure of the Universe and cosmological perturbation theory. *Physics Reports*, 367:1–248, September 2002.

[12] V. Desjacques, D. Jeong, and F. Schmidt. Large-scale galaxy bias. *Physics Reports*, 733:1–193, February 2018.

[13] A. Taruya, T. Nishimichi, and S. Saito. Baryon acoustic oscillations in 2D: Modeling redshift-space power spectrum from perturbation theory. *Physical Review D*, 82(6):063522, September 2010.

[14] T. Nishimichi and A. Taruya. Baryon acoustic oscillations in 2D. II. Redshift-space halo clustering in N-body simulations. *Physical Review D*, 84(4):043526, August 2011.

[15] D. Baumann, A. Nicolis, L. Senatore, and M. Zaldarriaga. Cosmological non-linearities as an effective fluid. *Journal of Cosmology and Astroparticle Physics*, 7:51, July 2012.

[16] B. A. Reid, H.-J. Seo, A. Leauthaud, J. L. Tinker, and M. White. A 2.5 per cent measurement of the growth rate from small-scale redshift space clustering of SDSS-III CMASS galaxies. *Monthly Notices of the Royal Astronomical Society*, 444:476–502, October 2014.

[17] Florian Beutler, Shun Saito, Hee-Jong Seo, Jon Brinkmann, Kyle S. Dawson, Daniel J. Eisenstein, Andreu Font-Ribera, Shirley Ho, Cameron K. McBride, Francesco Montesano, Will J. Percival, Ashley J. Ross, Nicholas P. Ross, Lado Samushia, David J. Schlegel, Ariel G. Sánchez, Jeremy L. Tinker, and Benjamin A. Weaver. The clustering of galaxies in the SDSS-III Baryon Oscillation Spectroscopic Survey: testing gravity with redshift space distortions using the power spectrum multipoles. *Monthly Notices of the Royal Astronomical Society*, 443(2):1065–1089, 07 2014.

[18] Florian Beutler et al. The clustering of galaxies in the completed SDSS-III Baryon Oscillation Spectroscopic Survey: Anisotropic galaxy clustering in Fourier-space. *Monthly Notices of the Royal Astronomical Society*, 466(2):2242–2260, 2017.

[19] Shadab Alam, Metin Ata, Stephen Bailey, Florian Beutler, Dmitry Bizyaev, Jonathan A. Blazek, Adam S. Bolton, Joel R. Brownstein, Angela Burden, Chia-Hsun Chuang, Johan Comparat, Antonio J. Cuesta, Kyle S. Dawson, Daniel J. Eisenstein, Stephanie Escoffier, Héctor Gil-Marín, Jan Niklas Grieb, Nick Hand, Shirley Ho, Karen Kinemuchi, David Kirkby, Francisco Kitaura, Elena Malanushenko, Viktor Malanushenko, Claudia Maraston, Cameron K. McBride, Robert C. Nichol, Matthew D. Olmstead, Daniel Oravetz, Nikhil Padmanabhan, Nathalie Palanque-Delabrouille, Kaike Pan, Marcos Pellejero-Ibanez, Will J. Percival, Patrick Petitjean, Francisco Prada, Adrian M. Price-Whelan, Beth A. Reid, Sergio A. Rodríguez-Torres, Natalie A. Roe, Ashley J. Ross, Nicholas P. Ross, Graziano Rossi, Jose Alberto Rubiño-Martín, Shun Saito, Salvador Salazar-Albornoz, Lado Samushia, Ariel G. Sánchez, Siddharth Satpathy, David J. Schlegel, Donald P. Schneider, Claudia G. Scóccola, Hee-Jong Seo, Erin S. Sheldon, Audrey Simmons, Anže Slosar, Michael A. Strauss, Molly E. C. Swanson, Daniel Thomas, Jeremy L. Tinker, Rita Tojeiro, Mariana Vargas Magaña, Jose Alberto Vazquez, Licia Verde, David A. Wake, Yuting Wang, David H. Weinberg, Martin White, W. Michael Wood-Vasey, Christophe Yèche, Idit Zehavi, Zhongxu Zhai, and Gong-Bo Zhao. The clustering of galaxies in the completed SDSS-III Baryon Oscillation Spectroscopic Survey: cosmological analysis of the DR12 galaxy sample. *Monthly Notices of the Royal Astronomical Society*, 470(3):2617–2652, Sep 2017.

[20] Mikhail M. Ivanov, Marko Simonović, and Matias Zaldarriaga. Cosmological parameters from the boss galaxy power spectrum. *Journal of Cosmology and Astroparticle Physics*, 2020(05):042–042, May 2020.

[21] Guido d' Amico, Jérôme Gleyzes, Nickolas Kokron, Katarina Markovic, Leonardo Senatore, Pierre Zhang, Florian Beutler, and Héctor Gil-Marín. The cosmological analysis of the sdss/boss data from the effective field theory of large-scale structure. *Journal of Cosmology and Astroparticle Physics*, 2020(05):005–005, May 2020.

[22] Sebastián Pueblas and Román Scoccimarro. Generation of vorticity and velocity dispersion by orbit crossing. *Physical Review D*, 80(4), Aug 2009.

[23] D. Blas, M. Garny, and T. Konstandin. Cosmological perturbation theory at three-loop order. *Journal of Cosmology and Astroparticle Physics*, 1:10, January 2014.

[24] F. Bernardeau, A. Taruya, and T. Nishimichi. Cosmic propagators at two-loop order. *Physical Review D*, 89(2):023502, January 2014.

[25] Takahiro Nishimichi, Francis Bernardeau, and Atsushi Taruya. Response function of the large-scale structure of the universe to the small scale inhomogeneities. *Physics Letters B*, 762:247–252, November 2016.

[26] Atsushi Taruya and Stéphane Colombi. Post-collapse perturbation theory in 1D cosmology – beyond shell-crossing. *Monthly Notices of the Royal Astronomical Society*, 470(4):4858–4884, October 2017.

[27] Shohei Saga, Atsushi Taruya, and Stéphane Colombi. Lagrangian cosmological perturbation theory at shell-crossing. *Physical Review Letters*, 121(24):241302, December 2018.

[28] Anaëlle Halle, Takahiro Nishimichi, Atsushi Taruya, Stéphane Colombi, and Francis Bernardeau. Power spectrum response of large-scale structure in 1D and in 3D: Tests of prescriptions for post-collapse dynamics. *arXiv:2001.10417 [astro-ph]*, January 2020.

[29] Takahiro Nishimichi, Masahiro Takada, Ryuichi Takahashi, Ken Osato, Masato Shirasaki, Taira Oogi, Hironao Miyatake, Masamune Oguri, Ryoma Murata, Yosuke Kobayashi, and Naoki Yoshida. Dark quest. i. fast and accurate emulation of halo clustering statistics and its application to galaxy clustering. *The Astrophysical Journal*, 884(1):29, oct 2019.

[30] Nick Hand, Uroš Seljak, Florian Beutler, and Zvonimir Vlah. Extending the modeling of the anisotropic galaxy power spectrum to $k = 0.4 \text{ hMpc}^{-1}$. *Journal of Cosmology and Astroparticle Physics*, 2017(10):009, Oct 2017.

[31] Yosuke Kobayashi, Takahiro Nishimichi, Masahiro Takada, and Ryuichi Takahashi. Cosmological information content in redshift-space power spectrum of sdss-like galaxies in the quasinonlinear regime up to $k = 0.3 \ \ h \text{ mpc}^{-1}$. *Physical Review D*, 101:023510, Jan 2020.

[32] Planck Collaboration, P. A. R. Ade, N. Aghanim, M. Arnaud, M. Ashdown, J. Aumont, C. Baccigalupi, A. J. Banday, R. B. Barreiro, J. G. Bartlett, and et al. Planck 2015 results. XIII. Cosmological parameters. *Astronomy and Astrophysics*, 594:A13, September 2016.

[33] Y. P. Jing, H. J. Mo, and G. Börner. Spatial Correlation Function and Pairwise Velocity Dispersion of Galaxies: Cold Dark Matter Models versus the Las Campanas Survey. *The Astrophysical Journal*, 494:1–12, February 1998.

[34] U. Seljak. Analytic model for galaxy and dark matter clustering. *Monthly Notices of the Royal Astronomical Society*, 318:203–213, October 2000.

[35] J. A. Peacock and R. E. Smith. Halo occupation numbers and galaxy bias. *Monthly Notices of the Royal Astronomical Society*, 318:1144–1156, November 2000.

[36] Z. Zheng, A. A. Berlind, D. H. Weinberg, A. J. Benson, C. M. Baugh, S. Cole, R. Davé, C. S. Frenk, N. Katz, and C. G. Lacey. Theoretical Models of the Halo Occupation Distribution: Separating Central and Satellite Galaxies. *The Astrophysical Journal*, 633:791–809, November 2005.

[37] C. Alcock and B. Paczynski. An evolution free test for non-zero cosmological constant. *Nature*, 281:358, October 1979.

[38] T. Matsubara and Y. Suto. Cosmological Redshift Distortion of Correlation Functions as a Probe of the Density Parameter and the Cosmological Constant. *The Astrophysical Journal Letters*, 470:L1, October 1996.

[39] Teppei Okumura, Nick Hand, Uroš Seljak, Zvonimir Vlah, and Vincent Desjacques. Galaxy power spectrum in redshift space: Combining perturbation theory with the halo model. *Physical Review D*, 92(10):103516, Nov 2015.

[40] Yosuke Kobayashi, Takahiro Nishimichi, Masahiro Takada, Ryuichi Takahashi, and Ken Osato. Accurate emulator for the redshift-space power spectrum of dark matter halos and its application to galaxy power spectrum. *Physical Review D*, 102(6), Sep 2020.

[41] E. R. Harrison. Fluctuations at the threshold of classical cosmology. *Physical Review D*, 1:2726–2730, May 1970.

[42] Yaa B. Zeldovich. A hypothesis, unifying the structure and the entropy of the Universe. *Monthly Notices of the Royal Astronomical Society*, 160:1P, January 1972.

[43] Uros Seljak and Matias Zaldarriaga. A line-of-sight integration approach to cosmic microwave background anisotropies. *The Astrophysical Journal*, 469:437, Oct 1996.

[44] Jeremy L. Tinker, Brant E. Robertson, Andrey V. Kravtsov, Anatoly Klypin, Michael S. Warren, Gustavo Yepes, and Stefan Gottlöber. The large-scale bias of dark matter halos: Numerical calibration and model tests. *The Astrophysical Journal*, 724(2):878–886, Nov 2010.

[45] Florian Beutler et al. The clustering of galaxies in the completed SDSS-III Baryon Oscillation Spectroscopic Survey: baryon acoustic oscillations in the Fourier space. *Monthly Notices of the Royal Astronomical Society*, 464(3):3409–3430, 2017.

[46] N. Padmanabhan and M. White. Constraining anisotropic baryon oscillations. *Physical Review D*, 77(12):123540, June 2008.

[47] Hee-Jong Seo and Daniel J. Eisenstein. Probing Dark Energy with Baryonic Acoustic Oscillations from Future Large Galaxy Redshift Surveys. *The Astrophysical Journal*, 598:720–740, Dec 2003.

[48] W. Hu and Z. Haiman. Redshifting rings of power. *Physical Review D*, 68(6):063004, September 2003.

[49] D. J. Eisenstein, I. Zehavi, D. W. Hogg, R. Scoccimarro, M. R. Blanton, R. C. Nichol, R. Scranton, H.-J. Seo, M. Tegmark, Z. Zheng, S. F. Anderson, J. Annis, N. Bahcall, J. Brinkmann, S. Burles, F. J. Castander, A. Connolly, I. Csabai, M. Doi, M. Fukugita, J. A. Frieman, K. Glazebrook, J. E. Gunn, J. S. Hendry, G. Hennessy, Z. Ivezić, S. Kent, G. R. Knapp, H. Lin, Y.-S. Loh, R. H. Lupton, B. Margon, T. A. McKay, A. Meiksin, J. A. Munn, A. Pope, M. W. Richmond, D. Schlegel, D. P. Schneider, K. Shimasaku, C. Stoughton, M. A. Strauss, M. SubbaRao, A. S. Szalay, I. Szapudi, D. L. Tucker, B. Yanny, and D. G. York. Detection of the Baryon Acoustic Peak in the Large-Scale Correlation Function of SDSS Luminous Red Galaxies. *The Astrophysical Journal*, 633:560–574, November 2005.

[50] Doogesh Kodi Ramanah, Guilhem Lavaux, Jens Jasche, and Benjamin D. Wandelt. Cosmological inference from Bayesian forward modelling of deep galaxy redshift surveys. *Astronomy and Astrophysics*, 621:A69, 2019.

[51] C.-P. Ma and J. N. Fry. Deriving the Nonlinear Cosmological Power Spectrum and Bispectrum from Analytic Dark Matter Halo Profiles and Mass Functions. *The Astrophysical Journal*, 543:503–513, November 2000.

[52] R. Scoccimarro, R. K. Sheth, L. Hui, and B. Jain. How Many Galaxies Fit in a Halo? Constraints on Galaxy Formation Efficiency from Spatial Clustering. *The Astrophysical Journal*, 546:20–34, January 2001.

[53] A. Cooray and R. Sheth. Halo models of large scale structure. *Physics Reports*, 372:1–129, December 2002.

[54] J. F. Navarro, C. S. Frenk, and S. D. M. White. The Structure of Cold Dark Matter Halos. *The Astrophysical Journal*, 462:563, May 1996.

[55] B. Diemer and A. V. Kravtsov. A Universal Model for Halo Concentrations. *The Astrophysical Journal*, 799:108, January 2015.

[56] Benedikt Diemer and Michael Joyce. An accurate physical model for halo concentrations. *The Astrophysical Journal*, 871(2):168, Jan 2019.

[57] Benedikt Diemer. Colossus: A python toolkit for cosmology, large-scale structure, and dark matter halos. *The Astrophysical Journal Supplement Series*, 239(2):35, Dec 2018.

[58] C. Hikage, M. Takada, and D. N. Spergel. Using galaxy-galaxy weak lensing measurements to correct the finger of God. *Monthly Notices of the Royal Astronomical Society*, 419:3457–3481, February 2012.

[59] J. C. Jackson. A critique of Rees's theory of primordial gravitational radiation. *Monthly Notices of the Royal Astronomical Society*, 156:1P, 1972.

[60] Uroš Seljak. Redshift-space bias and β from the halo model. *Monthly Notices of the Royal Astronomical Society*, 325:1359–1364, August 2001.

[61] Martin White. The redshift-space power spectrum in the halo model. *Monthly Notices of the Royal Astronomical Society*, 321:1–3, February 2001.

[62] C. Hikage, R. Mandelbaum, M. Takada, and D. N. Spergel. Where are the Luminous Red Galaxies (LRGs)? Using correlation measurements and lensing to relate LRGs to dark matter haloes. *Monthly Notices of the Royal Astronomical Society*, 435:2345–2370, November 2013.

[63] A. Oka, S. Saito, T. Nishimichi, A. Taruya, and K. Yamamoto. Simultaneous constraints on the growth of structure and cosmic expansion from the multipole power spectra of the sdss dr7 lrg sample. *Monthly Notices of the Royal Astronomical Society*, 439(3):2515–2530, Feb 2014.

[64] S. Masaki, C. Hikage, M. Takada, D. N. Spergel, and N. Sugiyama. Understanding the nature of luminous red galaxies (LRGs): connecting LRGs to central and satellite subhaloes. *Monthly Notices of the Royal Astronomical Society*, 433:3506–3522, August 2013.

[65] S. More, H. Miyatake, R. Mandelbaum, M. Takada, D. N. Spergel, J. R. Brownstein, and D. P. Schneider. The Weak Lensing Signal and the Clustering of BOSS Galaxies. II. Astrophysical and Cosmological Constraints. *The Astrophysical Journal*, 806:2, June 2015.

[66] H. A. Feldman, N. Kaiser, and J. A. Peacock. Power-spectrum analysis of three-dimensional redshift surveys. *The Astrophysical Journal*, 426:23–37, 1994.

[67] Nick Hand, Yin Li, Zachary Slepian, and Uroš Seljak. An optimal fft-based anisotropic power spectrum estimator. *Journal of Cosmology and Astroparticle Physics*, 2017(07):002–002, Jul 2017.

[68] R. W. Hockney and J. W. Eastwood. *Computer Simulation Using Particles.* 1981.

[69] Kazuhiro Yamamoto, Masashi Nakamichi, Akinari Kamino, Bruce A. Bassett, and Hiroaki Nishioka. A measurement of the quadrupole power spectrum in the clustering of the 2df qso survey. *Publications of the Astronomical Society of Japan*, 58(1):93–102, Feb 2006.

[70] Román Scoccimarro. Fast estimators for redshift-space clustering. *Physical Review D*, 92(8), Oct 2015.

[71] Davide Bianchi, Héctor Gil-Marín, Rossana Ruggeri, and Will J. Percival. Measuring line-of-sight-dependent fourier-space clustering using ffts. *Monthly Notices of the Royal Astronomical Society: Letters*, 453(1):L11–L15, Aug 2015.

[72] K. Heitmann, M. White, C. Wagner, S. Habib, and D. Higdon. The Coyote Universe. I. Precision Determination of the Nonlinear Matter Power Spectrum. *The Astrophysical Journal*, 715:104–121, May 2010.

[73] K. Heitmann, D. Higdon, M. White, S. Habib, B. J. Williams, E. Lawrence, and C. Wagner. The Coyote Universe. II. Cosmological Models and Precision Emulation of the Nonlinear Matter Power Spectrum. *The Astrophysical Journal*, 705:156–174, November 2009.

[74] E. Lawrence, K. Heitmann, M. White, D. Higdon, C. Wagner, S. Habib, and B. Williams. The Coyote Universe. III. Simulation Suite and Precision Emulator for the Nonlinear Matter Power Spectrum. *The Astrophysical Journal*, 713:1322–1331, April 2010.

[75] Carl Edward Rasmussen and Christopher K. I. Williams. *Gaussian Processes for Machine Learning (Adaptive Computation and Machine Learning).* The MIT Press, 2005.

[76] Mischa Knabenhans, Joachim Stadel, Stefano Marelli, Doug Potter, Romain Teyssier, Laurent Legrand, Aurel Schneider, Bruno Sudret, Linda Blot, Saeeda Awan, Carlo Burigana, Carla Sofia Carvalho, Hannu Kurki-Suonio, and Gabriele Sirri. Euclid preparation: II. The EuclidEmulator – a tool to compute the cosmology dependence of the nonlinear matter power spectrum. *Monthly Notices of the Royal Astronomical Society*, 484(4):5509–5529, 01 2019.

[77] Euclid Collaboration, M. Knabenhans, J. Stadel, D. Potter, J. Dakin, S. Hannestad, T. Tram, S. Marelli, A. Schneider, R. Teyssier, S. Andreon, N. Auricchio, C. Baccigalupi, A. Balaguera-Antolínez, M. Baldi, S. Bardelli, P. Battaglia, R. Bender, A. Biviano, C. Bodendorf, E. Bozzo, E. Branchini, M. Brescia, C. Burigana, R. Cabanac, S. Camera, V. Capobianco, A. Cappi, C. Carbone, J. Carretero, C. S. Carvalho, R. Casas, S. Casas, M. Castellano, G. Castignani, S. Cavuoti, R. Cledassou, C. Colodro-Conde, G. Congedo, C. J. Conselice, L. Conversi, Y. Copin, L. Corcione, J. Coupon, H. M. Courtois, A. Da Silva, S. de la Torre, D. Di Ferdinando, C. A. J. Duncan, X. Dupac, G. Fabbian, S. Farrens, P. G. Ferreira, F. Finelli, M. Frailis, E. Franceschi, S. Galeotta, B. Garilli, C. Giocoli, G. Gozaliasl, J. Graciá-Carpio, F. Grupp, L. Guzzo, W. Holmes, F. Hormuth, H. Israel, K. Jahnke, E. Keihanen, S. Kermiche, C. C. Kirkpatrick, B. Kubik, M. Kunz, H. Kurki-Suonio, S. Ligori, P. B. Lilje, I. Lloro, D. Maino, O. Marggraf, K. Markovic, N. Martinet, F. Marulli, R. Massey, N. Mauri, S. Maurogordato, E. Medinaceli, M. Meneghetti, B. Metcalf, G. Meylan, M. Moresco, B. Morin, L. Moscardini, E. Munari, C. Neissner, S. M. Niemi, C. Padilla, S. Paltani, F. Pasian, L. Patrizii, V. Pettorino, S. Pires, G. Polenta, M. Poncet, F. Raison, A. Renzi, J. Rhodes, G. Riccio, E. Romelli, M. Roncarelli, R. Saglia, A. G. Sánchez, D. Sapone, P. Schneider, V. Scottez, A. Secroun, S. Serrano, C. Sirignano, G. Sirri, L. Stanco, F. Sureau, P. Tallada Crespí, A. N. Taylor, M. Tenti, I. Tereno, R. Toledo-Moreo, F. Torradeflot, L. Valenziano, J. Valiviita, T. Vassallo, M. Viel, Y. Wang, N. Welikala, L. Whittaker, A. Zacchei, and E. Zucca. Euclid preparation: Ix. euclidemulator2 – power spectrum emulation with massive neutrinos and self-consistent dark energy perturbations. *arXiv:2010.11288 [astro-ph]*, 2020.

[78] Joseph DeRose, Risa H. Wechsler, Jeremy L. Tinker, Matthew R. Becker, Yao-Yuan Mao, Thomas McClintock, Sean McLaughlin, Eduardo Rozo, and Zhongxu Zhai. The aemulus project. i. numerical simulations for precision cosmology. *The Astrophysical Journal*, 875(1):69, Apr 2019.

[79] Thomas McClintock, Eduardo Rozo, Matthew R. Becker, Joseph DeRose, Yao-Yuan Mao, Sean McLaughlin, Jeremy L. Tinker, Risa H. Wechsler, and Zhongxu Zhai. The aemulus project. ii. emulating the halo mass function. *The Astrophysical Journal*, 872(1):53, Feb 2019.

[80] Zhongxu Zhai, Jeremy L. Tinker, Matthew R. Becker, Joseph DeRose, Yao-Yuan Mao, Thomas McClintock, Sean McLaughlin, Eduardo Rozo, and Risa H. Wechsler. The aemulus project. iii. emulation of the galaxy correlation function. *The Astrophysical Journal*, 874(1):95, Mar 2019.

[81] V. Springel. The cosmological simulation code GADGET-2. *Monthly Notices of the Royal Astronomical Society*, 364:1105–1134, 2005.

[82] R. Scoccimarro. Transients from initial conditions: a perturbative analysis. *Monthly Notices of the Royal Astronomical Society*, 299:1097–1118, October 1998.

[83] M. Crocce, S. Pueblas, and R. Scoccimarro. Transients from initial conditions in cosmological simulations. *Monthly Notices of the Royal Astronomical Society*, 373:369–381, 2006.

[84] T. Nishimichi, A. Shirata, A. Taruya, K. Yahata, S. Saito, Y. Suto, R. Takahashi, N. Yoshida, T. Matsubara, N. Sugiyama, I. Kayo, Y. Jing, and K. Yoshikawa. Modeling Nonlinear Evolution of Baryon Acoustic Oscillations: Convergence Regime of N-body Simulations and Analytic Models. *Publications of the Astronomical Society of Japan*, 61:321–, February 2009.

[85] P. Valageas and T. Nishimichi. Combining perturbation theories with halo models. *Astronomy and Astrophysics*, 527:A87, March 2011.

[86] S. Ba, W. A. Brenneman, and W. R. Myers. Optimal Sliced Latin Hypercube Designs. *Technometrics.*, 57:479–487, October 2015.

[87] Chiaki Hikage, Masamune Oguri, Takashi Hamana, Surhud More, Rachel Mandelbaum, Masahiro Takada, Fabian Köhlinger, Hironao Miyatake, Atsushi J. Nishizawa, Hiroaki Aihara, Robert Armstrong, James Bosch, Jean Coupon, Anne Ducout, Paul Ho, Bau-Ching Hsieh, Yutaka Komiyama, François Lanusse, Alexie Leauthaud, Robert H. Lupton, Elinor Medezinski, Sogo Mineo, Shoken Miyama, Satoshi Miyazaki, Ryoma Murata, Hitoshi Murayama, Masato Shirasaki, Cristóbal Sifón, Melanie Simet, Joshua Speagle, David N. Spergel, Michael A. Strauss, Naoshi Sugiyama, Masayuki Tanaka, Yousuke Utsumi, Shiang-Yu Wang, and Yoshihiko Yamada. Cosmology from cosmic shear power spectra with Subaru Hyper Suprime-Cam first-year data. *Publications of the Astronomical Society of Japan*, 71(2):43, April 2019.

[88] P. S. Behroozi, R. H. Wechsler, and H.-Y. Wu. The ROCKSTAR Phase-space Temporal Halo Finder and the Velocity Offsets of Cluster Cores. *The Astrophysical Journal*, 762:109, January 2013.

[89] S. Agarwal, F. B. Abdalla, H. A. Feldman, O. Lahav, and S. A. Thomas. PkANN - I. Non-linear matter power spectrum interpolation through artificial neural networks. *Monthly Notices of the Royal Astronomical Society*, 424:1409–1418, August 2012.

[90] S. Agarwal, F. B. Abdalla, H. A. Feldman, O. Lahav, and S. A. Thomas. PkANN - II. A non-linear matter power spectrum interpolator developed using artificial neural networks. *Monthly Notices of the Royal Astronomical Society*, 439:2102–2121, April 2014.

[91] W D Jennings, C A Watkinson, F B Abdalla, and J D McEwen. Evaluating machine learning techniques for predicting power spectra from reionization simulations. *Monthly Notices of the Royal Astronomical Society*, 483(3):2907–2922, Nov 2018.

[92] Emiliano Sefusatti, Martin Crocce, Roman Scoccimarro, and Hugh Couchman. Accurate Estimators of Correlation Functions in Fourier Space. *Monthly Notices of the Royal Astronomical Society*, 460(4):3624–3636, 2016.

[93] G. Cybenko. Approximation by superpositions of a sigmoidal function. *Mathematics of Control, Signals and Systems*, 2:303–314, Dec 1989.

[94] Dan Hendrycks and Kevin Gimpel. Gaussian error linear units (gelus), 2016.

[95] Adam Paszke, Sam Gross, Francisco Massa, Adam Lerer, James Bradbury, Gregory Chanan, Trevor Killeen, Zeming Lin, Natalia Gimelshein, Luca Antiga, Alban Desmaison, Andreas Köpf, Edward Yang, Zach DeVito, Martin Raison, Alykhan Tejani, Sasank Chilamkurthy, Benoit Steiner, Lu Fang, Junjie Bai, and Soumith Chintala. Pytorch: An imperative style, high-performance deep learning library, 2019.

[96] Diederik P. Kingma and Jimmy Ba. Adam: A method for stochastic optimization, 2014.

[97] P. J. E. Peebles. *The large-scale structure of the universe.* 1980.

[98] Irshad Mohammed and Uroš Seljak. Analytic model for the matter power spectrum, its covariance matrix and baryonic effects. *Monthly Notices of the Royal Astronomical Society*, 445(4):3382–3400, December 2014.

[99] Kevin S. McCarthy, Zheng Zheng, and Hong Guo. The effects of galaxy assembly bias on the inference of growth rate from redshift-space distortions. *Monthly Notices of the Royal Astronomical Society*, 487(2):2424–2440, Aug 2019.

[100] N. Padilla, S. Contreras, I. Zehavi, C. M. Baugh, and P. Norberg. The effect of assembly bias on redshift-space distortions. *Monthly Notices of the Royal Astronomical Society*, 486(1):582–595, Jun 2019.

[101] D. J. Eisenstein, J. Annis, J. E. Gunn, A. S. Szalay, A. J. Connolly, R. C. Nichol, N. A. Bahcall, M. Bernardi, S. Burles, F. J. Castander, M. Fukugita, D. W. Hogg, Ž. Ivezić, G. R. Knapp, R. H. Lupton, V. Narayanan, M. Postman, D. E. Reichart, M. Richmond, D. P. Schneider, D. J. Schlegel, M. A. Strauss, M. SubbaRao, D. L. Tucker, D. Vanden Berk, M. S. Vogeley, D. H. Weinberg, and B. Yanny. Spectroscopic Target Selection for the Sloan Digital Sky Survey: The Luminous Red Galaxy Sample. *The Astronomical Journal*, 122:2267–2280, November 2001.

[102] Hironao Miyatake, Surhud More, Rachel Mandelbaum, Masahiro Takada, David N. Spergel, Jean-Paul Kneib, Donald P. Schneider, J. Brinkmann, and Joel R. Brownstein. The Weak Lensing Signal and the Clustering of BOSS Galaxies. I. Measurements. *The Astrophysical Journal*, 806(1):1, Jun 2015.

[103] R. Scoccimarro. Redshift-space distortions, pairwise velocities, and nonlinearities. *Physical Review D*, 70(8):083007, October 2004.

[104] A. Taruya, T. Nishimichi, S. Saito, and T. Hiramatsu. Nonlinear evolution of baryon acoustic oscillations from improved perturbation theory in real and redshift spaces. *Physical Review D*, 80(12):123503, December 2009.

[105] Teppei Okumura, Masahiro Takada, Surhud More, and Shogo Masaki. Reconstruction of halo power spectrum from redshift-space galaxy distribution: cylinder-grouping method and halo exclusion effect. *Monthly Notices of the Royal Astronomical Society*, 469(1):459–475, 2017.

[106] Jacek Guzik, Bhuvnesh Jain, and Masahiro Takada. Tests of Gravity from Imaging and Spectroscopic Surveys. *Physical Review D*, 81:023503, 2010.

[107] Kazuyuki Akitsu, Masahiro Takada, and Yin Li. Large-scale tidal effect on redshift-space power spectrum in a finite-volume survey. *Physical Review D*, 95(8):083522, Apr 2017.

[108] Digvijay Wadekar and Román Scoccimarro. Galaxy power spectrum multipoles covariance in perturbation theory. *Physical Review D*, 102(12), Dec 2020.

[109] Max Tegmark, Andy Taylor, and Alan Heavens. Karhunen-Loeve eigenvalue problems in cosmology: How should we tackle large data sets? *The Astrophysical Journal*, 480:22, 1997.

[110] Max Tegmark. Measuring cosmological parameters with galaxy surveys. *Physical Review D*, 79:3806–3809, 1997.

[111] Daniel J. Eisenstein et al. Detection of the Baryon Acoustic Peak in the Large-Scale Correlation Function of SDSS Luminous Red Galaxies. *The Astrophysical Journal*, 633:560–574, 2005.

[112] Masahiro Takada and Olivier Doré. Geometrical constraint on curvature with BAO experiments. *Physical Review D*, 92(12):123518, Dec 2015.

[113] Teppei Okumura and Y. P. Jing. Systematic Effects on Determination of the Growth Factor from Redshift-space Distortions. *The Astrophysical Journal*, 726(1):5, Jan 2011.

[114] Takahiro Nishimichi and Akira Oka. Simulating the anisotropic clustering of luminous red galaxies with subhaloes: a direct confrontation with observation

and cosmological implications. *Monthly Notices of the Royal Astronomical Society*, 444(2):1400–1418, Oct 2014.

[115] M. Gronke, C. Llinares, D. F. Mota, and H. A. Winther. Halo velocity profiles in screened modified gravity theories. *Monthly Notices of the Royal Astronomical Society*, 449(3):2837–2844, 2015.

[116] W. Hu and I. Sawicki. Models of f(R) cosmic acceleration that evade solar system tests. *Physical Review D*, 76(6):064004, September 2007.

[117] Kurt Hinterbichler and Justin Khoury. Symmetron Fields: Screening Long-Range Forces Through Local Symmetry Restoration. *Physical Review D*, 104:231301, 2010.

[118] L. Gao, V. Springel, and S. D. M. White. The age dependence of halo clustering. *Monthly Notices of the Royal Astronomical Society*, 363:L66–L70, October 2005.

[119] Risa H. Wechsler, Andrew R. Zentner, James S. Bullock, Andrey V. Kravtsov, and Brandon Allgood. The Dependence of Halo Clustering on Halo Formation History, Concentration, and Occupation. *The Astrophysical Journal*, 652(1):71–84, Nov 2006.

[120] Liang Gao and Simon D. M. White. Assembly bias in the clustering of dark matter haloes. *Monthly Notices of the Royal Astronomical Society*, 377:L5–L9, 2007.

[121] Neal Dalal, Martin White, J. Richard Bond, and Alexander Shirokov. Halo Assembly Bias in Hierarchical Structure Formation. *The Astrophysical Journal*, 687(1):12–21, Nov 2008.

[122] A. Faltenbacher and S. D. M. White. Assembly Bias and the Dynamical Structure of Dark Matter Halos. *The Astrophysical Journal*, 708:469–473, January 2010.

[123] Dragan Huterer and Masahiro Takada. Calibrating the nonlinear matter power spectrum: Requirements for future weak lensing surveys. *Astroparticle Physics*, 23:369–376, 2005.

[124] B. Joachimi and P. Schneider. The removal of shear-ellipticity correlations from the cosmic shear signal: Influence of photometric redshift errors on the nulling technique. *Astronomy and Astrophysics*, 507:105, 2009.

[125] D. G. York, J. Adelman, J. E. Anderson, Jr., S. F. Anderson, J. Annis, N. A. Bahcall, J. A. Bakken, R. Barkhouser, S. Bastian, E. Berman, W. N. Boroski, S. Bracker, C. Briegel, J. W. Briggs, J. Brinkmann, R. Brunner, S. Burles, L. Carey, M. A. Carr, F. J. Castander, B. Chen, P. L. Colestock, A. J. Connolly, J. H. Crocker, I. Csabai, P. C. Czarapata, J. E. Davis, M. Doi, T. Dombeck,

D. Eisenstein, N. Ellman, B. R. Elms, M. L. Evans, X. Fan, G. R. Federwitz, L. Fiscelli, S. Friedman, J. A. Frieman, M. Fukugita, B. Gillespie, J. E. Gunn, V. K. Gurbani, E. de Haas, M. Haldeman, F. H. Harris, J. Hayes, T. M. Heckman, G. S. Hennessy, R. B. Hindsley, S. Holm, D. J. Holmgren, C.-h. Huang, C. Hull, D. Husby, S.-I. Ichikawa, T. Ichikawa, Ž. Ivezić, S. Kent, R. S. J. Kim, E. Kinney, M. Klaene, A. N. Kleinman, S. Kleinman, G. R. Knapp, J. Korienek, R. G. Kron, P. Z. Kunszt, D. Q. Lamb, B. Lee, R. F. Leger, S. Limmongkol, C. Lindenmeyer, D. C. Long, C. Loomis, J. Loveday, R. Lucinio, R. H. Lupton, B. MacKinnon, E. J. Mannery, P. M. Mantsch, B. Margon, P. McGehee, T. A. McKay, A. Meiksin, A. Merelli, D. G. Monet, J. A. Munn, V. K. Narayanan, T. Nash, E. Neilsen, R. Neswold, H. J. Newberg, R. C. Nichol, T. Nicinski, M. Nonino, N. Okada, S. Okamura, J. P. Ostriker, R. Owen, A. G. Pauls, J. Peoples, R. L. Peterson, D. Petravick, J. R. Pier, A. Pope, R. Pordes, A. Prosapio, R. Rechenmacher, T. R. Quinn, G. T. Richards, M. W. Richmond, C. H. Rivetta, C. M. Rockosi, K. Ruthmansdorfer, D. Sandford, D. J. Schlegel, D. P. Schneider, M. Sekiguchi, G. Sergey, K. Shimasaku, W. A. Siegmund, S. Smee, J. A. Smith, S. Snedden, R. Stone, C. Stoughton, M. A. Strauss, C. Stubbs, M. SubbaRao, A. S. Szalay, I. Szapudi, G. P. Szokoly, A. R. Thakar, C. Tremonti, D. L. Tucker, A. Uomoto, D. Vanden Berk, M. S. Vogeley, P. Waddell, S.-i. Wang, M. Watanabe, D. H. Weinberg, B. Yanny, N. Yasuda, and SDSS Collaboration. The Sloan Digital Sky Survey: Technical Summary. *The Astronomical Journal*, 120:1579–1587, September 2000.

[126] Beth Reid, Shirley Ho, Nikhil Padmanabhan, Will J. Percival, Jeremy Tinker, Rita Tojeiro, Martin White, Daniel J. Eisenstein, Claudia Maraston, Ashley J. Ross, Ariel G. Sánchez, David Schlegel, Erin Sheldon, Michael A. Strauss, Daniel Thomas, David Wake, Florian Beutler, Dmitry Bizyaev, Adam S. Bolton, Joel R. Brownstein, Chia-Hsun Chuang, Kyle Dawson, Paul Harding, Francisco-Shu Kitaura, Alexie Leauthaud, Karen Masters, Cameron K. McBride, Surhud More, Matthew D. Olmstead, Daniel Oravetz, Sebastián E. Nuza, Kaike Pan, John Parejko, Janine Pforr, Francisco Prada, Sergio Rodríguez-Torres, Salvador Salazar-Albornoz, Lado Samushia, Donald P. Schneider, Claudia G. Scóccola, Audrey Simmons, and Mariana Vargas-Magana. SDSS-III Baryon Oscillation Spectroscopic Survey Data Release 12: galaxy target selection and large-scale structure catalogues. *Monthly Notices of the Royal Astronomical Society*, 455(2):1553–1573, 11 2015.

[127] Digvijay Wadekar, Mikhail M. Ivanov, and Roman Scoccimarro. Cosmological constraints from boss with analytic covariance matrices. *Physical Review D*, 102(12), Dec 2020.

[128] Nick Hand, Yu Feng, Florian Beutler, Yin Li, Chirag Modi, Uroš Seljak, and

Zachary Slepian. nbodykit: An open-source, massively parallel toolkit for large-scale structure. *The Astronomical Journal*, 156(4):160, Sep 2018.

[129] Francisco-Shu Kitaura, Sergio Rodríguez-Torres, Chia-Hsun Chuang, Cheng Zhao, Francisco Prada, Héctor Gil-Marín, Hong Guo, Gustavo Yepes, Anatoly Klypin, Claudia G. Scóccola, and et al. The clustering of galaxies in the sdss-iii baryon oscillation spectroscopic survey: mock galaxy catalogues for the boss final data release. *Monthly Notices of the Royal Astronomical Society*, 456(4):4156–4173, Jan 2016.

[130] Sergio A. Rodríguez-Torres, Chia-Hsun Chuang, Francisco Prada, Hong Guo, Anatoly Klypin, Peter Behroozi, Chang Hoon Hahn, Johan Comparat, Gustavo Yepes, Antonio D. Montero-Dorta, Joel R. Brownstein, Claudia Maraston, Cameron K. McBride, Jeremy Tinker, Stefan Gottlöber, Ginevra Favole, Yiping Shu, Francisco-Shu Kitaura, Adam Bolton, Román Scoccimarro, Lado Samushia, David Schlegel, Donald P. Schneider, and Daniel Thomas. The clustering of galaxies in the SDSS-III Baryon Oscillation Spectroscopic Survey: modelling the clustering and halo occupation distribution of BOSS CMASS galaxies in the Final Data Release. *Monthly Notices of the Royal Astronomical Society*, 460(2):1173–1187, 04 2016.

[131] Anatoly Klypin, Gustavo Yepes, Stefan Gottlöber, Francisco Prada, and Steffen Heß. Multidark simulations: the story of dark matter halo concentrations and density profiles. *Monthly Notices of the Royal Astronomical Society*, 457(4):4340–4359, Feb 2016.

[132] J. Hartlap, P. Simon, and P. Schneider. Why your model parameter confidences might be too optimistic. unbiased estimation of the inverse covariance matrix. *Astronomy and Astrophysics*, 464(1):399–404, Dec 2006.

[133] N. Aghanim, Y. Akrami, M. Ashdown, J. Aumont, C. Baccigalupi, M. Ballardini, A. J. Banday, R. B. Barreiro, N. Bartolo, and et al. Planck 2018 results. *Astronomy and Astrophysics*, 641:A6, Sep 2020.

[134] Benjamin Audren, Julien Lesgourgues, Karim Benabed, and Simon Prunet. Conservative constraints on early cosmology with montepython. *Journal of Cosmology and Astroparticle Physics*, 2013(02):001–001, Feb 2013.

[135] Thejs Brinckmann and Julien Lesgourgues. Montepython 3: boosted mcmc sampler and other features. *arXiv:1804.07261 [astro-ph]*, 2018.

[136] F. Feroz, M. P. Hobson, and M. Bridges. Multinest: an efficient and robust bayesian inference tool for cosmology and particle physics. *Monthly Notices of the Royal Astronomical Society*, 398(4):1601–1614, Oct 2009.

[137] Sunao Sugiyama, Masahiro Takada, Yosuke Kobayashi, Hironao Miyatake, Masato Shirasaki, Takahiro Nishimichi, and Youngsoo Park. Validating a minimal galaxy bias method for cosmological parameter inference using hsc-sdss mock catalogs. *Physical Review D*, 102(8), Oct 2020.

[138] ChangHoon Hahn, Roman Scoccimarro, Michael R. Blanton, Jeremy L. Tinker, and Sergio Rodríguez-Torres. The effect of fiber collisions on the galaxy power spectrum multipoles. *Monthly Notices of the Royal Astronomical Society*, page stx185, Jan 2017.

[139] Jeremy L. Tinker, Erin S. Sheldon, Risa H. Wechsler, Matthew R. Becker, Eduardo Rozo, Ying Zu, David H. Weinberg, Idit Zehavi, Michael R. Blanton, Michael T. Busha, and Benjamin P. Koester. Cosmological Constraints from Galaxy Clustering and the Mass-to-number Ratio of Galaxy Clusters. *The Astrophysical Journal*, 745(1):16, January 2012.

[140] S. More, B. Diemer, and A. V. Kravtsov. The Splashback Radius as a Physical Halo Boundary and the Growth of Halo Mass. *The Astrophysical Journal*, 810:36, September 2015.